ANALYSIS AND OPTIMISATION OF AN ORGANIC OPTICAL LINK

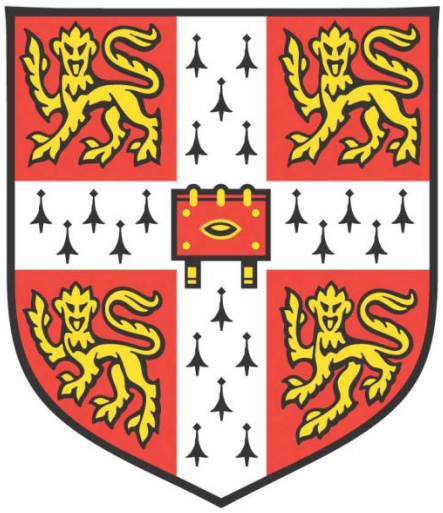

Priyanka Ekkanath de Souza

Jesus College

Department of Engineering

University of Cambridge

This dissertation is submitted for the degree of Doctor of Philosophy

September 2018

DECLARATION

This dissertation is the result of my own work and includes nothing which is the outcome of work done in collaboration except as declared in the Preface and specified in the text. It is not substantially the same as any that I have submitted, or, is being concurrently submitted for a degree or diploma or other qualification at the University of Cambridge or any other University or similar institution except as declared in the Preface and specified in the text. I further state that no substantial part of my dissertation has already been submitted, or, is being concurrently submitted for any such degree, diploma or other qualification at the University of Cambridge or any other University or similar institution except as declared in the Preface and specified in the text.

In accordance with the Department of Engineering guidelines, this thesis does not exceed 65,000 words, and it contains fewer than 150 figures.

Priyanka Ekkanath de Souza

ABSTRACT

Organic light-emitting diodes (OLEDs) have been historically used extensively for displays, and more recently for lighting applications. However, the low-cost of materials and direct-deposition manufacturing processes involved in organic semiconductor fabrication means that OLEDs are uniquely placed for low-cost integrated optical interconnects. This thesis presents novel high-speed analysis and optimisation of OLEDs for communications purposes. DC and small-signal measurement results for small-molecule OLEDs fabricated by Dr. Kou Yoshida at the University of St. Andrews are presented and are used to inform a detailed 5-layer OLED simulation model. Correlation is drawn between the experimental small signal impedance measurements and the experimental luminescent output, from which a novel electrical model is built to predict bandwidth. Extension of the OLED physical simulation shows for the first time that by using a constant fraction of the overall simulated device resistance (a 'luminescent resistance'), this RC-based model can be used to predict device small signal bandwidths, which suggests validity of both the simulation and the electrical modelling approach, provided that the exciton lifetime is less than the RC time-constant. This simulation is then used to forecast trends in device performance, allowing traditional inorganic semiconductor engineering tools to be brought into the field of organic device optimisation. Finally, these OLEDs are used in an optical link to provide a world-record equalisation-free OLED communications data rate of 130 Mbps.

To my families.

“Understand it well as I may, my comprehension can only be an infinitesimal fraction of all I want to understand.”

- Ada Lovelace

ACKNOWLEDGEMENTS

Firstly, I would like to thank my supervisor, Prof. Richard Penty, and my advisor, Prof. Ian White for all the opportunities, support and guidance they have offered over these years. I have learned much under their tutelage and without their encouragement and patience, completion of this thesis would not have been possible.

My thanks also go to Dr. Nikos Bamiedakis for all his essential time, support and assistance in setting up and running experiments, as well as for his feedback on my writing.

From the University of St. Andrews, my thanks go to Dr. Kou Yoshida for manufacturing the OLEDs used in this thesis, for all the time he spent answering my questions, and showing me around the cleanroom and through the whole OLED fabrication process. My thanks also go to Prof. Graham Turnbull and Prof. Ifor Samuel for their support of this and their helpful discussion.

I would also like to thank Dr. Guillaume Nataf for all his help in the thermal measurement of the OLEDs.

Thanks also go to Dr. Mario De Miguel Ramos for allowing use of the vector network analyser, and to Prof. Andrew Flewitt for giving permission to use his Silvaco license.

I would also like to thank Dr. David Cunningham for many insightful discussions about signal processing and equalisation.

From the Cavendish, for all their help in (as yet unsuccessful) inkjet printing OLEDs, my thanks go to Dr. Iyad Nasrallah for answering all my questions, setting up & training me on the Dimatix and prompt conversion of all my design files to printer-format, Dr. Guangru Li for his training in evaporation, as well as Prof. Henning Sirringhaus for permission to use the Cavendish cleanroom and the Dimatix printer.

Thanks also go to Kayla Friedman and Malcolm Morgan at the Centre for Sustainable Development for producing the template upon which this document is based.

I'd also like to thank all the members of the Centre for Photonic Systems (past and present) for being wonderful colleagues and friends.

From CAPE, particular thanks go to Jennifer McLaren-Jones and Cat Fitzpatrick for their general good cheer and friendship.

I would also like to thank all of my friends for their support, for being so understanding of all occasions missed because of work, and for their general good cheer. Special thanks go to Charlie Schoonman, Imogen Lambarth-Taylor and Victoria Barrett for their good advice, friendly lunches/dinners/coffees and sanity checks.

Of course, I would have never reached the end of my PhD without the support and assistance of my family. Thank you, mum and dad, for being the best parents, for always being there, for always offering to help, for all your words of advice and for being wonderful role-models. Thank you, Krish, for being the best little brother a sister could wish for.

Lastly, my thanks go to my fiancé, Tanuj, for always being there. From the very beginning of this journey, your eternal cheeriness and optimism has helped me through many late nights of work. You've been the greatest support anyone could have wished for.

PUBLICATIONS

1. P. E. de Souza, R. V, Penty and I. H. White, 'Artificial Neural Network Equalization for Integrated Polymer Optical Systems', *SIOE 2016*.

2. P. E. de Souza, N. Bamiedakis, K. Yoshida, P. P. Manousiadis, G. A. Turnbull, I. D. W. Samuel, R. V. Penty and I. H. White, 'High-Bandwidth Organic Light Emitting Diodes for Ultra-Low Cost Visible Light Communications Links', *ICTON 2018* (Invited).

IN PREPARATION

1. P. E. de Souza, N. Bamiedakis, K. Yoshida, P. P. Manousiadis, G. A. Turnbull, I. D. W. Samuel, R. V, Penty and I. H. White, 'Simulation studies on the behaviour of Organic Light Emitting Diodes', (in preparation).
2. P. E. de Souza, N. Bamiedakis, K. Yoshida, P. P. Manousiadis, G. A. Turnbull, I. D. W. Samuel, R. V, Penty and I. H. White, 'High-speed Modelling and Simulation of Organic Light Emitting Diodes for Communications', (in preparation).

CONTENTS

LIST OF TABLES

LIST OF FIGURES

List of Abbreviations and Acronyms

AFG	Arbitrary Function Generator
ANN	Artificial Neural Network
APD	Avalanche Photodiode
AWG	Arrayed Waveguide Gratings
BER	Bit Error Rate
BERT	Bit Error Rate Tester
CMOS	Complementary Metal Oxide Semiconductor
DC	Direct Current
DFE	Decision Feedback Equaliser
DMT	Discrete Multitone
EBL	Electron Blocking Layer
ECDM	Extended Correlated Disorder Model
(E)GDM	(Extended) Gaussian Disorder Model
EIL	Electron Injection Layer
EL	Electroluminescent
EML	Emissive Layer
ETL	Electron Transport Layer
FFE	Feedforward Equaliser
HBL	Hole Blocking Layer
HIL	Hole Injection Layer
HOMO	Highest Occupied Molecular Orbital
HTL	Hole Transport Layer
IR	Infra-Red

LIV	Light-Current-Voltage
LUMO	Lowest Unoccupied Molecular Orbital
MOST	Media Oriented Systems Transport
MZI	Mach-Zehnder Interferometer
(O)LED	(Organic) Light Emitting Diode
OOK	On-off keying
(O)PD	(Organic) Photodiode
PL	Photoluminescent
PLED	Polymer Light Emitting Diode
POF	Plastic Optical Fibre
PPM	Pulse Position Multitone
PRBS	Pseudo-Random Binary Sequence
SDM	Space Division Multiplexing
SM-OLED	Small Molecule Organic Light Emitting Diode
SM-OPD	Small Molecule Organic Photodiode
SOI	Silicon on Insulator
UHD-TV	Ultra-High Definition Television
UPS	Ultra-violet Photoelectron Spectroscopy
VNA	Vector Network Analyser
VLC	Visible Light Communications.
VR	Virtual Reality
XPS	X-ray Photoelectron Spectroscopy

LIST OF CHEMICALS USED

α-NPD	N,N'-di(naphthalene-1-yl)-N-N'-diphenylbenzidiene
BAlq	bis-(2-methyl-8-chinolinolato)-(4-phenyl-phenolato)-aluminium(III)
BPhen	4,7-diphenyl-1,10-phenanthroline
Cs	Caesium
F_6-TCNNQ	2,2'-(perfluoronaphthalene-2,6-diylidene)dimalononitrile
MADN	2-methyl-9,10-di(2-naphthyl)anthracene
Spiro-TTB	2,2',7,7'-tetrakis(N,N'-di-p-methylphenylamino)-9,9'-spirobifluorene
TBPe	2,5,8,11-tetra-tert-butylperylene

LIST OF APPENDICES

1 INTRODUCTION

1.1 Motivation

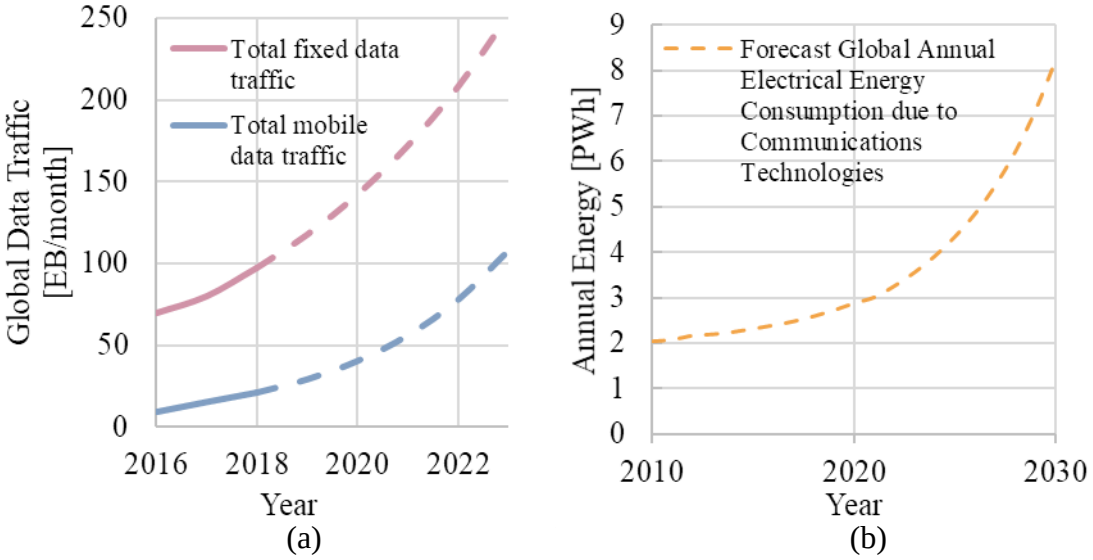

Fig. 1.1: (a) Forecast increase in global data traffic, redrawn based upon data from Ericsson Mobility Report, June 2018 [1], (b) Forecast electricity consumption due to communications technologies, redrawn based upon data from Andrae and Edler [2].

As the global rate of data exchange continues to increase at a staggering pace, the energy required to communicate information is also showing exponential growth trends, as seen in Fig. 1.1. The global energy usage attributable to communications technologies is forecast to represent 20% of global electricity consumption by 2030, of which 81% is expected to be consumed in data centres and transmission networks [2]. This growth in communications is set

to continue as we see the confluence of Internet of Things, Ultra High-Definition Television (UHD-TV), cloud computing and Big Data with technologies such as 5G and Radio over Fibre.

Consequently, it is imperative that work to reduce the energy-per-bit of data flow is concurrent with ongoing efforts to increase capacity and speed of end-to-end communications infrastructure links. For technologies to be adopted by industry, this expansion will need to occur in a cost-efficient manner. Tackling electronic bottlenecks in communications through photonic integration has already improved both the speed and the energy efficiency of internet communications, and it is necessary to extend this trend further onto the circuit board in order to achieve a reasonable energy per bit metric [3].

Current optical interconnect research explores different methods of interfacing electronics with optical technologies. While there is a large volume of research tackling the challenge of such bottlenecks in datacentres and high-performance computers, there is space within the market for low-cost optoelectronic interconnect technologies. In these instances, where cost, not speed, is the driving factor, high-volume, low-cost organic semiconductor technologies may prove to be the ideal trade-off technology for applications such as in cars, mobile phones, tablets, VR-systems, backplanes of UHD-TVs and other consumer technologies. At the moment, it is a challenge to directly compare the cost and speed of organic semiconductor technologies to inorganic semiconductors, largely because OLEDs represent a significantly less mature market than traditional LEDs, and because cost-improvements largely depend on volumes and equipment. Indeed, OLED lighting panels are estimated to have a cost of around $\$525/m^2$ in 2018, with this forecast to drop to $\$100/m^2$ by around 2025 as volumes of sales increase [4]. Furthermore, in the case of organic interconnects, cost-savings may be seen at a system- and integration-level, due to the direct deposition processing capabilities of organic semiconductors, rather than through comparison of the price of individual components.

The discovery of electroluminescence in polymer films by Partridge in 1983 [5] opened the doors for the development of organic light emitting diodes (OLEDs) by Tang and VanSlyke in 1987 [6]. Notably, their discovery of efficient, low-voltage electroluminescent diodes facilitated a new era of OLED devices; these were devices that demonstrated improved quantum efficiency and that did not require a high voltage (>100V) to observe electroluminescence, in contrast to the devices that had previously been reported in the literature [7]–[10]. The development of OLEDs then branched into two types: the evaporated small-molecule OLEDs

(SM-OLEDs), as originally developed by Tang and VanSlyke [6], and the subsequent invention of solution-processed polymer LEDs (PLEDs) by Burroughes et al. [11].

Since these early days, and despite the fact that organic semiconductors can have reliability problems (many organic semiconducting materials degrade when exposed to oxygen or water), OLED technology has matured into a commercial product. Currently, OLED displays alone are estimated to be a 20 billion dollar market in 2017 [12, p. 7]; this can be attributed to the high uptake of such displays in mobile devices due to the vivid colour rendering and improved energy efficiency associated with OLEDs. While research into OLED devices has historically focussed on display technologies, and more recently on lighting, this thesis presents OLEDs as an enabling technology that is ideally suited to low-cost optical interconnects, due to their easy manufacturability and integration potential. As opposed to the historic focus that OLEDs have received on improving brightness and quantum efficiency, we now look at optimising OLEDs for speed.

This thesis presents a systematic study of small-molecule OLEDs for communications applications. Chapter 2 provides background and motivation for the study of low-cost optical interconnects and discusses some of the existing interconnect technologies. In this chapter, OLEDs for communications are proposed for use as a low-cost integrated optical interconnect that has application in consumer electronics, as data consumption and generation continues to grow at an astonishing pace. Chapter 3 looks at the current understanding of the physics of organic semiconductors and OLEDs, as well as presenting some of the existing modelling and simulation that has been done in the literature. It is noted that the majority of published results have analysed OLED small signal impedance, without necessarily looking at how this electrical impedance affects the optical small signal response; the work presented here proposes an electrical model that demonstrates this for the first time. Chapter 4 presents DC measurements of the SM-OLEDs under study, and introduces the physical simulation used to model the OLEDs; the DC measurements of OLEDs that are missing one of the layers present in the ‘full stack’ is presented and found to fit well to simulation. Variation in identical devices manufactured on different substrates is ascribed to self-heating effects, and measurements to confirm this effect are presented. Chapter 5 presents the high-speed small-signal and large-signal measurements of these OLEDs; it was observed that under cooling, the optical bandwidths of the OLEDs were significantly reduced, suggesting that the thermally-varying mobility of the organic semiconductors is an important parameter in small signal optical

bandwidth. The large-signal measurements indicate a strong RC-limited electrical response for the OLEDs at all dimensions. In Chapter 6, electrical modelling of the small signal impedance is presented, and a methodology for correlating this small signal impedance to the optical bandwidth response is presented. The measurements presented in Chapter 5 are found to fit well to the suggested RC model, and a physical meaning for the resistance of this RC model as a Langevin recombination resistance (a proportion of the total resistance) is proposed. Furthermore, extension of the OLED simulation model to produce impedance parameters finds that by using a constant fraction of the simulated resistance as this aforementioned Langevin resistance, the physical simulation parameters very nicely reproduce the optical bandwidth response. The predictive ability of the simulation to model the OLED optical frequency response lends itself to device optimisation for speed, and forecasts of device bandwidths with varying layer thicknesses is undertaken. Finally, Chapter 7 presents world record 130 Mbps unequalised OLED data transmission, and with the implementation of a very simple 3-tap feedforward equaliser, this data rate is pushed to a world-record 200 Mbps transmission. Finally, conclusions and future work are presented in Chapter 8.

1.2 Novel Contributions

- A full 5-layer DC simulation of the OLED stack used is presented for the first time, and its output is experimentally validated. For comparison and for understanding, devices that exclude certain layers in the full OLED stack are manufactured, and the DC behaviour of these devices is simulated and found to fit well. This helps provide physical insight into the behaviour of various layers and their function within the whole stack.
- The self-heating effects of these OLEDs is measured, and the associated temperature-related behaviours are observed, leading to an understanding of the importance of the thermal behaviour of the substrate in system design.
- An electrical model is presented for the first time that relates the impedance measurements of the OLED to the optical bandwidth measurements of the device. It is observed that for the full stack OLEDs, their optical frequency response is well described by an RC time constant. The physical meaning of this time constant is proposed for the first time; the bandwidth response is described as the current response through a ‘Langevin recombination resistance’ in parallel with the OLED capacitance,

which explains this OLED behaviour. For the first time, an analytical expression for this resistance is proposed.

- A novel simulation of the small signal impedance response of this OLED stack is presented, and is found to fit well to the shape and final values of the measured small signal impedance, with deviations ascribed to differences in contact resistances and charge trapping in the measurements.
- The OLED bandwidth is found to be well predicted by the simulation model, by using a proportion of the simulated resistance as the 'Langevin recombination resistance' in parallel with the simulated capacitance in the aforementioned electrical model. Through use of a single fitting parameter, α, for any given device, that describes the Langevin fraction of the total simulated resistance, the electrical model in conjunction with the simulation model predicts the bandwidth behaviour for a single device across different bias currents. This is the first time this type of bandwidth-predictive model is presented, and enables bandwidth optimisation of OLEDs to be undertaken in a systematic manner for the first time.
- World-record 130 Mbps unequalised OLED data transmission is achieved, and with the implementation of a very simple adaptive 3-tap FFE-filter, OLED data transmission at a world-record 200 Mbps is shown to be possible, demonstrating OLED communications links as capable of reasonable data rates for many current and future consumer applications.

2 OPTICAL INTERCONNECTS

This chapter introduces the principle of the optical interconnect and some of the existing technologies used in high-speed optical interconnects. It is suggested that many of the existing optical interconnect technologies are applicable to relatively high-cost systems, and that organic optical interconnects may be able to provide moderate-speed integrated interconnects at low-cost. State-of-the-art existing organic devices and optical links are presented.

2.1 Introduction

Fundamentally, an optical interconnect is a method of transmitting information from one point to another. Given this relatively broad definition, the use of the term ‘optical interconnect’ can have different meanings based upon the technological context.

Historically, optical interconnects arose from the development of the laser and of high-quality optical fibres and amplifiers in the 1980s. This technological leap revolutionised global communications, allowing fibre optic systems to replace copper lines for long-distance telecommunications [13]. From this time, the advantages of optical interconnects over electrical interconnects have been apparent, with the adoption of photonic interconnects moving further and further into the traditional domain of electronics. Photonic technologies have been progressively moving upstream from long-haul communications to shorter datacommunications distances and to optical inter-rack interconnects within datacentres [14]. Research focus is now looking at methods of greater integration of photonics with electronics: both inter- and, eventually, intra-chip links. The reasoning behind this progressive adoption of

optical interconnects is clear: they offer a cost-effective method of transmitting information at high speed, at lower energies than their electrical equivalents [15]. They are free from many of the challenges that plague integrated circuit design, such as electromagnetic interference, impedance matching and parasitic capacitances, and can offer reduced cross talk and power dissipation [16]. In addition, the ability to multiplex different signals along a single optical line offers the advantage of compactness and reduced area relative to complex electrical interconnects [15].

While much research into optical interconnects has been driven by the pressure to meet the high-speed datacommunications requirements within datacentres, there are multiple technologies competing with electrical interconnection technologies at different data rates and length scales, each with their own advantages and disadvantages. Some of these options for optical interconnects of different formats include silicon photonics [17]–[19], plasmonics [20]–[22], free space optics [23]–[25], optical fibres [26]–[30] and integrated polymer waveguides of different configurations [31], [32]. These technologies are not necessarily mutually exclusive, and it is likely that there will be space to use different interconnect configurations, depending upon the specific application, length-scale, required speed and cost.

Given the relatively high system-price of many of the above proposed optical interconnect technologies, it is suggested that a significant market exists for low-cost integrated optical interconnects, especially as price is often a significant factor in technological adoption by industry. This work proposes organic optical systems as a good trade-off between speed and cost for such low-cost links. Applications in which these types of low-cost interconnects may be applicable are those such as in cars (where optical interconnects based on polymer optical fibre are already standardised [33]), in backplanes for ultra-high definition televisions (UHD-TV), mobile phones, augmented/virtual reality systems, and many other consumer devices. Furthermore, the relative low-cost of organic materials and their processing, in combination with the ability to integrate such devices in novel ways makes them advantageous when considering future flexible electronic products. This type of organic optical interconnect shows promise for low-power applications, such as in low-cost sensors, for on-board short-distance (~cm) communications or as low-cost opto-isolators. However, the disadvantage of organic devices is their reliability, as organic materials can have lifetime difficulties due to their sensitivity to oxygen and water. Nevertheless, with appropriate engineering and in relevant

applications, this may not be an impediment to organic optical links, as evidenced by the wide uptake of OLED displays.

Given the historical context of optical interconnect research within datacommunications, this chapter presents some of the proposed technologies for high-speed optical interconnects for datacentres, as they provide good insight into the status of the latest interconnect technologies. From this, the state of organic communications as a low-cost (and lower-speed) complement to these systems is presented.

2.2 Optical Interconnects for Datacentre Applications

As data flows increase around the world, continued use of our existing electronic interconnect infrastructure is consuming too much energy and causing bottlenecks in data rate [34]. As a result, research has been ongoing into various optical interconnects, with technologies competing for different markets within this space. A few different technologies have been proposed to tackle this bottleneck at different length scales. As datacentre inter-rack interconnects have become fibre-based, the next step is the emergence of intra-rack optical interconnects. While the majority of intra-rack interconnects are currently copper-based, one option for replacing intra-rack high-speed copper interconnects is the polymer waveguide optical backplane, which has advantages as it is a high-speed, low-loss and low-cost technology [35]. Another serious contender for short-range communications are silicon photonic waveguides [36]. However, the higher losses experienced by these waveguides would suggest that this technology would be best suited to fairly short distances of the order of a few centimetres or lesser. Beyond silicon photonics, plasmonics is also a potential technology for realisation of ultra-short on-chip very fast optical interconnects [37]; this is once again due to the high losses in such links. This perhaps suggests a high-speed ecosystem with polymer waveguides (or alternate technologies such as fibre optic cables) used for slightly longer intra-rack interconnects, with the silicon photonics platform well suited to the inter- or intra-chip scale.

2.2.1 Optical Backplane Technology

In contrast to many of the alternatives, polymer optical backplane technology offers a low-cost method of integration with existing electronics processing, whilst enabling the high-bandwidths, low-energy and small-sizes of optical interconnect technology. Polymer

waveguides are a low-cost solution that allows the optical interconnect to migrate onto the printed circuit board.

Within the Centre for Photonic Systems group, an error-free (BER < 10^{-12}) 4 x 10 Gbps optical signal has been transmitted through siloxane waveguides [38] and various waveguide components (such as bends, splitters and combiners) necessary to achieve on-board routing functionality and enable the implementation of different interconnection architectures have been demonstrated. A regenerative optical bus architecture has been designed and prototyped [39], and uptake of this terabit-capacity technology has the potential to move electro-optic integration one step closer to chip-level [35].

IBM have also heavily invested in polymer optical interconnect technology; their first generation polymer optical interconnect technology achieved 16 x 10 Gbps [40] by coupling the light into acrylate polymer waveguides using mirrors and lenses [41]. Their next generation polymer optical interconnect technology achieved 15 x 15 Gbps error-free (BER < 10^{-12}), this time with siloxane polymer waveguides [42].

Alternative configurations have also been explored; in 2013 Schmidtke *et al*. demonstrated a 960 Gbps optical interconnect system, by using both polymer waveguides and optical fibres in an optical backplane system [43]. This value has since been surpassed by Chujo *et al.* reporting a 7.2 Tbps optical backplane. They use ribbon fibre (polyimide) sheets to connect a high number of optical fibres, producing a high data-density within a small area (288 x 53 mm^2) [44].

IBM and Dow Corning have also produced *flexible* polymer waveguides for optical interconnect applications. They manufactured layers of waveguides on flexible substrates with propagation loss of less than 0.05 dB cm^{-1} between 760 and 860 nm [45]. The flexibility afforded by polymer waveguides allows an extra design dimension in optoelectronic integration technologies that is not afforded by competitors such as free-space optics [45].

2.2.2 Silicon Photonics

It is increasingly becoming apparent that silicon photonics is an emerging dominant technology for high-speed short-range interconnects for application within high-performance computing and datacentres. Research into silicon photonics has been largely driven by the desire to integrate photonics with CMOS electronics. Silicon has the advantage that it is relatively low-cost, and is optically transparent in the 1200-1700 nm telecommunications bands [46]. This has

allowed silicon waveguides to form the basis of these optical interconnects, although silicon waveguides suffer from relatively higher losses than their polymer equivalents, largely due to sidewall roughness. This means that silicon waveguide manufacturing processes have strict tolerances in order to achieve relatively low losses. Nevertheless, low-loss silicon photonic waveguides still typically exhibit propagation losses of the order of 0.3 dB cm^{-1} [47], [48]. However, from the silicon photonics platform, advanced waveguide devices such as ring resonators [49]–[52], arrayed waveguide gratings (AWGs) [53]–[55], Mach-Zehnder interferometers (MZIs) [56]–[58] and electro-absorption modulators [59], [60] have also been demonstrated.

The indirect bandgap nature of silicon has meant that integration of optical sources and detectors is a challenge for silicon photonics. Germanium is often used for photodetectors [61], [62] (and for electro-absorption modulators [60]), but the additional manufacturing required to add Ge to the silicon wafer adds cost and complexity to the overall interconnect. Still, the ability to monolithically integrate germanium devices on silicon often makes germanium photodetectors preferable to indium phosphide devices.

Relative to photodiode integration, integration of an appropriate optical source with the silicon photonics platform has proved quite challenging; current technologies explore methods of heterogeneously integrating appropriate laser sources with the silicon photonic components [63]. Options have included flip-chip processing [64]–[66], photonic wire bonding [67], [68] bonding III-V materials to the silicon or SOI substrates, either through fusion bonding [69], [70] or adhesive bonding [71], [72], or finally through epitaxial growth of semiconductor lasing materials on Si or SOI [73]–[76], using multiple buffer layers to reduce threading dislocations due to lattice mismatch. However, these epitaxially grown lasers suffer from poorer performance, yield and reliability [36], [77], which further makes these types of heterogeneous integrations less commercially attractive.

Furthermore, more than 90% of CMOS manufacturing is undertaken on bulk silicon [78], rather than on the silicon on insulator (SOI) configurations necessary for silicon photonic applications. Indeed, the SOI requirements for the electronics industry are not necessarily aligned with the photonics industry, with buried oxide thicknesses used in silicon photonics much higher than in CMOS manufacturing [79], and with the strict manufacturing tolerances required for high-quality silicon photonic devices. In the case of heterogeneous integration of III-Vs with silicon

photonics, this adds further manufacturing steps and expense to the overall photonic integrated circuit.

Nevertheless, although there are challenges to overcome, silicon-based photonics will likely have a future in high-speed optical interconnect technologies for high-performance, high-cost applications. This leaves space within the market for low-cost communications ecosystems to grow, such as those afforded by organic semiconductor communications links.

2.3 Low-Cost Organic Optical Interconnects

The ability to manufacture organic semiconductors using relatively low-cost materials and processes means that they are ideal for use in low-cost organic optical links, such as in cars, industrial sensors, entertainment systems, mobile phones and other consumer electronics. The high-speed polymer waveguides mentioned in §2.2.1 provide an ideal platform for such low-cost links, although polymer optical fibre (POF) is also commercially available for use in low-cost optical interconnects, and the final configuration of such a link would likely depend upon end-user application. In any case, the limiting component of such links is frequently the active device (OLED or OPD), and as such, this section looks at existing high-speed organic LEDs and photodiodes. As modulation rate is often a limiting factor in organic light emitting devices, a brief mention is made with regards to external organic modulators, which would be highly compatible with this organic ecosystem and have the potential to significantly increase the speeds of such organic optical interconnects.

2.3.1 OLEDs for Communications

Fundamentally, OLEDs for communications need to be optimised for bandwidth. For such devices to be considered in communications applications, OLEDs need to demonstrate at the very least ~MHz modulation rates, with the expectation that with advanced coding and equalisation techniques, such devices may aspire to ~Gbps data rates.

In order to manufacture fast-switching OLEDs, there are four critical parameters that must be taken into account: the device area, such that the capacitance-led RC-limit of these devices is minimised; the mobility of the organic semiconductor materials, such that there is fast carrier transport; good energy alignment between different layers, such that there is good charge injection; and short exciton lifetime, such that the charge carriers rapidly recombine to emit

light. A comparison of the state of the art OLED modulation rates may be found below in Table 2-1.

Table 2-1: State of the art OLED modulation rates

OLED Type	Modulation/Data Rate	Ref.
SM-OLED	100 MHz	[80]
SM-OLED	10 MHz	[81]
SM-OLED	≤10 MHz	[82]
SM-OLED	5 Mbps	[83]
SM-OLED	2.8 Mbps	[84]
PLED	63 MHz	[85]
PLED	20 MHz	[86]
PLED	20 Mbps	[87]

Historically, it has been quite a challenge to produce OLED devices with fast modulation rates, with early typical reported values of the order of ≤10 MHz [81]–[83]. Solution-processed OLEDs have lagged behind evaporated OLEDs in terms of modulation rates, with state of the art solution-processed OLED modulation rates of 63 MHz produced by Barlow *et al*. [85]. This is quite significant, given that previous attempts to fabricate solution-processed OLEDs had produced devices with modulation rates of the order of ~kHz [88], [89].

However, the highest reported modulation rates for OLEDs have been achieved by small-molecule OLEDs (SM-OLEDs), with the highest modulation rates achieved by Ohmori *et al*. in 2002 [80]. These small molecule OLEDs (SM-OLEDs) produced through vacuum evaporation techniques were capable of fast 100 MHz switching rates [90], [91].

With such limited available OLED bandwidths, it is reasonable to question the use of organic LEDs over organic lasers. Unfortunately, while optically-pumped organic lasers have been demonstrated since the 1990s [92], conclusive proof of electrically-pumped organic semiconductor lasers is yet to be demonstrated. This is largely due to the properties of the organic semiconductors themselves, including high-absorption losses, low carrier mobility and

high-losses at the contacts [93]; it is suggested that electrical pumping would require currents of the order of kA cm^{-2}, which is a significant challenge for organic materials [94].

In any review of OLEDs for communications, mention must be made of visible light communications (VLC), as this is a field in which organic semiconductors have thrived. As many organic LED materials have been developed from research into display technologies, these materials lend themselves well to use of the unregulated visible portion of the electromagnetic spectrum. By modulating LEDs used for lighting at an unnoticeably high rate, these same devices can be used simultaneously for communications (Li-Fi). Furthermore, advanced techniques can be used to overcome the inherent bandwidth limitation of LEDs for lighting. In the literature, artificial neural network (ANN) equalisation has reported a 20 Mbps transmission from a 350 kHz bandwidth polymer LED; a factor of improvement of over 55 [87]. Furthermore, the ability to use wavelength division multiplexing in addition to such equalisation techniques can result in high aggregate bandwidths: OLEDs implemented in VLC systems with an ANN equaliser have achieved over 54 Mbps aggregate capacity using three OLEDs with bandwidths of only 350, 110 and 600 kHz [95].

In addition to such novel equalisation techniques, different modulation formats have been proposed for VLC systems. The simplest modulation format is, of course, on-off keying (OOK), but other proposed formats have included pulse-position (PPM) and discrete multitone modulation (DMT) [96]–[99]. The advantages of these formats are that they are relatively robust to the variable channels and signal to noise ratios inherent in visible light communications. In particular, DMT allows sub-division of the bandwidth to optimally fit the response of the channel; this type of bit-loading may be useful to maximise the data rate through bandwidth-limited channels, such as those limited by the modulation rates of OLEDs as is the case in the communications links proposed here.

It is clearly possible to use advanced modulation and equalisation techniques to produce data rates that vastly exceed OLED bandwidth limitations. This is particularly important in VLC, where the primary function of the LED is for display or illumination purposes, and so the device dimensions are not necessarily able to be modified by communications engineers. However, where it is possible for low-cost links, and provided the active devices can modulate at the required speeds, simpler intensity modulation/direct detections schemes may be preferable.

2.3.2 OPDs for Communications

Similarly to OLEDs, OPDs for communications applications must exhibit high bandwidths. However, reported OPD bandwidths have historically been much higher than OLED bandwidths, with state of the art OPDs demonstrating a bandwidth of around 400 MHz [100]. These devices were manufactured by Peumans *et al*. from alternating thin layers of copper phthalocyanine (CuPc) and 3,4,9,10-perylenetetracarboxylic bisbenzimidazole (PTCBI). The alternating thin (0.5 nm) layers allows for efficient exciton dissociation and fast and efficient post-dissociation carrier tunnelling.

Other reported OPD responses have been significantly high, with an OPD made from N,N'-bis (2,5-di-tert-butylphenyl) 3,4,9,10-perylene dicarboximide (BPPC) and CuPc demonstrating a cutoff frequency of 70 MHz with peak responsivity between 500 and 550 nm [101]. Using F8T2 and PCBM, another OPD demonstrated modulation at 60 MHz [86] with responsivity between 400 and 500 nm [102]. These are frequencies of interest for integrated communications links with OLEDs emitting at these wavelengths.

2.3.3 Organic Modulators

An area that has been the subject of research has been electro-optic modulation using polymers. Such materials have the capacity to achieve modulation rates higher than that of traditional lithium niobate [103], and are suitable for short links [104]. Polymer electro-optic modulators have demonstrated modulation rates beyond 150 GHz [104], [105], and as OLEDs have relatively limited modulation rates, integrated engineering of such modulators into an optical interconnect may facilitate significant data rates.

In particular, the compatibility of polymer electro-optic modulators with polymer waveguides makes them an interesting prospect for integration in waveguide optical interconnections. Groumas *et al*. have demonstrated a 100 Gbaud link, based upon 100 GHz polymer electro-optic modulators integrated with a polymer waveguide and polymer Bragg-grating [106]. The very respectable modulation rates developed by polymer electro-optic modulators suggests that this is a very promising technology.

2.3.4 End-to-End Organic Optical Links

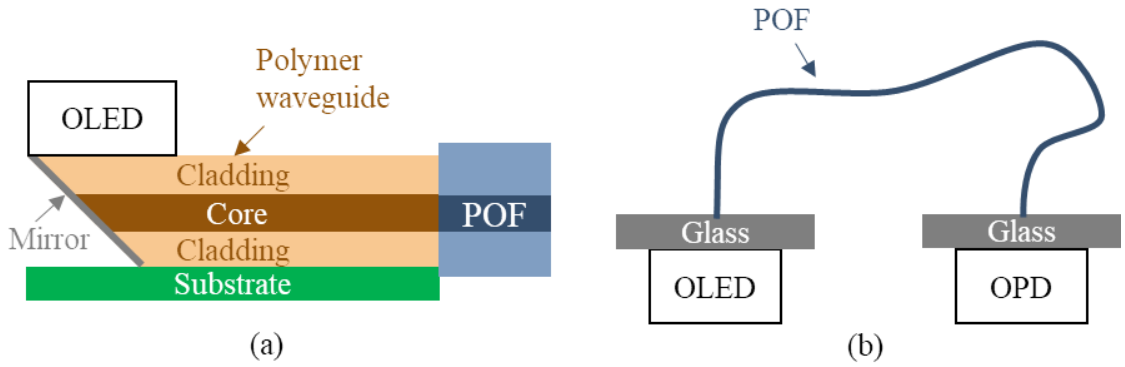

Fig. 2.1: Different methods of OLED integration in an organic optical link. In (a) the OLED is directly evaporated onto a polymer waveguide, as reported by Ohmori *et al.* [107] and (b) the OLED is glued to a POF, as reported by Punke *et al.* [84].

Finally, in terms of the state of the art with regards to end-to-end polymer interconnects, the highest speeds so far achieved have been demonstrated by Ohmori *et al*. with a 5 Mbps integrated end-to-end organic link using a polymer waveguide, OLED and OPD [107]. Although the OLED used in this link was capable of modulation at 100 MHz, the overall speed of transmission was limited by the OPD to 5 Mbps, as the OPD that they manufactured was not as fast as those reported in §0. In terms of organic POF links, Punke *et al*. similarly demonstrated a 2.8 Mbps organic link using an OLED and an OPD [84].

Different architectures have been proposed for integrated optical links. Ohmori et al. evaporated OLEDs directly onto polymer waveguides, which are separately coupled to POF, as shown in Fig. 2.1(a) [107]. The light-coupling was facilitated by a 45° mirror cut into the waveguides. In the case of Punke et al., the bottom-emitting OLED and bottom-absorbing OPD were butt-coupled to POF and attached using glue, shown in Fig. 2.1(b) [84].

Other reported methods of OLED integration with waveguides have involved coupling light through use of a diffuser, and simple evanescent coupling, as shown in Fig. 2.2, below [108], [109].

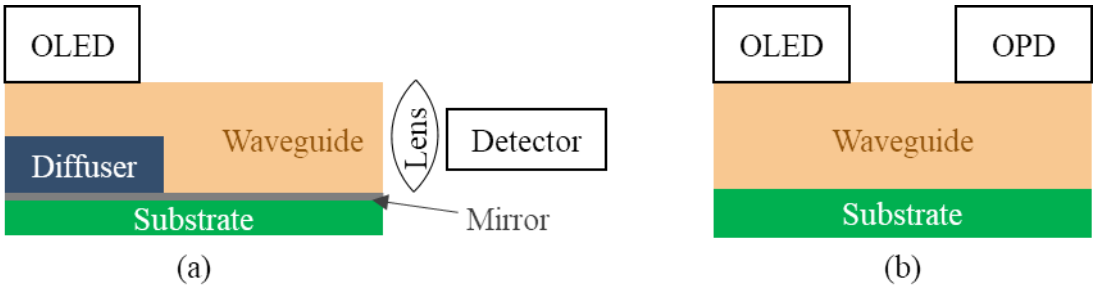

Fig. 2.2: OLED-waveguide integration (a) through use of a diffuser, as reported by Lin *et al*. [108] and (b) through evanescent coupling, as reported by Ramuz *et al.* [109].

2.4 Conclusions

In this chapter, various approaches to optical interconnects have been introduced. In recent years, it is becoming relatively clear that research is converging upon silicon photonics as an option for chip-scale high-speed and high-performance optical interconnects for use in data centres and high-performance computing, although there are still challenges to be overcome before this technology is widely adopted.

In contrast, there has been less work carried out in the areas of low-cost and low-energy photonic interconnect technologies to feed the increasing data demand on the consumer-side of this relationship. The relative low-complexity processing afforded by organic materials means that there is market potential for low-cost organic optical interconnects operating at modest data rates. While multimode polymer waveguide interconnects are on the way to being commercialised, there is the potential to integrate such components with active organic devices such as OLEDs and OPDs to form compact integrated photonic systems. While these links will not easily achieve the ≫Gbps that will shortly be required in datacentres, the ~Mbps that they can achieve (which can be enhanced by advanced modulation formats, wavelength multiplexing and equalisation techniques) will likely have use in alternate short-range, low-energy and low-cost communications requirements, such as on-board in end-user electronics and sensing circuits. In addition to this, the ability to manufacture organic devices on flexible substrates enables a host of new applications, such as flexible interconnects within vehicles or wearables. While OLEDs for displays are a relatively mature technology, little work has been done so far with regards to bandwidth performance and optimisation for speed. The literature has shown that current state of the art organic devices are capable of modulating at ~100 MHz, although little detailed analysis has been done on this so far. The novel results and analysis presented in

this thesis represents one step towards understanding and optimising organic device behaviour for communications.

3 PRINCIPLES OF ORGANIC SEMICONDUCTORS

This chapter provides an overview of the current understanding of organic semiconductor and OLED behaviour, with the aim of providing background understanding of the operation of the OLEDs and in order to build up to the modelling that will be introduced in later chapters. A picture is built of the doped organic layers that enable ohmic contacts to be formed, of the carrier blocking and transport layers that facilitate carrier flow into the centre of the OLED, where carriers form coulombically-bound excitons that recombine to emit light. The mobility is described as a thermally-activated hopping behaviour that empirically exhibits temperature-, field- and carrier-dependence, which helps describe some of the characteristics of organic LED behaviour.

3.1 Introduction

In order to improve the performance of organic LEDs for communications, it is first necessary to begin building an understanding of the physics of organic semiconductors. This chapter provides a brief introduction into such physics, and the significant differences that organic semiconductors demonstrate relative to inorganic semiconductors, such as their thermally-enhanced mobility. For many years, the carrier transport behaviour of organic semiconductors was not well understood and is still the subject of some debate. The purpose of this chapter is to introduce some of the physics that helps to explain some of the observed behaviours, and

concurrently build up a picture of the operation of organic LEDs. From a foundation of physical understanding, it is possible to construct electrical and physical models of OLED behaviour, and work towards simulation as a tool to be used both for better understanding of complex behaviours and for low-cost device optimisation.

3.2 Hybridisation of Orbitals

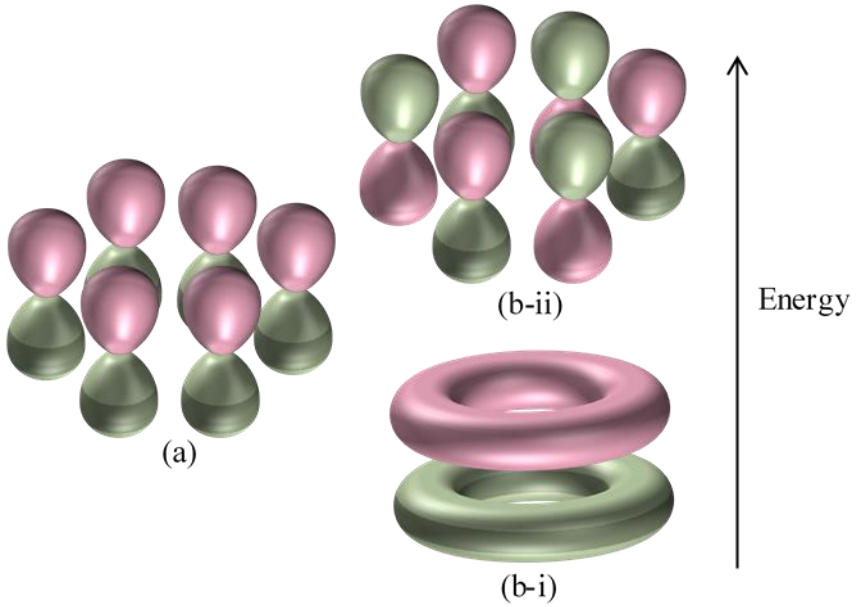

Fig. 3.1: (a) p-orbitals, which can overlap in a conjugated molecule to form (b-i) bonding and (b-ii) antibonding orbitals.

The vast majority of organic semiconductors materials are π-conjugated; that is to say, they have alternating single and double bonds. While three of the outer-shell electrons on each carbon atom form covalent σ-bonds with adjacent carbon atoms, the final electron forms a delocalized π-bond due to overlapping p-orbitals. This charge delocalisation exists along the conjugated backbone of the molecule, and thereby allows electrons and holes to travel. These π-orbitals can form as either bonding or as antibonding orbitals, as shown in Fig. 3.1. These bonding and antibonding orbitals have different energy levels, and, in the presence of the overlap of many p-orbitals, can form two energetic ‘bands’ – the highest occupied molecular orbital (HOMO) and the lowest unoccupied molecular orbital (LUMO). Thus, analogously to inorganic semiconductors, organic semiconductors form a ‘band gap’, caused by the difference in the energy levels of the HOMO and LUMO. The electron-delocalisation associated with the overlapping orbitals allows charges to travel along the conjugation length of a single molecule.

However, transport between disordered molecules must be undertaken by phonon-assisted quantum-mechanical tunnelling, which results in a characteristic intra-molecular 'hopping' transport mechanism [110]. This is in contrast to the conventional band-like transport that is observed in inorganic semiconductors (and is indeed much slower). However, the exact mechanism of carrier transport within organic semiconductors is still the subject of some debate within the academic community; this chapter will discuss some of the proposed mobility models in greater detail.

It must also be noted that organic semiconductors fall into two major groups: small molecules, and polymers. Small molecule materials are predominantly vacuum processed, but frequently display higher mobilities than their solution-processed polymer cousins. Some common organic materials are presented below in Fig. 3.2; the conjugated portions of each of these molecules (the benzene rings) can clearly be observed.

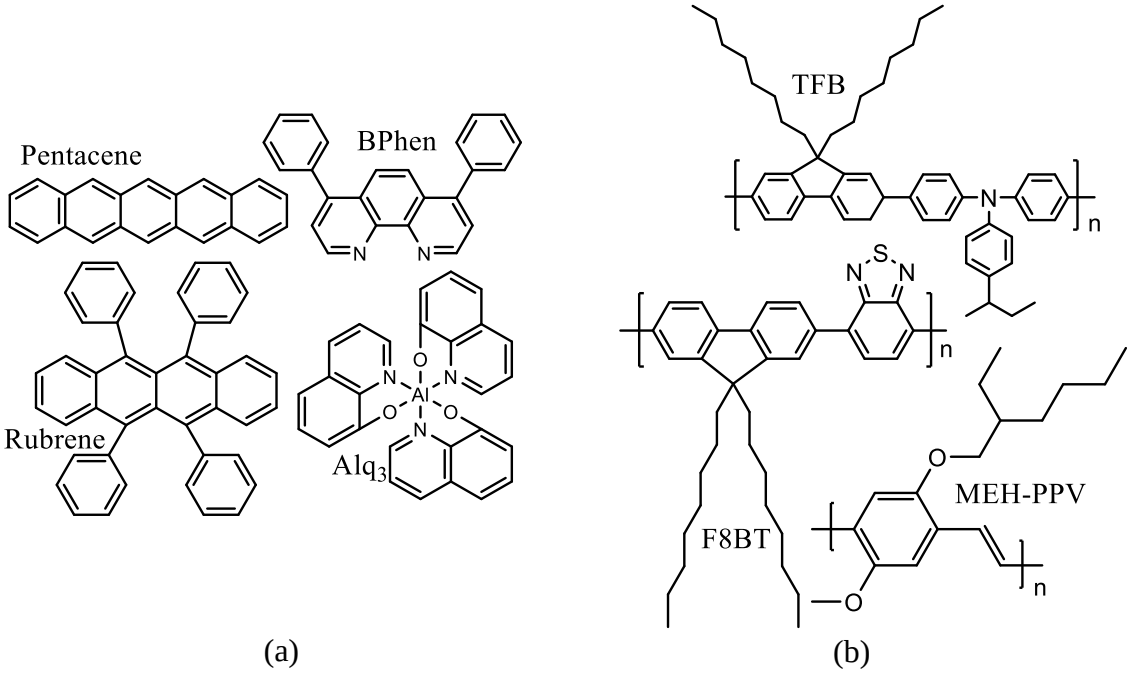

Fig. 3.2: Some common (a) small molecule and (b) polymer organic semiconductors.

The aggregate effect of having multiple atoms and molecules as in a deposited layer of material broadens the singular HOMO and LUMO levels into a Gaussian distribution of HOMO and LUMO levels. By this mechanism, the density of states of a material is best described by Eq. (3.1), below.

$$g(E) = \frac{N_0}{\sqrt{2\pi\sigma^2}} \exp\left(-\frac{(E - E_0)^2}{2\sigma^2}\right) \quad (3.1)$$

This expression for density of states is defined by the density of sites N_0, the disorder within the material σ, and the energy level at the centre of the band E_0.

3.3 Doping Principles

In a similar manner to inorganic semiconductors, organic semiconductors can indeed be doped, and improvements in conductivities and mobilities[1] are observed as a result [112], [113]. Doping of organic semiconductors has been undertaken using a variety of compounds and molecules [114], with p-type doping frequently undertaken by molecular dopants, as their large molecular sizes help to reduce problems associated with dopant diffusion [115]. However, n-type doping of organic semiconductors is frequently undertaken by alkali metals or metal salts, due to the challenge in finding molecular compounds with appropriate energy levels [114].

Commonly proposed theory suggests that the mechanism of molecular doping is via a two-step process wherein a dopant forms an ionised charge-transfer state with the host molecule. This charge transfer state then thermally dissociates such that the charge is then mobile and able to hop between molecules [116], [117].

$$MMA \rightleftharpoons M[M^+A^-] \rightleftharpoons MM^+A^- \rightleftharpoons M^+MA^- \quad (3.2)$$

Alternative suggested doping mechanisms have included orbital hybridisation between the host and the dopant [118], although research investigating the exact doping mechanism of organic semiconductors is still ongoing, as this mechanism is not fully understood [119].

Dopant concentrations in organic semiconductors are normally significantly higher than in inorganic semiconductors; usually of the order of a few wt. % of the host material. Despite this,

[1] Doping has been measured to both increase and decrease mobility of organic semiconductors, depending on the semiconductor and dopant. Measurements of decreased mobility is normally due to increased trap states [111], However, improved mobility for some materials is explained by the fact that doping can act to fill trap states and thereby improve the mobility [112]. Furthermore, in strongly disordered organic materials, at high doping levels the potential wells of dopant sites can overlap, enabling higher mobility [113]. Thus, the effect of doping on mobility is not easily generalised, and significantly depends upon the specific materials and concentrations used.

doping efficiencies $\left(\eta = \frac{p}{N_A}\right)$ in organic semiconductors are normally measured to be fairly low (< 10%) [115], [116], [120], [121].

While doping can improve the carrier injection and mobility, it can also act to quench light emission. However, doping is necessary for efficient charge injection at contacts, where UPS measurements have shown that doping in charge-injection layers act to move the Fermi level closer to the transport level [115], [122], [123]. At metal/organic interfaces, this presents 'band-bending' that allows more efficient charge injection and allows for the formation of quasi-ohmic contacts [124].

3.4 Charge Transport

The specifics of charge transport within organic semiconductors is still the subject of some debate [125]–[130]. Different mobility models take different effects into account, such as polaronic disorder[2], and have received varying levels of experimental validation and consensus within the literature. The true mobility of these semiconductors may be some combination of proposed mobility models, and the degree to which these different models apply may also depend on the specifics of the organic semiconductor under study. In this section, some of the more commonly proposed mobility models for disordered organic semiconductors are introduced.

3.4.1 Hopping Transport Models

It is widely acknowledged that carrier transport within disordered, amorphous organic semiconductors is via localised hopping between molecules [110]. Two commonly used hopping rates to define an overall mobility for the organic semiconductor are the Miller-Abrahams hopping rate, and the Marcus hopping rate [131], [132].

[2] A polaron is a quasi-particle that describes both the local charge carrier (such as an electron), plus the distortion associated with that charge carrier upon the local molecules, as the charge carrier acts to distort the local bonds in a disordered organic solid.

Miller-Abrahams Hopping

$$v_{ij} = \nu_0 \exp\left(-2\gamma a\left(\frac{R_{ij}}{a}\right)\right)\begin{cases}\exp\left(-\dfrac{E_j - E_i}{kT}\right) & E_j > E_i \\ 1 & E_j \leq E_i\end{cases} \quad (3.3)$$

Miller-Abrahams hopping describes the hopping rate (v_{ij}) in terms of a hopping attempt frequency (ν_0), an inverse localisation radius of the wave function (γ), the distance between state i and state j (R_{ij}), the lattice constant (a), and the energy of the state ($E_{j,i}$). Effectively, the first exponential represents a tunnelling portion of the hopping rate, and the second represents a thermal activation required for the electron to hop to an energetically higher state.

Marcus Hopping

$$v_{ij} = \frac{\left|I_{ij}\right|^2}{\hbar}\sqrt{\frac{\pi}{\lambda kT}}exp\left(-\frac{\left(\Delta G_{ij} + \lambda\right)^2}{4\lambda kT}\right) \quad (3.4)$$

The Marcus hopping rate is similar to the Miller-Abrahams hopping rate in that it contains both a tunnelling contribution and a thermally activated portion, but is slightly more sophisticated in that it includes a contribution due to polaronic effects (λ). I_{ij} represents the transfer integral between the two sites (i.e. represents the overlap of the wavefunctions), λ is the molecular reorganisation energy associated with relaxation of the molecule and ΔG_{ij} is the difference in energies of the two sites.

3.4.2 Extended Gaussian Disorder Model (EGDM)

Both of the hopping rates mentioned in the previous section have been used to develop mobility models for organic semiconductors [125], [133]–[137]. One early model based upon the Miller-Abrahams rate was developed by Bässler, known as the Gaussian Disorder Model (GDM) [138]. Based upon a Gaussian density of states, the $2\gamma a$ term in the Miller-Abrahams model is split into a contribution from positional disorder Σ and an energetic disorder portion σ. Monte-Carlo analysis of this system then produces the GDM expression for mobility, shown in Eq. (3.5).

$$\mu(\hat{\sigma}, F) = \mu_0 \exp\left(-\frac{4\hat{\sigma}^2}{9}\right)\begin{cases}\exp\left(C(\hat{\sigma}^2 - \Sigma^2)\sqrt{F}\right) & for\ \Sigma \geq 1.5 \\ \exp\left(C(\hat{\sigma}^2 - 2.25^2)\sqrt{F}\right) & for\ \Sigma < 1.5\end{cases} \quad (3.5)$$

In this model, C is an empirical constant found to be 2.9×10^{-4} (cm/Vs)$^{0.5}$, μ_0 is the zero-field mobility, and F is the electric field [138].

However, this model does not take into account the effect of carrier density upon the mobility. In order to correct for this, the Extended Gaussian Disorder Model (EGDM) was developed by Pasveer *et al.* [139], also similarly based upon numerical solution of Miller-Abrahams hopping rates. This model defines the mobility based upon temperature, carrier density and electric field, as per Eqs. (3.6-3.11).

$$\mu(T,p,E) \approx \mu(T,p) f(T,F) \tag{3.6}$$

$$\mu(T,p) = \mu_0(T) \exp\left(\frac{1}{2}(\hat{\sigma}^2 - \hat{\sigma})(2pa^3)^{\delta}\right) \tag{3.7}$$

$$\mu_0(T) = \mu_0 c_1 \exp(-c_2 \hat{\sigma}^2) \tag{3.8}$$

$$\delta \equiv \frac{2\ln(\hat{\sigma}^2 - \hat{\sigma}) - \ln(\ln 4)}{\hat{\sigma}^2}, \mu_0 \equiv \frac{a^2 v_0 e}{\sigma} \tag{3.9 - 3.10}$$

$$f(T,F) = \exp\left\{0.44\left(\hat{\sigma}^{\frac{3}{2}} - 2.2\right)\left[\sqrt{1 + 0.8\left(\frac{Fea}{\sigma}\right)^2} - 1\right]\right\} \tag{3.11}$$

In these equations, the disorder parameter σ is converted into a dimensionless disorder parameter $\hat{\sigma} = \frac{\sigma}{kT}$, p is the charge carrier density, a is the lattice constant, ν_0 is the hopping attempt frequency, and c_1 and c_2 are found empirically to be $c_1 = 1.8 \times 10^{-9}$ and $c_2 = 0.42$ [139].

The EGDM does not take into account correlation between energetic and positional disorder; an alternative formalism taking this into account has been developed from Miller-Abrahams hopping rates, known as the Extended Correlated Disorder Model (ECDM) [140]. This model is described by the following set of equations, and may provide a better description of mobility in materials where polaronic effects are significant.

$$\mu(T,p,F) = \left(\left(\mu_{low}(T,p,F)\right)^{q(\hat{\sigma})} + \left(\mu_{high}(p,F)\right)^{q(\hat{\sigma})}\right)^{\frac{1}{q(\hat{\sigma})}} \tag{3.12}$$

$$q(\hat{\sigma}) = \frac{2.4}{1 - \hat{\sigma}} \tag{3.13}$$

$$\mu_{low}(T,p,F) = \mu_0(T) g(T,p) f(T,F,p) \tag{3.14}$$

$$\mu_0(T) = \mu_0 c_1 \exp(-0.29\hat{\sigma}^2) \tag{3.15}$$

$$g(T,p) = \begin{cases} \exp\left[(0.25\hat{\sigma}^2 + 0.7\hat{\sigma})(2pa^3)^{\delta}\right] & pa^3 < 0.025 \\ g(T, 0.025a^{-3}) & pa^3 \geq 0.025 \end{cases} \tag{3.16}$$

$$f(T,F,p) = \exp\left[h(F^*)\left(1.05 - 1.2(pa^3)^{r(\hat{\sigma})}\right)\left(\hat{\sigma}^{\frac{3}{2}} - 2\right)\left(\sqrt{1+2F^*} - 1\right)\right] \tag{3.17}$$

$$r(\hat{\sigma}) = 0.7\hat{\sigma}^{-0.7} \tag{3.18}$$

$$h(E^*) = \begin{cases} \frac{4}{3}\left(\frac{F^*}{0.16}\right) & F^* \leq 0.08 \\ \left[1 - \frac{4}{3}\left(\frac{F^*}{0.16} - 1\right)^2\right] & 0.08 < F^* \leq 0.16 \\ 1 & F^* > 0.16 \end{cases} \tag{3.19}$$

$$\mu_{high}(p,\mathrm{F}) = \exp(-2\,\gamma a)\left(\frac{a\nu_0}{F}\right)(1 - pa^3) \tag{3.20}$$

$$\delta \equiv 2.3\frac{\ln(0.5\hat{\sigma}^2 + 1.4\hat{\sigma}) - 0.327}{\hat{\sigma}^2}, F^* \equiv \frac{eaF}{\sigma}$$

c_1 is empirically found to be 1.0×10^{-9} [140].

3.4.3 Poole-Frenkel Mobility Model

The growing complexity and variants of organic semiconductor mobility models represents attempts to unify the behaviour of different organic semiconductors under different conditions. However, this presents some complication, as there are now multiple mobility models used to fit measurements of different materials. In the absence of consensus to a unified mobility model, the empirical Poole-Frenkel temperature and field-dependent mobility model of the form in Eqs. (3.21-3.22) shows a good fit to measured mobility characteristics, although it does not provide explanation for these results [141]–[144].

$$\mu(F,T) = \mu_0(T)\exp\left(\gamma\sqrt{F}\right) \tag{3.21}$$

$$\mu_0(T) = \mu_0\, exp\left(-\frac{\Delta}{kT}\right) \tag{3.22}$$

In these equations, μ_0 refers to the zero-field low-temperature mobility, Δ is an activation energy, k is the Boltzmann constant, T is temperature, γ is a field-dependence factor and F is the electric field.

The ready availability of data fit to the Poole-Frenkel model means that it is possible to emulate overall device behaviour for engineering purposes, without the requirement for detailed description of the molecular dependencies upon transport, such as the aforementioned polaronic effects. With this in mind, the empirical Poole-Frenkel mobility model offers much advantage (and reduced complexity) for the purposes of device design and optimisation.

3.5 Recombination

The low relative permittivity of organic semiconductors (~3) means that localised electrons and holes in these materials form coulombically bound quasi-particles known as excitons. In organic semiconductors, these are called Frenkel excitons [145], which have relatively small radii (existing on the same molecule); in inorganic semiconductors, the excitons tend to have large radii and are known as Wannier-Mott excitons [146]. Charge-transfer excitons also exist in organic semiconductors, where the bound exciton exists between different adjacent molecules. In organic semiconductors, it is the relaxation of these excitons that provides the luminescence seen in OLED devices. Where the exciton exists across two molecules in an organic semiconductor (such as a dopant and a host), the exciton effectively bonds the molecules and can be known as an exciplex (excited complex) or excimer (excited dimer).

An important consideration in the context of recombination is the spin states of these excitons. Depending upon the spin state, these excitons may be either considered to be singlet excitons (spin quantum number $S = 0$), or triplet excitons ($S = 1$). As electrons are spin-1/2 particles, there are three states with $S = 1$, and one state where $S = 0$; therefore, according to standard spin statistics, this would suggest a singlet:triplet generation ratio of 1:3. As the electrons in singlet excitons have opposing spin, recombination of singlet excitons does not violate Pauli's exclusion principle, and this radiative recombination has a relatively short lifetime (~ns) [147]. This type of recombination is termed fluorescence. However, as triplet excitons are formed from electrons with the same spin state, direct radiative recombination of such excitons is theoretically forbidden, and these excitons have a much longer lifetime (~μs) [148]. Although theoretically impermissible, triplet states can eventually radiatively decay due to spin-orbit coupling, and this slow emission from triplet states is termed phosphorescence.

In contrast to research into OLEDs for displays, where phosphorescence is a mechanism by which enhanced device efficiencies may be obtained, in the context of OLEDs for

communications, fast fluorescence is preferable to slow phosphorescent decay, which can limit device modulation rates.

Fig. 3.3, below, shows some of the different energetic transitions possible within an organic semiconductor.

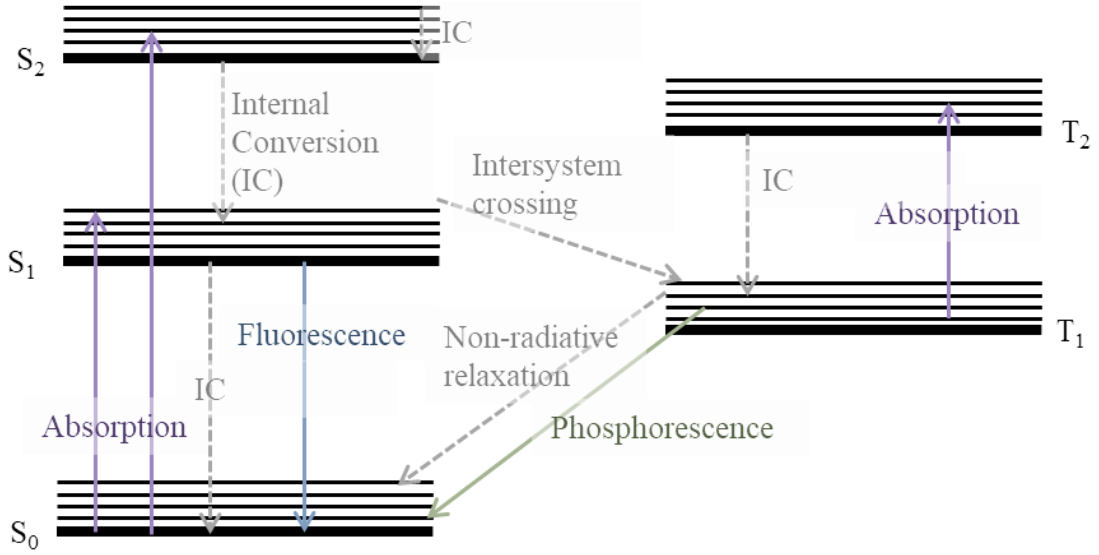

Fig. 3.3: Jablonski diagram to show different types of radiative (solid lines) and non-radiative (dashed lines) energetic transitions within an organic semiconductor. S_n and T_n refer to singlet and triplet energy levels.

Excitons may also travel within an organic semiconductor through three different mechanisms: photon emission and re-absorption, Förster or Dexter transfer [149], [150]. The first of these mechanisms occurs when an exciton recombines to form a photon, which is re-absorbed elsewhere in the material. The second mechanism, Förster transfer, as shown in Fig. 3.4(a), is a process that occurs through resonant dipole interactions between two molecules to transfer the exciton from one molecule to another, and can occur at distances of up to 10 nm [151]. This is mechanism is important in doped organic LEDs, as it allows host-molecules to transfer excitons to fast-emitting fluorescent (or phosphorescent) dopant molecules. The final mechanism, Dexter transfer, (Fig. 3.4(b)) is very short range, as the molecules must have overlap of their wavefunctions. Dexter transfer, involves electrons tunnelling from one molecule to another due to this overlap of wavefunctions.

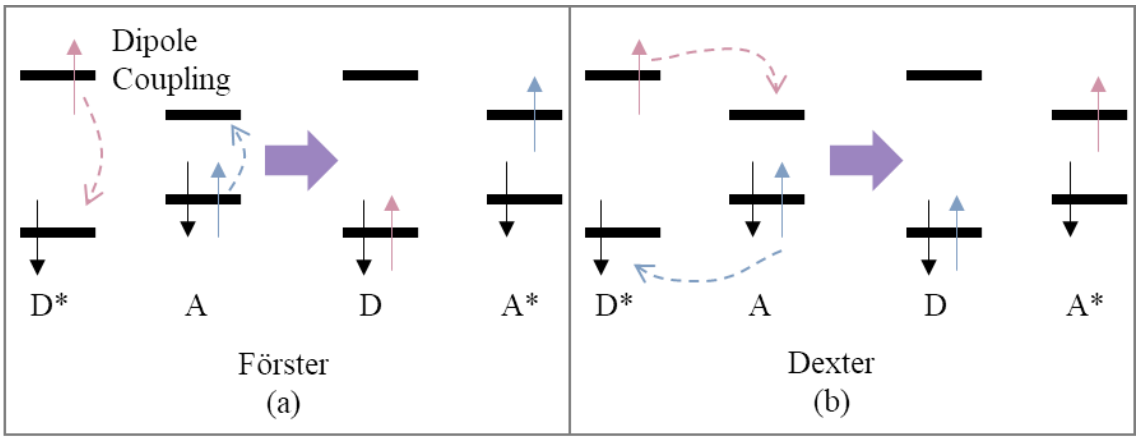

Fig. 3.4: (a) Förster resonant excitonic transfer and (b) Dexter excitonic transfer.

Mathematically, 'recombination' (the formation of excitons) within organic semiconductors is often described as a Langevin recombination process, with a rate parameter given by Eq. (3.23) [152], [153].

$$R_L = \frac{q\left[\mu_n(\boldsymbol{E}) + \mu_p(\boldsymbol{E})\right]}{\varepsilon_r \varepsilon_0}\,(np - n_i^2) \tag{3.23}$$

This description of recombination is derived assuming that carriers will recombine provided their coulombic attraction energy is larger than their thermal kinetic energy. It is therefore possible to define a maximum radius r at which these energies are equal.

$$E(r) = \frac{q^2}{4\pi\varepsilon_0\varepsilon_r r} = kT \tag{3.24}$$

$$r = \frac{q^2}{4\pi\varepsilon_0\varepsilon_r kT} \tag{3.25}$$

Taking a typical organic semiconductor ε_r of 3, at 300 K, this radius is 18.6 nm, which is an ample distance compared to the molecular-scale confinement of excitons in organic semiconductors.

Defining a recombination current density J_{rec} in a layer of thickness L as the product of the recombination rate R_L and the electronic charge q, we arrive at Eq. (3.26).

$$J_{rec} = qR_L L \tag{3.26}$$

We can take a (hole) drift recombination current flowing into a sphere of radius r around a single electron as Eq (3.27).

$$I_p = pq\mu_p F.4\pi r^2 \tag{3.27}$$

And equivalently for an electron drift current due to a single hole:

$$I_n = nq\mu_n F.4\pi r^2 \tag{3.28}$$

From Coulomb's law, we know that the electric field between an electron and a hole is given by Eq. (3.29).

$$F = \frac{q}{4\pi\varepsilon_0\varepsilon_r r^2} \tag{3.29}$$

Thus,

$$I_p = \frac{pq^2\mu_p}{\varepsilon_0\varepsilon_r}, \qquad I_n = \frac{nq^2\mu_n}{\varepsilon_0\varepsilon_r} \tag{3.30}$$

The total recombination current is the sum of these currents due to I_n and I_p; to scale this individual current to a volume V, I_p (I_n) must be multiplied by the volumetric number of electrons (holes), N (P). The total current density due to recombination can then be given by Eq. (3.32).

$$J_{rec} = \frac{I_p N}{A} + \frac{I_n P}{A} = I_p\left(\frac{N}{V}\right)\left(\frac{V}{A}\right) + I_n\left(\frac{P}{V}\right)\left(\frac{V}{A}\right) \tag{3.31}$$

$$J_{rec} = L\left[nI_p + pI_n\right] \tag{3.32}$$

Equating the expressions for Eqs. (3.26) and (3.32), we find an expression for the recombination rate R_L :

$$R_L = \frac{nI_p + pI_n}{q} = \frac{npq\mu_p}{\varepsilon_0\varepsilon_r} + \frac{npq\mu_n}{\varepsilon_0\varepsilon_r} = \frac{q\left(\mu_n + \mu_p\right)}{\varepsilon_0\varepsilon_r} np \tag{3.33}$$

However, this expression for recombination rate does not take into account the thermal generation of intrinsic carriers or the field-dependent mobility. Taking these into account produces the full Langevin rate equation given by Eq. (3.23).

3.6 Organic LEDs

Based on the information presented in the previous sections, it is now possible to build a picture of the operation of an OLED. Holes are injected into the HOMO from the anode and electrons into the LUMO from the cathode. These charge carriers hop towards each other under the action

of the electric field, where they meet to form an exciton. The lifetime of such an exciton is short, and the electron and hole soon recombine, thereby emitting light.

Although it is possible to produce OLEDs with a single organic material between two contacts, the performance of such a device can frequently be improved by the inclusion of other materials to help with charge injection, transport and recombination. Highly doped high-conductivity electron or hole injection layers (EIL/HILs) help to form ohmic contacts and improve charge injection. Doped emissive layers (EMLs) can facilitate excitonic transfer and result in faster recombination times. The inclusion of electron or hole blocking layers (EBL/HBL) with high energetic barriers help to confine our electrons and holes within the emissive layer and achieve charge balance. Moving recombination away from the contact layers also helps to reduce exciton quenching. An idealised picture of the overall operation of an OLED under forward bias can then be seen in Fig. 3.5.

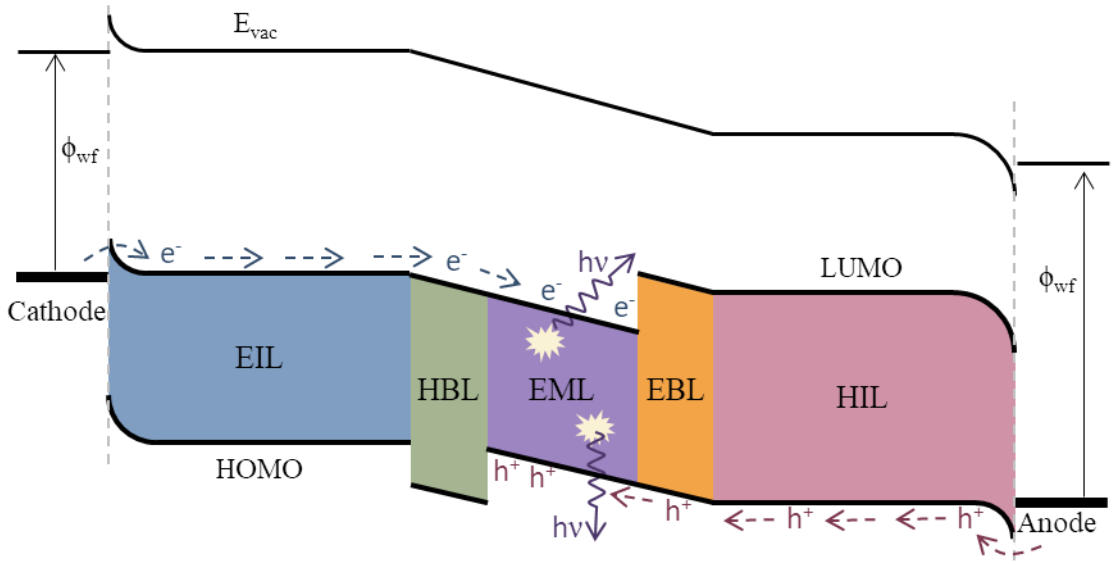

Fig. 3.5: OLED operation under forward bias. Redrawn after [154].

3.6.1 Modelling and Simulation of OLEDs

Various work has been done on simulation and modelling of OLED devices; this section will look at some of the published results in this field.

Electrical Modelling

Impedance spectroscopy is a common technique used in analysis of organic devices and materials, with RC parameters predominantly fitting one of the two models given in Fig. 3.6, below.

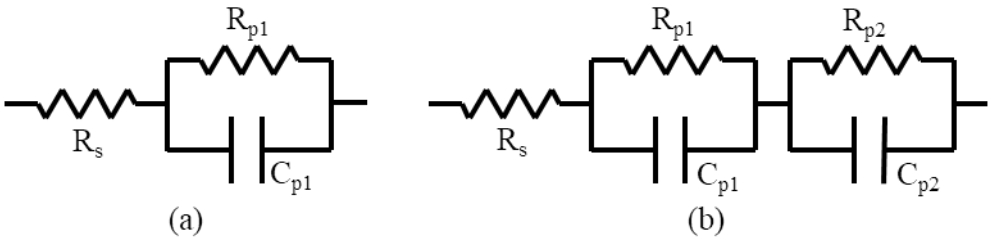

Fig. 3.6: The (a) single-layer and (b) double-layer OLED model often used to fit impedance spectroscopic measurements [155]–[165].

The resistance model shown in Fig. 3.6(a) is often used to fit single organic layer OLEDs [155]–[162], whereas Fig. 3.6(b) is often used for more complex model-fitting, where multiple time constants are seen in the impedance response [155], [159], [163]–[165]. In the models in Fig. 3.6, R_s refers to the series contact resistances, and each R_p-C_p combination refers to a layer within the device. For single-organic layers, Fig. 3.6(a) is appropriate, but where there is bipolar injection, Fig. 3.6(b) can be used, where one R_p-C_p combination refers to the electron transport layers, and another to the hole transport layers.

Some variations on these electrical models are seen in the literature, such as in Fig. 3.7, where Nam *et al.* added a series contact inductance for good parameter fitting [166].

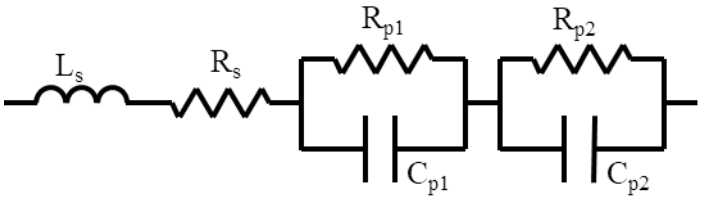

Fig. 3.7: Impedance model used for OLEDs by Nam *et al.*; redrawn from [166].

In one instance, Zeng *et al.* fit a different RC model (Fig. 3.8) to the pulse response of a 6-layer small molecule μ-OLED, and extracted overall time constants from the pulse measurements [167]. Two time constants were drawn from the OLED, one related to the measured current decay time (the 'electrical response'), and one related to the measured electroluminescent decay time (the 'optical response'). Their OLED structure demonstrated faster electrical response than

optical response, but there was no correlation given between the electrical measurements and optical speeds.

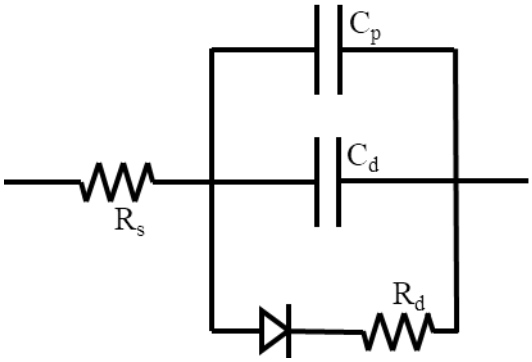

Fig. 3.8: Electrical model used by Zeng *et al.* to describe OLED response. R_s is a series (electrode) resistance, C_p is a parasitic capacitance, C_d is the device junction capacitance and R_d is the diode resistance. Redrawn from [167].

Admittance spectroscopic measurements undertaken by Martens *et al.* on a single-layer OLED produced three different electrical models based upon the bias [168]. Once again, correlation of the luminescent frequency response of these circuit parameters was not included in this analysis.

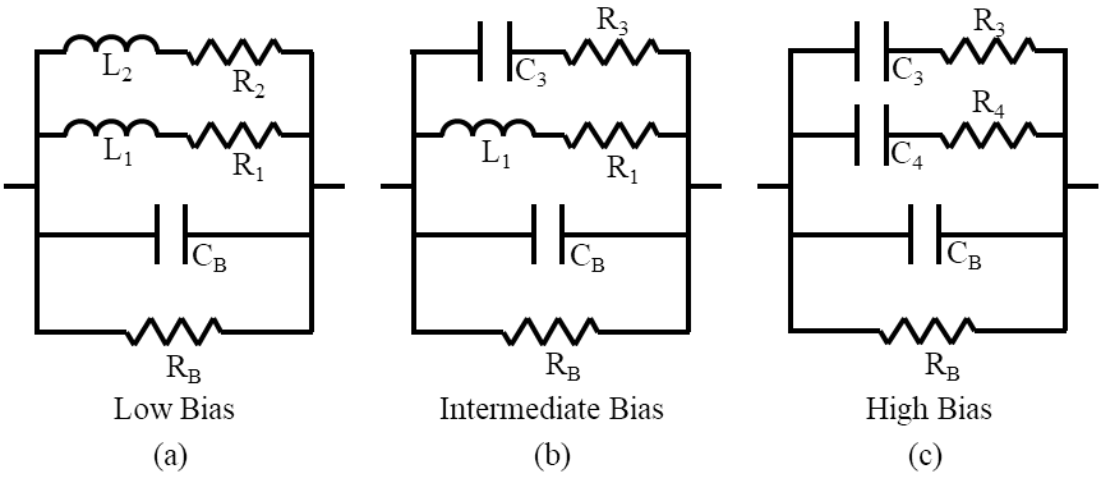

Fig. 3.9: Electrical models fit to impedance measurements for a single layer OLED according to Martens *et al.* Redrawn from [168].

One purely simulated study undertaken by Nguyen and Schmeits involved admittance parameter extraction from a 2-layer OLED numerical simulation. The results of this simulation were fit to two different models, depending on the bias of the OLED [169]. At 0 V bias, they fit a response as in Fig. 3.10(a) and at 3V, the model evolved to Fig. 3.10(b). Each resistance and capacitance in this model corresponds to different regions of conduction or depletion within

the OLED. Unfortunately, experimental validation of this OLED model was not provided, nor was any correlation found between the small signal electrical model and electroluminescent response.

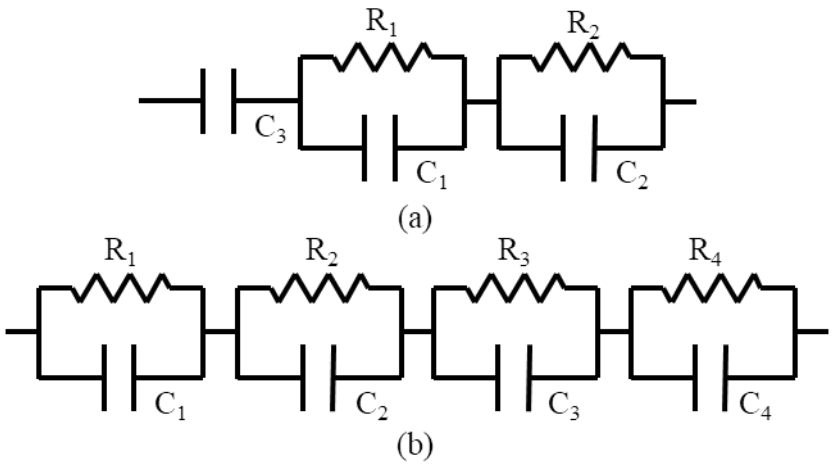

Fig. 3.10: Equivalent electrical models for simulated small signal response of two-layer OLED. (a) is the model at 0 V bias and (b) is the model at 3 V bias. Redrawn from [169].

Whilst admittance spectroscopy is a valuable tool for understanding the electrical properties of organic materials, it is the optical frequency response of the OLED that is of significance in the context of organic optical communications. To the best of the author's knowledge, this thesis provides the first attempt to correlate the measured electrical admittance response and optical frequency response. Of course, this approach is only valid provided that the exciton recombination time (singlet lifetime) is less than the electrical response of the system.

Simulation and Numerical Modelling

Simulation and numerical modelling is an essential tool in order to better understand the behaviour of complicated organic device structures and materials. Various organic simulation models have been applied over the years, ranging from the molecular-level small-scale models that have facilitated better understanding of carrier transport to the large-scale drift-diffusion models commonly used in the field of inorganic semiconductors [170].

For example, the original paper that first introduced the Gaussian Disorder Model (GDM) by Bässler in 1993, developed the model through Monte-Carlo simulation of charge carrier hopping in a material with a Gaussian density of states [138]. The Extended Gaussian Disorder Model was also developed from numerical studies of hopping charge carriers [139]. Indeed, Monte-Carlo simulations have even been undertaken for entire OLED stacks [171], although the great advantage of mobility models such as the EGDM is that they have allowed models to

scale to the device level, without requiring simulation on the individual carrier-scale. Thanks to the development of these effective mobility models, and the improved understanding of the physics behind organic devices, there are now many instances in the literature of organic device drift-diffusion simulation [172]–[177]. The ability to apply simulation to device development is an important step towards low-cost optimisation.

In this thesis, physical and electrical modelling and characterisation of a multi-stack OLED is presented, with the aim of optimising the devices for communications purposes. The work presented here represents the first known demonstration of an experimentally-validated holistic five-layer OLED simulation fitting both DC current-voltage and small signal characteristics. While there are certainly many OLED simulation models published in the literature, many of them have focussed on simpler single- or double-layer devices [169], [178]–[180] or have not included small signal characteristics [181].

3.7 Conclusions

This chapter has introduced the basic mechanisms of operation of organic LEDs, from doped layers that facilitate the charge injection, through to the hybridisation of organic orbitals that allows the hopping transport of carriers, to the Langevin mechanism that describes the recombination. It is seen that organic semiconductors exhibit HOMO and LUMO levels that are analogous to valence and conduction bands in inorganic semiconductors, although in contrast to the band-like transport observed in inorganic semiconductors, this transport is through localised phonon-assisted hopping. From the EGDM, it is seen that the empirically-observed field and temperature-dependent mobilities of the form $\mu = \mu_0(T)\exp\left(\beta\sqrt{E}\right)$ are a consequence of this localised hopping transport amongst disordered materials exhibiting a Gaussian density of states. The low relative permittivity of organic semiconductor materials also gives rise to coulombically bound electron-hole pairs, known as excitons. It is the recombination of singlet excitons that gives rise to fluorescence, and it is this fast-emission that is required to implement fast OLEDs for communications.

Understanding of the physics behind these devices has allowed high-level modelling and simulation to be developed in the research leading to this thesis. The following chapters will introduce measurements and simulation results for different OLED devices within this context.

4 STUDIES ON SMALL-MOLECULE OLEDS

This chapter introduces the specific small-molecule OLEDs under study along with their manufacture, and presents the electrical, optical and thermal characteristics of these devices. An electrical and thermal simulation used to model the overall OLED is introduced, and a reasonably good fit is found between experimental results and simulation, suggesting that this model is appropriate for trend-forecasting and analysis. It is believed that this is the first time that this OLED stack has been simulated in this manner. It is found that deviations between simulation and measurement may be ascribed to thermal self-heating effects, which will by necessity be an important consideration for device reliability in future organic optical links.

4.1 Introduction

In order to bring the tools of simulation to the development of organic devices, it is necessary to have a good understanding of the operation of the OLED. The purpose of this chapter is to present a systematic study of an OLED stack, by analysing the function of devices without various layers of the stack from which to build understanding of the device as a whole. With this information, a detailed OLED drift-diffusion simulation model may be constructed and validated, building upon the known physics introduced in Chapter 3, and leading up to modelling the device modulation for communications purposes. These types of drift-diffusion models have been successfully used to describe OLED behaviour in the literature, although

there has been very little work done in this area with regards to analysis of the high-speed modulation of organic devices [182]–[184].

In Chapter 3, it was also mentioned that thermal effects have significant impact upon the behaviour of disordered organic semiconductors, due to the thermally-activated charge hopping behaviour [185]; therefore, measurement of the self-heating of the full OLED devices is of interest and is undertaken in this chapter, in order to explain some of the variance in device behaviour.

4.2 OLED Manufacture

All of the OLEDs presented in this thesis are top-emitting small-molecule OLEDs manufactured by Dr. Kou Yoshida at the University of St. Andrews using shadow mask thermal evaporation in high vacuum (EvoVac, Angstron Engineering) at a pressure of 3×10^{-7} mbar. The devices were evaporated onto glass substrates with a thickness of 1.1 mm. Organic and contact layer thicknesses are measured during evaporation using standard quartz crystal monitors.

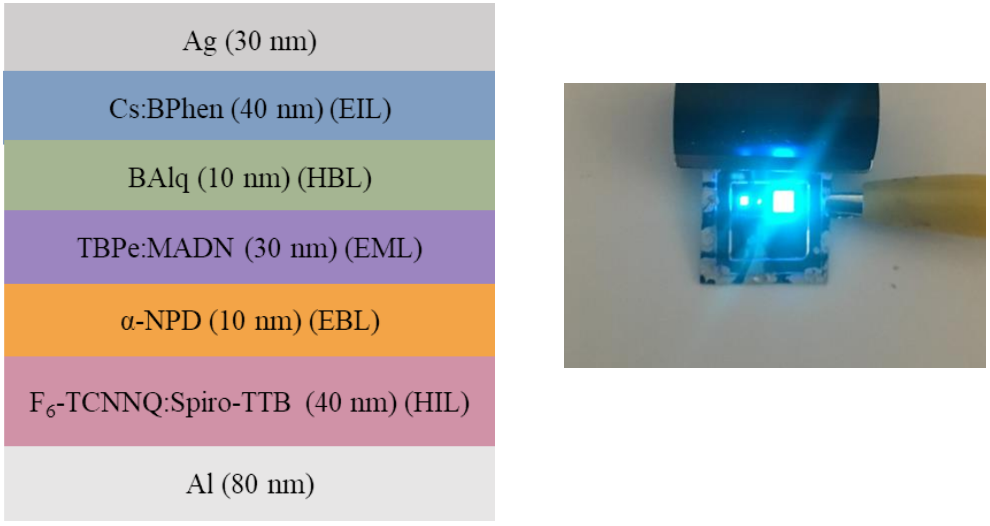

Fig. 4.1: (a) The layers of the small-molecule OLED under study, and (b) OLEDs on silicon substrates under operation (from left to right, 1.1 mm^2, 0.12 mm^2 and 9 mm^2).

The OLED layers as shown in Fig. 4.1 (a) were deposited sequentially without breaking vacuum starting with 80 nm of aluminium for the bottom anode, 40 nm of 2,2',7,7'-tetrakis(N,N'-di-p-methylphenylamino)-9,9'-spirobifluorene (Spiro-TTB) doped

with 4wt% 2,2'-(perfluoronaphthalene-2,6-diylidene)dimalononitrile (F_6-TCNNQ) as the hole injection layer (HIL), 10 nm of N,N'-di(naphthalene-1-yl)-N-N'-diphenylbenzidiene (α-NPD) as the electron blocking layer (EBL), 30 nm of 2-methyl-9,10-di(2-naphthyl)anthracene (MADN) doped with 2.76 wt% 2,5,8,11-tetra-tert-butylperylene (TBPe) as the emissive layer (EML), 10 nm of bis-(2-methyl-8-chinolinolato)-(4-phenyl-phenolato)-aluminium(III) (BAlq) as the hole blocking layer (HBL), 40 nm of 4,7-diphenyl-1,10-phenanthroline (BPhen) doped with 2 wt% caesium as an electron injection layer (EIL), 30 nm of silver was evaporated as the cathode, and a 40 nm α-NPD capping layer was evaporated on the thin silver to enhance the out-coupling of emitted light to the air. The chemical structure of these materials may be found in Table 4-1.This final α-NPD layer is ignored in the electrical simulation and modelling studies, as it is an optical diffuser layer that is not electrically connected and thus believed to have no effect upon the electrical properties of the OLED. Furthermore thin silver is used as the top contact due to its easy manufacturability relative to ITO, and as it forms a good contact with the EIL. Alternate bottom-emitting OLEDs that use ITO as the anode instead of aluminium were found to have very little performance difference, so for the manufacturing reasons mentioned above, thin silver is preferred.

These devices were encapsulated in a nitrogen atmosphere using epoxy and a small strip of dessicant attached to the 0.6 mm glass lid. The devices were fabricated with three different area dimensions: 0.3×0.4 mm^2 (S), 1×1.1 mm^2 (M) and 3×3 mm^2 (L). As the development of these OLEDs has largely been through trial-and-error, in order to better understand the function of each of the layers and layer parameters, multiple four-layer devices were also fabricated to use as control samples; these devices are missing one of the functional layers above. Additionally, alternate devices with a 20 nm EML layer doped with 1.5 wt% TBPe are grown on both the 1.1 mm standard glass substrates and also on 675 μm silicon substrates with 300 nm of SiO_2 grown on each side.

For luminescent and charge-injection efficiency, the transport within the full-stack OLEDs is bipolar, with charge injection facilitated by the doped layers. The effect of the doping is to pin the Fermi level of the organic layer relative to the metal contact, thereby enabling charge injection at each contact, as described in §3.6 [114].

Table 4-1: The chemical structure of the materials used in these OLEDs

Chemical Structure	Chemical Name
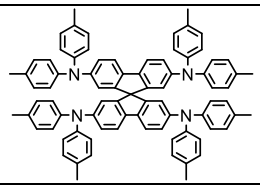	2,2',7,7'-tetrakis(N,N'-di-p-methylphenylamino)-9,9'-spirobifluorene (Spiro-TTB)
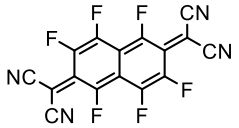	2,2'-(perfluoronaphthalene-2,6-diylidene)dimalononitrile (F_6-TCNNQ or F_6-TNAP)
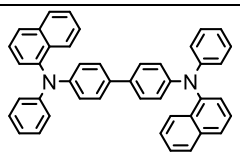	N,N'-di(naphtalene-1-yl)-N,N'-diphenylbenzidine (α-NPD or NPB)
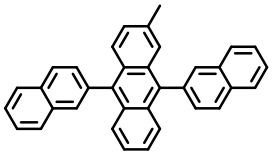	2-methyl-9,10-bis(naphthalen-2-yl)anthracene (MADN)
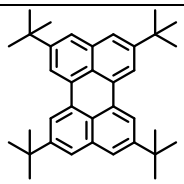	2,5,8,11-tetra-tert-butylperylene (TBPe)
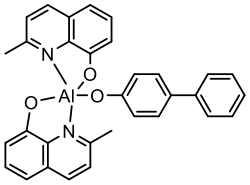	bis-(2-methyl-8-chinolinolato)-(4-phenyl-phenolato)-aluminium(III) (BAlq or $BAlq_3$ or $BAlq_2$)
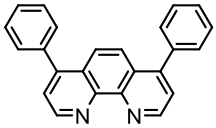	4,7-diphenyl-1,10-phenanthroline (BPhen)

4.3 Experimental Investigation

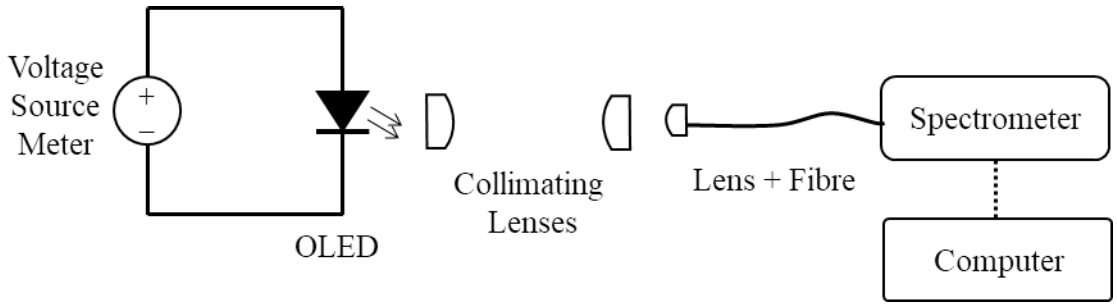

Fig. 4.2: Experimental setup for spectral measurements.

Spectral measurements were taken for the OLEDs presented here using light coupled via a collimating lens and optical fibre into a high resolution spectrometer (Ocean Optics HR2000+CG-UV-NIR), as shown in Fig. 4.2.

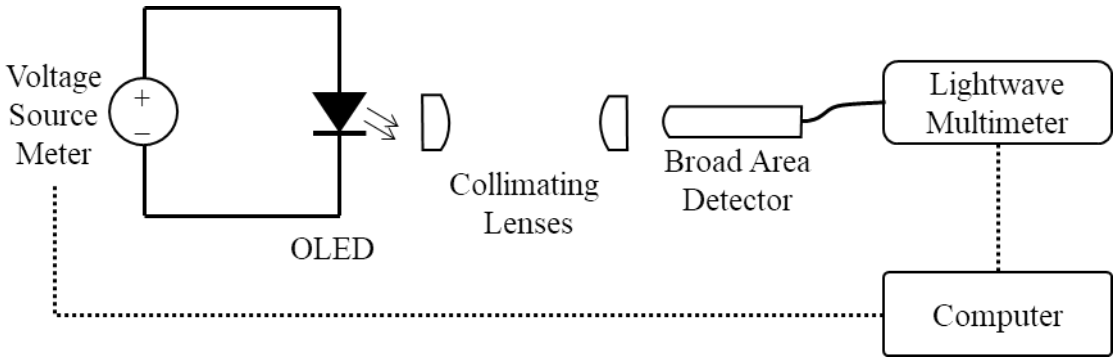

Fig. 4.3: Experimental setup for Light-Current-Voltage (LIV) measurements.

Continuous-mode Light-Current-Voltage (LIV) measurements for these OLEDs were taken in free space with light coupled into a broad-area detector (HP81520A) via an aspheric optical lens (Thorlabs) and measured by a lightwave multimeter (HP8153A) set to detect at the relevant optical peaks measured by the spectrometer, as shown in Fig. 4.3. In both cases, a source meter (Keithley 2400-LV) was used to provide the power to the devices. For devices measured on a heatsink, a temperature controller (ILX Lightwave LDT-5910B) was used to regulate the substrate temperature.

4.4 Experimental Results

4.4.1 Current-Voltage & Light-Voltage Characterisation

Unless stated otherwise, the results presented in the following section are for the devices with a 30 nm EML on glass substrates.

As can be seen from Fig. 4.4 - Fig. 4.6, below, the OLEDs have a turn-on voltage around 2.8 V and emit light in direct proportionality to the current in the device. As mentioned in §3.6, the light output from OLEDs is generally described by bimolecular Langevin recombination [186]. It is also interesting to note the increase in conductance and light output at the highest bias points for the small and medium OLED devices – this is likely due to thermal or trap-filling effects during the measurement sweep, as will be seen in §4.4.3, this sharp increase is not seen in the same OLED materials evaporated in the same manner upon silicon substrates. The 9 mm^2 OLEDs have a higher current density at the same bias potential than the smaller devices, indicating that heating improves the conductance of these large OLEDs relative to the smaller devices.

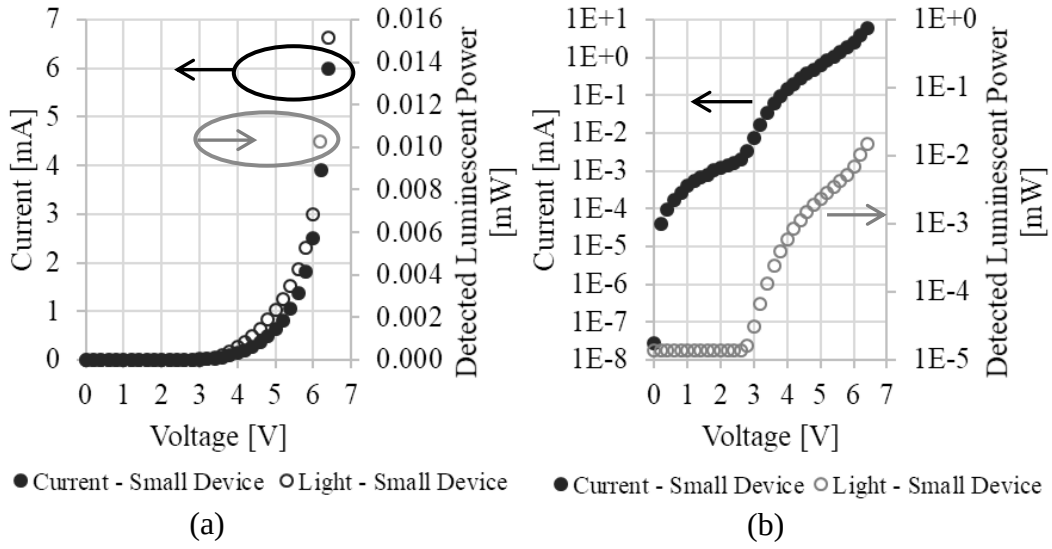

Fig. 4.4: (a) Current-Voltage (solid circles) and Light-Voltage (hollow circles) characteristics of the 0.12 mm^2 OLEDs on glass; (b) shows the same data on a semi-log scale.

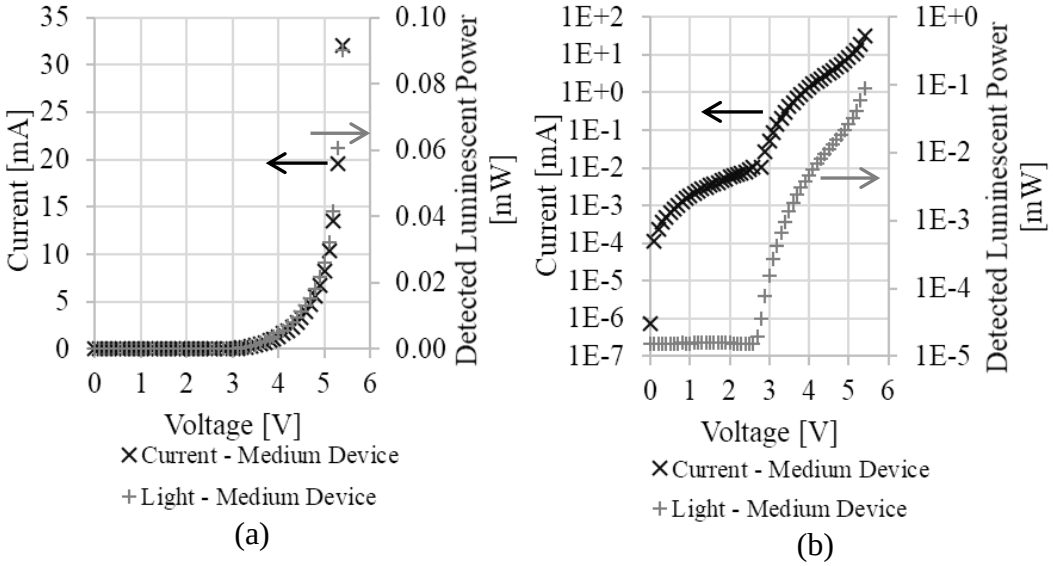

Fig. 4.5: (a) Current-Voltage (black cross) and Light-Voltage (grey plus) characteristics of the 1.1 mm^2 OLEDs on glass; (b) shows the same data on a semi-log scale.

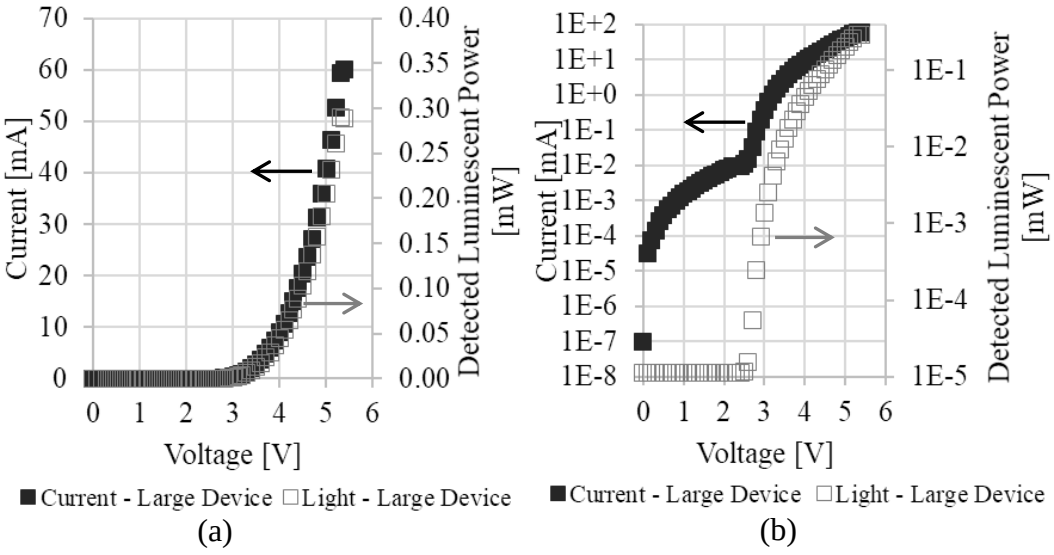

Fig. 4.6: (a) Current-Voltage (solid square) and Light-Voltage (hollow square) characteristics of the 9 mm^2 OLEDs on glass; (b) shows the same data on a semi-log scale.

4.4.2 Spectra

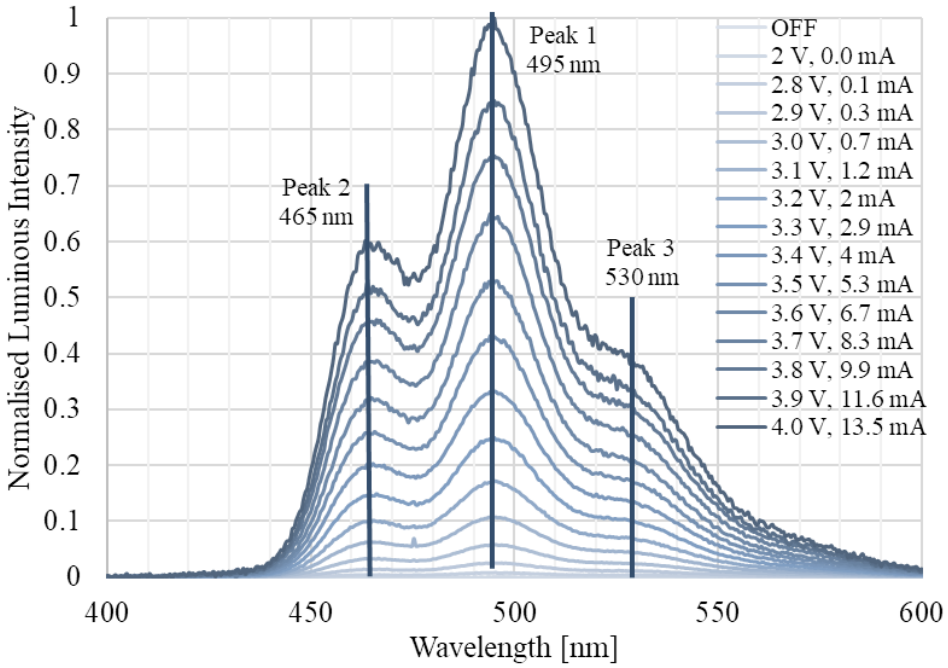

Fig. 4.7: Luminescent spectra of bottom-emitting 9 mm^2 devices with 20 nm EML on ITO-coated glass substrates.

To avoid microcavity effects, spectral measurements are taken of bottom-emitting devices with a 20 nm 1.5 wt.% doped EML with ITO as an anode instead of the aluminium bottom contact shown in Fig. 4.1. These samples were also very kindly provided by Dr. Kou Yoshida at the University of St. Andrews. The results of the spectral measurements are produced in Fig. 4.7. The OLEDs emit blue light with a spectral peak of 495 nm (Peak 1), with secondary peaks at 465 nm (Peak 2) and at 530 nm (Peak 3), which do not change with bias current. Peaks 1 and 2 closely correspond to the emissive peaks shown in photoluminescent (PL) measurements of TBPe [187]–[189]. The 530 nm longer wavelength emission (Peak 3) and longer ‘tail’ is indicative of an exciplex/charge-transfer state within the TBPe:MADN [190].

In this instance, although blue light is within the low-attenuation window of SI-POF, these wavelengths are chosen due to the relatively fast-response of the emitter layer. As organic emissive materials are continually being developed, it is hoped that as materials research progresses, appropriate emitters well-suited to the specific channel can be developed, such as in the infra-red.

4.4.3 Thermal Effects

Temperature has a significant effect upon the operation of the OLED devices. In order to confirm this for the devices under consideration, Fig. 4.8 compares the stable operating currents of OLEDs (with a 20 nm EML) on glass to the devices on silicon, measured without external temperature control at room temperature. In each case, the devices were allowed 30 s for the temperature to settle before the next data point was taken.

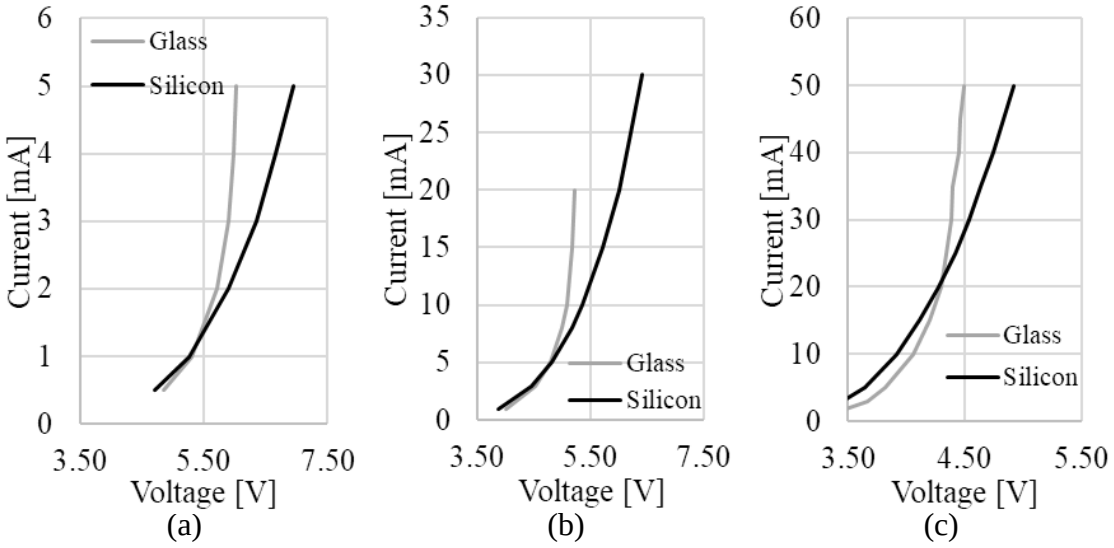

Fig. 4.8: (a) 0.12 mm^2, (b) 1.1 mm^2 and (c) 9 mm^2 OLEDs on glass compared to OLEDs on silicon.

Fig. 4.8 clearly shows that in all cases, at high current densities, the devices on glass substrates have a higher conductance than the devices on silicon. The glass of the substrates has a thermal conductivity of 0.0109 W·cm^{-1}·K^{-1}, and silicon has a value of thermal conductivity more than 100 times larger at 1.49 W·cm^{-1}·K^{-1}. Given that 300 nm of insulating SiO_2 is grown on the surface of the silicon, with largely similar electrical properties to the glass, it is expected that the current-voltage deviation measured between devices on glass and on silicon shown in Fig. 4.8 arises from Joule heating of the devices and not through any electrical influence. As the temperature of the devices increases, the mobility increases; this temperature-dependent behaviour of organic semiconductors is well established in the literature [191]–[194] and is largely the behaviour observed in the devices presented here, although the temperature range studied for these applications is too narrow to determine the exact nature of the mobility temperature dependence, i.e. whether it follows the Arrhenius dependence of the form $\frac{1}{T}$ (Eqs 3.21-3.22) or the EGDM dependence of the form $\frac{1}{T^2}$ (Eqs. 3.6-3.11) [139] [185].

The lifetime of OLEDs is believed to be strongly related to the glass transition temperature of the materials [195]. It is likely that the closer the operating temperature approaches the glass transition temperatures of the materials, the lower the lifetime of the devices, and so these aforementioned heating effects will likely have an adverse impact. This trade-off must be considered in any application considering OLEDs for communications.

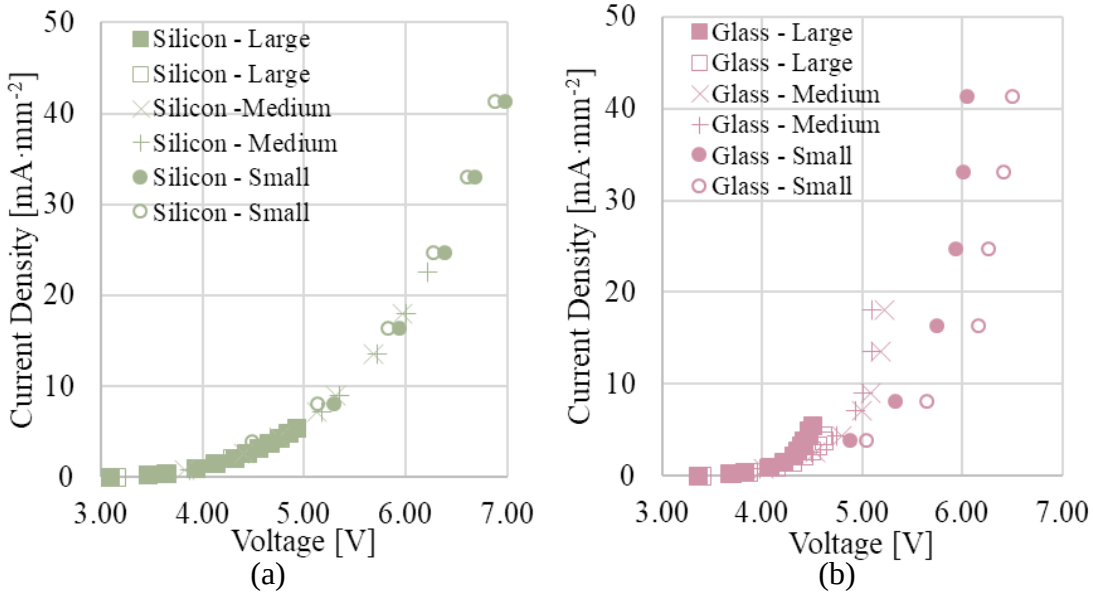

Fig. 4.9: J-V plots for (a) OLEDs on silicon and (b) OLEDs on glass.

It is also possible to observe the effect of the thermal mobility enhancements in plots of the current density on silicon and on glass, as in Fig. 4.9 for the devices with a 20 nm EML. The current density of the devices on silicon all fall on the same curve irrespective of area, as shown in Fig. 4.9(a), whereas for the devices on glass substrates, the larger devices exhibit higher current densities than their smaller equivalents at the same bias potential, as shown in Fig. 4.9(b).

The devices on glass were also measured on a temperature-controlled heat sink set to 16°C, and are seen to have lower current-density than when the same devices were measured without a heat sink. It is seen in Fig. 4.10(a) that the devices cooled to 16°C exhibit a lower current-density and less variance than the same devices in Fig. 4.9(b). In Fig. 4.10(b), we see the J-V curves of the smallest devices cooled to 16°C better match the curves of the devices on silicon, indicating that the mobility enhancement is indeed thermally driven.

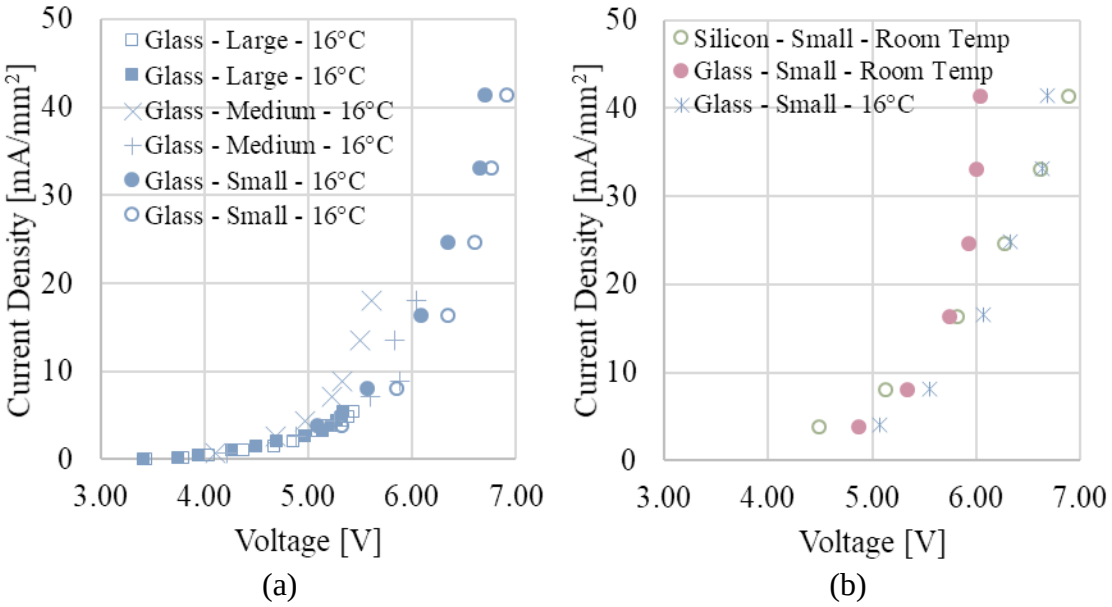

Fig. 4.10: (a) J-V curves for OLEDs on glass substrates on a heatsink at 16°C and (b) J-V curves of OLEDs on glass substrates at room temperature, at 16°C and on silicon substrates at room temperature.

4.4.4 Self-Heating Measurements

In order to better understand the substrate thermal effects, infra-red imaging is used to estimate the temperature of the devices under operation. Thermal measurements are taken in collaboration with Dr. Guillaume Nataf from the Department of Materials & Metallurgy at the University of Cambridge using a FLIR SC7500-MB thermal imaging camera, with a spectral range of 2.5-5.1 μm. Devices of all three dimensions on glass and on silicon are measured; the devices were set to a DC bias point, and allowed approximately 120 seconds to come to a thermal equilibrium before the bias was ramped to the next operating point.

The camera system provides images as in Fig. 4.11, of the devices and is calibrated to provide the temperatures associated with each pixel of the image. In Fig. 4.11, the OLED is formed at the centre of the cross (denoted by an arrow), although the rapid thermalisation of the metals causes the emitting centre of the OLED to appear dark in infra-red images. The bright areas show the glass/air interface of the devices where there is no metal to conduct away the heat; the insulating nature of these areas mean that they likely show the closest value to the real internal temperature of the OLEDs. It is possible to extract the average temperature of groups of pixels (illustrated by ellipses and boxes in Fig. 4.11), and the corresponding results of this are shown in Fig. 4.12 for the 0.12 mm^2 OLEDs. A small piece of black tape is also placed close to the OLED on the surface of the glass as an approximate black body in order to calibrate the initial

temperature. However, since the tape is placed sufficiently far from the OLED and on top of the cover glass, it is not possible to use this black body to provide an accurate measurement for the temperature within the OLED itself during the operation of the device.

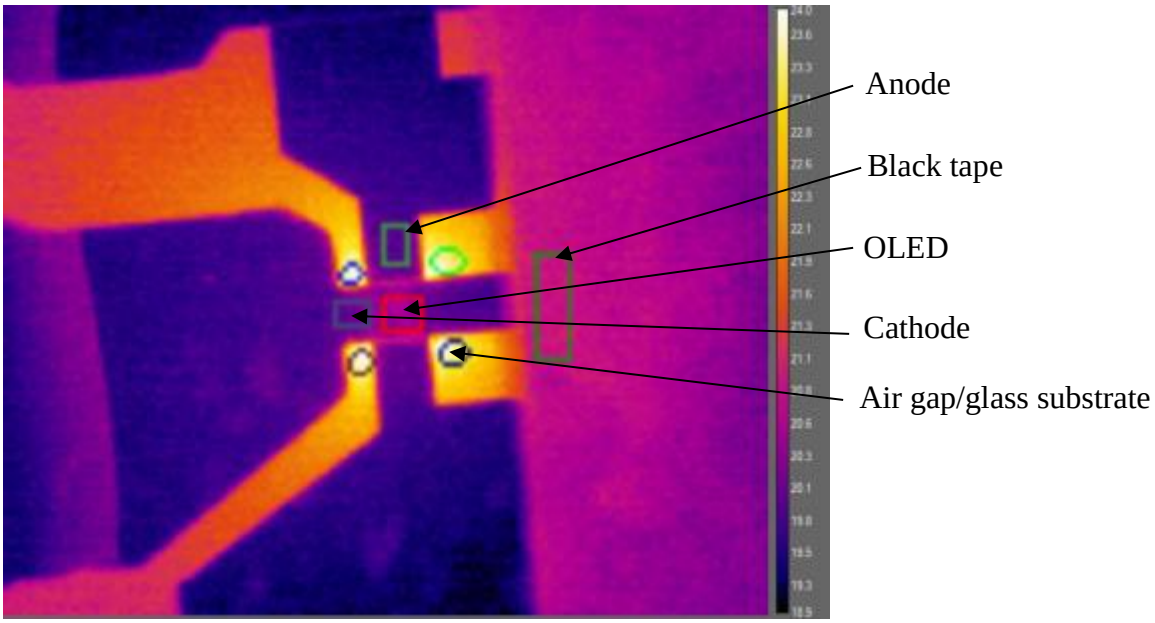

Fig. 4.11: Thermal image of 0.12 mm^2 OLED on glass.

It can be seen from Fig. 4.12 that, as expected, the measurements show a clear increase in temperature with operating current. The temperature measurements for the LED, anode and cathode all show a temperature lower than that of the air surrounding the device, likely due to the low emissivity (and good thermal conduction) of the metal. The tape also shows good match with the air temperatures at the low-current operation of the device, indicating that these values are appropriately calibrated and show a reasonable approximation of the device operating temperature. The thermal images are also able to show a spike at around 240 s where the value for the current was misadjusted and corrected, and a spike at around 600 s, where the current is briefly set to 5 mA.

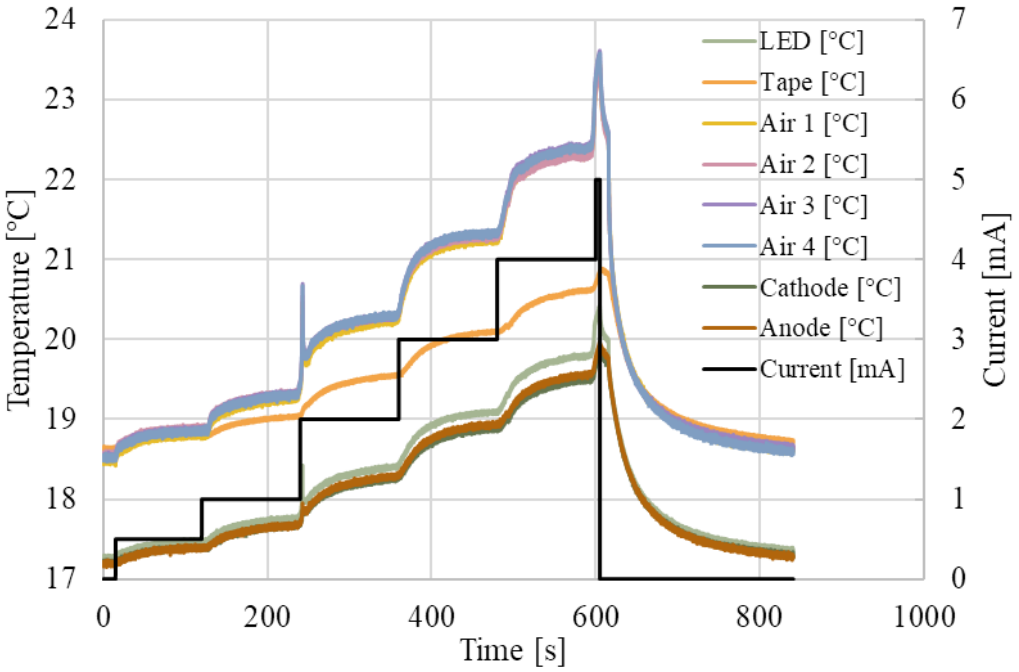

Fig. 4.12: Temperature measurements for 0.12 mm^2 OLED on glass over time as the current is ramped. The secondary y-axis shows the current variation with time in black. The different coloured lines correspond to the shapes drawn on the OLED image in Fig. 4.11.

Equivalent measurements for the 9 mm^2 OLEDs on silicon (Fig. 4.13, below) show some differences between that of glass, as the thermal conductivity of the silicon is much higher than that of the glass.

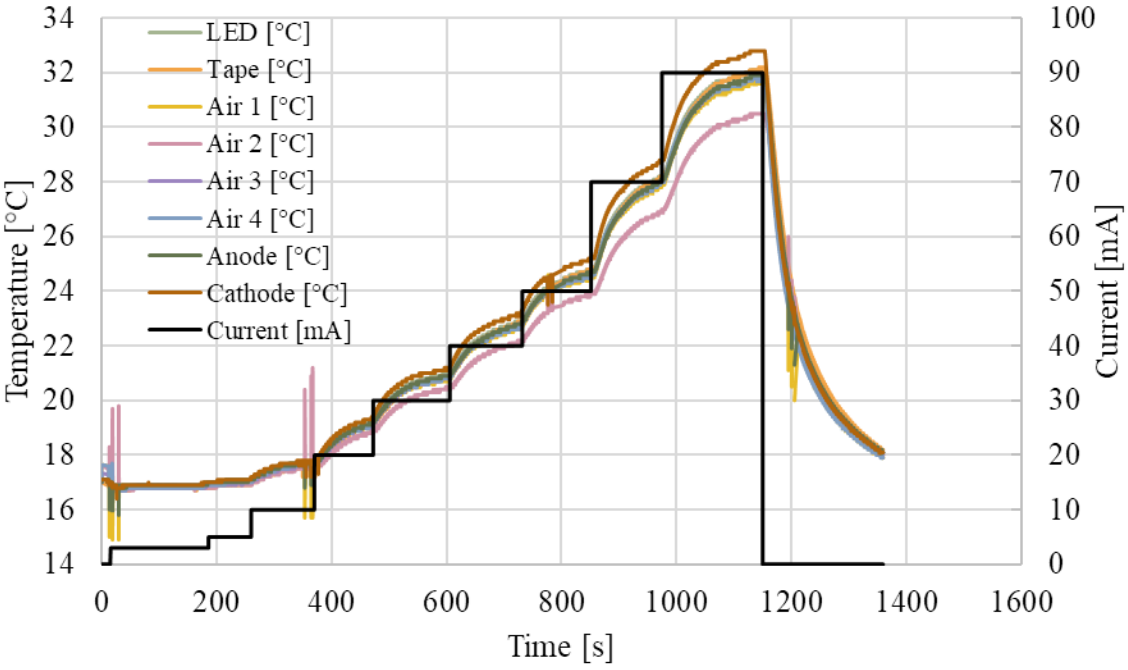

Fig. 4.13: Temperature measurements for 9 mm^2 OLEDs on silicon over time as the current is ramped. The secondary y-axis shows the current variation with time in black. The different coloured lines correspond to different positions on the OLED image.

The measurements in Fig. 4.13 at different points on the devices show less variance than the devices on glass. For devices of the same size and at the same current, the OLEDs on silicon show a significantly reduced operating temperature, as shown in Fig. 4.14. The devices on silicon typically require more than double the current to show the same relative increase in temperature. In addition, the devices on silicon were capable of sustaining much higher currents before experiencing thermal instability, indicating that the breakdown of the devices is indeed driven by self-heating.

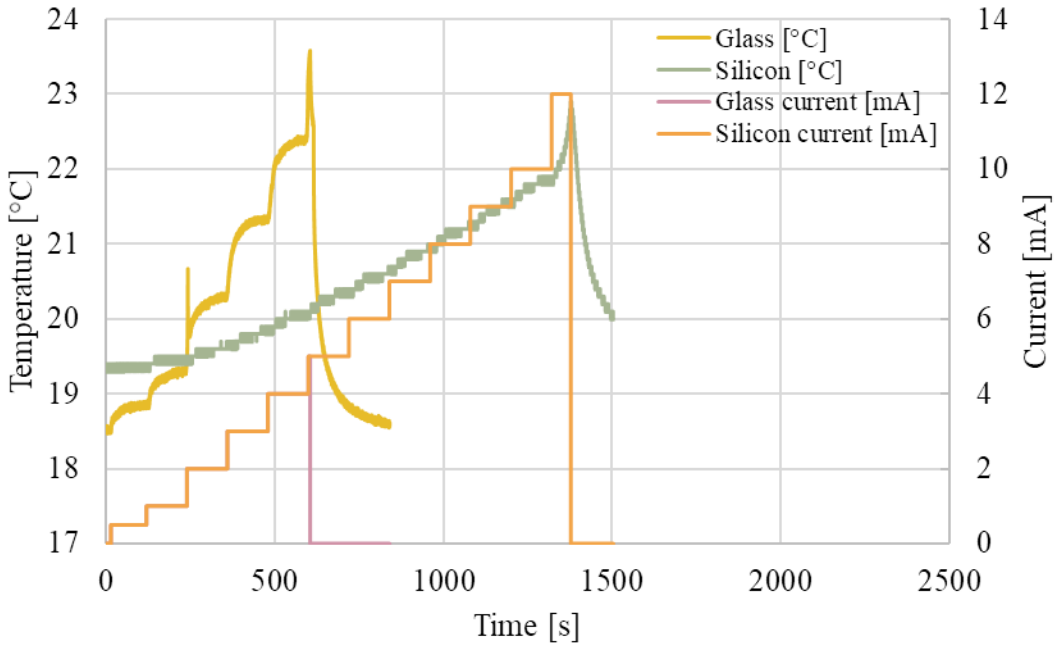

Fig. 4.14: Temperature measurements for 0.12mm^2 OLEDs over time as the current is ramped. The secondary y-axis shows the current variation with time.

The measurements plotted in Fig. 4.14 show the relative differences in temperature for the 0.12 mm^2 OLEDs on glass and on silicon as the bias current is ramped from 0 to 4 mA for the OLEDs on glass and 0 to 12 mA for the OLEDs on silicon. The temperatures plotted are those measured at the corners ('Air gap' in Fig. 4.11), where the metal contacts did not act to obscure the real temperatures of the devices.

When comparing the final 'plateau' temperature against each bias current, as in Fig. 4.15, below, it is clear that the glass devices heat up much faster than the silicon devices, and that the smaller devices fare better than the larger devices.

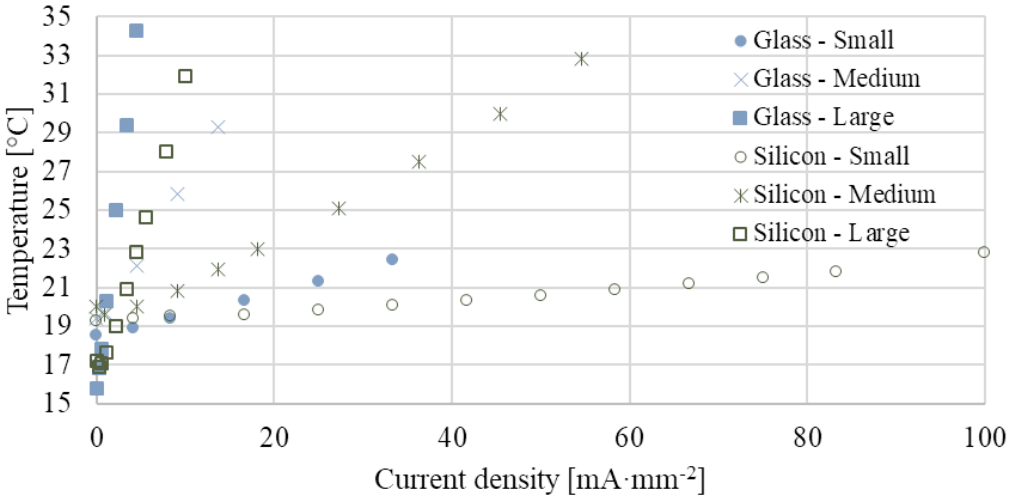

Fig. 4.15: Measured operating temperature for the OLEDs against current density.

However, it must be noted that these temperatures are likely to still be less than the actual temperatures achieved in the devices themselves. Firstly, these measurements are taken at the corners, and not actually at the centre of the devices, where it would be reasonable to assume the temperature is highest. However, as previously mentioned, the low emissivity/high thermal conduction of the metal contacts means that it is not possible to probe the temperature of the centre of the devices in this manner. Secondly, the surface glass (Schott D 263® T eco thin glass) that is used to encapsulate the devices has relatively low transmittance (<50%) at the infra-red wavelengths measured by the camera [196]. Finally, for the OLEDs on glass, since the organic layers are thin (240 nm) relative to the substrate (1.1 mm) and the glass is a good thermal insulator, the IR camera may have difficulty resolving the temperature of the thin film, and may be probing an average of the hot OLED temperature, and the temperature of the cooler substrate. If this hypothesis holds, it may be possible to use Fourier's law of thermal conduction (Eq. 4.1) to calculate the actual temperatures of the OLED.

$$q_x = -k\frac{dT}{dx} \tag{4.1}$$

In this equation, q_x is the heat flux density, which may be assumed to be proportional to the electrical power density input to the OLED, k is the thermal conductivity of the substrate and $\frac{dT}{dx}$ is the temperature gradient.

For the glass substrate, the thermal conductivity is 0.0109 $W \cdot cm^{-1} \cdot K^{-1}$ [197], for silicon this is 1.49 $W \cdot cm^{-1} \cdot K^{-1}$ [198] and for intrinsic, thermally grown thin-film silica, this is

0.013 W·cm^{-1}·K^{-1} [199]. Taking $q_x \propto J \cdot V \approx J \cdot V$, where J is the current density and V is the voltage at each bias point, it is possible to calculate $\frac{dT}{dx}$, and thereby calculate a $\Delta T \approx \frac{dT}{dx}\Delta x$ using half of the thickness of the substrate as Δx due to the averaging effect of the camera mentioned above. This approximation is expected to provide a reasonable engineering approximation to the real device temperature from the probed 'average' temperature, as the emission efficiency of the OLEDs is of the order of a few percent. It is also assumed that the nitrogen at the top surface of the OLED is insulating; the thermal conductivity of nitrogen is 2.6×10^{-4} W·cm^{-1}·K^{-1} [200] so this assumption should not significantly impact the results. This calculation does not account for for the low transmittance of the encapsulating glass and the low emissivity of the cathode.

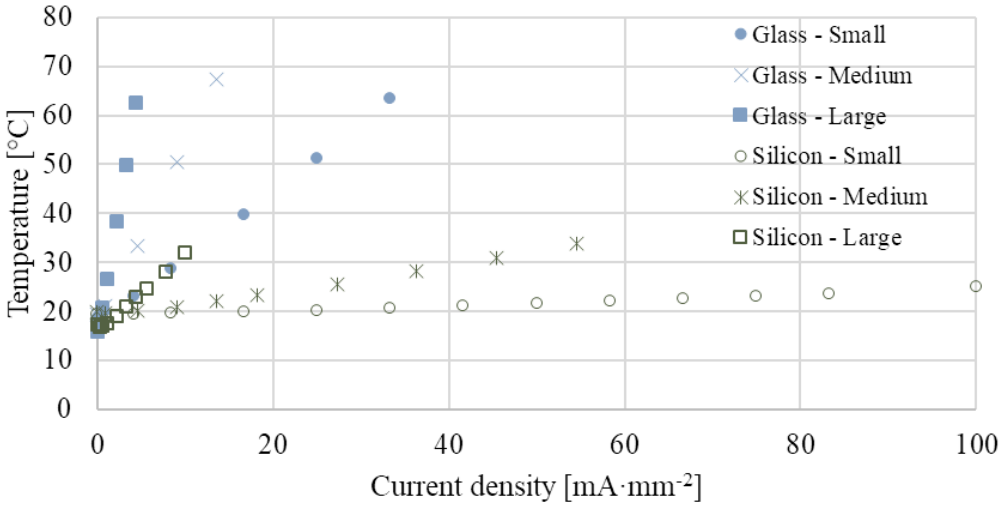

Fig. 4.16: Adjusted operating temperature of OLEDs.

The results of this, as shown in Fig. 4.16, demonstrate a stark difference between the temperature of the devices on silicon and on glass. The glass devices heat up much faster than the silicon devices, which explains the faster turn-on of the devices on glass compared to the devices on silicon, and the rapid degradation of the devices on glass at high bias. At a bias of 40 mA, the 9 mm^2 OLEDs on glass may be operating at over 62°C. Given that the glass transition temperature of a pure BPhen layer is 62°C, this may help explain the onset of thermal instability for all of the devices on glass, although the glass transition temperature of doped BPhen will be higher than 62°C, as described in [201].

Table 4-2: Glass transition temperature T_g of OLED materials.

Material	Glass Transition Temperature T_g [°C]
Spiro-TTB	146 [202]
α-NPD	95 [202]
MADN	120 [203]
BAlq	99 [204]
BPhen	62 [205]

4.4.5 Experimental measurements: LIV & Spectra for additional devices

To further understand the behaviour of the organic materials, additional OLEDs were manufactured without one of the layers existing in the 'full stack' devices. As development of OLEDs has predominantly been through a trial-and-error basis, with often large variations in published values of material parameters, these additional devices enable confirmation of layer function and device behaviour, and can be used to feed data into OLED simulation models.

The following devices were all manufactured by Dr. Kou Yoshida on 1.1 mm thick glass, and the measurements presented are for the 9 mm^2 'Large' OLEDs. The spectra are measured at currents of 10 mA for all devices except the devices without α-NPD and without Spiro-TTB; this is because these latter devices had very low luminescent power output relative to input current and needed to be driven at higher currents to mitigate some of the noise in the spectral measurements. The experimental LIV measurement results were very kindly taken and provided by Dr. Nikos Bamiedakis [206].

The dynamic performance of these devices is investigated in Chapter 5.

Without the Spiro-TTB Layer

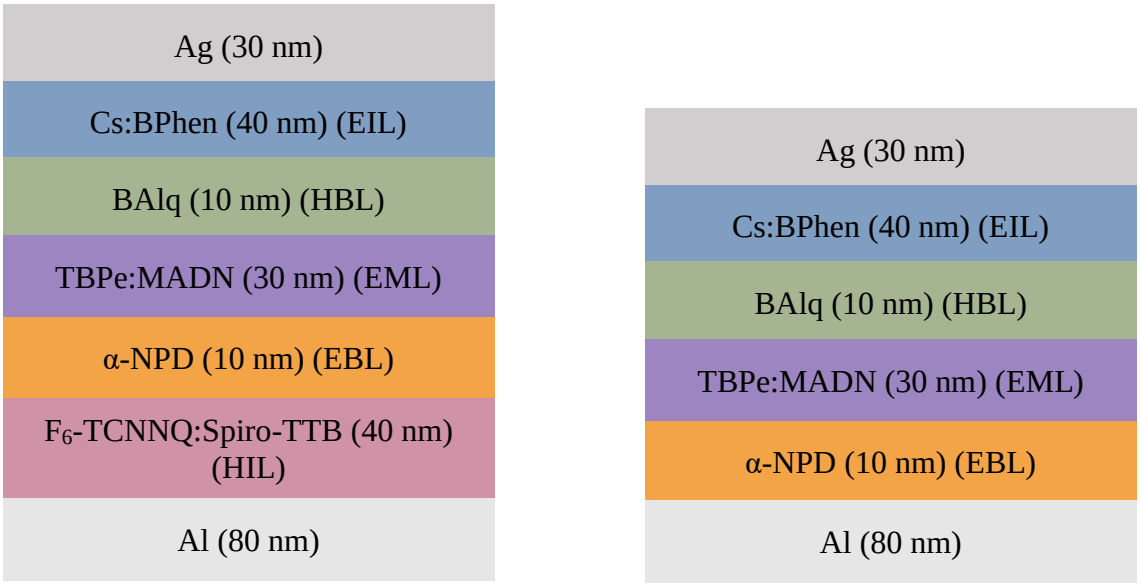

Fig. 4.17: Layers of (a) full stack and (b) devices without the HIL.

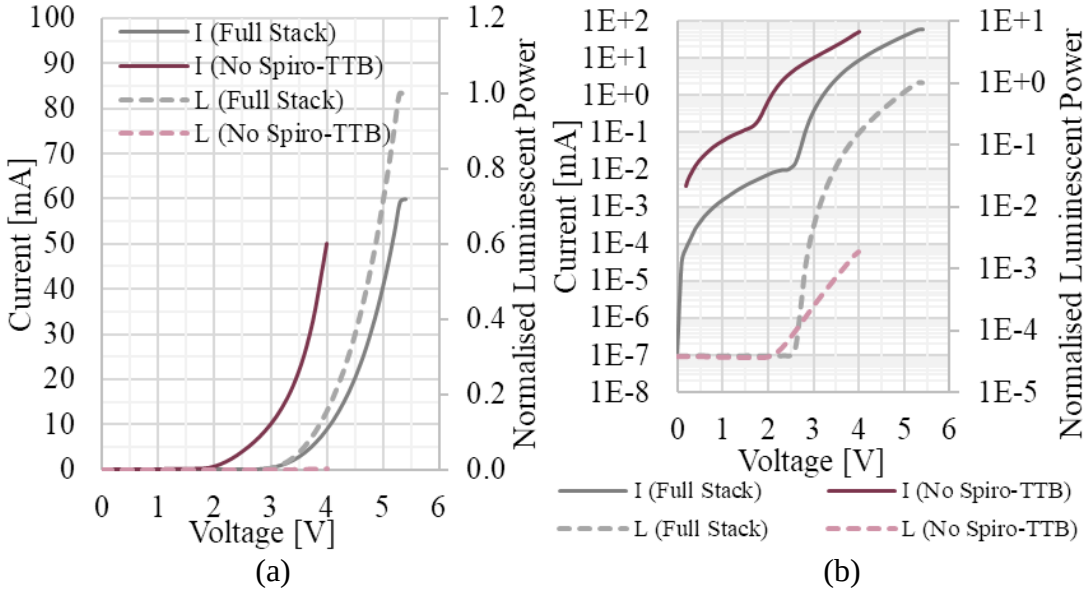

Fig. 4.18: (a) Current-Voltage (solid) and Light-Voltage (dashed) curves for OLEDs without an HIL (b) shows the same data on a semi-log scale.

We can see from

Fig. 4.18, above, that without the Spiro-TTB layer the devices emit very little light (even at high current) and function much like diodes with a higher leakage current than the full-stack

devices. These devices have a 'turn-on' at 1.7 V, around 1.1 V lower than the full stack devices at 2.8 V. Even at significant current, the light output is much reduced compared to the 'full stack' devices. Without the HIL, it is likely that the device mainly conducts through electron injection, with some holes injected directly into the α-NPD from the anode accounting for the small light-output. However, without the Fermi pinning/interface states effect of the doped HIL, this injection is not very efficient and the light output shows a similarly poor slope.

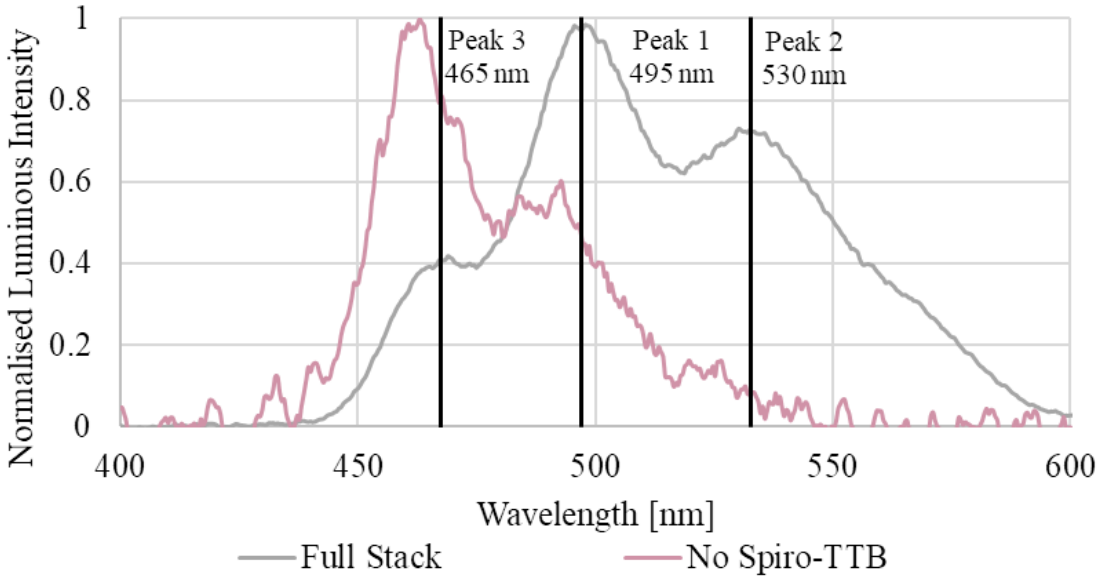

Fig. 4.19: Output electroluminescent spectrum of full stack OLEDs and OLEDs without an HIL.

Normalising the output power for both devices for comparability, we can see from Fig. 4.19 that the output electroluminescent (EL) spectrum of the devices without a HIL strongly corresponds to the photoluminescent (PL) emission of the TBPe dopant. The change in relative strengths of the two peaks (465 nm and 495nm) is possibly due to a change in charge transfer between MADN and TBPe under conditions of low hole injection.

The shift in spectra between the full stack devices in Fig. 4.7 and in Fig. 4.19 may also be due to microcavity effects [207], as these devices have metal contacts at both the cathode and the anode, as opposed to the transparent anode used for the measurements in Fig. 4.7.

Organic materials have a relative permittivity of very approximately 3, so the wavelength of the light within the cavity may be calculated approximately as

$$\lambda = \frac{\lambda_0}{\sqrt{\varepsilon_r}} = \frac{495}{\sqrt{3}} = 286\ nm \qquad (4.2)$$

We may see microcavity effects where an integer number of half-wavelengths can be sustained within the cavity. As $\frac{\lambda}{2}$=143 nm, this is of the same order as the thickness of the OLED (130 nm), and so microcavity phenomena may have some effect in these devices.

Without the α-NPD Layer

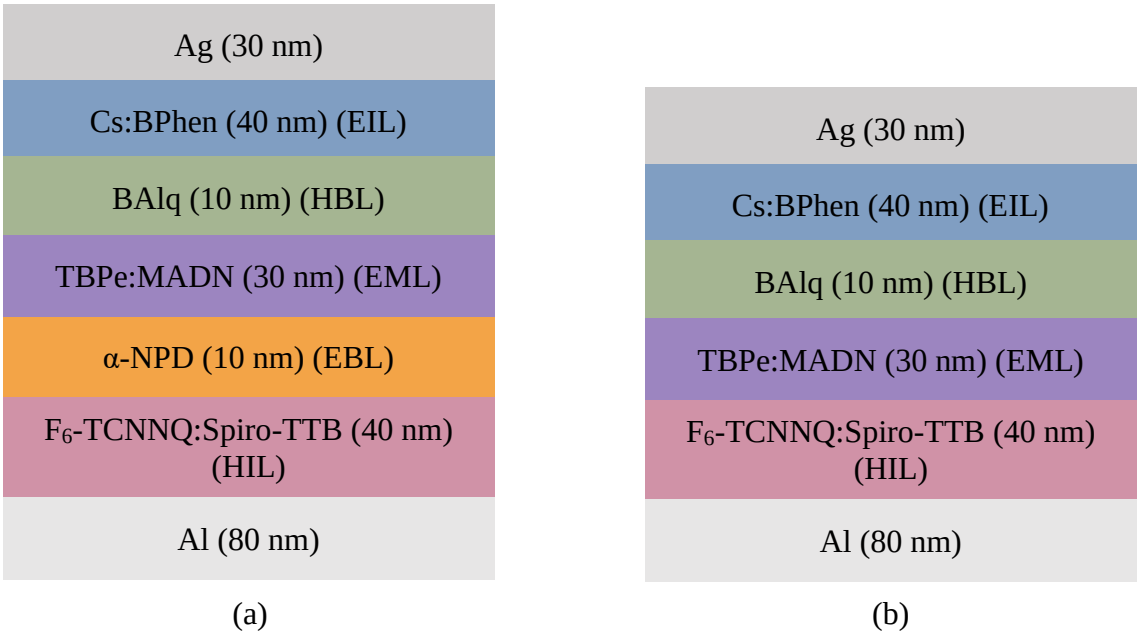

Fig. 4.20: Layers of (a) full stack and (b) devices without the EBL.

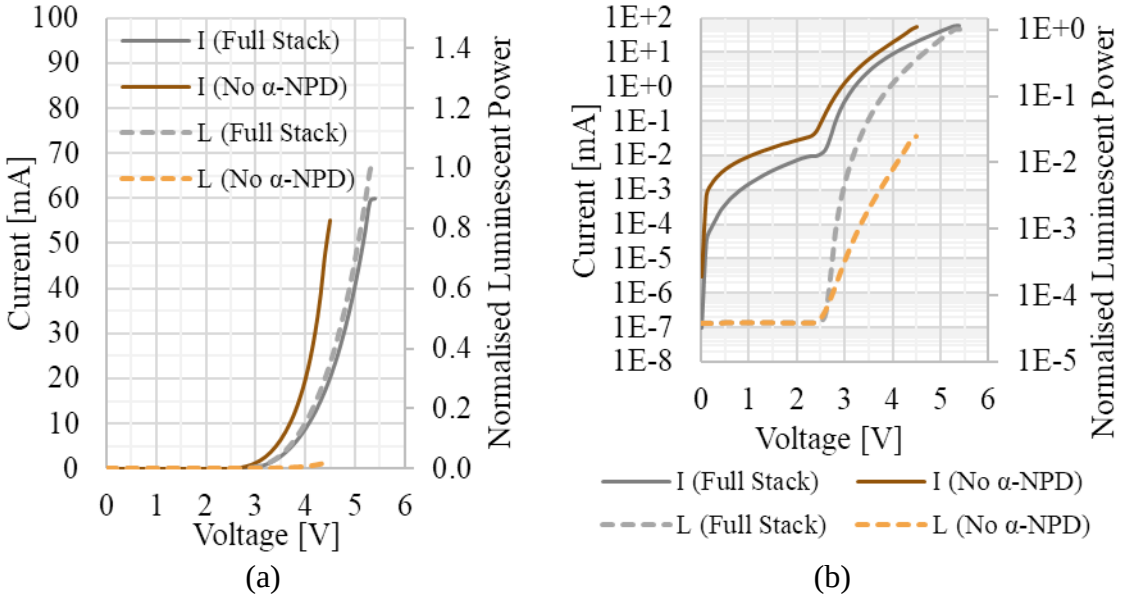

Fig. 4.21: Current-Voltage (solid) and Light-Voltage (dashed) curves for OLEDs without an EBL (b) shows the same data on a semi-log scale.

Without the α-NPD, light output is low (

Fig. 4.21, above), suggesting that this layer has a significant effect upon charge injection. Without this EBL, holes are unable to transport between the HIL and the EML, and there is a large energetic gap between the HOMO of the Spiro-TTB and the MADN, reducing the electroluminescent efficiency of the device. It can be seen from

Fig. 4.21 that in contrast to the devices without a Spiro-TTB layer (

Fig. 4.18), that the turn on of the device does not change; the Spiro-TTB layer acts to pin the internal built-in bias V_{bi} of the device; this can be explained further by looking at the simulation results presented in §4.5.

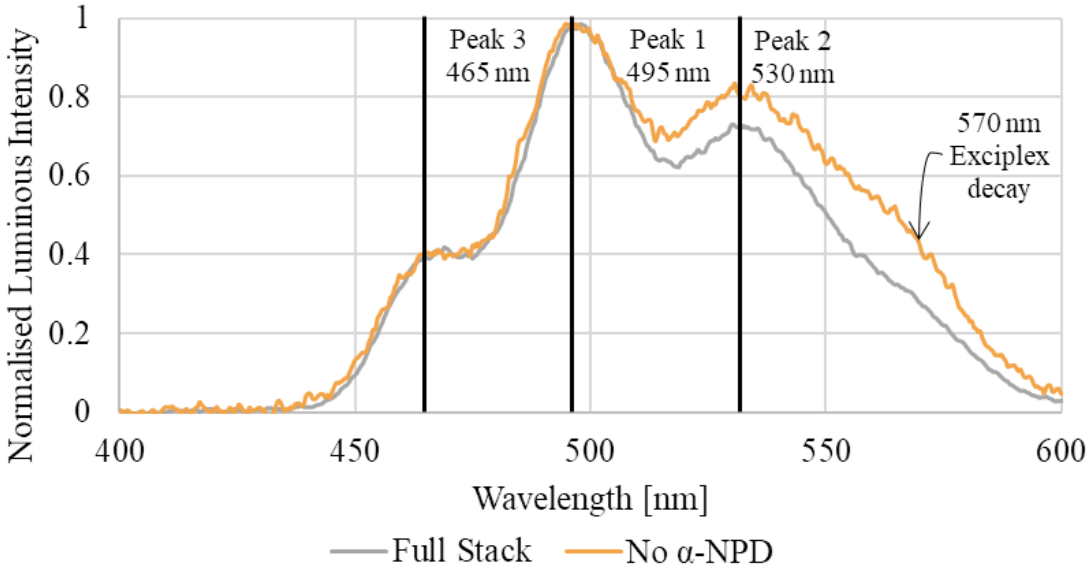

Fig. 4.22: Output electroluminescent spectrum of full stack OLEDs and OLEDs without an EBL.

The output spectrum of the devices without α-NPD (Fig. 4.22) closely matches that of the full stack devices, with an extended tail at the longest wavelength of emission. This may be due to an imbalance of charge injection within these devices causing greater exciplex formation within the EML layer, and thus causing greater proportion of exciplex decay creating this ‘excess’ at around 570 nm.

Without the EML Layer

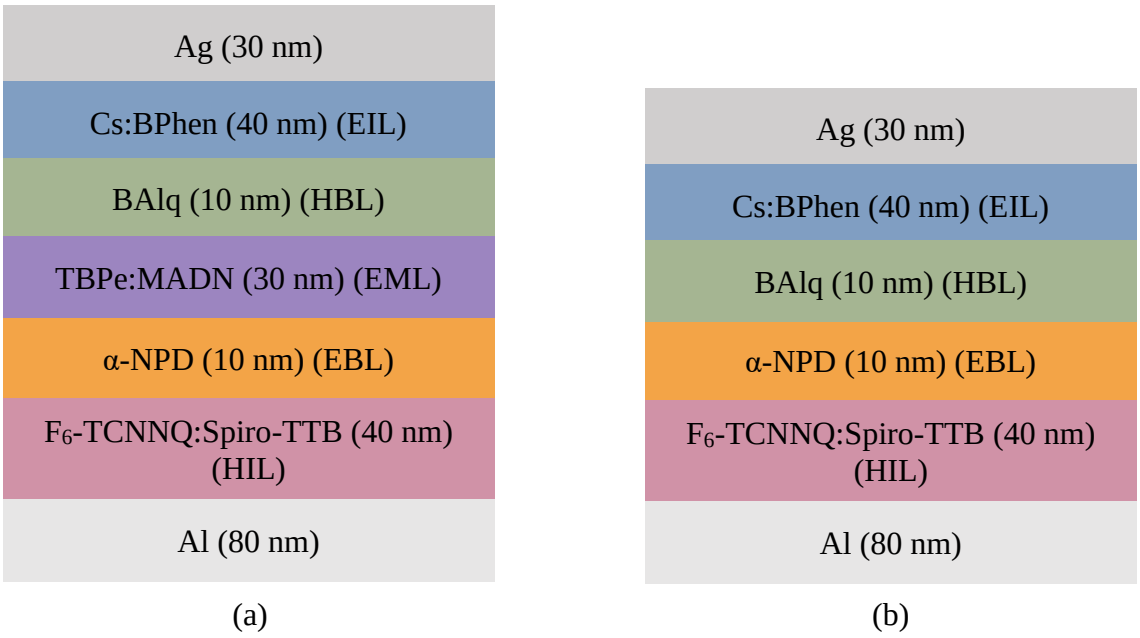

Fig. 4.23: Layers of (a) full stack and (b) devices without the EML.

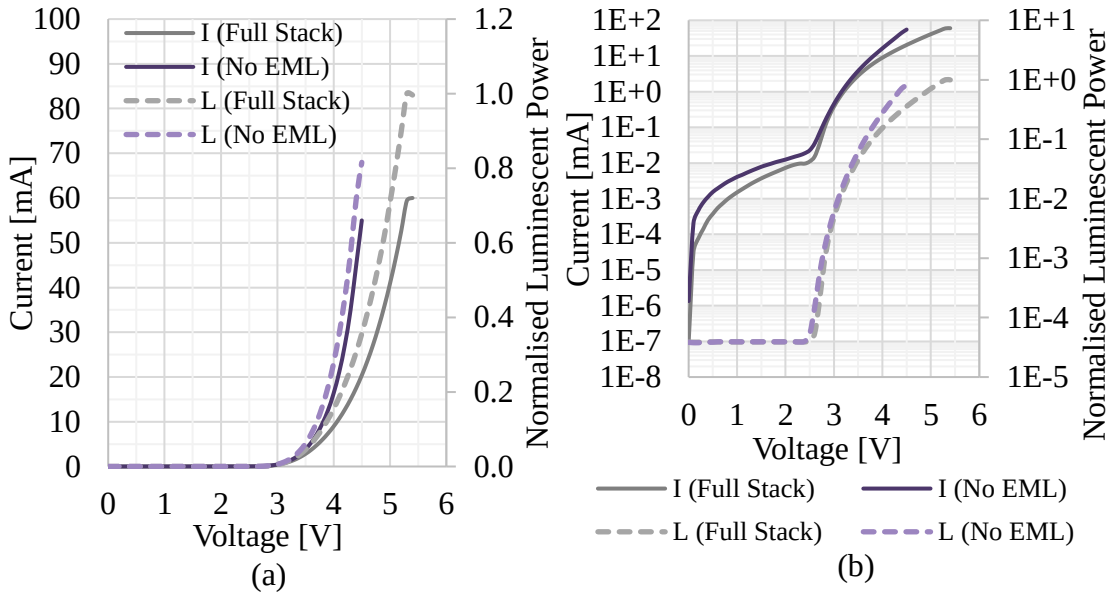

Fig. 4.24: Current-Voltage (solid) and Light-Voltage (dashed) curves for OLEDs without an EML (b) shows the same data on a semi-log scale.

Interestingly, without the TBPe:MADN emissive layer, this device still exhibits good light-current characteristics (Fig. 4.24), with a similar turn-on voltage and a lower differential resistance than the devices without the TBPe:MADN layer, potentially since the device without an EML is 23% thinner and due to the low mobilities of MADN (4.1×10^{-8} $cm^2 \cdot V \cdot s^{-1}$, field

enhancement factor 2.2×10^{-3} $(cm \cdot V^{-1})^{0.5}$ [208]) relative to α-NPD (3.2×10^{-4} $cm^2 \cdot V \cdot s^{-1}$, field enhancement factor of 8×10^{-4} $(cm \cdot V^{-1})^{0.5}$ [209]) and BAlq (9.5×10^{-7} $cm^2 \cdot V \cdot s^{-1}$, field enhancement factor of 3.8×10^{-3} $(cm \cdot V^{-1})^{0.5}$ [209]).

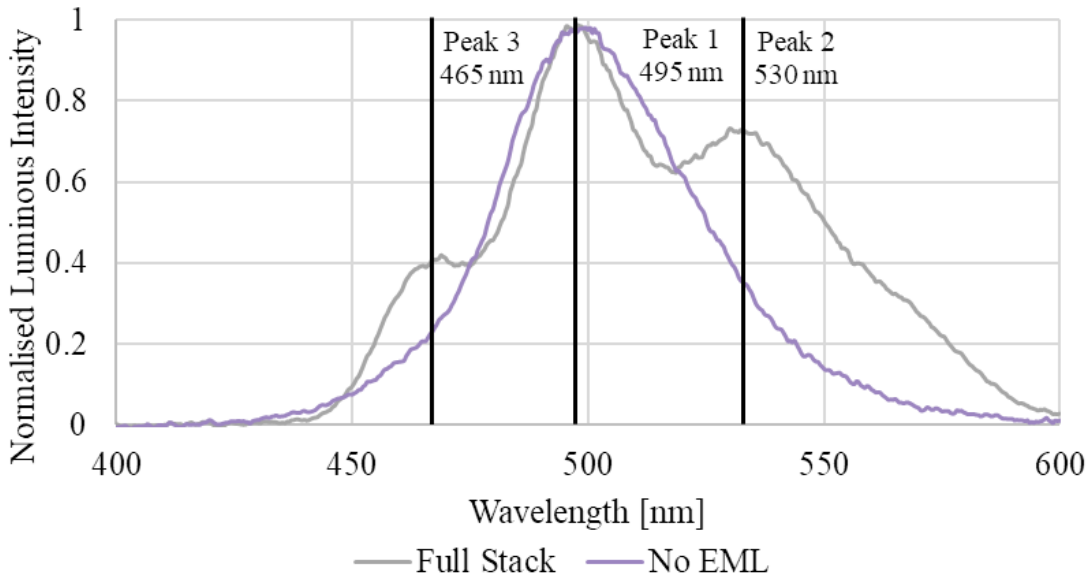

Fig. 4.25: Output electroluminescent spectrum of full stack OLEDs and OLEDs without an EML.

The electroluminescent spectrum of the devices without an EML show a similar (but wider) major peak to the full stack devices, and do not exhibit the side-peaks. This wavelength peak is similar to the photoluminescence peak of BAlq, and the charge-transfer peak of co-evaporated BAlq:α-NPD devices [210]; it is also possible that this peak appears as a result of α-NPD emission in combination with micro-cavity effects shifting the position of the peak, or some combination of the above. However, the relatively low bandwidth measurements of this device (§5.3.4), combined with the thin layers indicates that there may be significant charge-transfer exciton generation; in [210], the CT exciton has a lifetime of 40 ns, compared to 9 ns for the BAlq and less than 3 ns for the α-NPD. This is despite the higher reported mobility of the α-NPD and BAlq compared to MADN.

Without the BAlq Layer

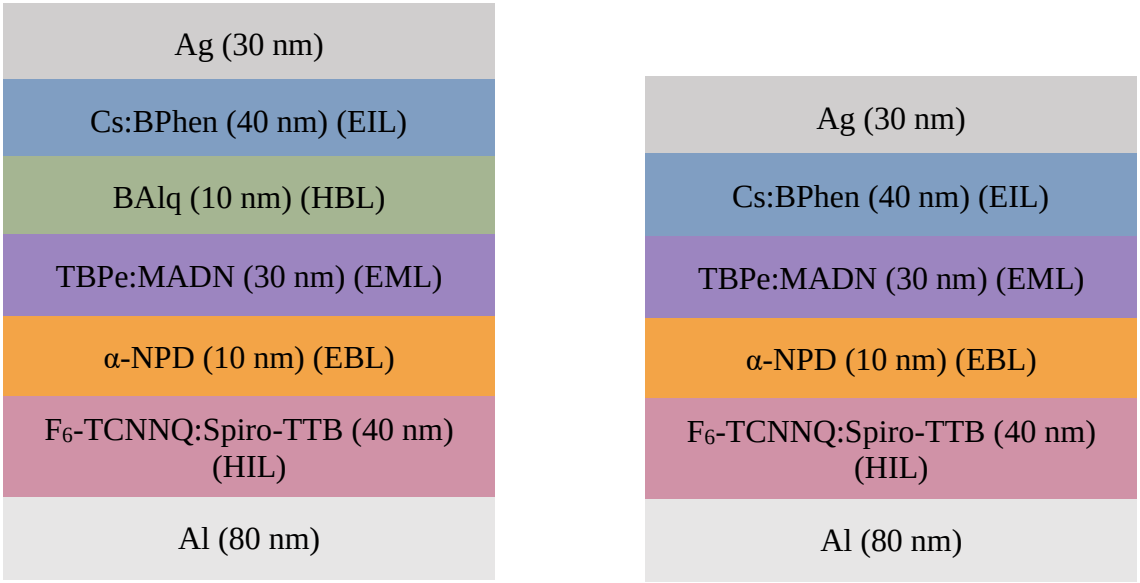

Fig. 4.26: Layers of (a) full stack and (b) devices without the HBL.

Without BAlq, Fig. 4.27 below shows that the turn-on voltage of the OLEDs is much the same, and the devices also have similar light emission compared to the full stack devices, although the devices exhibit higher leakage current, and a lower differential resistance. This may be due to the relatively low mobility of the BAlq materials and reduction in device thickness causing higher equivalent internal electric fields in the devices without BAlq. As OLED materials exhibit field-enhanced mobilities, these factors may explain the lower differential resistance of the OLED devices without an HBL.

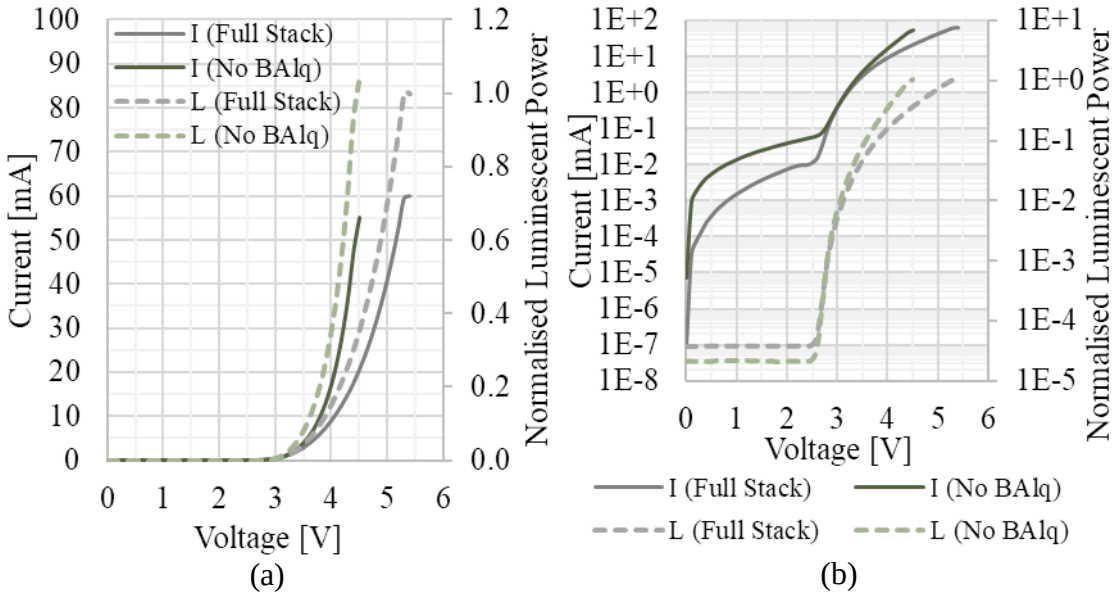

Fig. 4.27: Current-Voltage (solid) and Light-Voltage (dashed) curves for OLEDs without an HBL (b) shows the same data on a semi-log scale.

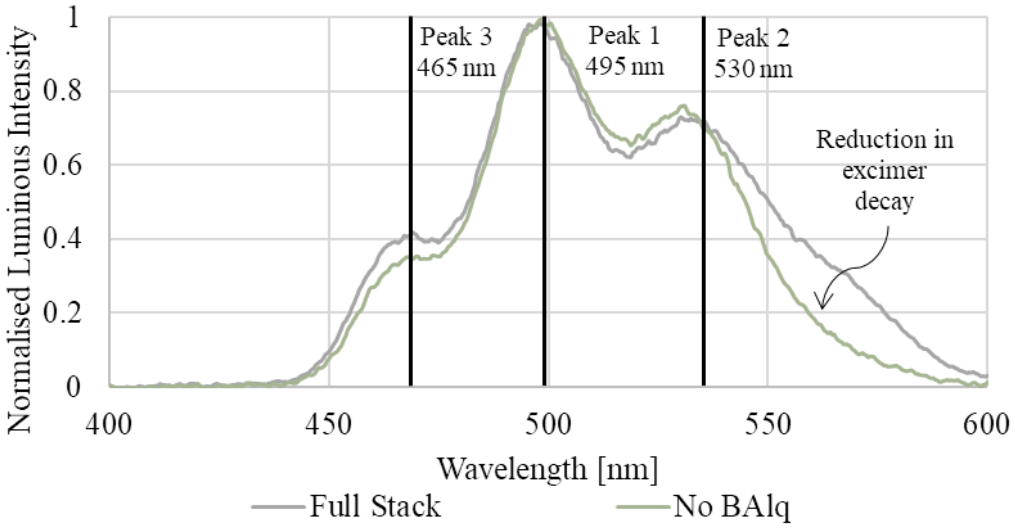

Fig. 4.28: Output electroluminescent spectrum of full stack OLEDs and OLEDs without an HBL.

Fig. 4.28 shows a reduced tail for the longest wavelength peak in the devices without BAlq; these devices show the opposite effect compared to the devices without α-NPD. This fits with the hypothesis that this tail is caused by electron-injection causing negatively charged exciplexes within the EML. The BAlq layer is designed to improve electron injection into the EML, and so without this, we may see fewer of the excimers that contribute to this 'tail' (the converse of the effect seen in Fig. 4.22).

Without the BPhen Layer

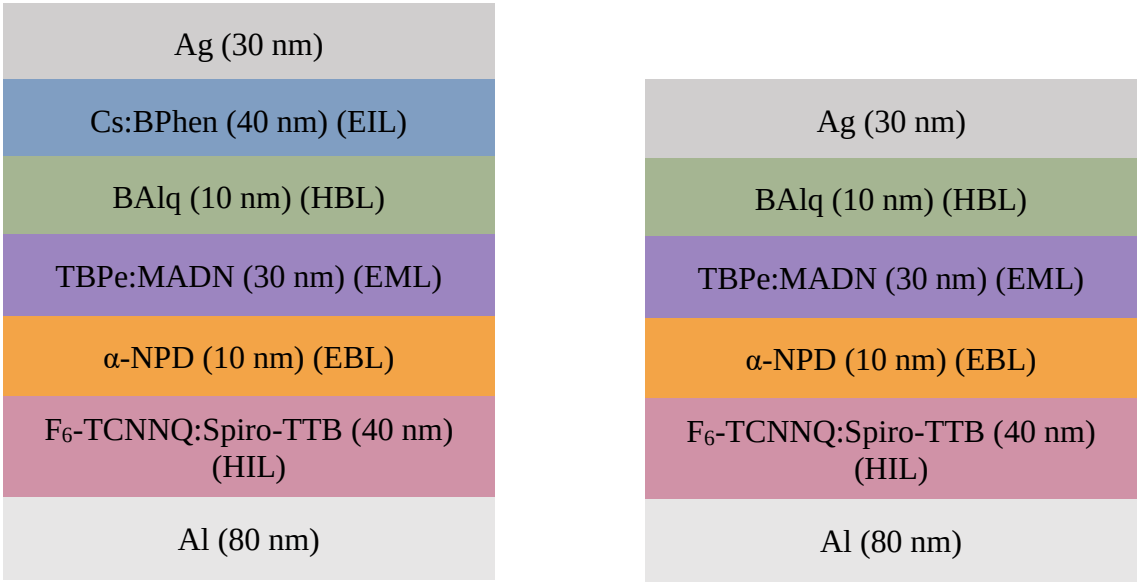

Fig. 4.29: Layers of (a) full stack and (b) devices without the EIL.

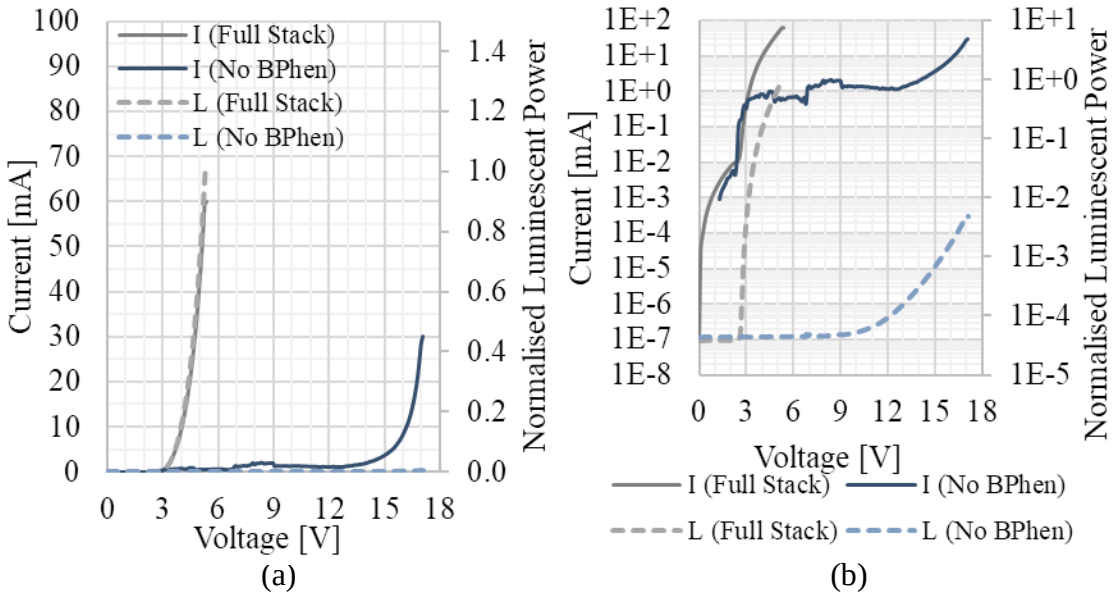

Fig. 4.30: Current-Voltage (solid) and Light-Voltage (dashed) curves for OLEDs without an EIL (b) shows the same data on a semi-log scale.

As shown in Fig. 4.30, these devices exhibit a curious non-linear behaviour; they turn on at ~1.8 V, and then maintain a current of ~1 mA until a high bias of 12-15 V is achieved. At this point, the current through the device increases in a diode-like fashion, and the light output significantly improves. It is likely that from 1.8 V to around 12 V, the device is a predominantly

unipolar device. However, at a high enough potential, electrons are injected into the device which causes the increase in both light and current. The emission spectrum (Fig. 4.31) is similar to the device without Spiro-TTB, and again corresponds to the PL emission of the TBPe dopant in the EML.

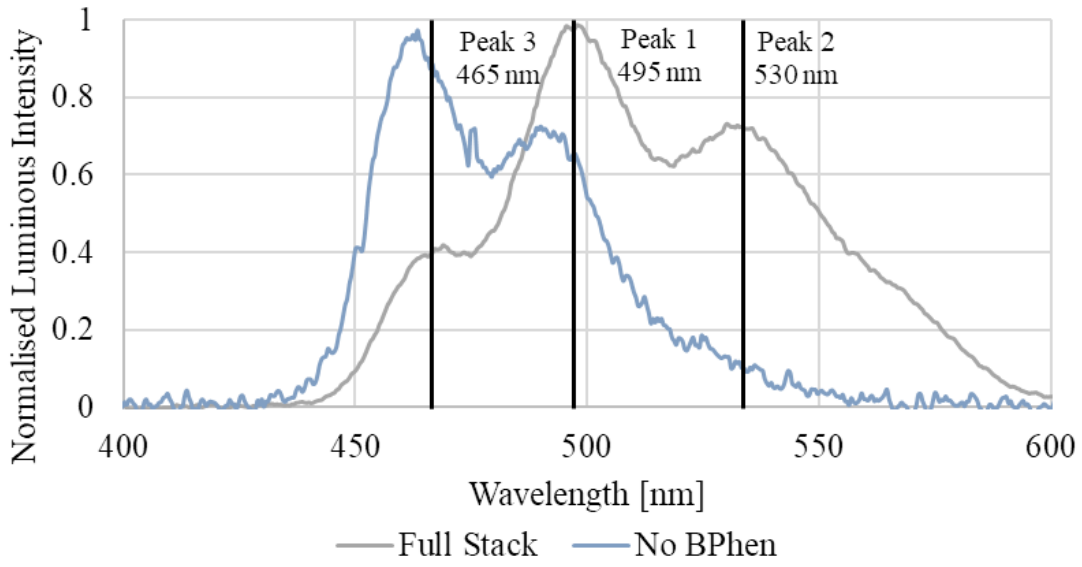

Fig. 4.31: Output electroluminescent spectrum of full stack OLEDs and OLEDs without an EIL.

While further measurements pertaining to the dynamic response of the OLEDs is provided in Chapter 5, it can be concluded that three devices provide bright DC luminescent output: the full OLED, the OLEDs without the BAlq (HBL) layer, and the OLEDs without the MADN:TBPe (EML) layer.

4.5 DC Simulation

The OLED devices are simulated in commercial Silvaco ATLAS software [211]. The software itself solves Poisson's equation (Eqs. 4.3 – 4.4) and the continuity (Eqs. 4.5 – 4.6) and constitutive equations (Eqs. 4.7-4.8) in order to model semiconductor device behaviour.

$$\nabla \cdot (\varepsilon \nabla \phi) = -\rho \tag{4.3}$$

$$\boldsymbol{E} = -\nabla \phi \tag{4.4}$$

where ε is the permittivity, ϕ is the scalar electric potential field, ρ is the charge density and $\boldsymbol{E}$ is the electric field.

Carrier continuity equations:

$$\frac{\partial n}{\partial t} = \frac{1}{q}\nabla \cdot \boldsymbol{J}_n + G_n - R_n \tag{4.5}$$

$$\frac{\partial p}{\partial t} = \frac{1}{q}\nabla \cdot \boldsymbol{J}_p + G_p - R_p \tag{4.6}$$

where n and p are the electron or hole concentration, $\boldsymbol{J}_n$and $\boldsymbol{J}_p$ are the electron and hole current densities, G_n and G_p are the electron and hole generation rates, R_n and R_p are the electron and hole recombination rates, and q is the electronic charge.

The drift-diffusion constitutive equations for electrons and holes are:

$$\boldsymbol{J}_n = qn\mu_n\boldsymbol{E}_n + qD_n\nabla n \tag{4.7}$$

$$\boldsymbol{J}_p = qp\mu_p\boldsymbol{E}_p + qD_p\nabla p \tag{4.8}$$

where μ_n and μ_p are electron and hole mobilities, and D_n and D_p are the diffusion coefficients for electrons and holes, defined by Eq. (4.9).

$$D_n = \frac{\mu}{q}\frac{n}{\frac{dn}{dE_f}}, D_p = \frac{\mu}{q}\frac{p}{\frac{dp}{dE_f}} \tag{4.9}$$

4.5.1 Simulation Setup

In order for Silvaco to accurately simulate organic semiconductor devices, device models appropriate to organic materials have been implemented. The different device layers are modelled with thicknesses as in Fig. 4.1, although the device width is simulated as 1 μm and scaled to the final device area. The non-linear scaling of current exhibited by the devices on glass due to self-heating effects (Fig. 4.9(b)) is not modelled.

Density of States

As is common in organic semiconductors, the density of states ($g_{c,v}$) is assumed to be Gaussian [138], [212], [213]:

$$g_c(E - E_c) = \frac{N_c}{\sqrt{2\pi}\sigma_c} exp\left(-\frac{(E - E_c)^2}{2\sigma_c^2}\right) \tag{4.10}$$

$$g_v(E_v - E) = \frac{N_v}{\sqrt{2\pi}\sigma_v} exp\left(-\frac{(E_v - E)^2}{2\sigma_v^2}\right) \tag{4.11}$$

$$n(E_f) = \int_{-\infty}^{\infty} g_c(E - E_c) f(E - E_f) dE \quad (4.12)$$

$$p(E_f) = \int_{-\infty}^{\infty} g_v(E_v - E) \left(1 - f(E - E_f)\right) dE \quad (4.13)$$

where N_c and N_v are the electron and hole site densities, σ_c and σ_v are the widths of the density of states, E_c and E_v are the energies of the centres of the conduction and valence densities of states and E_f is the Fermi energy level. Fermi-Dirac statistics $f(E)$ provide the electron density in the 'conduction band' ($n(E)$) and hole density in the 'valence band' ($p(E)$). Although charge transport within amorphous room temperature organic semiconductors is not expected to be 'band-like', and is better described as localised hopping of charges between molecules, this approximation works well for simulation purposes. Where the electron and hole site density parameters are not found in the literature, these have been assumed to be equal to the approximate molecular density of the semiconductor, as shown in Table B - 1 in Appendix B. Similarly, the relative permittivity ε_r has been assumed to be 3.1 where not found in the literature, which is the approximate permittivity of most organic materials. The E_c and E_v parameters are equivalent to the HOMO and LUMO (or Ionisation Potential and Electron Affinity) levels reported in the literature. Where the energetic disorder is not found in the literature, it has been assumed to be 0.1 eV. The specific values used for these parameters may be found in Table B - 1.

Doping and Contacts

Doping is modelled as an additional Gaussian band within the doped layers:

$$g_c(E - E_c) = \frac{N_c}{\sqrt{2\pi}\sigma_c} exp\left(-\frac{(E - E_c)^2}{2\sigma_c^2}\right) + \frac{N_{gc}}{\sqrt{2\pi}\sigma_{gc}} exp\left(-\frac{\left(E - E_c + \Delta E_{gc}\right)^2}{2\sigma_{gc}^2}\right) \quad (4.14b)$$

$$g_v(E - E_c) = \frac{N_v}{\sqrt{2\pi}\sigma_v} exp\left(-\frac{(E - E_c)^2}{2\sigma_c^2}\right) + \frac{N_{gv}}{\sqrt{2\pi}\sigma_{gv}} exp\left(-\frac{\left(E - E_v + \Delta E_{gv}\right)^2}{2\sigma_{gv}^2}\right) \quad (4.15b)$$

where N_{gc} and N_{gv} provide the carrier 'guest' site densities due to the dopant; this has been set to be equal to the dopant molecular density within the host material, and the energetic disorder has been set to 0.05 eV, as shown in Table B - 1. The addition of an uniform doping concentration of charge is required in the HIL, EML and EIL in order to model the doped layers;

the doping concentrations used correspond to doping efficiencies of ~2-3%, which are values commonly observed in organic semiconductors [115], [116], [120], [121].

Except where otherwise indicated, the contacts are assumed to be ohmic. It has been shown that significant doping of organic layers provides quasi-ohmic contacts – for the anode, the doping provides a shift in the Fermi-level [122], [214], and highly-doped layers provide behaviour similar to 'band-bending' to allow holes to tunnel through, which provides the a quasi-ohmic p-contact. Although the description of a 'band structure' is not strictly accurate, experimental measurements have confirmed the existence of this local 'band-bending' or dipole state generation at interfaces [215], [216]. At the cathode, the Cs:BPhen forms a quasi-ohmic contact with the silver deposited on top of it; silver deposited onto Cs:BPhen has a work function of 2.4 eV, as has been observed in ultraviolet photoelectron spectroscopy (UPS) and x-ray photoelectron spectroscopy (XPS) measurements [217]. This workfunction lowering effect compared to bulk materials has been observed in other metal/organic top contact interfaces and is believed to be due to the existence of a layer of organic semiconductor on the surface of the contact metal, reducing its workfunction at the interface [218].

Mobility

Many mobility models have been used to fit charge transport within organic semiconductors, notably the Extended Correlated Disorder Model (ECDM) [140] and the Extended Gaussian Disorder Model (EGDM) [139]. Both of these models attempt to explain the field-, temperature- and thickness-dependence measured in a wide range of organic materials. However, there is still some debate amongst the scientific community as to the exact mobility mechanism (and it is possible that the actual mobility mechanism is some combination of the aforementioned models, and that different semiconductors exhibit different degrees of correlated and uncorrelated behaviour). However, for simplicity, as organic semiconductor mobility data is often reported empirically according to the Poole-Frenkel model, and in order to emulate the device behaviour for Engineering purposes, it is assumed that since the device layers are <50 nm thick, that the Poole-Frenkel Field-dependent mobility model will provide a reasonable approximation to the carrier transport within the organic layers at operating device potentials:

$$\mu_n(\boldsymbol{E}) = \mu_{n0}\, exp\left(\gamma_n\sqrt{|\boldsymbol{E}|}\right) \tag{4.16}$$

$$\mu_p(\boldsymbol{E}) = \mu_{p0}\, exp\left(\gamma_p\sqrt{|\boldsymbol{E}|}\right) \tag{4.17}$$

μ_{n0} and μ_{p0} are zero-field mobilities for electrons and holes, $\boldsymbol{E}$ is the electric field and γ_n and γ_p are the Poole-Frenkel field-enhancement mobility factors. If the activation energy at zero field and the temperature-dependent field-enhancement factors are known, then these can also be included in the mobility, although these parameters are not known and not modelled for this device. However, when the Poole-Frenkel mobility model is used, the reported mobilities of organic semiconductors can vary by orders of magnitudes according to the layer thicknesses [219]–[221]. In order to manage this effect, the mobility was chosen to vary according to an $\mu_o = \mu_{t0}\exp(At)$ relation, where t is the layer thickness and A is a fitting parameter, with the assumption that this relation holds within the range of the thicknesses used for these devices. Where data to fit the thickness relation could not be found, the parameters were estimated and modified until they gave an approximate reported mobility. These parameters can be found in Table B - 1.

Transport Between Layers

Injection from one semiconductor layer to another is modelled as thermionic emission, where the probability of a carrier crossing from one organic layer to another is given by Staudigel *et al.* [222]:

$$G\left(\Delta E_{eff}\right) = \mathrm{c}\cdot\int_{-\infty}^{\infty} g_v(E_{v1})dE_{v1}\cdot \int_{-\infty}^{\infty} g_v(E_{v2})dE_{v2}\begin{cases}\exp\left(-\dfrac{E_{v2}+\Delta E_{eff}-E_{v1}}{kT}\right) & E_{v2}+\Delta E_{eff} > E_{v1}\\ 1 & E_{v2}+\Delta E_{eff} \le E_{v1}\end{cases} \quad (4.18)$$

$$\Delta E_{eff} = \Delta E - qF_{av}a_{av} \quad (4.19)$$

ΔE is the energy difference between band edges, F_{av} is the average electric field across the layer, a is the average molecule size between the sides of the barrier, and c is chosen such that $G(0)$ normalises to 1. From this, the current at the interface is calculated as in [211]:

$$J_n = qv_n\left(n^+ - n^- G\left(\Delta E_{eff}\right)\right) \quad (4.20)$$

$$J_p = qv_p\left(p^+ - p^- G\left(\Delta E_{eff}\right)\right) \quad (4.21)$$

where J_n (J_p) are electron (hole) current densities, n^+ (p^+) and n^- (p^-) refer to the carrier densities on different sides of the junction, and v_n (v_p) refers to the electron (hole) thermal velocity,

$$v_n = \frac{A_n^* T_L^2}{qN_C}, \qquad v_p = \frac{A_p^* T_L^2}{qN_V} \tag{4.22}$$

where T_L is the lattice temperature, N_C (N_V) refer to the carrier density of states and A_n^* (A_p^*) refers to the Richardson constant which is calculated from the electron (hole) effective mass m_n^* (m_p^*) according to Eq. (4.23).

$$A_n^* = \frac{4\pi q k^2 m_n^*}{h^3}, \qquad A_p^* = \frac{4\pi q k^2 m_p^*}{h^3} \tag{4.23}$$

Trapping

Traps are modelled as exponentially-decaying bands (g_A, g_D) characterised by a density of acceptor (donor) trap states H_A (H_D) and a characteristic temperature T_{CA} (T_{CD}) [223]:

$$g_A(E) = \frac{H_A}{kT_{CA}} exp\left(\frac{E - E_C}{kT_{CA}}\right), \qquad g_D(E) = \frac{H_D}{kT_{CD}} exp\left(\frac{E_V - E}{kT_{CD}}\right) \tag{4.24}$$

In this simulation, $H_{A,D}$ are set to a value of 1×10^{18} cm^{-3} and $T_{CA,D}$ are set to 1200 K in each layer [222].

Interface defects are also modelled as having a surface trap concentration of 1.4×10^{10} , a characteristic temperature of 5500 K and an carrier capture cross-section of 1×10^{-14} cm^2 or 1×10^{-16} cm^2 depending on the type of carrier and trap (i.e. acceptor traps have a larger hole capture cross section than electron capture cross section and vice-versa for donor traps) [222].

Recombination and Excitons

Recombination is modelled according to the bimolecular Langevin Recombination model, where the recombination rate is given by:

$$R_L = r_L(x, y, t)(np - n_i^2) \tag{4.25}$$

Where the Langevin recombination rate coefficient r_L is given by:

$$r_L(x, y, t) = \frac{q\left[\mu_n(\boldsymbol{E}) + \mu_p(\boldsymbol{E})\right]}{\varepsilon_r \varepsilon_0} \tag{4.26}$$

In addition to the electron and hole drift diffusion equations Eqs. (4.7) and (4.8), in organic semiconductors, it is necessary to include singlet and triplet exciton continuity equations.

$$\frac{dS(x, y, t)}{dt} = 0.25R_L - \frac{S(x, y, t)}{\tau_s} + \nabla\left(D_s \nabla S(x, y, t)\right) - K_{nrs} S(x, y, t) \tag{4.27}$$

$$\frac{dT(x,y,t)}{dt} = 0.75R_L - \frac{T(x,y,t)}{\tau_t} + \nabla\big(D_T \nabla T(x,y,t)\big) - K_{nrt}T(x,y,t) \qquad (4.28)$$

Equations (4.27) and (4.28) are describing the rate of change of singlet exciton density $S(x,y,t)$ and triplet exciton density $T(x,y,t)$ as a function of the Langevin recombination rate R_L, singlet (triplet) radiative decay lifetime τ_s (τ_t), singlet (triplet) exciton diffusion constant D_s (D_T), defined as in Eq. (4.29) and the singlet (triplet) non-radiative decay constant K_{nrs} (K_{nrt}).

$$D_S = \frac{L_{DS}^2}{\tau_S}, D_T = \frac{L_{DT}^2}{\tau_T} \qquad (4.29)$$

L_{DS} (L_{DT}) is the singlet (triplet) diffusion length. These exciton rates are used to calculate luminescent power. The 0.25 and 0.75 pre-factors to the Langevin recombination rate are according to standard spin statistics.

These equations ignore the effect of singlet dissociation, inter-system crossing, triplet-triplet annihilation, and quenching rates due to singlet-triplet, singlet-singlet, triplet-triplet, singlet-polaron, triplet-polaron and dipole-dipole interactions, although these can be implemented if these rates are known.

The final simulation parameters and input file may be found in Appendices B & C.

4.5.2 Simulation Results

Based upon the model inputs and parameter values introduced in the previous section, the DC behaviour for the full stack OLEDs is modelled. From this, the simulation is developed to reproduce the behaviour of the OLEDs manufactured without certain layers, in order to improve understanding of the OLED behaviour and simulation validation. The energy level alignments of the full stack OLED can be seen below in Fig. 4.32.

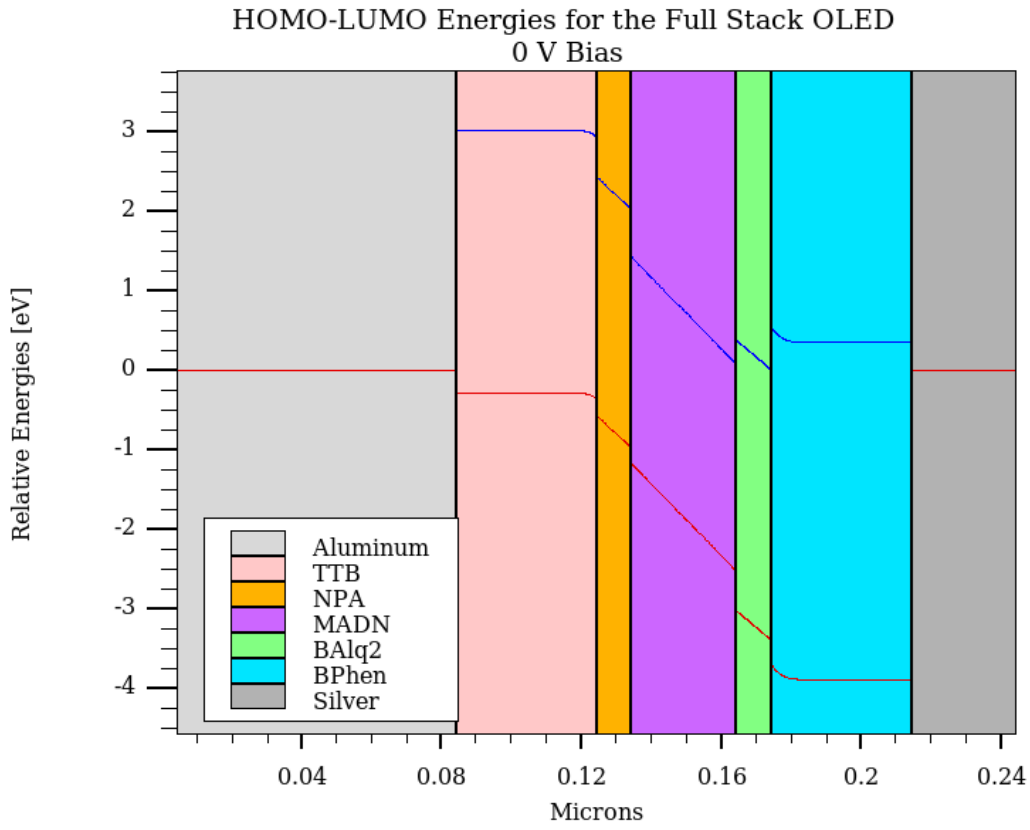

Fig. 4.32: The relative HOMO (red) and LUMO (blue) levels exported from the simulation model at a 0 V bias.

Simulation is a powerful tool that allows the systematic physics-based methodology of traditional semiconductor engineering to be used in complement with the trial-and-error of experimental device development. Further, it allows insights into behaviour within the OLED devices, which can be difficult to extract from device measurement.

Full Stack

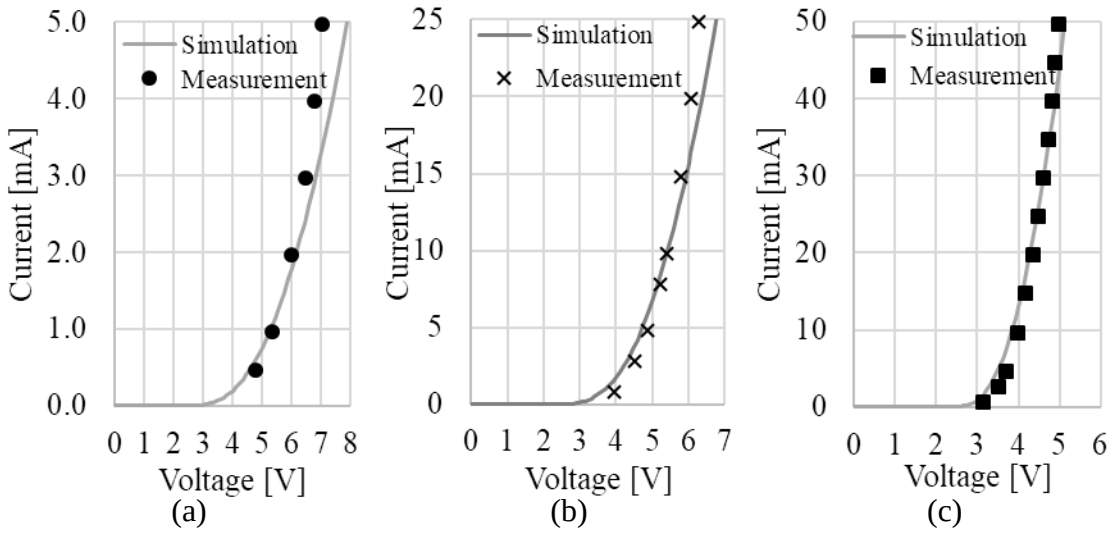

Fig. 4.33: Current-Voltage for the (a) 0.12 mm^2, (b) the 1.1 mm^2 and (c) the 9 mm^2 OLEDs on silicon (points) and simulation (lines).

We can see in Fig. 4.33 that the simulation model offers a very good fit for the measured OLEDs of all different dimensions on silicon substrates. Of course, as per Fig. 4.9, this simulation model does not take into account the thermal mobility enhancement, and so will likely underestimate the current for the devices on glass.

Without the Spiro-TTB Layer

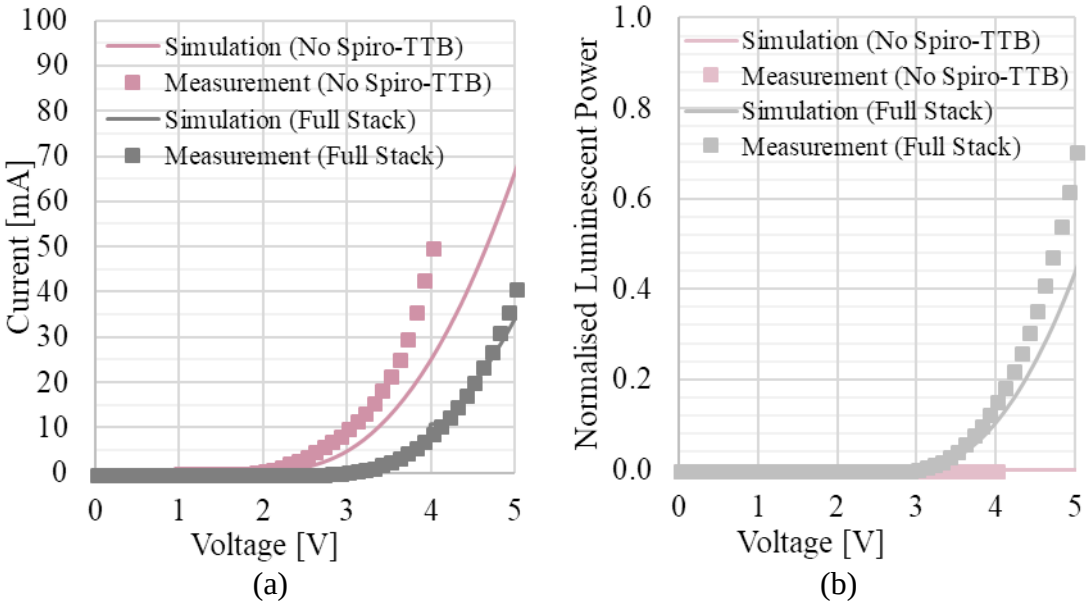

Fig. 4.34: (a) Current-Voltage and (b) Light-Voltage measurement and simulation comparison for the 9 mm^2 OLEDs on glass substrates with and without the HIL.

It can be seen from Fig. 4.34 that the simulation shows good trends compared to measurement, with the exception of the thermally enhanced mobility at higher currents. The simulation predicts that the turn-on voltage of the device without Spiro-TTB is lower than the turn-on of the full stack device, although the simulation shows a slightly higher turn-on voltage than seen in measurements; this may be ascribed to the uncertainty in mobility levels and HOMO/LUMO levels described in the literature. The simulation shows that the devices without Spiro-TTB are electron-only, with very little light output, even at high current densities. The discrepancy seen between the simulation and measurement currents may be due to an overly-pessimistic modelling of the electron-mobility in these electron-only devices.

Without the α-NPD Layer

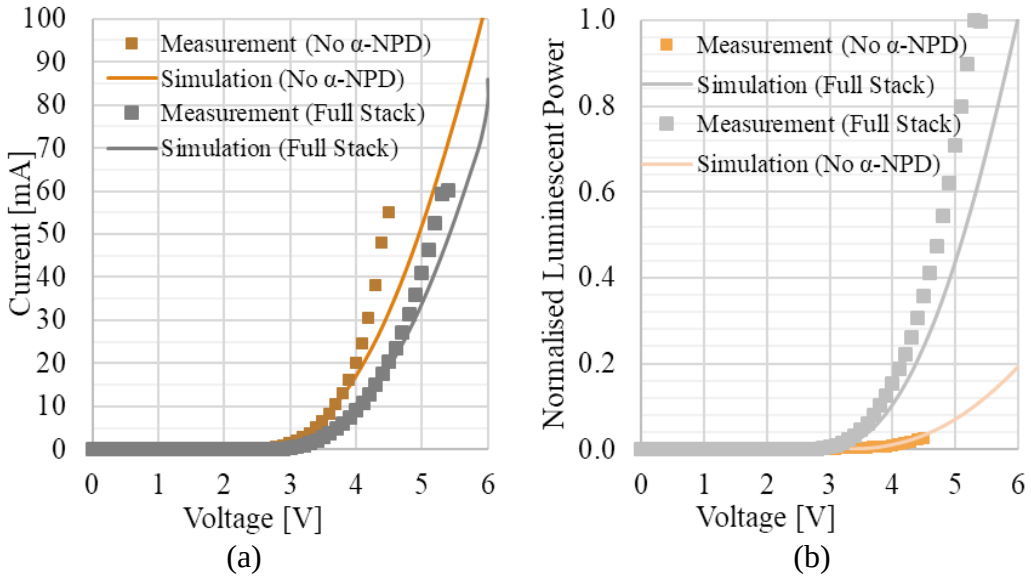

Fig. 4.35: (a) Current-Voltage and (b) Light-Voltage measurement and simulation comparison for the 9 mm^2 OLEDs on glass substrates with and without the HBL.

The current-voltage curves in Fig. 4.35(a) show a reasonably good fit between experiment and simulation, except at high-current, which is likely to be due to the thermal mobility enhancement previously mentioned. In order to account for the low-luminescence behaviour of the OLEDs without the α-NPD layer, the HOMO level of the Spiro-TTB layer had to be reduced by 0.3 eV relative to published values, to 4.9 eV, and the non-radiative exciton recombination rate was increased within the Spiro-TTB layer. Both of these changes are reasonable, as the HOMO level for Spiro-TTB has also been reported as 4.9 eV [224] (this may also be due to interface states at the Spiro-TTB/MADN boundary) and high doping is commonly accepted as causing quenching of luminescent excitons [225]. The effect of this change in HOMO, is to reduce the hole injection from the Spiro-TTB layer and move most of the recombination from within the EML to the Spiro-TTB layer, where excitons recombine in a non-radiative manner. However, the energy difference between the MADN and Spiro-TTB layers means that some holes do have enough energy to be injected into the MADN layer, where they radiatively recombine, and produce the relatively low amount of luminescent output. From this, it can be understood that the α-NPD layer acts less as an Electron Blocking Layer (EBL), but more as a Hole Transport Layer (HTL), providing an intermediate energy level for holes injected into the Spiro-TTB layer to jump to, before jumping into the EML. This also makes sense, as the reported LUMO levels for α-NPD relative to MADN and Spiro-TTB mean that it does not really

act to block electron transport from the MADN to the Spiro-TTB, as this interface is already large and only made smaller with the inclusion of α-NPD.

Without the EML Layer

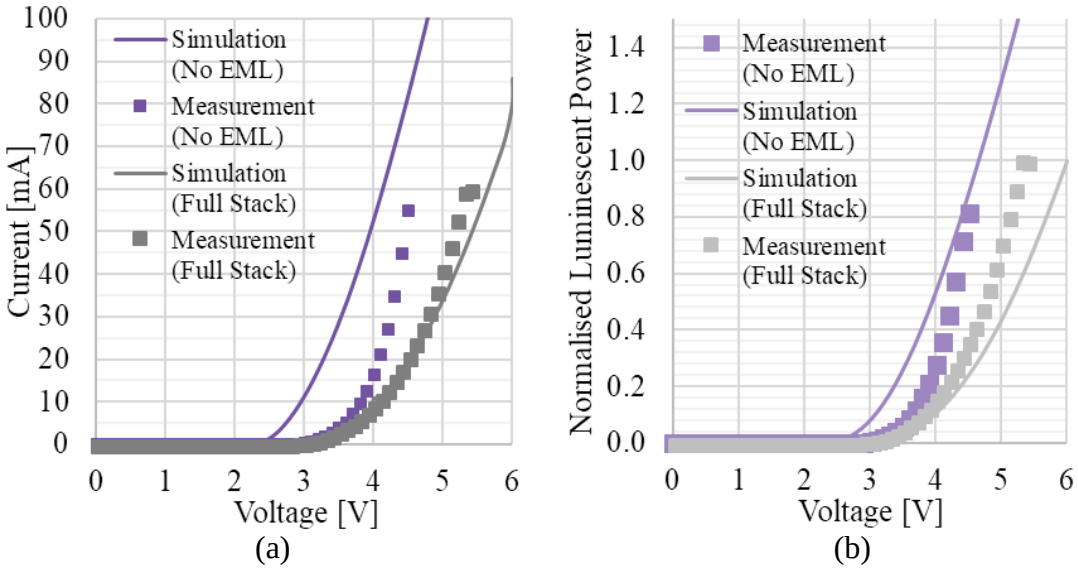

Fig. 4.36: (a) Current-Voltage and (b) Light-Voltage measurement and simulation comparison for the 9 mm^2 OLEDs on glass substrates with and without the EML.

The simulation for the devices without an emissive layer shows a higher current and higher light output than the full stack devices; the mobility in the simulation is likely overestimated compared to the real values. This effect may be due to the thin BAlq and α-NPD layers having lower mobility than the mobility values measured using thick films, and is thereby significantly overestimated in these devices. Fig. 4.37 shows the results for the same simulation model re-run with the pre-factor mobility μ_0 values reduced by a factor of 100 in the BAlq and α-NPD layers. The turn-on voltage for both these simulations is the same potential, as it is set by the pinning of the Fermi level of the carrier injection layers.

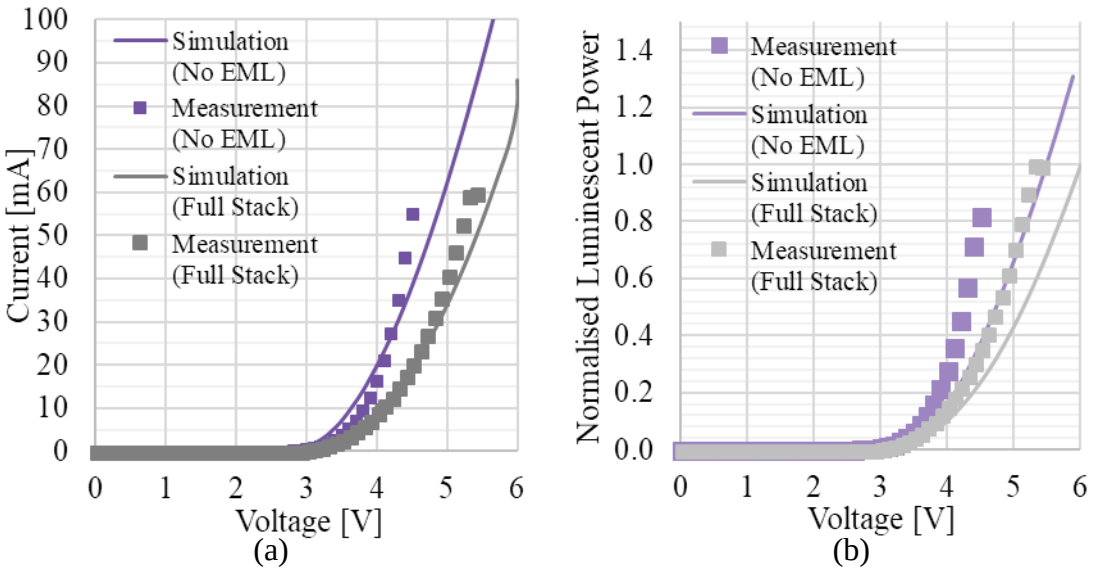

Fig. 4.37: Alternate low-mobility (a) Current-Voltage and (b) Light-Voltage simulation comparison for the 9 mm^2 OLEDs on glass substrates with and without the EML.

Without the BAlq Layer

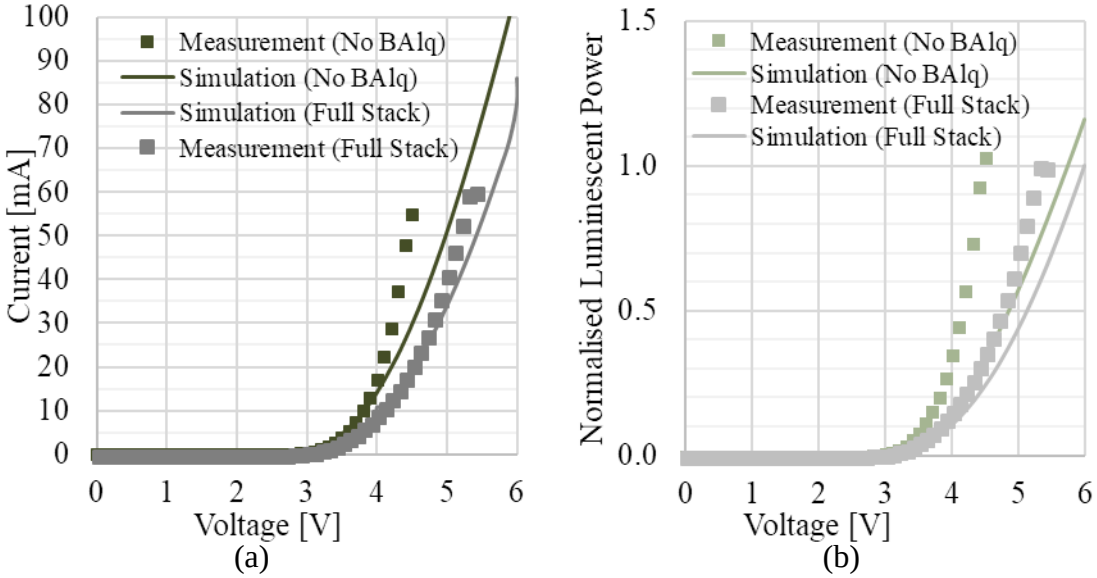

Fig. 4.38:(a) Current-Voltage and (b) Light-Voltage measurement and simulation comparison for the 9 mm^2 OLEDs on glass substrates with and without the ETL.

We can see from Fig. 4.38 that the model fits reasonably well between experiment and simulation, and the trends shown are as expected; the current in the device without BAlq is higher at the same potential compared to the full stack device. The simulation shows higher luminescent output power in the devices without the ETL compared to the full stack device,

which fits with measurement trends. We see a similar deviation between the measurement and simulation at higher currents as seen previously, but this may be explained by the thermal mobility enhancements. In contrast to the α-NPD layer, it appears that the BAlq does not have a critical role in the DC operation of the OLEDs.

Without the BPhen Layer

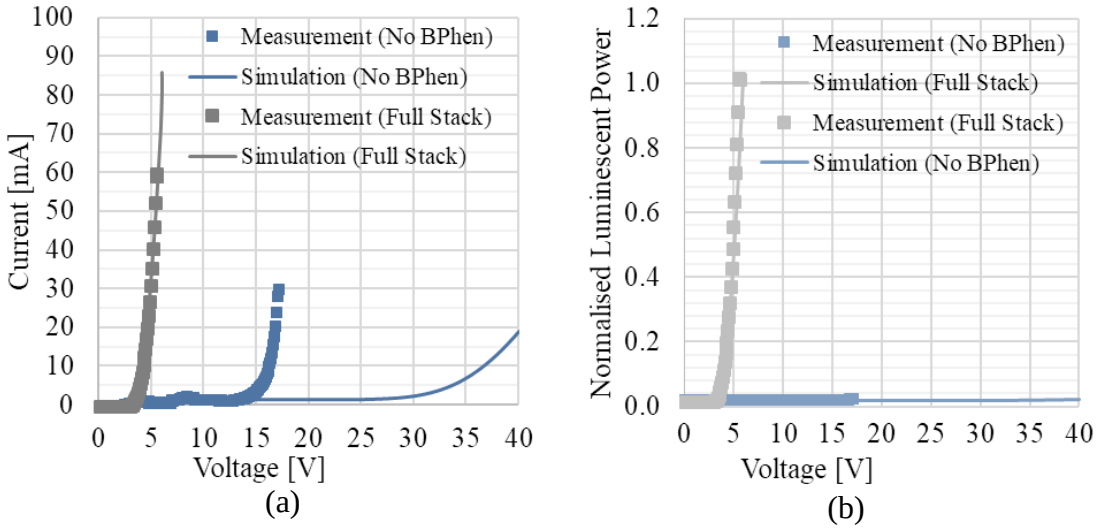

Fig. 4.39: (a) Current-Voltage and (b) Light-Voltage measurement and simulation comparison for the 9 mm^2 OLEDs on glass substrates with and without the EIL.

The devices without the BPhen layer exhibit a strange behaviour, and, as shown in Fig. 4.39, this could be emulated in simulation, although for this behaviour the model required non-ohmic contacts to be modelled in the device. The workfunction of the aluminium anode is modelled as 4.2 eV, and the silver cathode is set to a workfunction of 3.35 eV. Under these conditions, the simulation shows the device turning on to a constant hole current of 1 mA. As the bias increases, electrons can tunnel into the device, and we begin to see both an increase in current and light output (although this is far from the level achieved by the full-stack devices). The configuration of this simulation suggests that these devices are no longer bulk-limited, but injection limited, due to the BAlq-Ag contact. The bias at which this second ‘turn on’ occurs is much higher in simulation than in experiment, although experimentally it was observed that this voltage differed significantly between different devices.

It is postulated that the high-voltage turn-on discrepancy between simulation and experiment is due to a higher level of disorder in the OLED and the presence of interface states, which may vary between samples. This would have significant impact upon the density of states within the

device and upon the point at which we see carrier tunnelling into the device. In addition, as before, heating of the device may act to increase the tunnelling into the device and reduce the potential at which we see turn on. Nevertheless, the simulation was able to model the general shape of the unexpected behaviour of these diodes in both current and light output, despite the highly unusual characteristic. To the best of my knowledge, this type of behaviour has not been seen in the literature; however, through simulation it has been possible to understand this characteristic for the first time.

4.5.3 Self-heating Simulation

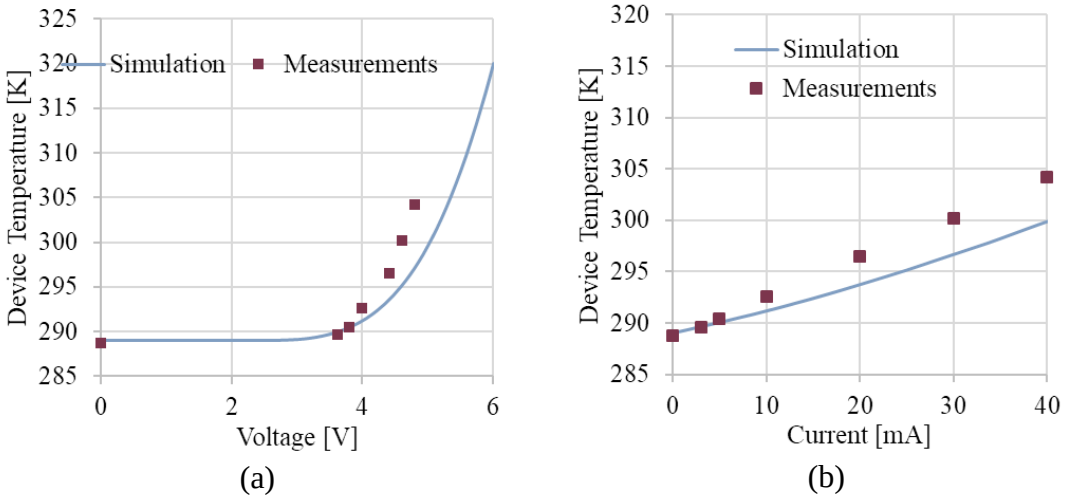

Fig. 4.40:(a) Temperature-Voltage and (b) Temperature-Current curves showing the results of the self-heating simulation (lines) and of the temperature measurements (points) discussed in §4.4.4.

A very basic self-heating simulation of the OLED devices on glass substrate was undertaken in Silvaco ATLAS, by implementing thermal conductivities and specific heat capacities for the organic layers and for the substrate. The thermal conductivities for the organic layers were set to a constant 0.004 W cm^{-1} K^{-1}, which is fairly typical for organic materials [226]–[229], and for the substrate, this was set to 4.95×10^{-5} W cm^{-1} K^{-1} [197], as the device substrate thickness was scaled to only 5 μm (rather than 1.1 mm) to make the calculation more computationally efficient. The specific heat capacity of the organic layers was set to a constant 2.04 J cm^{-3} K^{-1} [230], and the substrate again proportionally scaled as 420 J cm^{-3} K^{-1} [197]. These values are compared against the measured temperatures for the centres of the OLEDs (as the simulation accounts for the conductivity of the metal contacts), and the results from this calculation are shown in Fig. 4.40. These results show the large devices heating by ~15 K, which is of the same

order of magnitude as the self-heating measurements obtained in §4.4.4. The underestimation of the temperature suggests that the specific heat capacity and thermal conductivity of these OLED materials may be even lower than input into the simulation, with a more detailed 3D thermal simulation required to fully understand the thermal behaviour of the devices. Nevertheless, the simulated and measured temperature difference is significant enough to increase the semiconductor mobilities. At high enough currents, this can cause thermal runaway and breakdown.

4.6 Conclusions

In this chapter, the DC measurements of the OLED devices showed that they have a turn-on of around 2.8 V and emit blue light at 495 nm, with secondary spectral peaks at 465 and 530 nm. The shorter-wavelength emission is likely due to the TBPe dopant in the MADN layer, whereas the longer-wavelength light is indicative of an exciplex/charge-transfer exciton within the emissive layer.

Measurements of OLEDs on glass and OLEDs on silicon substrates show markedly different performance, wherein chemically and structurally identical diodes on different substrates have exhibited different behaviour. In particular, the OLEDs on glass substrates demonstrated non-linear scaling of the current with device area. Thermal imaging measurements confirm that this is a thermal effect, with the OLEDs on silicon demonstrating both a lower operating temperature and a more consistent behaviour with different device areas. It is found that 9 mm^2 devices on 1.1 mm glass substrates heat by at least 18.5°C at only 40 mA. For the same devices on silicon substrates at the same bias current, this temperature increase is measured to be only 5.6°C. As a result, all the large devices on glass show a thermal mobility enhancement that means the current seen in measurements exceeds the simulation model at high bias. This is corroborated by a self-heating simulation, that predicts similar temperature increases for a scaled version of the 9 mm^2 OLEDs on glass substrates.

Measurement of OLEDs excluding certain layers is used to better understand the function of each layer relative to the whole stack, and information from this is fed into a detailed OLED drift-diffusion simulation model, that gives good fit with the experimental results. It is believed that this is the first time that this OLED stack has been analysed in this way. From the measurements and the simulation, it is understood that the turn-on voltage of the whole stack is determined by the injection layers, as their doped nature causes a Fermi-level pinning. In

corroboration of this, all the OLEDs that include the contact carrier injection layers but exclude central layers exhibit the same turn-on voltage, both in simulation and in measurement. It is also determined that the carrier injection layers facilitate the formation of ohmic contacts; without the Spiro-TTB layer, the device becomes a low-turn-on electron-only diode, and without the BPhen, the device becomes injection-limited by the barriers at the contact interfaces, initially presenting a hole-only current until the voltage is high enough for the carrier injection barrier at the cathode to be overcome.

The α-NPD layer is determined to be essential for the function of the OLED, not as an nominal electron blocking layer, but as a hole transport layer, providing an intermediate energy step between the hole injection layer (HIL) and the emissive layer (EML), and without it, the luminescent output is low. This is because few holes have the energy to jump over this energetic barrier, and much of the recombination then occurs non-radiatively in the Spiro-TTB layer, as the high-levels of doping in this layer quench luminescent emission. It is also observed from the emission spectra that without the α-NPD layer, there is an increased proportion of light from the longer-wavelength exciplex. Conversely, this longer-wavelength is suppressed in OLEDs without the BAlq layer, suggesting that it is a charge imbalance caused by an excess of electrons that causes these negatively-charged exciplexes in the emission spectrum.

Interestingly, the OLEDs without the emissive layer are indeed still quite emissive, showing a bright blue luminescent output. This is assumed to be due to a charge-transfer exciton existing between the α-NPD and BAlq layers; measurements that further confirm this are discussed in Chapters 5 and 6.

Overall, the measurements taken in this chapter suggest that all of the layers are necessary for various reasons: the EIL and HIL are critical for balanced charge injection; the EBL acts more as a hole transport layer (HTL); the EML provides fast carrier recombination; and it will be shown in Chapter 5 that the HBL is required do improve the device bandwidth.

The drift-diffusion simulation model, although simplified, demonstrates many of the behaviours of the OLEDs as measured. It includes the Gaussian densities of states, exciton generation, empirical Poole-Frenkel mobilities and thermionic emission of carriers between organic layers. It has demonstrated a reasonably good agreement with measurements for all of the OLEDs presented in this chapter, and forms a foundation from which further analysis and optimisation may be undertaken.

5 HIGH-SPEED MEASUREMENTS

Small signal measurements are a useful tool to evaluate the potential communications performance of a selection of the OLEDs presented in Chapter 4. This chapter presents the small signal measurements taken for an optical link incorporating each of the OLEDs that show powerful enough light outputs and the effects of varying EML thickness and electric-field are characterised. The impact of the thermal self-heating upon the small signal response of the OLEDs is seen by placing them on a heat sink and the consequent reduction in device bandwidth is measured. The fastest OLEDs are the 0.12 mm^2 devices with a 30 nm EML on glass substrates, which achieve a 42 MHz 3 dB electrical bandwidth. Large signal measurements show the capacitive nature of even the small 0.12 mm^2 OLEDs, which limits the achievable bandwidths for communications.

5.1 Introduction

The advantage of OLEDs lies in their low system-cost and their manufacturability. However, the challenge of using disordered organic materials lies in their inherent low mobility and reliability issues. The low mobility is particularly problematic when it comes to manufacturing OLEDs for communications, as this can result in high RC time constants. While historically OLEDs have been developed for displays, this means that their operation has often been optimised for luminescence and not necessarily modulation speed. This has resulted in an interest in increasing efficiencies by encouraging emission from triplet states [231]–[233], which, of course, is detrimental to OLEDs for communications due to the longer lifetimes of

the triplet excitons, as discussed in Chapter 3. As many organic materials have been characterised with regards to their luminescent efficiency, and not necessarily their speed, this presents a challenge in developing OLEDs for communications; organic compounds that would perhaps be promising for communications purposes may have been neglected due to their moderate luminous efficiency (and low-triplet emission).

Even considering the more recent development of (O)LEDs for lighting and the subsequent interest in LiFi, the primary function of these LEDs is illumination, and they are often consequently large area devices. The resultant high capacitance causes these (O)LEDs to have relatively low bandwidths, and there is much work ongoing in the area of visible light communications to increase the available communications bandwidth of such devices [87], [96], [234]. Indeed, as encountered in visible light communications, many of the LEDs used for lighting are blue GaN LEDs with a yellow phosphor used to produce white light, and the slow-response of the phosphor can limit the overall performance of the optical link, in a similar fashion to the slow triplet phosphorescence limiting OLED speeds [235], [236].

Having investigated the DC performance of the OLEDs and used that to build a simulation model in Chapter 4, it is now necessary to understand the modulation performance of the OLED and to evaluate their communications performance and limitations within this context. This chapter presents the experimental small-signal and large signal modulation results for the aforementioned OLEDs, in order to understand some of the factors influencing the bandwidth. It is expected that OLED bandwidths are limited either by the low carrier mobilities and charge accumulation at interfaces, or by exciton recombination times. In measurement of the small signal response, low carrier mobilities and charge accumulation are electronic phenomena, which will directly relate to measurements of the small-signal resistances and capacitances of the devices, which will be presented in Chapter 6. However, as excitons are electronically neutral quasi-particles, it is expected that their recombination lifetime will not be seen in measurement of the small signal resistance and capacitance of the OLED.

5.2 Experimental Setup

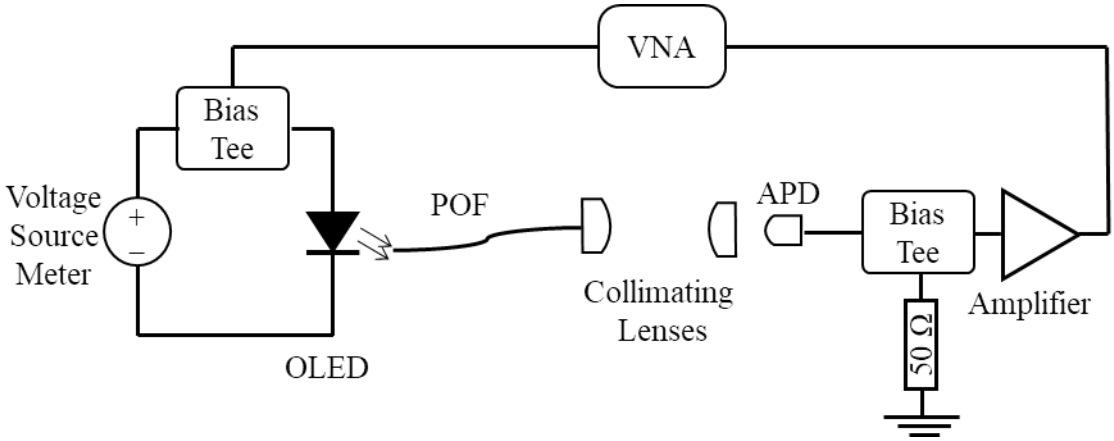

Fig. 5.1: Experimental schematic for the small signal measurements.

The bandwidths of the OLEDs were measured using a vector network analyser (VNA, Keysight N9913A), as shown in Fig. 5.1. The OLEDs are biased to a DC operating point using a source meter (Keithley 2400LV) and this DC signal is combined with the -10 dBm signal from the VNA via a bias-tee (Mini Circuits 15542). The output optical signal was butt coupled into a 1 mm diameter plastic optical fibre (POF) 1 m patch cord and fed into an 800 μm diameter avalanche photodiode (APD, First Sensor AD800-11) via a pair of aspheric optical lenses (Thorlabs). The received optical signal was then passed through a bias-tee (Mini Circuits 15542) before being amplified (Mini-Circuits ZFL-1000LN+) and fed back into the VNA. The VNA produces S-parameters, where the S_{21} parameter relates the output power to the applied input power, whereas the S_{11} parameter relates the reflected power from the device to the applied input power. The VNA was calibrated such that the output from its S_{21} measurement directly provides the frequency response of the OLED, as the bandwidths of the photodiode, amplifier and POF are all >350 MHz.

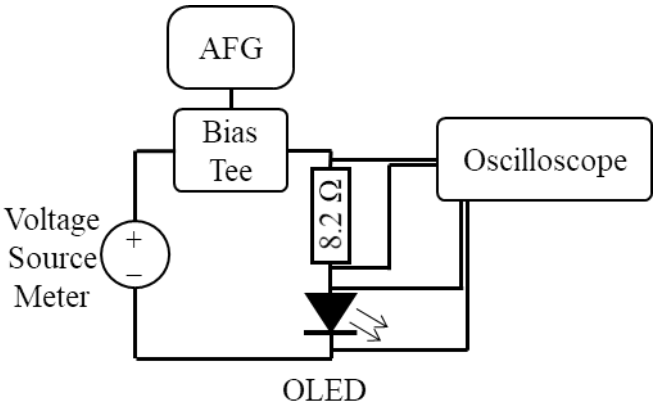

Fig. 5.2: Experimental schematic for the large signal measurements.

For large signal measurements, a 0.5 V_{pp} square wave signal from an arbitrary function generator (AFG, Tektronix AFG3102C) was fed into the OLEDs via a bias tee (Mini Circuits 15542), as shown in Fig. 5.2. The current into and voltage across the OLED was then measured using two probes fed into an oscilloscope (Tektronix DPO 3014).

5.3 Experimental Results

5.3.1 S_{21}

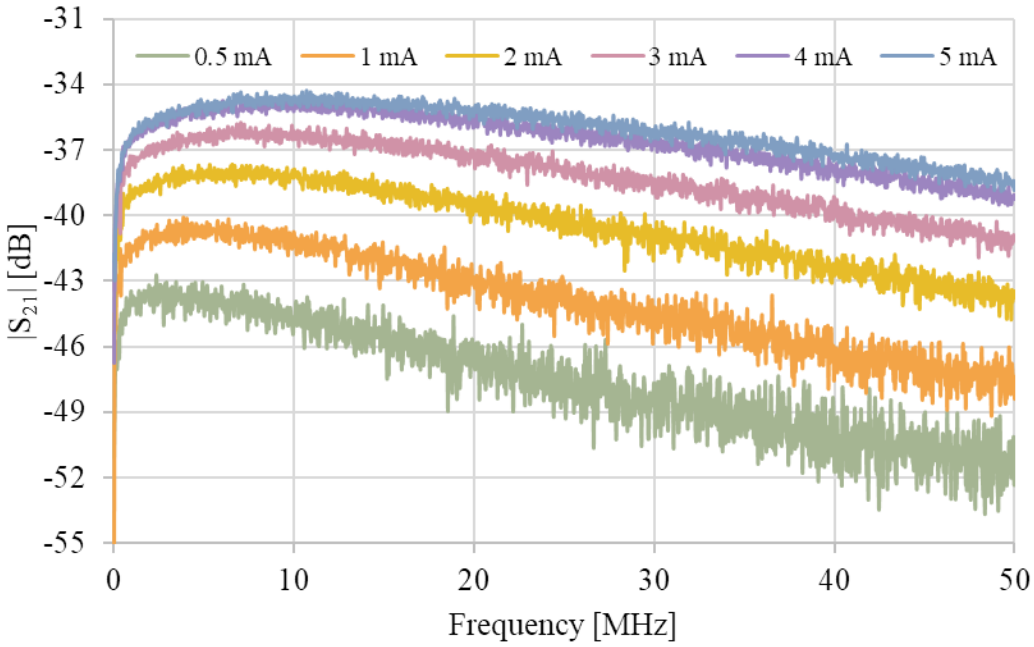

Fig. 5.3: $|S_{21}|$ measurements for the 0.12 mm^2 OLEDs with a 30 nm EML on glass at different bias currents.

The S_{21} measurements for the smallest OLEDs on glass show the highest bandwidths. From Fig. 5.3, it can be seen that the bandwidth increases dramatically with bias current, with the position of the peak response also moving to higher frequencies as the current increases. As will be discussed in §5.3.2, this effect is likely due to thermal effects, in particular, thermal mobility enhancements. However, it can be seen from Fig. 5.3 that at a DC bias current of 5 mA, a small signal bandwidth of more than 42 MHz is achieved. It is also notable that the rate of increase of bandwidth starts to decline after 3 mA bias. The roll-off observed at very low frequency is due to the filtering of the bias-tee.

A similar shape for the 1.1 mm^2 and 9 mm^2 OLED frequency responses can be seen in Fig. 5.4, below, with the bandwidth improving with bias current in all cases. Nevertheless, the bandwidth of the OLEDs becomes significantly worse as the device area increases, with the 1.1 mm^2 OLEDs achieving a maximum bandwidth of 14 MHz at 20 mA and the 9 mm^2 achieving only 3.6 MHz at 50 mA bias current. This is to be expected, as the relatively low mobility of the organic semiconductors and large area of the devices implies that these devices have a significant capacitance that limits the achievable small signal bandwidth.

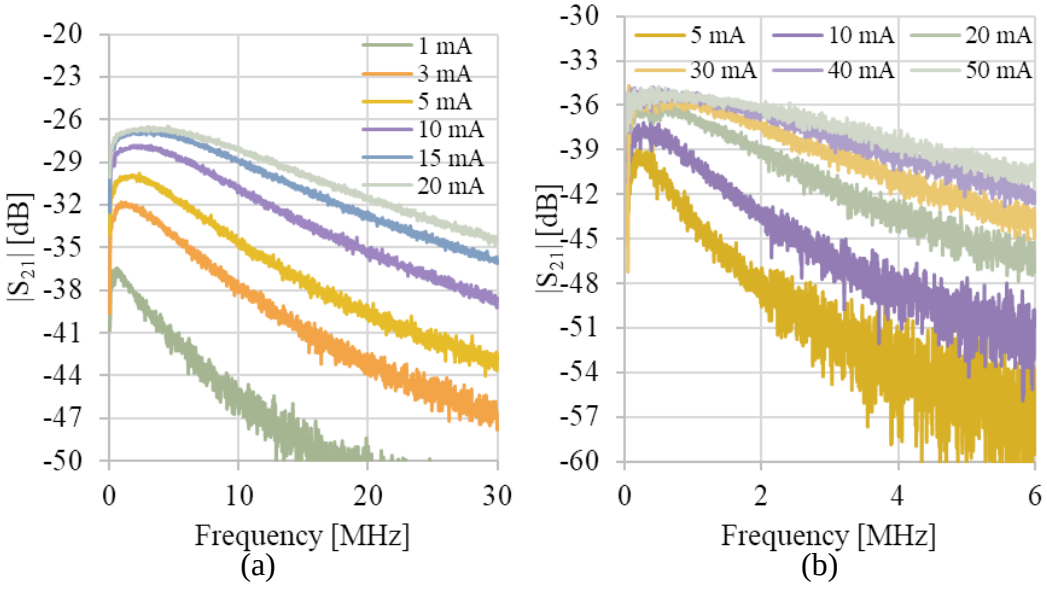

Fig. 5.4: $|S_{21}|$ measurements for (a) the 1.1 mm^2 and (b) the 9 mm^2 OLEDs with a 30 nm EML on glass substrates at different bias currents.

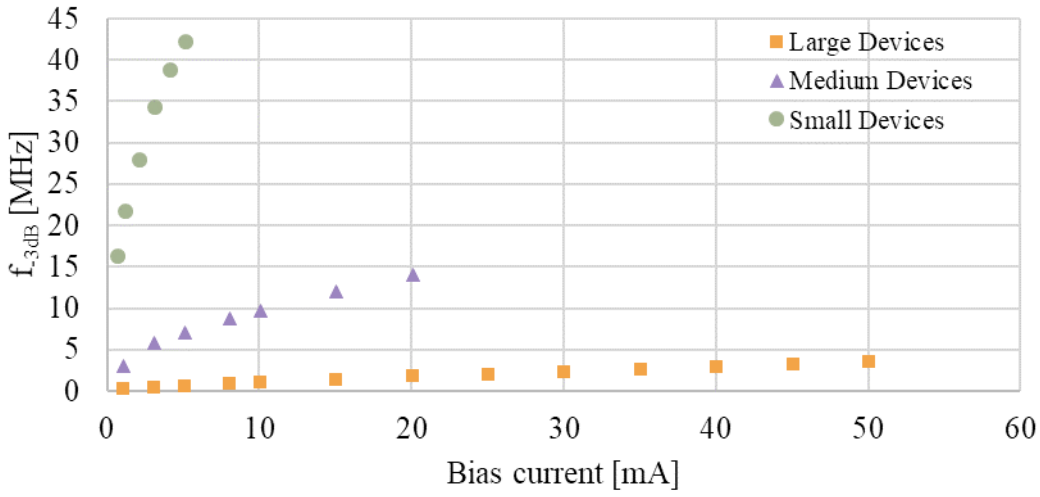

Fig. 5.5: 3 dB bandwidths of OLEDs with 30 nm EML on glass at different bias currents.

We can see the significant change in OLED electrical 3 dB bandwidths[3] between the different OLED sizes in Fig. 5.5. The 0.12 mm^2 OLEDs have a 3 dB bandwidth more than ten times higher than the 9 mm^2 device. While the area of the smallest devices is almost 100 times less than the largest, the conductance of the 9 mm^2 devices is much higher than that of the 0.12 mm^2 devices, hence the reduction in device capacitance for the smallest devices is moderated by the increased resistance

In addition, the power output of the smallest devices is, of course, lower than for the larger devices, and there will be a trade-off between reducing the device area for the purposes of improving the bandwidth and worsening the available signal to noise ratio for communications. As these OLEDs are intended for low-cost short distance on-board communications, such an optimisation may tend towards smaller devices areas in order to maximise bandwidth and not the absolute signal power.

5.3.2 Thermal Effects

As has been shown in Chapter 4, heating effects can have a significant effect upon the DC operation of OLEDs, and the mobility enhancement seen in DC operation can also be seen in

[3] Due to the square-law of the detection process, the electrical 3 dB bandwidth (half the electrical power) is lower than the optical 3dB bandwidth (half the optical power). Indeed, the optical 3 dB frequency is the same as the electrical 6 dB frequency. As the S_{21} measures the electrical response, the bandwidths quoted are the electrical bandwidths, and it is the electrical response that is plotted in this thesis.

the small signal measurements taken of the OLEDs. Two sets of S_{21} measurements for the same OLEDs with a 20 nm EML doped to 1.5 wt.% are presented in Fig. 5.6.

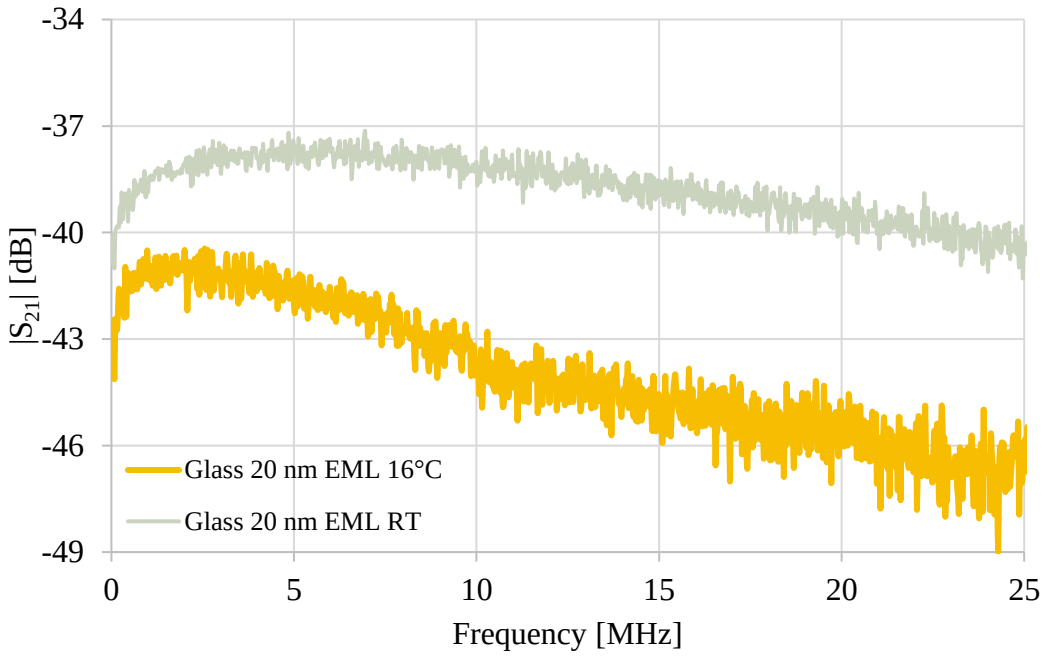

Fig. 5.6: $|S_{21}|$ measurements for 0.12 mm^2 OLEDs placed on a heat sink at 16°C and without any temperature control applied. Both measurements are for a bias current of 5 mA.

It can be seen that when the OLEDs are cooled, the shape of the frequency response significantly changes in many ways: the low-frequency response climbs to its peak much earlier; the peak is measured at around 2 MHz when the devices are placed on a heat sink. As seen in the uncooled devices measured in Fig. 5.3, this shift of peak response to higher frequencies is also seen as the current increases; it would make sense for this to occur if this effect is temperature-related. For the non-temperature controlled devices, it can be seen that the peak S_{21} response is measured around 7 MHz, and the decay of the response is much flatter than the cooled devices. The light output is reduced for all the temperature controlled devices of all sizes relative to the uncontrolled devices, and the signal appears noisier in the cooled devices. These measurements are taken consecutively using the same devices with the same equipment with the heat sink turned on or off, therefore the effect of optical misalignment between measurements may be considered negligible. This behaviour is consistent with our understanding of thermally-activated charge hopping within the organic materials $\left(\mu \propto \exp\left(-\frac{1}{T^2}\right)\right.$ or $\left.\mu \propto \exp\left(-\frac{1}{T}\right)\right)$ [191].

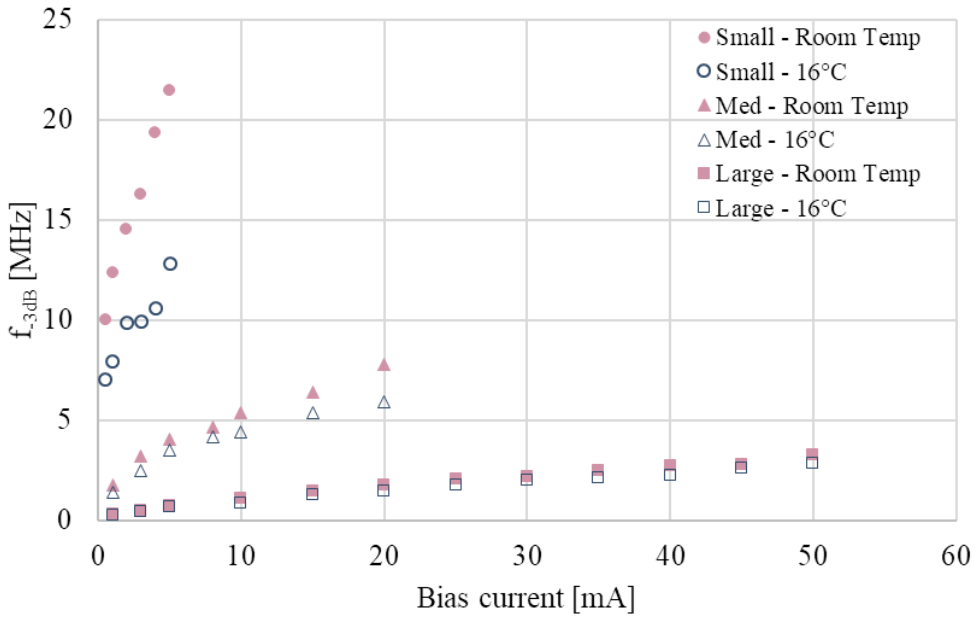

Fig. 5.7: Electrical 3 dB measurements for the OLEDs with a 20 nm EML on glass substrates measured on a heat sink set to 16°C (hollow), and measured without any temperature control (solid).

Comparison of the electrical 3 dB bandwidth of the OLEDs at different sizes and bias currents with and without temperature control can be found in Fig. 5.7. The smallest OLEDs experience a halving of their electrical bandwidths, whereas the cooling has less effect on the 1.1 mm^2 and 9 mm^2 OLEDs. This is likely because the heat sink is unable to extract the heat generated in these larger devices as efficiently as the smaller devices, probably due to the high thermal impedance of the glass.

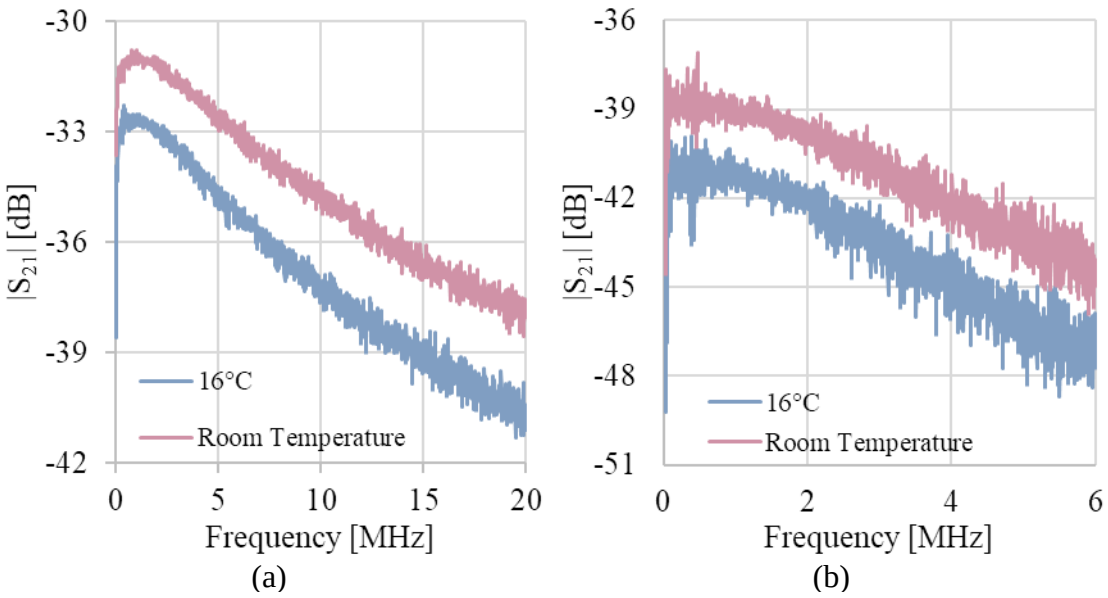

Fig. 5.8: $|S_{21}|$ measurements for (a) 1.1 mm^2 OLEDs at 20 mA and (b) 9 mm^2 OLEDs at 50 mA.

Fig. 5.8 shows the $|S_{21}|$ measurements for the 1.1 mm^2 and 9 mm^2 and it can be seen that the response of the cooled devices have the same shape as the uncooled devices, with the same position of the peak and similar decay of the response.

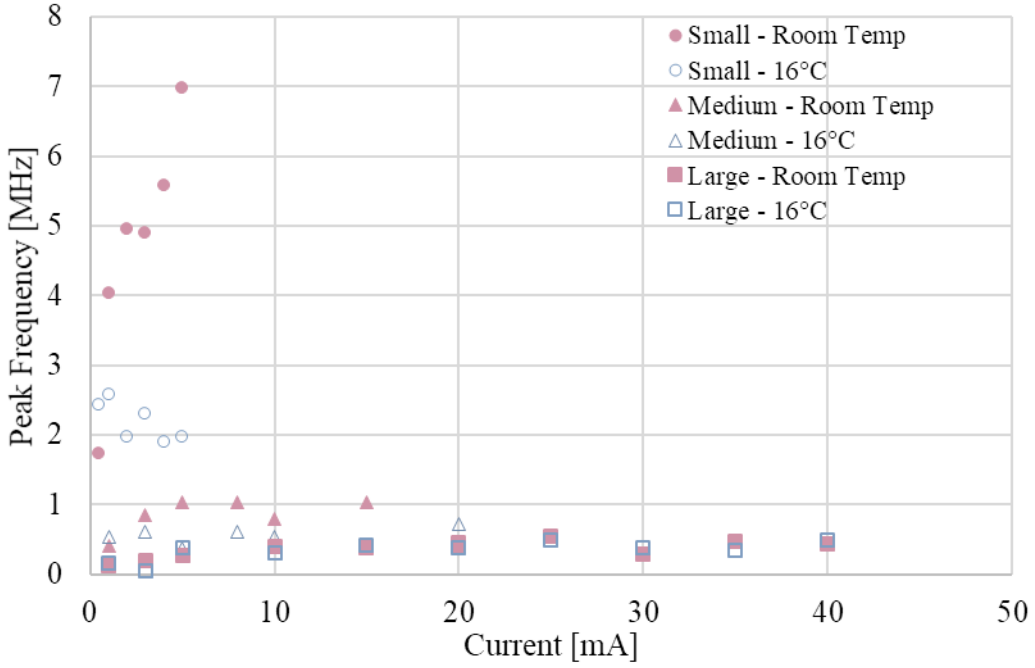

Fig. 5.9: Measurements of the frequency of the peak $|S_{21}|$ response of the OLEDs.

Measurements of the frequency of the peak of the response (Fig. 5.9) show a large reduction for the 0.12 mm^2 OLEDs with cooling, a smaller reduction for the 1.1 mm^2 and almost no reduction for the 9 mm^2 OLEDs, consistent with the measured change in bandwidths.

5.3.3 Substrate Dependence

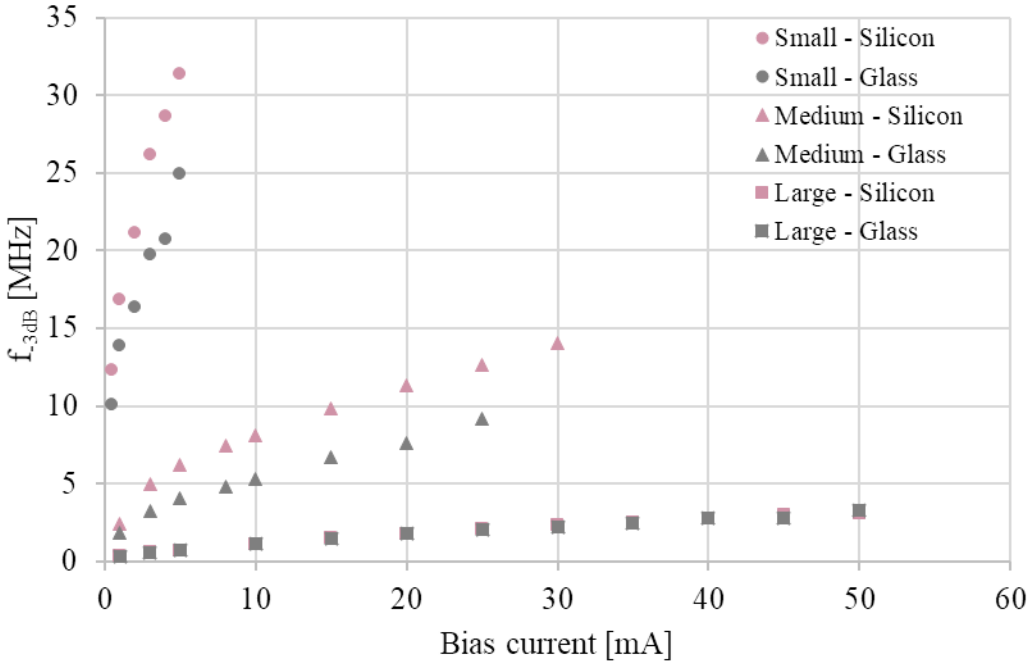

Fig. 5.10: Electrical 3 dB bandwidths measured for OLEDs on silicon and equivalent devices on glass substrates.

Interestingly, the devices on silicon have significantly outperformed their counterparts on glass substrates (Fig. 5.10), despite their lower internal operating temperature. Although there is little difference in performance for the 9 mm^2 devices, the silicon devices significantly outperform the glass devices in the 1.1 mm^2 and 0.12 mm^2 configurations. Further analysis to explain this behaviour is discussed in Chapter 6.

It can be seen from Fig. 5.11, below, that the shape of the S_{21} curves of the devices on silicon is quite different from those on glass, in particular at low frequency, where the device achieves its peak response at a lower frequency than the device on glass. The measured response for substrates on silicon is also much less noisy than the devices on glass, likely due to reduced thermal noise; there are fewer thermally-generated carriers in the cooler OLEDs on silicon than the OLEDs on glass. In addition, the high-frequency roll-off is slower for the devices on silicon. This may be due to the higher DC potential (and consequently electric field) that the devices on

silicon must operate at to sustain the same current as the devices on glass. For two devices biased to the same DC potential, as in Fig. 5.12, the bandwidths are similar (21 MHz for silicon, 20 MHz for glass), which is within experimental uncertainty for these measurements and at low currents where heating effects are lessened.

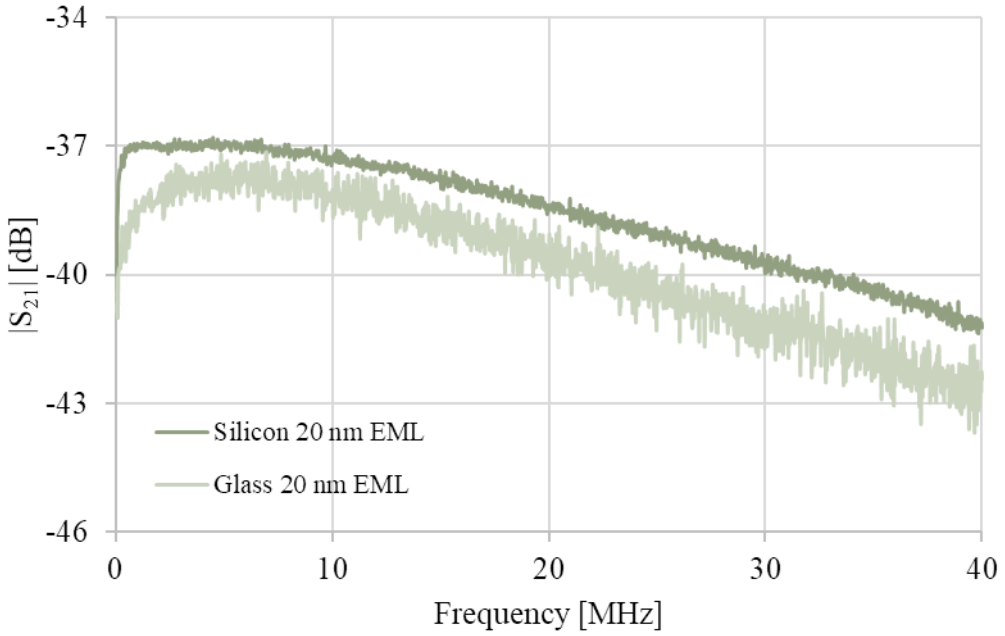

Fig. 5.11: $|S_{21}|$ of 0.12 mm^2 devices on silcon and on glass substrates at a DC bias current of 5 mA.

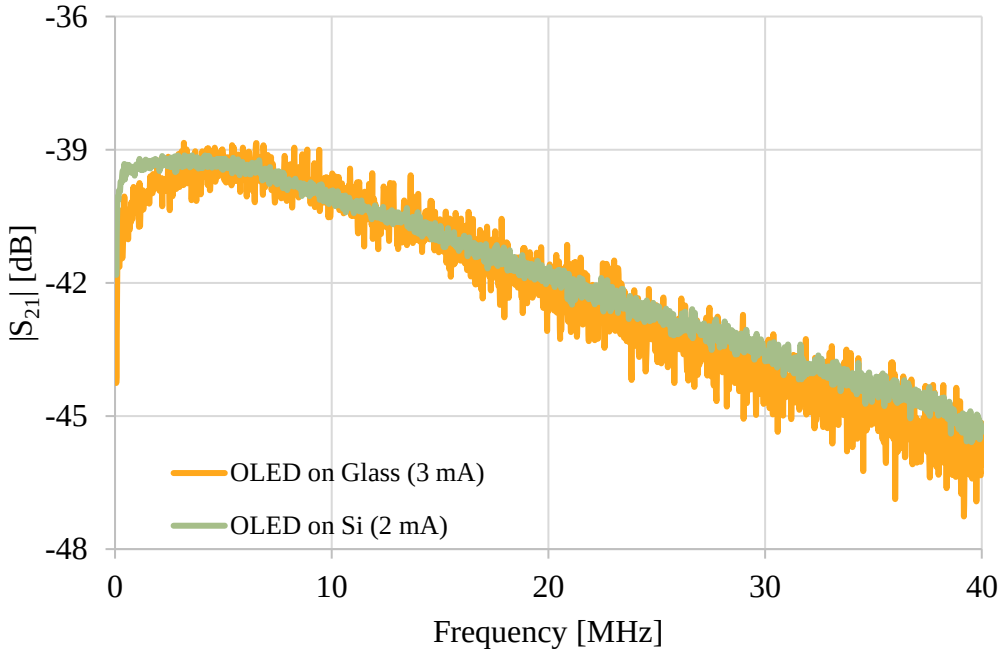

Fig. 5.12: $|S_{21}|$ Measurements for two 0.12 mm^2 OLEDs biased to the same potential.

5.3.4 Layer Dependence

Emissive Layer Dependence

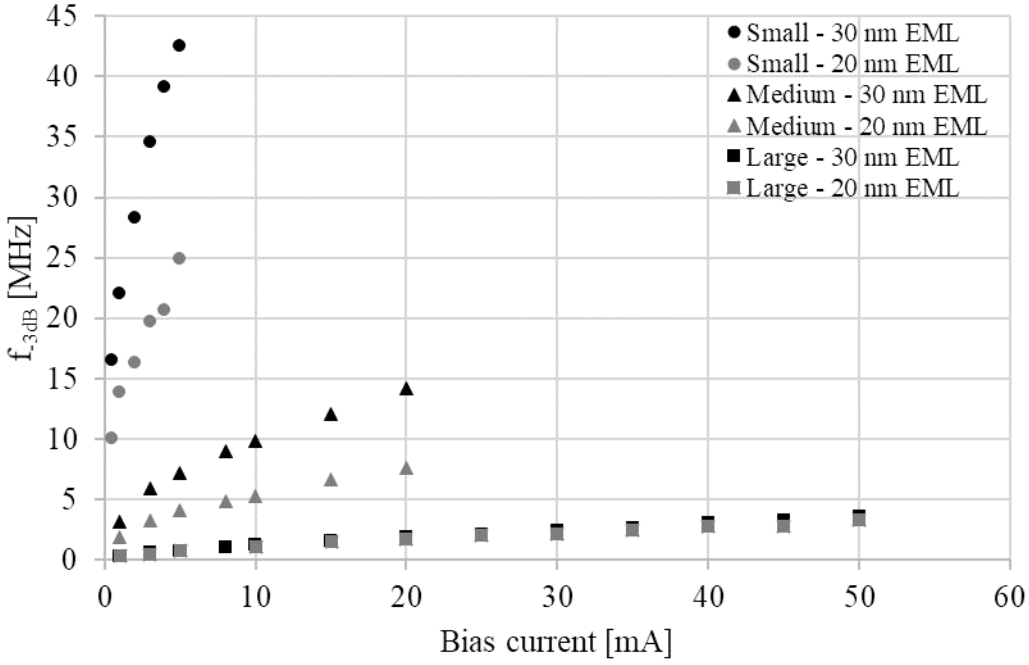

Fig. 5.13: Electrical bandwidths of OLEDs with a 20 nm EML doped to 1.5 wt% and 30 nm EML doped to 2.76 wt%.

It can be seen in Fig. 5.13 that the thickness of the emissive layer plays a significant role in determining the electrical bandwidths of the OLEDs. The 3 dB bandwidth doubles from 21 MHz for the 20 nm EML to 42 MHz for the 0.12 mm^2 devices with the 30 nm EML at 5 mA. Both sets of devices are on the same 1.1 mm glass substrates. Whereas both the 0.12 mm^2 and the 1.1 mm^2 devices show doubled bandwidths for the 30 nm EML devices, the 9 mm^2 devices have almost identical bandwidths.

Fig. 5.14 shows the relative change in shape of the $|S_{21}|$ response of the OLEDs between the silicon substrates, the 20 nm EML devices on glass substrates and the 30 nm EML substrates at bias currents of 5 mA. The response of the devices on silicon are not as noisy as the devices on the glass substrates, with the 30 nm EML exhibiting a peak response at a higher frequency than either of the other two devices.

The DC characteristic of the devices with a 20 nm and 30 nm EML are very similar (Fig. 5.15, below), so this bandwidth enhancement may be accounted for by a reduced capacitance for the thicker devices. The thicker devices have a higher small signal resistance, but this is far

outweighed by the reduction in device capacitance. The electrical modelling of these devices in Chapter 6 investigates this effect in greater detail. It is also observed that empirical Poole-Frenkel zero-field prefactor carrier mobilities tend to increase with layer thickness [219], [220], [237], which may further account for the further mobility enhancement in the bandwidth of the thicker devices. The increased doping between the 20 nm and 30 nm EML devices may also have an effect, although further control samples would be required in order to confirm whether any changes in behaviour are due to doping or thickness-changes.

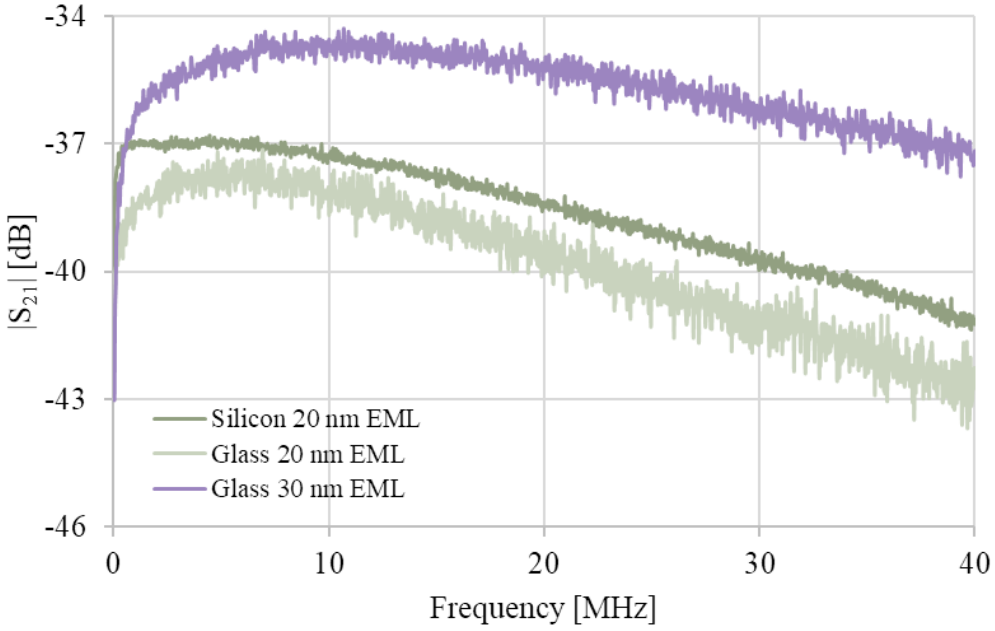

Fig. 5.14: $|S_{21}|$ response for 0.12 mm^2 OLEDs at a DC bias current of 5 mA.

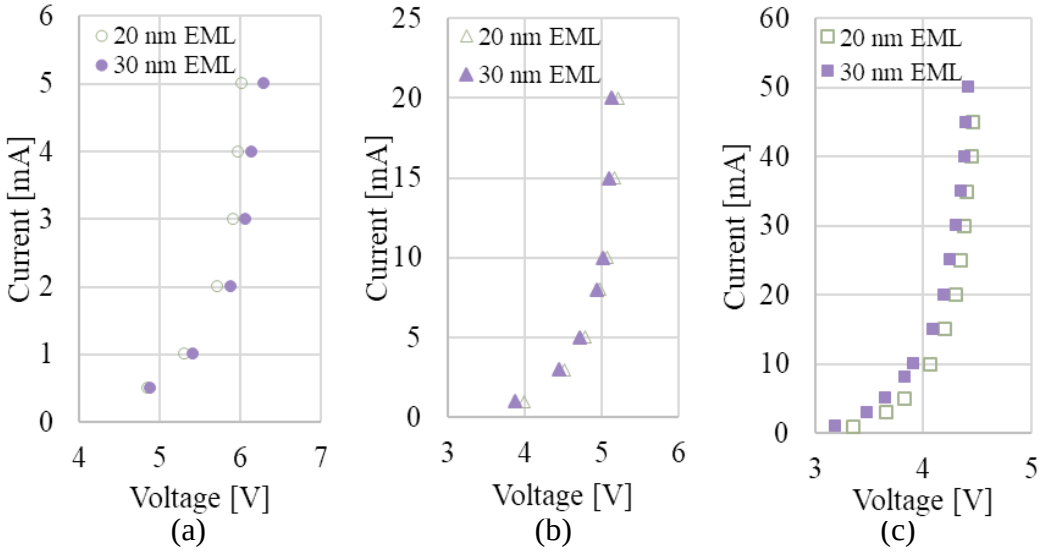

Fig. 5.15: Comparison of current-voltage curves for OLEDs with 20 nm 1.5 wt% doped and 30 nm 2.76 wt% doped EML at (a) 0.12 mm^2, (b) 1.1 mm^2 and (c) 9 mm^2.

Without the BAlq Layer

The devices without the BAlq layer show significant light output, as shown in Fig. 4.38, and S_{21} measurements for these devices relative to the full stack devices is presented in Fig. 5.16 and Fig. 5.17.

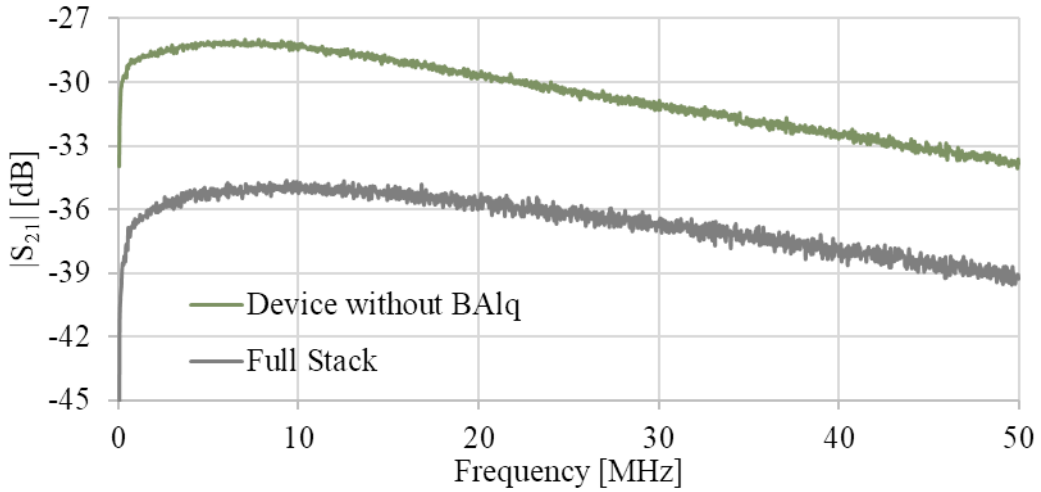

Fig. 5.16: $|S_{21}|$ for 0.12 mm^2 devices at a bias current of 4 mA on glass substrates.

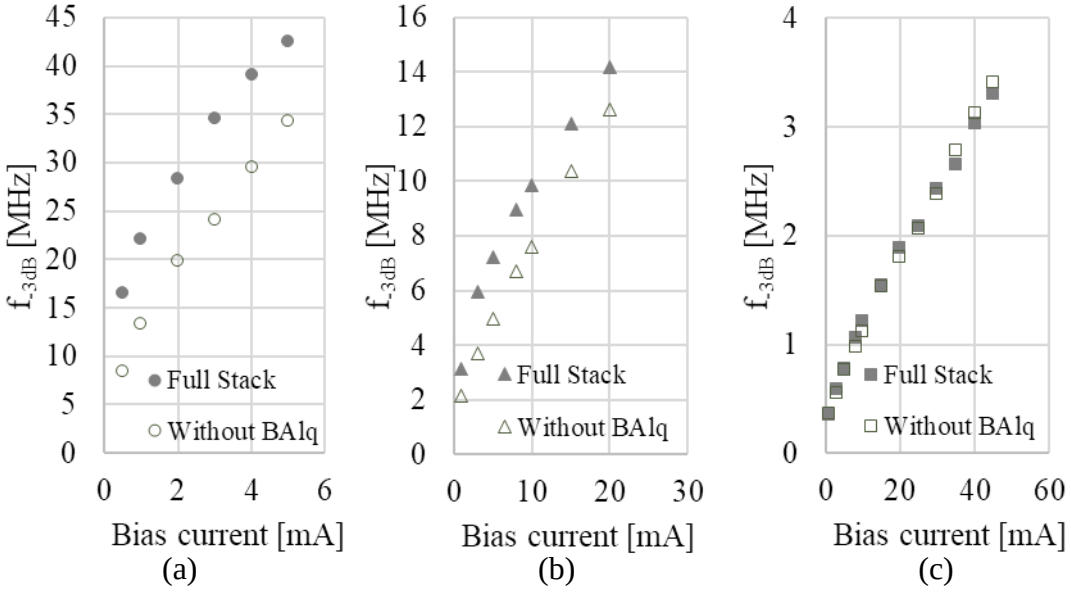

Fig. 5.17: Electrical 3 dB bandwidth measurements for OLEDs without the BAlq layer with areas of (a) 0.12 mm^2, (b) 1.1 mm^2 and (c) 9 mm^2.

It can be seen from Fig. 5.17 that excluding the BAlq layer makes little difference to the bandwidth of the 9 mm^2 OLEDs, but significantly reduces the 3 dB bandwidth for the 1.1 mm^2 and the 0.12 mm^2 devices. As the devices without the BAlq layer have a greater luminous intensity at the same voltage than the full stack devices (Fig. 4.27), the lower bandwidth for the OLEDs without the BAlq layer is potentially due to the higher electric fields within the full stack devices, as the DC bias voltage for the full stack OLEDs is higher at the same current. At a DC bias of 4.88 V (0.5 mA), the 0.12 mm^2 full stack OLEDs achieve a bandwidth of 20 MHz, and at a comparable 4.97 V (2 mA), the 0.12 mm^2 OLEDs without BAlq also achieve 20 MHz. This may be the effect of the field dependence of the OLED mobilities.

Without the EML

It can be seen from Fig. 5.18 that the shape of the response is very different from the full-stack devices, with the peak response occurring at much lower frequencies, and with a faster roll-off than the full-stack devices. This is potentially because light generation in these devices is due to slow charge-transfer excitons, as opposed to the singlet excitons generated in the full-stack devices. This thereby means that these OLEDs are limited by excitonic recombination rates rather than electrical RC limits, as shown in Fig. 5.19. This is discussed further in Chapter 6, where S_{11} measurements indicate that the capacitance of these devices is not significantly altered compared to the full stack devices.

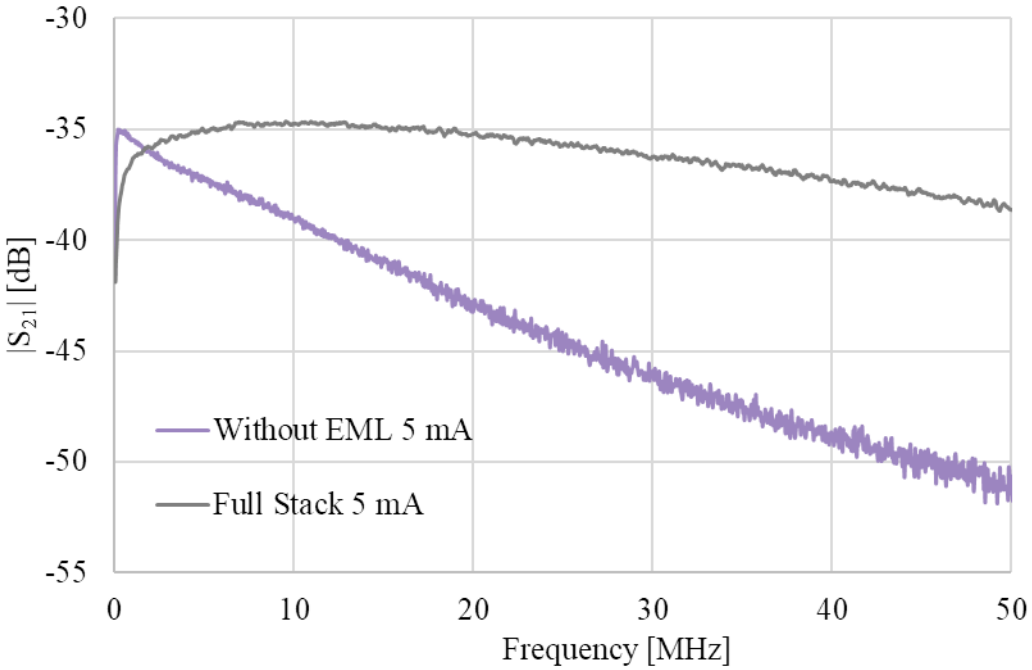

Fig. 5.18: $|S_{21}|$ response for 0.12 mm^2 OLEDs without an EML compared to full stack OLEDs at 5 mA.

It can be seen in Fig. 5.19, below, that the bandwidths for these devices does not significantly change with device dimension, which is further evidence that these devices are not RC limited, but rather limited by relatively slow exciton generation and recombination.

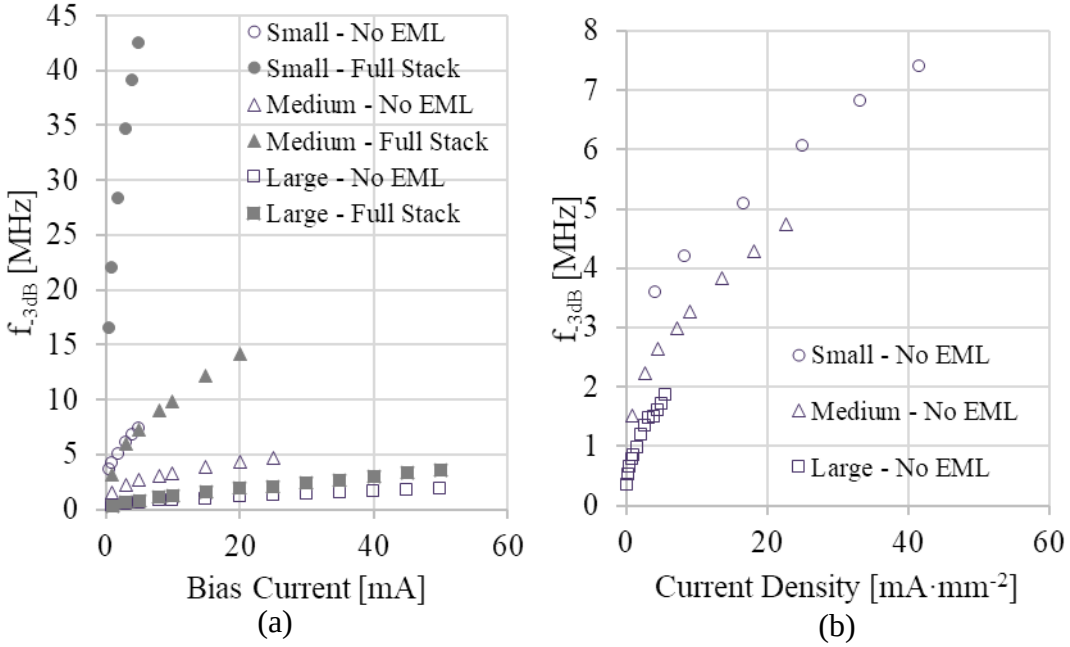

Fig. 5.19: (a) $|S_{21}|$ bandwidth measurements for the devices without an EML, compared to full stack devices (b) Bandwidth measurements of different size devices plotted against their current density.

5.3.5 Large Signal Measurements

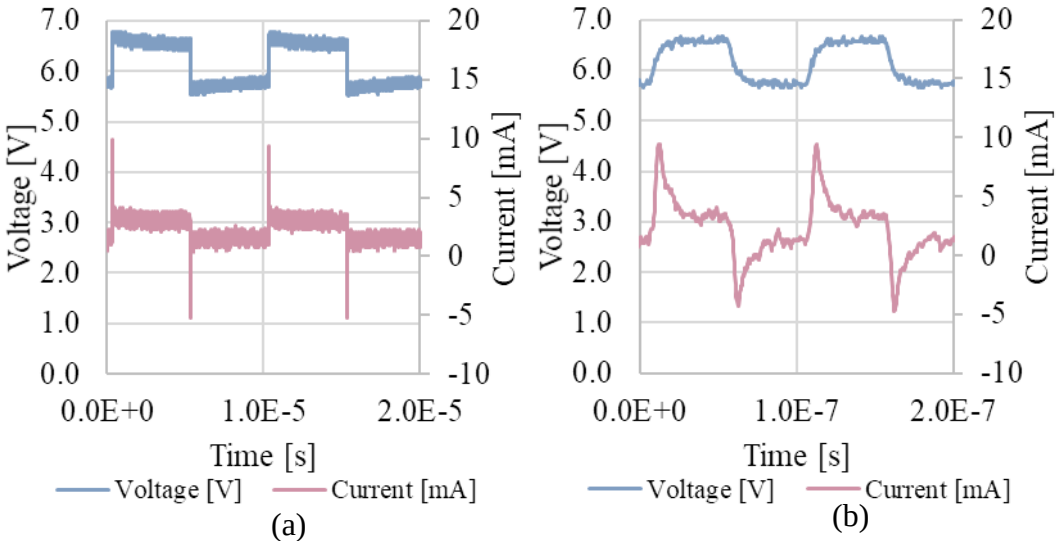

Fig. 5.20: Large signal measurements for the 0.12 mm^2 OLEDs at a DC bias current of 2 mA at (a) 100 kHz and (b) 10 MHz.

The capacitive nature of the OLEDs is observed in the large signal modulation measurements presented in Fig. 5.20. A clear capacitive current spike of the form $I=I_o \exp\left(-\frac{t}{RC}\right)$ can be seen as the OLEDs charge and discharge, and similarly the voltage follows a capacitor charging curve of the form $V=V_0\left(1-\exp\left(-\frac{t}{RC}\right)\right)$. As is seen in Fig. 5.21, this response has an inherent filtering effect upon the response of the OLED and will limit the achievable bandwidths. Large signal measurements for the 1.1 mm^2 and 9 mm^2 OLEDs may be found in Appendix A.

The rise-time for the voltage pulse measured in Fig. 5.20 (b) corresponds to a time constant $\tau = RC$ of approximately 5.0 ± 0.6 ns; this is an approximation due to the quantisation of the oscilloscope measurements. This corresponds to a 3 dB bandwidth of around 32 ± 4 MHz, which corresponds well to the measured small signal bandwidth of 28 MHz at this current. It is also observed that these parameters fit well to the small signal model that is introduced in the following chapter.

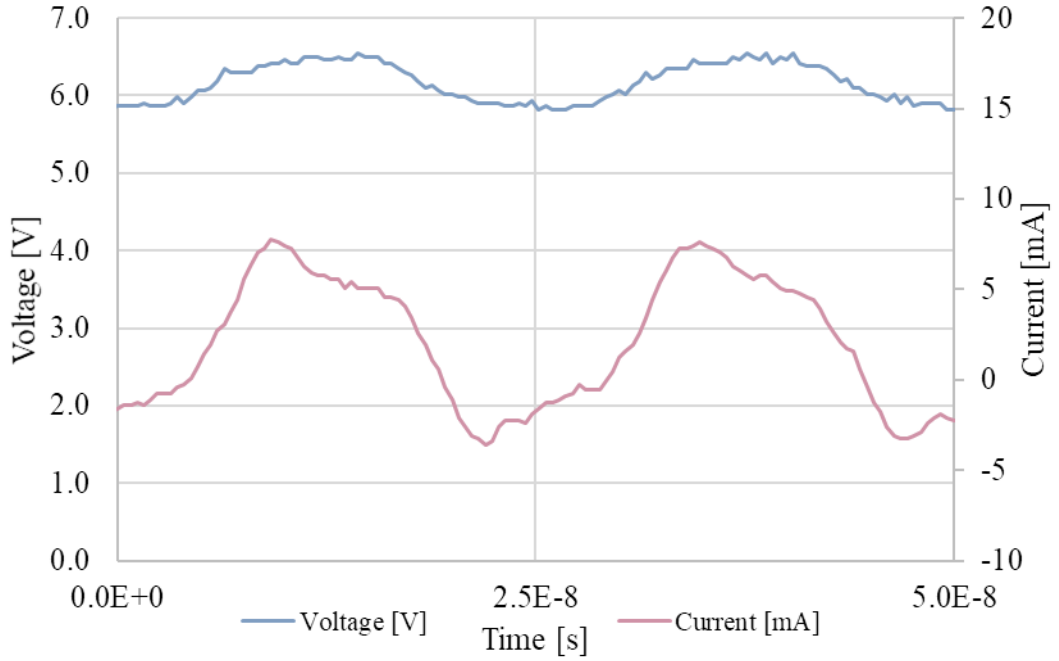

Fig. 5.21: Current and voltage response of the 0.12 mm^2 OLEDs biased to 2 mA with an applied 40 MHz 0.5 V_{pp} square wave.

5.4 Conclusions

Small signal measurements for various OLEDs are presented in this chapter. A strong bandwidth dependence on area is seen amongst all of the OLEDs that include a MADN:TBPe EML, with the 0.12 mm^2 OLEDs incorporating a 30 nm EML demonstrating a 42 MHz electrical bandwidth. This area-dependence indicates that these devices are RC limited (and not limited by exciton recombination), which is confirmed by large-signal measurements of the current and voltage response across the OLED. This is in contrast to the OLEDs fabricated without the EML layer, whose 3 dB bandwidths did not vary as significantly with area, suggesting that these devices are limited by much slower charge transfer exciton recombination times.

It has been shown that thermal effects play a significant role in extending small signal device bandwidths. The thermally-activated nature of organic LEDs means that, in contrast to traditional inorganic materials, heating improves the luminous efficiency and small signal bandwidths of these devices. However, when looking at application of these devices for communications, there is a trade-off between the improved bandwidth and luminous efficiency due to thermal heating and increased thermal noise and breakdown. It is also seen that the achieved bandwidths have a field-dependence, and so by incorporating the devices on an

appropriate substrate or heatsink, it may be possible to avoid the thermal noise and instability and improve the bandwidths by driving the devices at a higher bias than is possible on a thermally insulating substrate and thereby compensate for the reduced bandwidth. This would improve the signal to noise ratio and hence improve the overall link quality.

6 HIGH-SPEED MODELLING & OPTIMISATION

This chapter presents a novel method of modelling the small signal optical response of the OLEDs presented in Chapters 4 and 5, and correlates these parameters to measured impedance parameters calculated through S_{11} measurements. It is found that, as long as the OLED does not appear to be limited by exciton recombination times, this model fits well all OLED device areas and operating bias currents. Furthermore, extension of the physical modelling introduced in Chapter 4 corroborates these measurements and validates the simulation, allowing for extension of the simulation into the realms of device optimisation. As far as is understood, this is the first time this type of corroborated small signal simulation analysis has been presented for organic devices.

6.1 Introduction

Thus far, characterisation of the OLEDs with regards to their DC parameters has been presented and fed into a physics-based simulation model. The application of these OLEDs is in communications links, and so the small-signal optical frequency response has been measured. This, in conjunction with large signal measurements, has suggested an RC-based optical response. However, there has been relatively little progress made to date in the literature to tie the optical frequency response of OLEDs (as measured by the S_{21} response in the previous chapter) to the measured electrical and physical behaviours. This type of characterisation is

fundamentally valuable to optimisation of OLEDs for communications applications, and, for the first time, this chapter attempts to bridge this gap by relating measurements of the optical frequency response to an electrical model corroborated by the impedance response of the OLEDs, and further links this electrical model to the physical simulation of the OLEDs.

The structure of this analysis will be to use the measured complex S_{11} response to define a simple RC model for the S_{21} response. As previously discussed, the device capacitance is observed to limit the full-stack OLED bandwidths, which corroborates the capacitive spikes seen in the large signal measurements in Chapter 5. From this basis, it is found that a proportion of the measured total small signal resistance is used to fit a model to the measured output S_{21}, which is assumed to be an equivalent luminescent fraction of the total device resistance.

Limitations of this small signal analysis are seen in the devices without an EML. The S_{11} parameters show similar behaviour to the full stack devices, but the S_{21} behaviour is shown to be poorly modelled by the RC model due to excitonic effects.

Nevertheless, it is found that extraction of the small signal resistance and capacitance parameters from the simulation introduced in Chapter 4 affords a similar analysis of the S_{21} response, with the advantage of being able to calculate equivalent circuit parameters without experimental noise. A good fit is found for the S_{21} modelling of the OLEDs on silicon substrates across all bias currents.

This leads to trend-forecasting for the purposes of device optimisation for small signal response, with the assumption that validation will need to be undertaken on thermally appropriate substrates. This model can be built upon in the future for improved simulations as our knowledge of the library of organic materials and understanding of the relevant models improves.

6.2 Electrical Modelling

6.2.1 S_{11} Parameter Extraction

Simultaneous measurements of the complex S_{11} parameters were taken with the S_{21} measurements presented in Chapter 5. Taking the S_{11} to be equal to the reflection coefficient of the transmission line, these S_{11} parameters may be converted into Z_{11} parameters using Eq. (6.1).

$$Z_{11} = Z_0 \frac{1 + S_{11}}{1 - S_{11}} \tag{6.1}$$

With a characteristic impedance $Z_0 = 50\ \Omega$, Eq. (6.1) returns complex impedance parameters for the OLED.

Assuming a small signal model of the form in Fig. 6.1, it follows that Z_{11} can be equated to the parameters of the model, R_s, R_p and C_p, where R_s is equivalent to the contact resistance of the device, R_p is the current path through the OLED and C_p is the intrinsic device capacitance. Similar impedance spectroscopic techniques have been used in the literature to analyse OLEDs in terms of their electrical response [155], [238]–[241].

$$Z_{11} = R_s + \frac{R_p}{1 + j\omega C_p R_p} \tag{6.2}$$

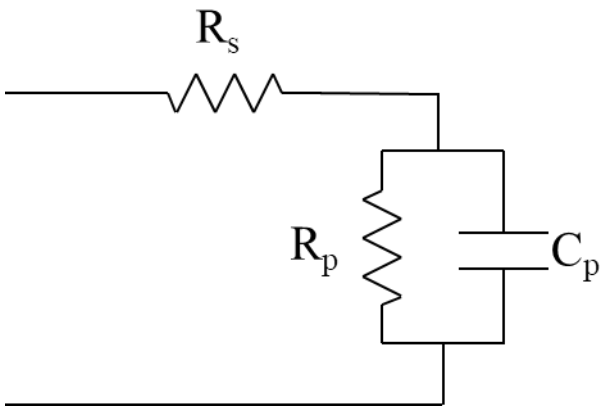

Fig. 6.1: Small signal equivalent circuit model for the OLED.

Equivalently, Z_{11} may be expressed by the equation

$$Z_{11} = R_s + \frac{R_p\left(1 - j\omega C_p R_p\right)}{1 + \omega^2 C_p^2 R_p^2} \tag{6.3}$$

$$Re(Z_{11}) = R_s + \frac{R_p}{1 + \omega^2 C_p^2 R_p^2} \tag{6.4}$$

$$Im(Z_{11}) = -\frac{\omega C_p R_p^2}{1 + \omega^2 C_p^2 R_p^2} \tag{6.5}$$

The separating of Z_{11} into real and imaginary parts provides two equations for three unknowns. However, noting that as $\omega \to \infty$, $Re(Z_{11}) \to R_s$, an approximation to R_s may be found from

the value of $Re(Z_{11})$ at high frequencies, and this value may be subtracted from $Re(Z_{11})$ to form $Re'(Z_{11})$, as per Eq. (6.6).

$$Re'(Z_{11}) = Re(Z_{11}) - R_s = \frac{R_p}{1 + \omega^2 C_p^2 R_p^2} \tag{6.6}$$

Thus, an analytic solution for R_p and C_p may be found from Eqs. (6.5-6.7).

$$\frac{-Im(Z_{11})}{Re'(Z_{11})} = \omega C_p R_p \tag{6.7}$$

The results of this analysis of R_p and C_p for the 0.12 mm^2 OLEDs on silicon substrates are shown in Fig. 6.2, with a value for R_s of 17 Ω. Interestingly, the values for C_p collapse to a single value at all bias currents, indicating a single value of small signal capacitance for the device. At low frequency, the capacitance is seen to be significantly higher than at high frequency, which may be due to charge-trapping effects [242]. At high enough frequency, these traps cannot react in time to the changing field and so we see only the constant capacitance, whereas at low frequency they influence the S_{11} measurements. The value for the small signal R_p is seen to vary with both bias current and frequency. As bias current increases, R_p decreases – this is consistent with the instantaneous value for $\frac{dV}{dI}$ decreasing as the current is increased on the current-voltage curve. R_p is also seen to significantly decrease with frequency, although the extent of the change reduces as bias current increases, suggesting that this effect may also be due to charge trapping increasing the equivalent resistance of the OLED. As the bias current increases, traps are filled and their effect upon the OLED is reduced.

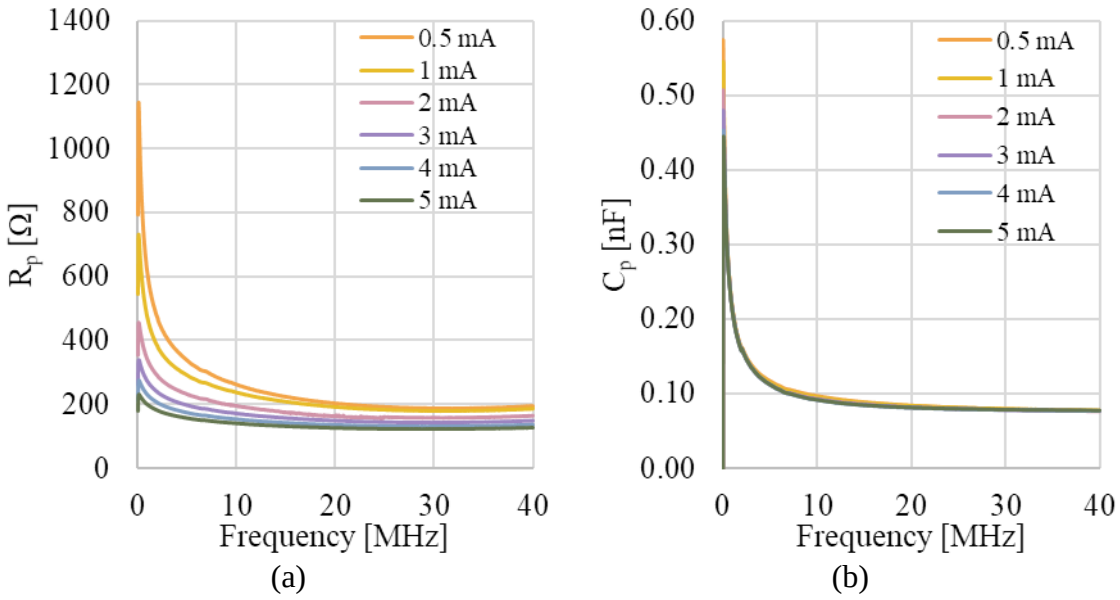

Fig. 6.2: (a) R_p and (b) C_p as a function of frequency and bias current for 0.12 mm^2 OLEDs on silicon substrates.

Splitting R_p into a constant term R_1 and a frequency-varying trapping term R_ω, i.e. $R_p(\omega) = R_1 + R_\omega(\omega)$, it is possible to produce a small signal model of the OLED. This splitting is illustrated schematically below in Fig. 6.3.

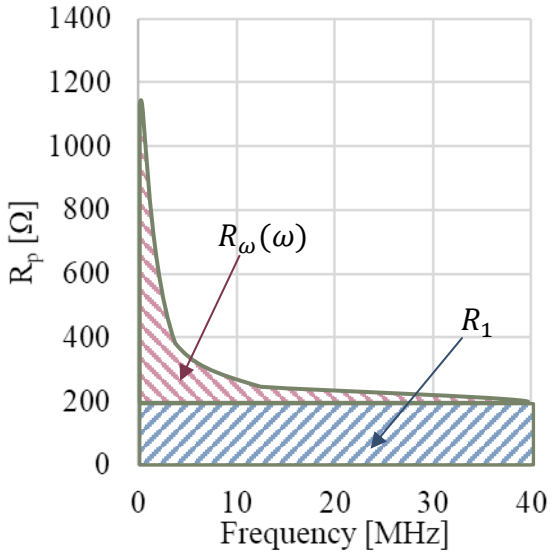

Fig. 6.3: Schematic illustration of proposed R_p split between a constant term and a frequency varying term.

Assuming that the photodiode and POF do not limit the response of the OLED (as their bandwidth response is > 650 MHz), and that the current through the R_1 component is proportional to the light response, the S_{21} response may be modelled as Eq. (6.8).

$$S_{21} = H(\omega) \propto \frac{I_1}{I_t} = \frac{1}{1 + j\omega C_1 R_1} \tag{6.8}$$

However, using the high-frequency values of R_1 significantly underestimates the 3 dB bandwidth of the OLED. Through knowledge of C_1 and of the 3 dB bandwidth of the OLED, it is possible to use $f_{-3dB} = \frac{1}{2\pi R_o C_1}$ to work out R_o, the equivalent luminescent portion of the total resistance R_1.

The physical meaning to R_0 is proposed as an equivalent resistance to the luminescent portion of the Langevin recombination. Starting with Eq. (3.26), where R_L is the Langevin recombination rate, q is the electronic charge, L is the thickness of the luminescent layer of the device, and J_{rec} is the recombination current:

$$J_{rec} = qR_L L \tag{3.26}$$

Neglecting the effect of diffusion, and considering only the drift-current, by Ohm's law this can be equated to:

$$J_{rec} = \sigma E \tag{6.9}$$

where σ is a radiative conductance parameter and E is the electric field.

Effectively,

$$\sigma = \frac{qR_L L}{E} \tag{6.10}$$

Expressing the conductance as a resistance through a layer with area A:

$$R_{rec} = \frac{L}{\sigma A} = \frac{E}{AqR_L} = \frac{E\varepsilon_r\varepsilon_0}{Aq^2\left[\mu_n(E) + \mu_p(E)\right](np - n_i^2)} \tag{6.11}$$

Of course, not all of the excitons that are generated by Langevin recombination will recombine radiatively, but this provides a physical basis and context for R_0 as an equivalent luminescent resistance related to the Langevin recombination rate.

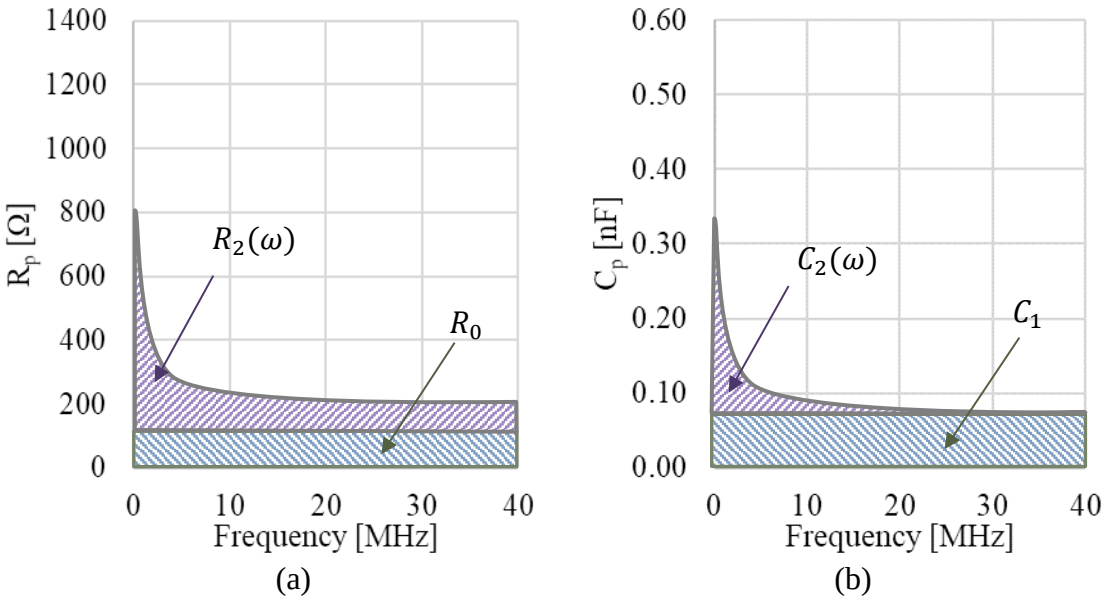

Fig. 6.4: Schematic illustration of proposed R_p split between a constant term R_0 and a frequency varying term $R_2(\omega)$ and C_p split between a constant term C_1 and a frequency varying term $C_2(\omega)$.

This suggests an alternate equivalent circuit, in Fig. 6.5, which is consistent with both the fitting of the results from the S_{21} and the R_p and C_p parameters from the S_{11} measurements. The effect of splitting out of R_p and C_p into the terms $R_o, C_1, C_2\ (\omega)$ and $R_2(\omega)$ is to separate out the luminescent and non-luminescent portions of the measured parameters.

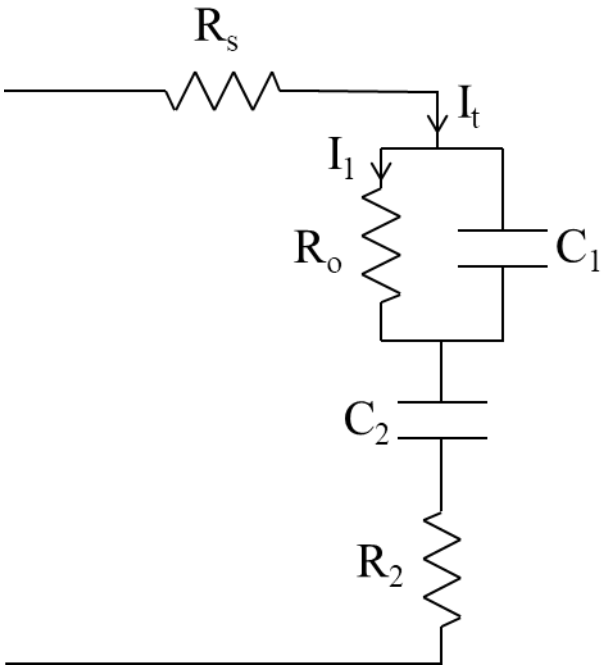

Fig. 6.5: Equivalent small signal model for the OLED based upon S_{11} measurements.

At high frequencies, the capacitance due to traps, C_2, becomes short circuited, and only the device capacitance due to accumulation of charges, C_1, remains, which is consistent with the results in Fig. 6.2(b), indicating that C_p represents the combination of C_1 and C_2. R_2 represents both the frequency-invariant portion and a frequency-varying portion of the non-luminescent small signal resistance of the OLED such that $R_p = R_o + R_2(\omega)$, i.e. R_2 represents the sum of a resistance due to traps (the frequency-variant portion), and a resistance due to the transport properties of the non-luminescent organic layers. R_o represents the resistance associated with Langevin recombination in the emissive layer. R_o and R_2 both vary with bias. This is consistent with the change in instantaneous $\frac{dV}{dI}$ of the OLED as bias increases, consistent with the results in Fig. 6.2(a) and consistent with Eq. (6.11). The R_s, C_2 and R_2 terms do not result in light output, so the S_{21} response of the OLED is consistently reproduced by Eq. (6.8). The high-pass response of the bias-tee may be included into the system by including the response given in Eq. (6.12), with $R_f C_f$ chosen to provide a 100 kHz cut-off, corresponding to the high-pass response of bias-tee. The combined response of the OLED [Eq. (6.8)] with the low-pass filter [Eq. (6.12)] may be found in Fig. 6.6.

$$G(\omega) = \frac{j\omega R_f C_f}{1 + j\omega R_f C_f} \tag{6.12}$$

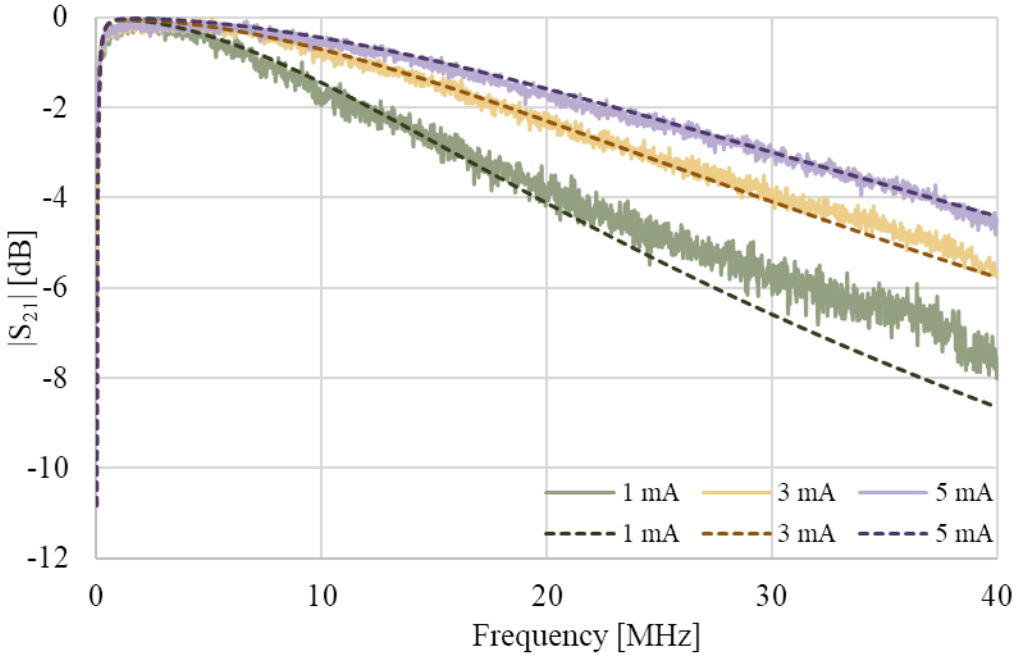

Fig. 6.6: Fitting between the small signal model (dashed lines) and S_{21} measurements (solid lines) for the 0.12 mm^2 OLED at different bias currents.

It can be seen from Fig. 6.6 that at high currents, the model shows good fitting to the measurements across all frequencies; the values of the parameters used for this fitting may be found in Table 6-1. For low bias currents, the fit is very good at low frequencies, but deviates at higher frequencies. The shape of the deviation suggests that the value for R_o reduces at higher frequencies, perhaps suggesting R_o takes the alternate form given in Fig. 6.7. However, as the effective value R_o provides a sufficient small signal response, the exact equivalent parameters for R_{o1}, R_{o2} and C_{o2} have not been calculated.

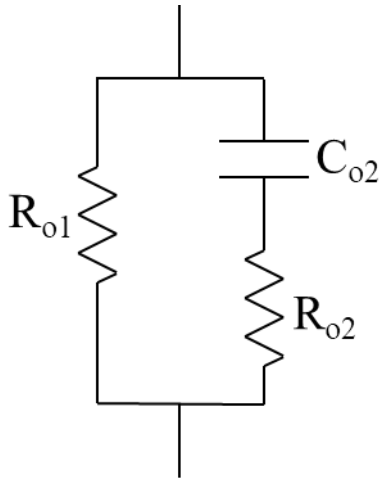

Fig. 6.7: Small signal equivalent circuit model for R_o to account for high-frequency behaviour at low bias currents.

Fig. 6.8 shows the variation of R_p and $C_p$with bias and frequency for the 1.1 mm^2 OLEDs. For these calculations, R_s is set to 6 Ω. It is observed that these parameters show the same shape response as the 0.12 mm^2 OLEDs, with similar trapping characteristics. Notably, a variation in C_p at 1 mA is measured relative to the other bias currents, which may help explain the relatively poor fitting of the S_{21} in Fig. 6.10(a) compared to the other devices and other bias currents.

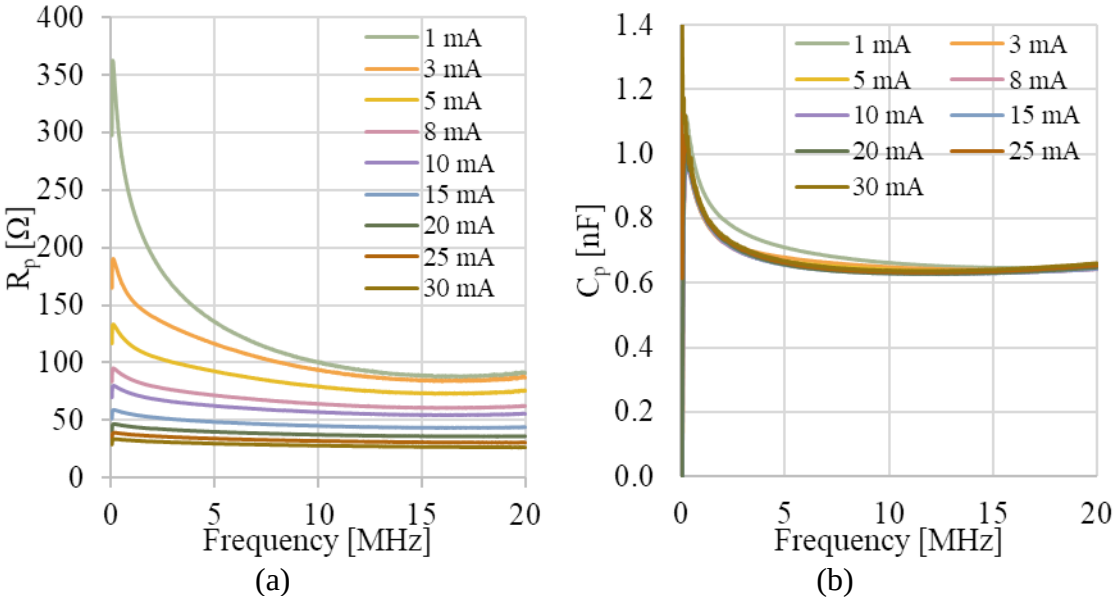

Fig. 6.8: Variation in (a) R_p and (b) C_p with frequency and bias current for the 1.1 mm^2 OLEDs on silicon.

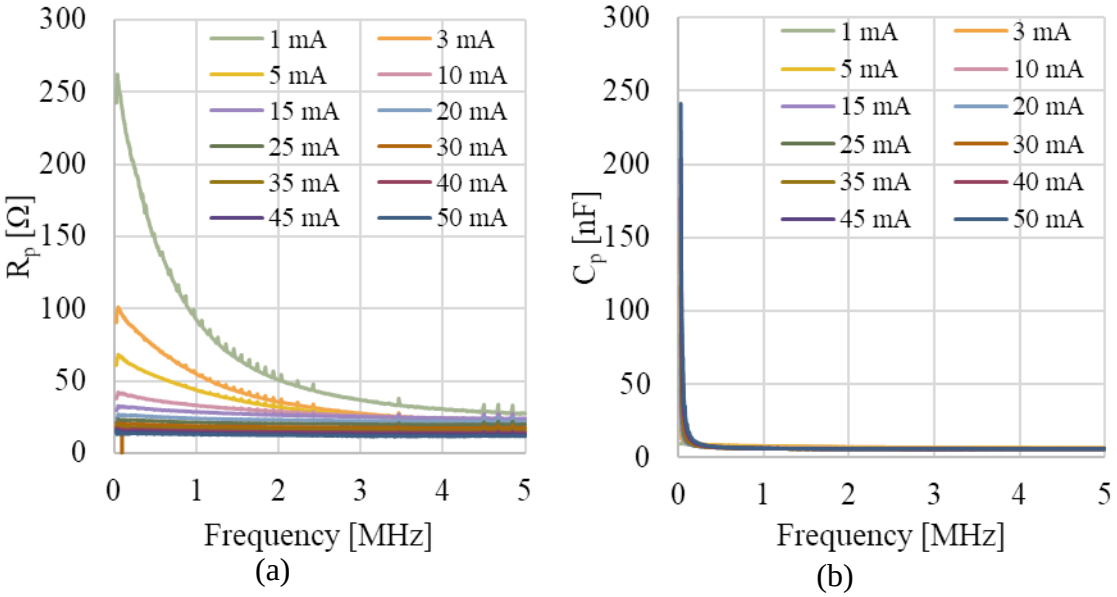

Fig. 6.9: Variation in (a) R_p and (b) C_p with frequency and bias current for the 9 mm^2 OLEDs on silicon.

Similar calculations are undertaken for the 9 mm^2 OLEDs and are presented in Fig. 6.9, and show similar shape response to the smaller area devices. A value of 3.1 Ω is used for R_s to calculate R_p and C_p.

The high frequency measurements for C_p may be used to model the S_{21} response of the OLEDs. These results are presented in Fig. 6.10 for the 1.1 mm^2 and 9 mm^2 OLEDs, with the fitting values for R_0 and C_1 found in Table 6-1.

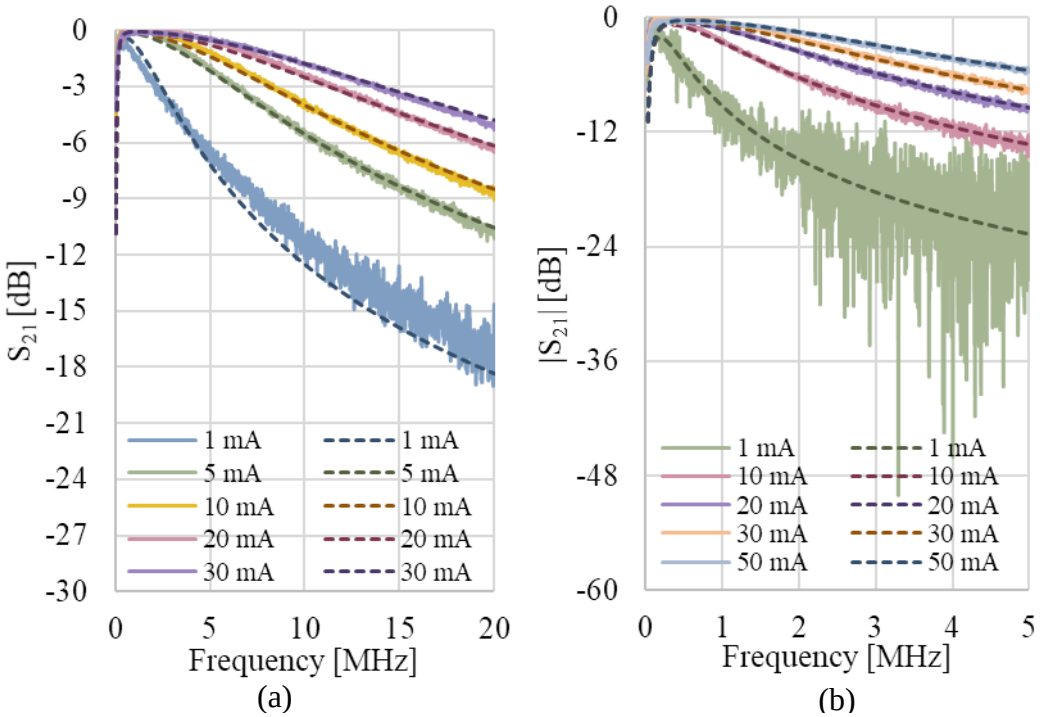

Fig. 6.10: $|S_{21}|$ measurements (solid lines) and model (dashed lines) for (a) the 1.1 mm^2 and (b) the 9 mm^2 OLEDs on silicon substrates at different bias currents.

The fitting between the model and the measurements is good at all biases and frequencies, with the exception of the measurements for the 1.1 mm^2 at 1 mA, and at high frequencies, where the response is slightly under-estimated, in a similar fashion to the 0.12 mm^2 OLED at 1 mA.

Table 6-1: Small signal parameters used to model the OLED $|S_{21}|$ response.

	0.12 mm² OLED											
I_{DC} [mA]	0.5		1		2		3		4		5	
R_o [Ω]	201		131		102		87		77		70	
C_1 [pF]	76.7		76.4		76.0		75.8		75.7		75.7	
	1.1 mm² OLED											
I_{DC} [mA]	1	3	5	8	10	15	20	25	30			
R_o [Ω]	100	49	40	33	30	25	22	19	17			
C_1 [nF]	0.65	0.65	0.64	0.64	0.64	0.64	0.65	0.65	0.66			
	9 mm² OLED											
I_{DC} [mA]	1	3	5	10	15	20	25	30	35	40	45	50
R_o [Ω]	68	43	34	23	18	15	13	12	11	9.9	9.1	8.7
C_1 [nF]	6.3	6.5	6.5	6.2	6.0	5.9	5.9	5.9	5.8	5.9	5.9	5.9

For each of the devices on silicon, the value of C_1 extracted from the measurements appears to scale very nicely. Equating C_1 to a geometric capacitance $\frac{\varepsilon A}{d}$, and assuming a very approximate constant overall relative permittivity of 3, as is standard for organic devices, it is possible to calculate an estimated value for d as per Eq. (6.13).

$$d = \frac{\varepsilon A}{C_1} \tag{6.13}$$

Table 6-2: Capacitance calculations for the devices on silicon.

		0.12 mm²	**1.1 mm²**	**9 mm²**
Silicon	C_1 [nF]	0.076	0.65	5.9
	$\frac{C_1}{A}$ [nF mm^{-2}]	0.63	0.59	0.66
	$d = \frac{\varepsilon A}{C_1}$ [nm]	42	45	40

The calculations presented in Table 6-2 suggest an equivalent parallel plate capacitor with plate separation of 40 nm in these devices[4]. As this device has a 20 nm EML and 10 nm EBL and HBL layers, this suggests that there may be charge accumulation at the Spiro-TTB/α-NPD and BPhen/BAlq interfaces creating this capacitance.

6.2.2 Comparison of Devices with a 20 nm EML

Similar calculations for the 20 nm EML devices on glass show unexpected results. Plots of C_p and R_p against frequency for the 0.12 mm^2 are shown in Fig. 6.11. Surprisingly, the capacitance of the room temperature devices on glass is much higher than the equivalent capacitance measurement for devices on silicon. When these devices on glass are cooled, the capacitance is less than that of the devices on silicon.

[4] Of course, the total capacitance for capacitors in series are limited by the smallest capacitance, so this does not preclude a higher capacitance existing in the OLED stack. There's also the potential effect of charge accumulation at multiple interfaces, so this calculation is not necessarily so straightforward, especially for semiconductors, where $C = Im\left(\frac{Y(\omega)}{\omega}\right)$, where $Y(\omega)$ is the admittance. However, these results are corroborated by simulation in §6.3. Moreover, for fitting to the S_{21}, this would imply a higher R than is calculated to exist in the device from the S_{11} measurements.

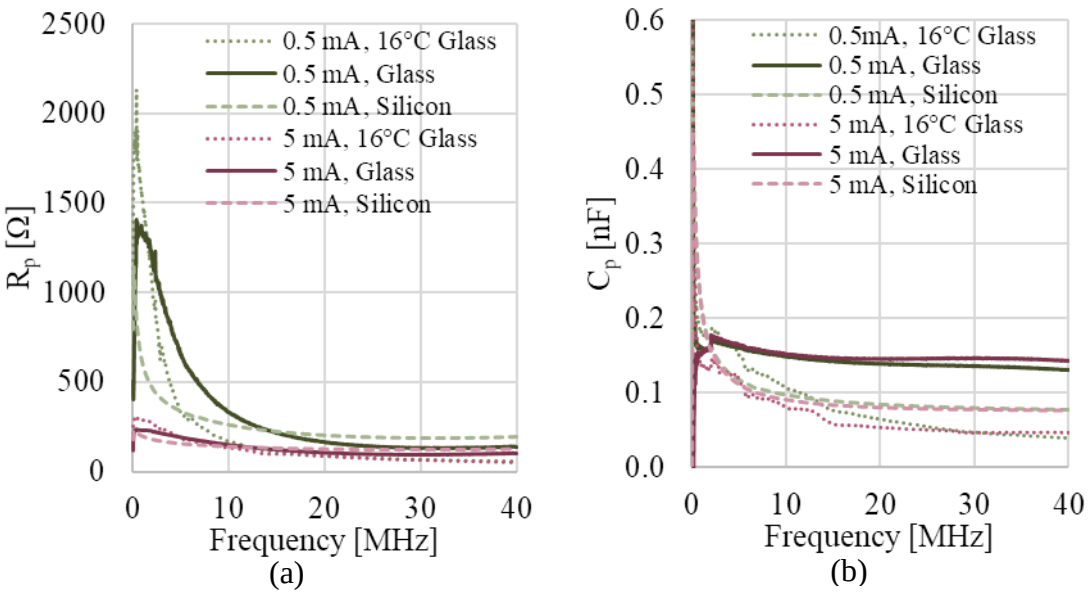

Fig. 6.11: Variation of (a) R_p and (b) C_p with frequency and bias current for the 0.12 mm^2 OLEDs on silicon compared to glass and on a heat sink set to 16°C.

The equivalent S_{21} model for these OLEDs suggests that the bandwidth of the devices on silicon is higher relative to the devices on glass due to the higher capacitance of the glass devices. Table 6-3 provides the equivalent R_o and C_1 parameters of these measurements, and Fig. 6.12 shows the fitting of these parameters to the measured $|S_{21}|$ values. The capacitance of 156 nF corresponds to a $d = \frac{\varepsilon A}{C}$ of just 20 nm, which would correspond to the thickness of the EML. It may be that the higher temperatures in the device on glass mean that carriers can thermionically hop the energy barriers and accumulate at the edge of the EML, which increases the device capacitance accordingly. Furthermore, the reduction of the small signal R_o on glass relative to the devices on silicon would also be consistent with a thermally enhanced mobility. However, despite the higher mobility of the devices on glass, the overall small signal bandwidth of these devices is reduced due to the high device capacitance.

Table 6-3: R_o and C_1 parameters for the 0.12 mm² OLEDs with a 20 nm EML.

0.12 mm² OLED							
I_{DC} [mA]		0.5	1	2	3	4	5
Silicon 20nm EML	R_o [Ω]	201	131	102	87	77	70
	C_1 [pF]	76.7	76.4	76.0	75.8	75.7	75.7
Glass 20 nm EML	R_o [Ω]	100	81	67	60	51	47
	C_1 [pF]	158	159	163	159	160	157
Glass 16°C 20 nm EML	R_o [Ω]	543	332	270	298	307	257
	C_1 [pF]	41.7	60.2	59.9	53.7	49.0	48.4

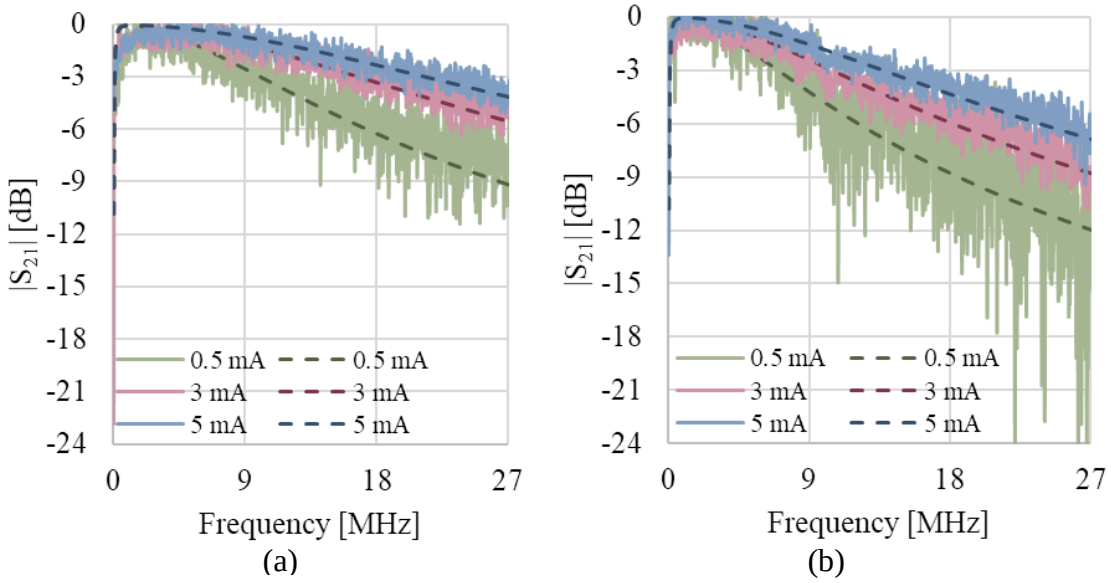

Fig. 6.12: $|S_{21}|$ measurements (solid lines) and $|S_{21}|$ modelling fit (dashed lines) for the 0.12 mm² OLEDs on (a) glass substrates and (b) glass substrates cooled to 16°C.

In contrast to the relatively consistent values found for C_1 for the room temperature measurements, it is seen from Table 6-3 that the device small signal capacitance shows much

higher variance when the devices on glass are cooled to 16°C. It is observed that the S_{11} and S_{21} measurements for the cooled devices are much noisier than the uncooled devices. It is possible that the balance between heat extraction from the heat sink and generation from the device self-heating is causing this erratic behaviour in the system. Under the assumption that these capacitance measurements accurately reflect the device behaviour under cooling, these capacitance values correspond to values of $d = \frac{\varepsilon A}{C}$ between 53-66 nm. A potential reason for these larger values of d may be that there is additional charge accumulation in between different layers, as the carriers cannot thermally hop between layers as easily, creating a more complex net capacitance at cooler temperatures. It may also be that carriers cannot be thermally injected from one of the contacts as easily and the assumption of two quasi-ohmic contacts no longer holds. If, for example, the anode (as it is closer to the heat sink) is injecting fewer holes, and the current is not charge balanced, there would be a greater proportion of electrons than holes and there would be less luminescent power output (similar to the devices without Spiro-TTB). With a lesser proportion of the current going to luminescent recombination, this would present as a higher value of R_o (in addition to the lower mobility) and lower luminescent power output even at high bias currents. This is consistent with observations, where there was a reduction in $|S_{21}|$ power between uncooled and cooled devices at the same current bias.

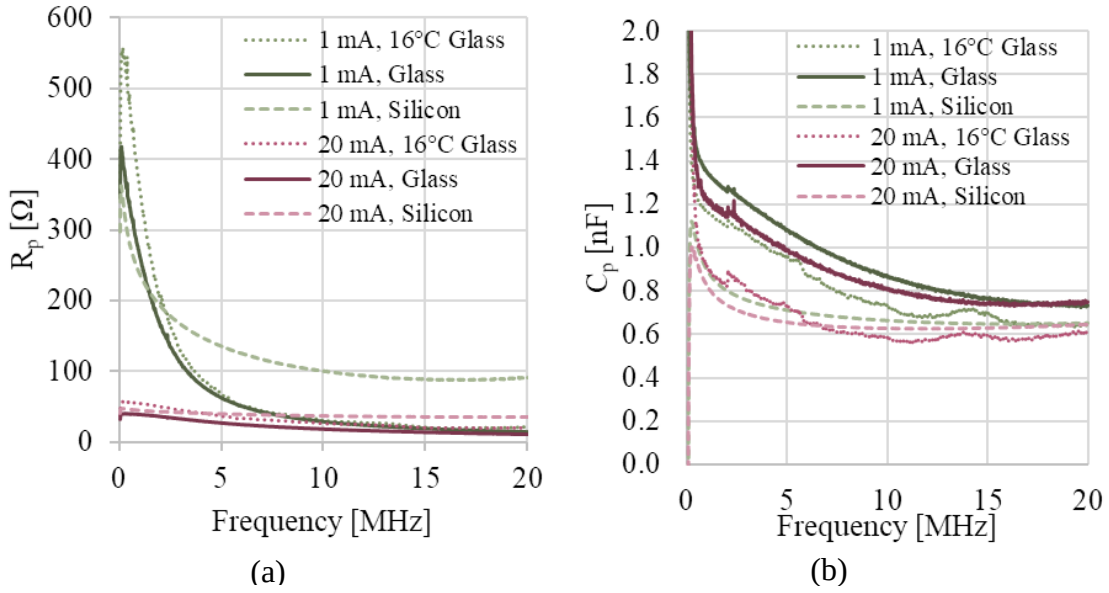

Fig. 6.13: Variation of (a) R_p and (b) C_p with frequency and bias current for the 1.1 mm^2 OLEDs on silicon compared to glass and on glass with heat sink set to 16°C.

Fig. 6.13 shows the R_p and C_p measurements for the 1.1 mm^2 OLEDs. Very little difference is seen between the R_p measurements at 16°C and uncooled, although there is a slight reduction in C_p between the uncooled and 16°C devices. Relative to the devices on silicon, the uncooled devices on glass show a higher C_p and a lower R_p. This may be related to higher thermally-generated mobilities in the devices on glass.

Table 6-4: R_o and C_1 parameters for the 1.1 mm^2 OLEDs with a 20 nm EML.

1.1 mm^2 OLED									
I_{DC} [mA]		1	3	5	8	10	15	20	25
Silicon 20nm EML	R_o [Ω]	100	49	40	33	30	25	22	19
	C_1 [nF]	0.65	0.65	0.64	0.64	0.64	0.64	0.65	0.65
Glass 20 nm EML	R_o [Ω]	116	66	52	44	40	32	28	
	C_1 [nF]	0.73	0.74	0.74	0.75	0.75	0.75	0.75	
Glass 16°C 20 nm EML	R_o [Ω]	171	122	120	109	178	45	52	
	C_1 [nF]	0.65	0.62	0.61	0.53	0.29	0.83	0.62	

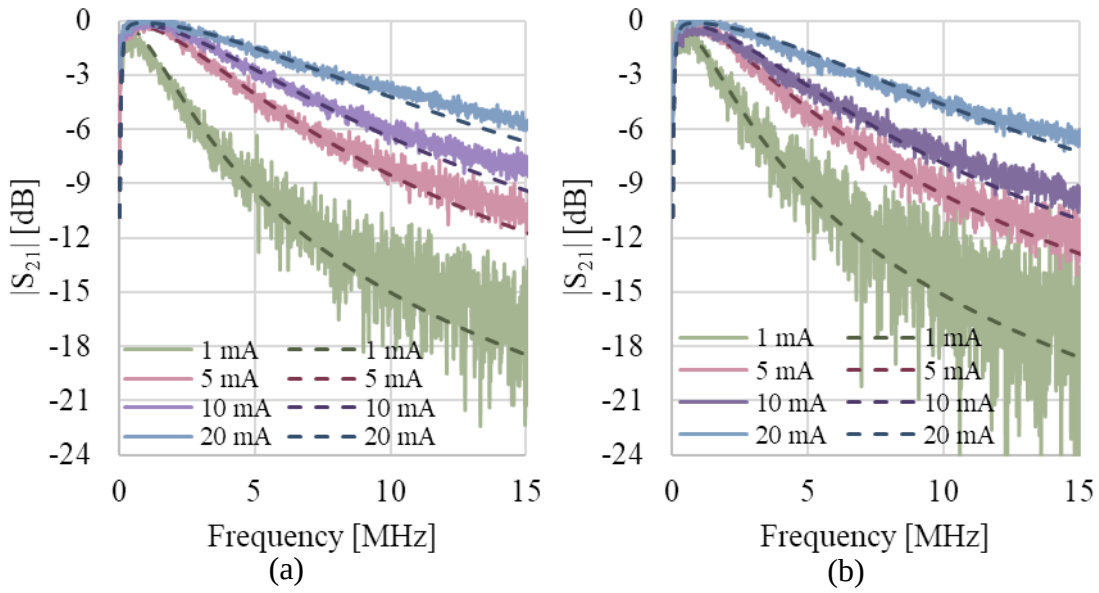

Fig. 6.14: $|S_{21}|$ measurements (solid lines) and $|S_{21}|$ modelling fit (dashed lines) for the 1.1 mm^2 OLEDs on (a) glass substrates and (b) glass substrates cooled to 16°C.

We can see from Table 6-4 that the C_1 fitting parameters for the OLEDs cooled to 16°C have a much higher variance than those uncooled. The cooled devices also show a higher small signal R_o, related to the lower mobility of the cooled devices. Contrary to expectation, R_o for the OLEDs on silicon is lower than on glass. An explanation for this is that R_o represents only the fraction of the measured value R_p that contributes to light emission. Since R_p is higher on silicon than on glass, this perhaps suggests that the proportion of R_p that contributes to light emission is higher in the devices on glass than the devices on silicon. This would infer that the devices on glass have better luminescent efficiency than the devices on silicon, which would be consistent with the improved carrier transport and Langevin recombination in the hotter devices. It is also noted again that the relatively poorer bandwidth performance of the OLEDs on glass compared to silicon is likely due to their higher small signal capacitance values.

Fig. 6.15, below, presents the R_p and C_p measurements of the devices with an area of 9 mm^2. It can be seen that R_p does not significantly change between devices on glass and on silicon, and cooling only has a significant effect upon the value of R_p at low biases. C_p is also consistent at different bias currents for the uncooled devices on glass and on silicon. However, once again the cooled devices show a greater variation in C_p (and C_1) than the uncooled devices. It is also of note that the capacitance for the cooled devices is lower than for the uncooled devices, despite the large variance in measurement values, perhaps because fewer charges can hop the energetic

barriers between layers at lower temperatures and therefore have a greater separation distance d.

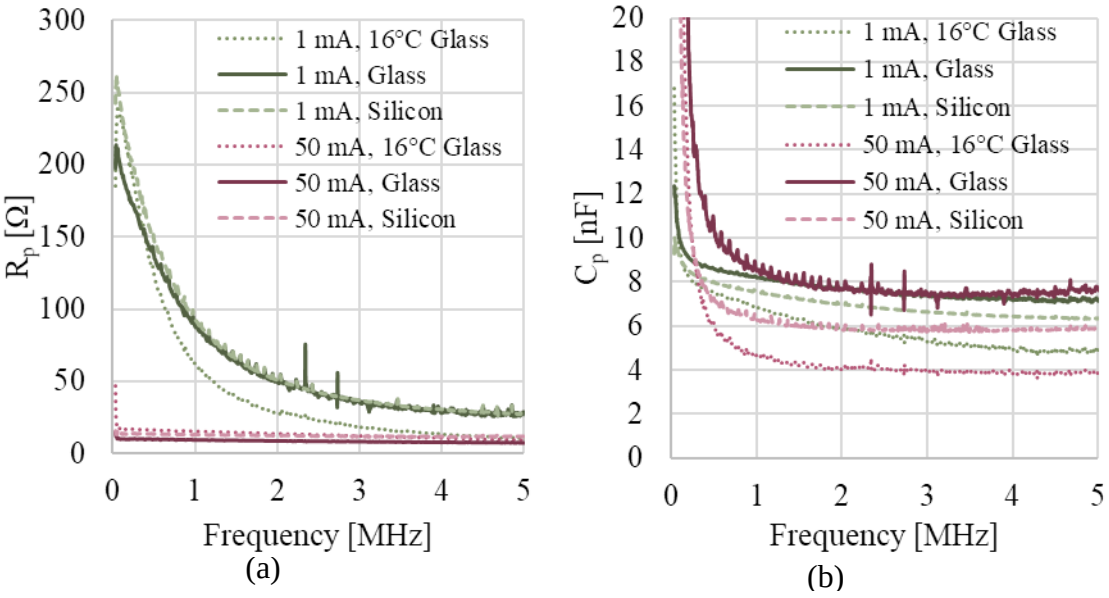

Fig. 6.15 Variation of (a) R_p and (b) C_p with frequency and bias current for the 9 mm^2 OLEDs on silicon compared to glass and on a heat sink set to 16°C.

Table 6-5: R_o and C_1 parameters for the 9 mm² OLEDs with a 20 nm EML.

9 mm² OLED												
I_{DC} [mA]		1	5	10	15	20	25	30	35	40	45	50
Silicon 20nm EML	R_o [Ω]	68	34	23	18	15	13	12	11	9.9	9.1	8.7
	C_1 [nF]	6.3	6.5	6.2	6.0	5.9	5.9	5.9	5.8	5.9	5.9	5.9
Glass 20 nm EML	R_o [Ω]	70	30	20	15	13	11	10	8.7	7.6	7.4	6.2
	C_1 [nF]	7.1	7.1	7.0	7.0	7.0	7.2	7.2	7.4	7.6	7.7	7.9
Glass 16°C 20 nm EML	R_o [Ω]	130	50	37	30	32	24	22	21	18	14	15
	C_1 [nF]	4.6	4.6	4.9	4.1	3.5	3.8	3.5	3.5	3.9	4.2	3.8

Extraction of the small signal circuit fitting model parameters presented in Table 6-5 show that there is relatively small difference between the R_o values for the devices on silicon or on glass. However, under cooling, the values for R_o increase significantly, again likely due to a reduction in thermally assisted mobility. The fitting of this model to the $|S_{21}|$ measurements is found in Fig. 6.16. The large measurement noise for the devices biased to 1 mA is due to the low output signal power at such low bias potentials; the signal to noise ratio is poorer.

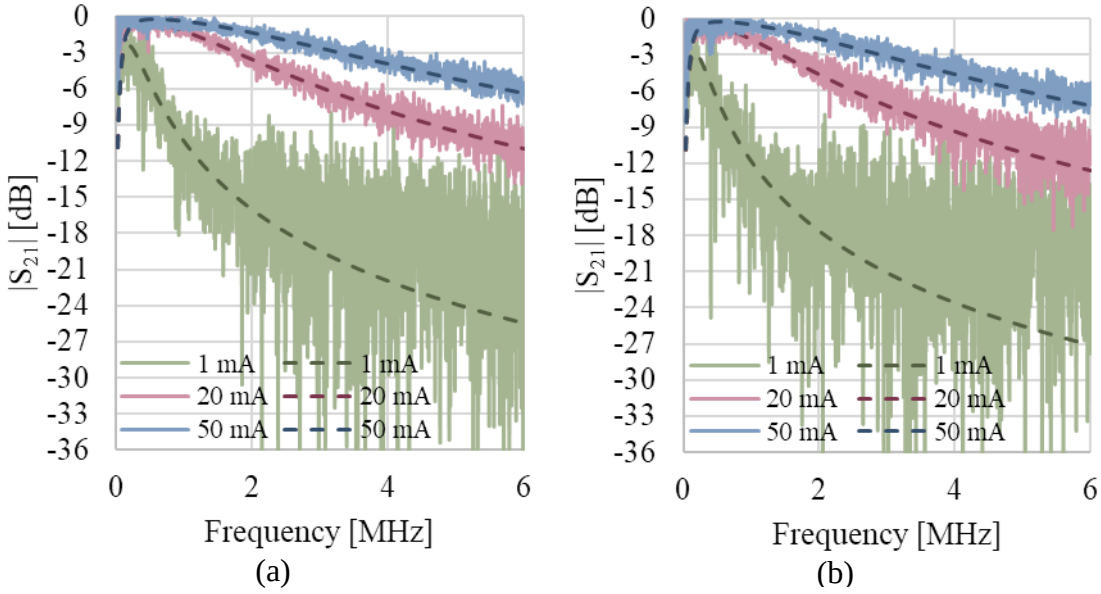

Fig. 6.16: $|S_{21}|$ measurements (solid lines) and $|S_{21}|$ modelling fit (dashed lines) for the 9 mm^2 OLEDs on (a) glass substrates and (b) glass substrates cooled to 16°C.

It may be noted that for all devices of all areas with a 20 nm EML, that the values for C_1 are highest in the devices on glass, followed by the devices on silicon, and finally the cooled devices on glass.

6.2.3 Comparison of Devices with Varying Thickness

The same modelling techniques have been used to extract the R_p and C_p values for the OLEDs with 30 nm EMLs. The following subsection presents the results of this analysis, and compares the full stack devices with a 30 nm EML to the devices manufactured without a BAlq layer and manufactured without an EML. The results for the devices with a 20 nm EML on glass are included for completeness and are presented in Fig. 6.17. All of these devices are on the same glass substrates.

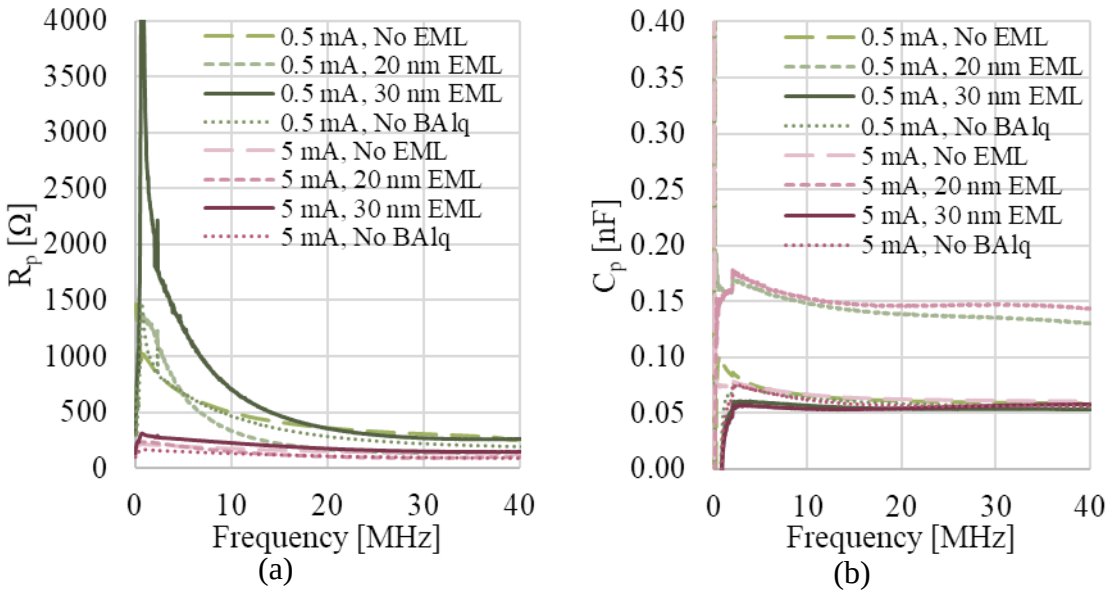

Fig. 6.17: Variation of (a) R_p and (b) C_p with frequency and bias current for 0.12 mm^2 OLEDs.

The measured R_p values for the devices with the 30 nm EML are higher than the other devices measured; this would be expected, as this device is thicker than the others measured. It is also seen that the C_p values for the devices with no EML, without BAlq and with a 30 nm EML are all similar, whereas the C_p for the OLEDs with a 20 nm EML are significantly higher. As previously suggested, this is possibly due to charge accumulation either side of the EML. However, in the devices without a BAlq layer and without an EML, these same interfaces do not exist and the same charge accumulation cannot occur. The device with the 30 nm EML has a lower measured capacitance than would be expected if charges were accumulating either side of the EML. This may be due to the higher doping level in this device, which creates more sites for charges to hop from the α-NPD and BAlq layers into the EML layers, reducing the interfacial barrier to injection into the EML. This would thereby move the charge accumulation layers to closer to the contact layers and further reduce the device capacitance.

Fitting of the S_{21} response to R_o and C_1 parameters provides responses as seen in Fig. 6.18. The R_o and C_1 parameters used can be found in Table 6-6. A reasonably good fit is found for the devices with the 30 nm EML and without the BAlq layer. The RC time constants provided for the devices with the 30 nm EML also provide good consistency with the time constants measured in the large signal measurements in Chapter 5. It can be seen that the difference in capacitance between the OLEDs without BAlq and the full-stack OLEDs is not significant, but that it is the difference between the values of R_o for these devices that causes the signficant

performance difference. This is likely related to the MADN:BPhen interface affecting charge transport relative to the full stack devices.

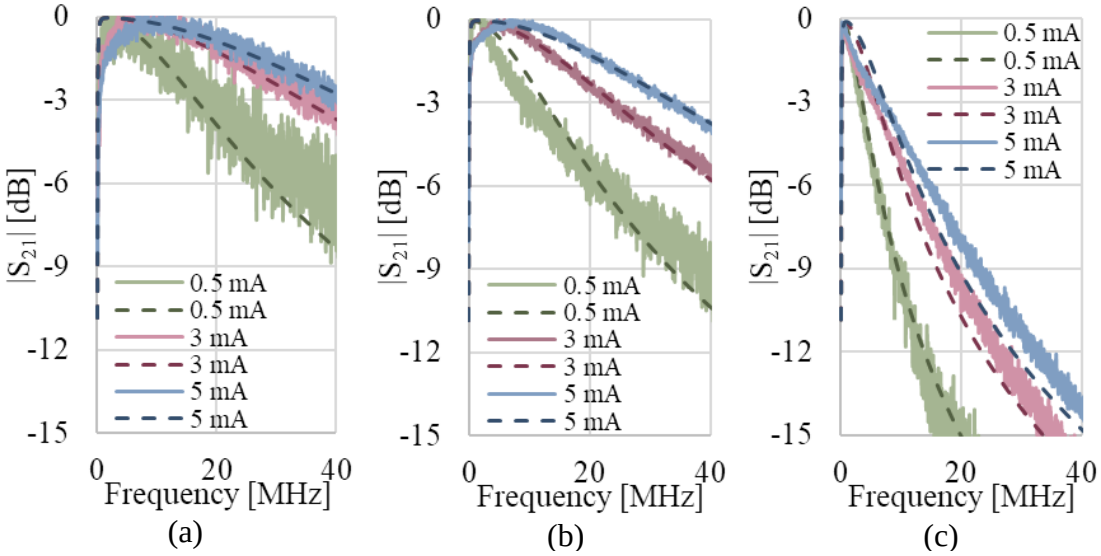

Fig. 6.18: $|S_{21}|$ measurements and modelling fit for the 0.12 mm^2 OLEDs on glass (a) with a 30 nm EML, (b) without the BAlq layer and (c) without an EML.

The influence of electric field also affects the value of R_o. At ~4.9 V, R_o for the full stack OLEDs is 190 Ω, and for the OLEDs without BAlq, R_o is 148 Ω, although the bias currents for each are 0.5 mA and 2 mA respectively. This is likely due to the field-dependence of the mobility (Eqs. 6.14 & 6.15) and the mobility-dependence of Langevin recombination.

$$\mu(\boldsymbol{E}) = \mu_0 \, exp\left(\gamma\sqrt{|\boldsymbol{E}|}\right) \tag{6.14}$$

$$R_L = \frac{q\left[\mu_n(\boldsymbol{E}) + \mu_p(\boldsymbol{E})\right]}{\varepsilon_r \varepsilon_0}(np - n_i^2) \tag{6.15}$$

In comparison, the fit of the devices without the EML to the model is relatively poor, with a significant change in shape of the response. The R_p and C_p measurements for the OLEDs without an EML are similar to the measurements for the devices without the BAlq layer, thus it would be reasonable to expect a similar S_{21} response. However, it is suggested that the slow response of these devices without the EML is limited by the slow excitonic response of the OLED, and not necessarily by the electrical properties measured in the S_{11} modelling. It has been suggested in the literature that a BAlq:NPB charge-transfer exciton has a lifetime of 40 ns [210]. From these results, and from the results in Fig. 5.19, it would suggest that the charge-transfer exciton in these devices may have a lifetime even higher than this. The relative-stability

of this exciton would mean that it is not the RC-response that limits the bandwidth of this device, but the exciton lifetime. This would explain the relatively poor fit of the model used here. It is of note that the equivalent values of R_o at bias currents of ≥2 mA are higher than values measured for R_p at any frequency, further suggesting that R_o is a non-physical parameter in this instance and that this model is inappropriate for the OLEDs without an EML. Although the fit is poor, the parameters for the device without the EML are included in Table 6-6 for completeness.

Table 6-6: R_o and C_1 fitting parameters for the S_{21} response of the 0.12 mm² OLEDs.

0.12 mm² OLED							
I_{DC} [mA]		0.5	1	2	3	4	5
Glass 20 nm EML	R_o [Ω]	100	81	67	60	51	47
	C_1 [pF]	158	159	163	159	160	157
Glass 30 nm EML	R_o [Ω]	190	143	112	92	82	75
	C_1 [pF]	50.7	50.5	50.2	50.2	49.9	49.9
Glass No BAlq	R_o [Ω]	345	221	148	122	99	84
	C_1 [pF]	54.2	53.9	53.8	54.0	54.4	54.7
Glass No EML	R_o [Ω]	746	638	523	437	388	356
	C_1 [pF]	59.4	59.5	59.8	60.0	60.2	60.4

It has been shown in Chapter 4 that thermal effects are significant for devices on glass, as they cause operating behaviour to not scale with area in a simple fashion (unlike the devices on silicon). As the previous results pertaining to the 0.12 mm^2 are not then directly scalable to the larger devices, the same modelling techniques have been undertaken for the 1.1 mm^2 and for the 9 mm^2 OLEDs.

Measurements of the C_p values in Fig. 6.19 suggest that, as the capacitance of the OLEDs with the 30 nm EML is lowest, these would have the highest bandwidth, followed by the OLEDs without the BAlq layer, then the OLEDs with the 20 nm EML; this is indeed the case. Although the OLEDs without the EML have a similar capacitance to the OLEDs without the BAlq layer, these devices are excluded from this comparison for the excitonic reasons previously mentioned, as it is clear that the exciton recombination time limits the overall device bandwidth.

Equivalent S_{21} modelling is presented in Fig. 6.20 , with the model parameters presented in Table 6-7.

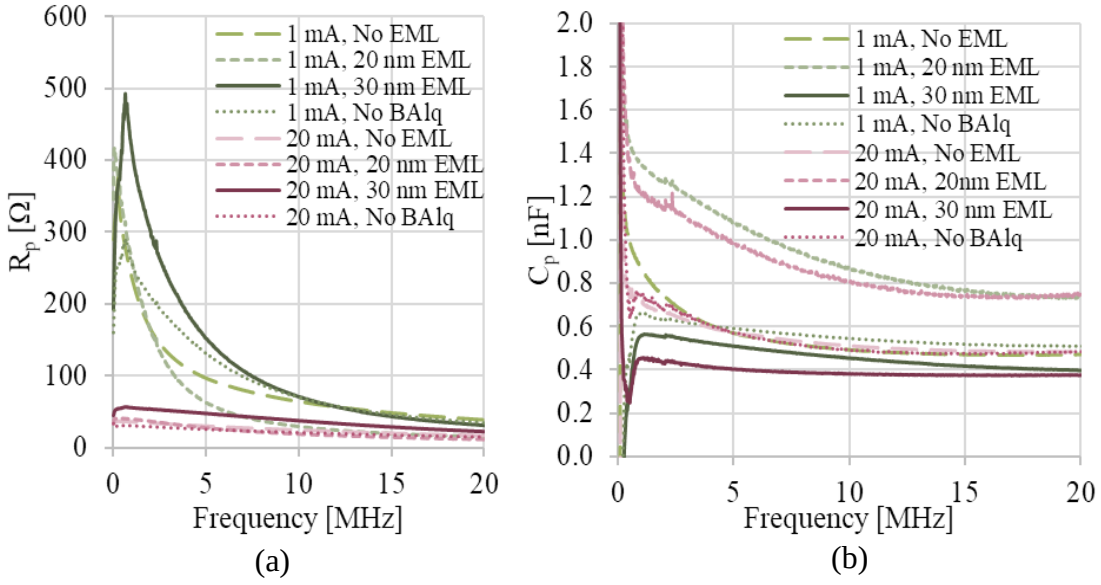

Fig. 6.19: Variation of (a) R_p and (b) C_p with frequency and bias current for the 1.1 mm^2 OLEDs on glass.

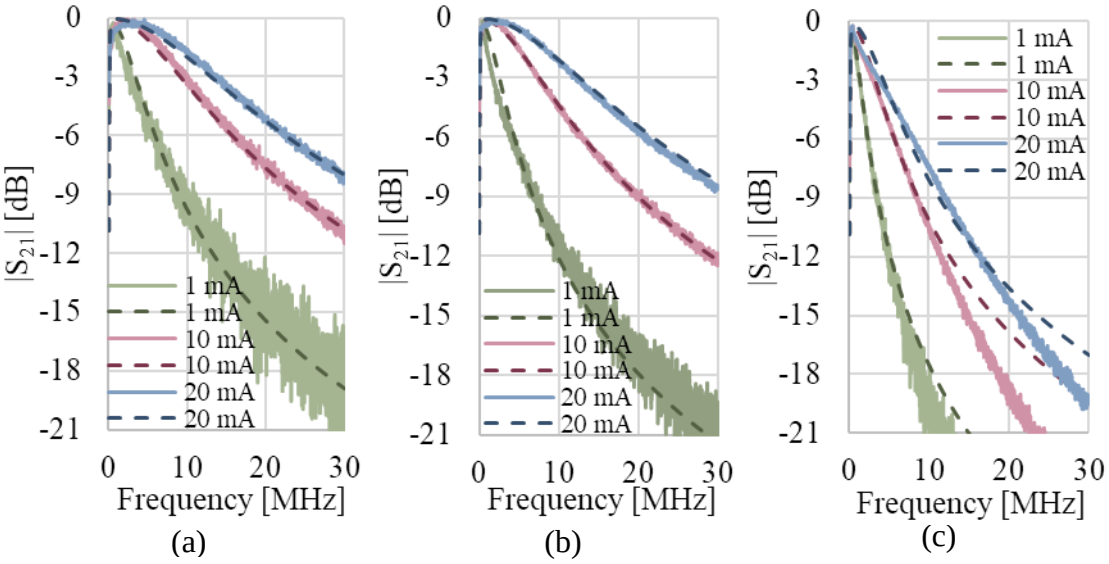

Fig. 6.20: $|S_{21}|$ measurements and modelling fit for the 1.1 mm^2 OLEDs on glass (a) with a 30 nm EML, (b) without the BAlq layer and (c) without an EML.

Table 6-7: R_o and C_1 parameters used for fitting to the S_{21} model for the 1.1 mm² OLEDs.

1.1 mm² OLED									
I_{DC} [mA]		1	3	5	8	10	15	20	25
Glass 20 nm EML	R_o [Ω]	116	66	52	44	40	32	28	
	C_1 [nF]	0.73	0.74	0.74	0.75	0.75	0.75	0.75	
Glass 30 nm EML	R_o [Ω]	131	69	57	46	41	34	29	
	C_1 [nF]	0.39	0.39	0.39	0.39	0.39	0.39	0.38	
Glass No BAlq	R_o [Ω]	145	85	63	47	41	30	25	20
	C_1 [nF]	0.52	0.51	0.51	0.51	0.51	0.51	0.51	0.51
Glass No EML	R_o [Ω]	219	147	124	110	100	85	77	70
	C_1 [nF]	0.50	0.50	0.50	0.50	0.49	0.49	0.48	0.47

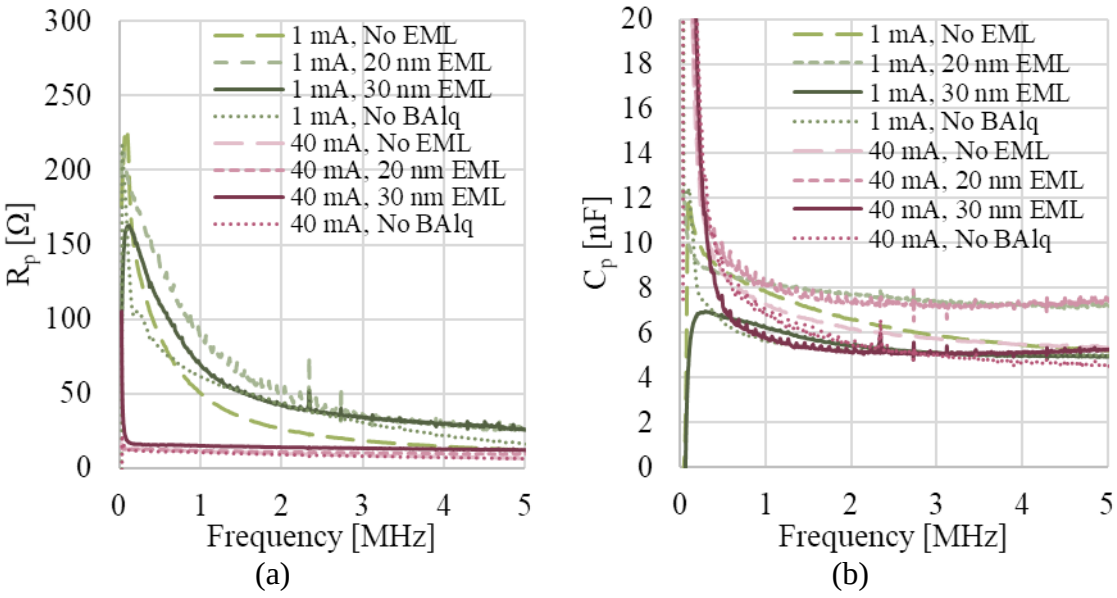

Fig. 6.21: Measurements of (a) R_p and (b) C_p against frequency at different bias currents for the 9 mm² OLEDs on glass.

Fig. 6.21 presents the R_p and C_p measurements for the 9 mm^2 OLEDs. Once again, the OLEDs with the 20 nm EML have the highest values for C_p.

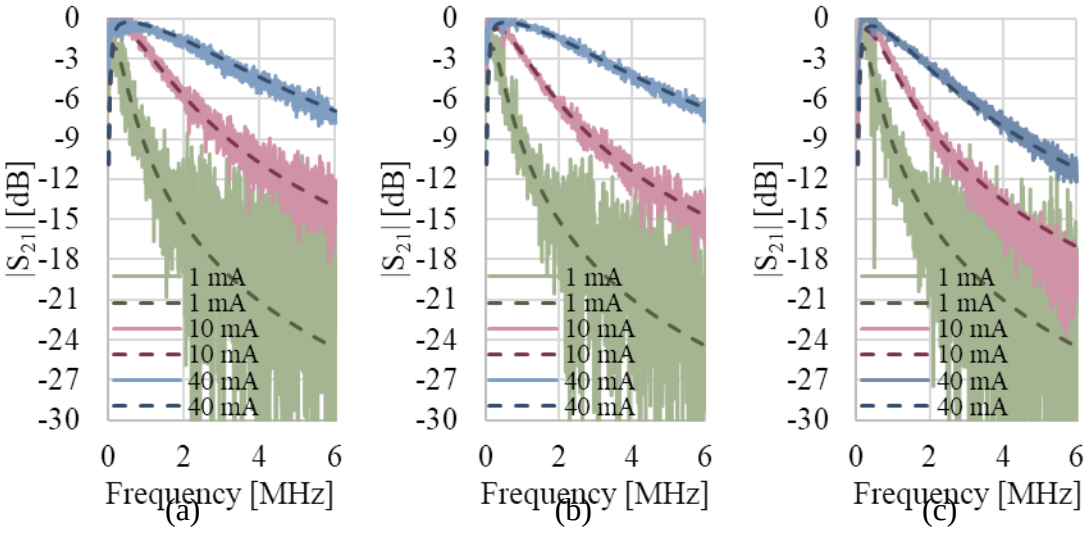

Fig. 6.22: $|S_{21}|$ measurements and modelling fit for the 9 mm^2 OLEDs on glass (a) with a 30 nm EML, (b) without the BAlq layer and (c) without an EML.

Fig. 6.22 shows the fit between the S_{21} parameters found in Table 6-8 and the S_{21} measurements. The relative improvement of the fit of the devices without an EML to the S_{21} model fitting may be because the electrical RC time constant starts to be of the same order of magnitude as the exciton lifetime, and thus the exciton lifetime is no longer the only factor limiting the bandwidth of these devices.

Table 6-8: R_o and C_1 parameters used for fitting to the S_{21} model for the 9 mm² OLEDs.

9 mm² OLED												
I_{DC} [mA]		1	5	10	15	20	25	30	35	40	45	50
Glass 20 nm EML	R_o [Ω]	70	30	20	15	13	11	10	8.7	7.6	7.4	6.2
	C_1 [nF]	7.1	7.1	7.0	7.0	7.0	7.2	7.2	7.4	7.6	7.7	7.9
Glass 30 nm EML	R_o [Ω]	89	42	27	22	18	16	13	12	10	9.3	8.4
	C_1 [nF]	5.0	4.9	4.8	4.8	4.8	4.8	4.9	5.0	5.1	5.2	5.3
Glass No BAlq	R_o [Ω]	84	41	28	21	18	16	14	12	10	9.5	
	C_1 [nF]	5.2	5.1	5.0	5.0	5.0	4.9	4.9	4.9	4.9	4.9	
Glass No EML	R_o [Ω]	83	46	35	30	25	22	20	20	18	17	16
	C_1 [nF]	5.4	5.4	5.4	5.3	5.3	5.3	5.3	5.3	5.4	5.4	5.4

The modelling in this section has shown that the bandwidth of the full stack OLEDs is limited by the device capacitance (as opposed to excitonic lifetimes), and may be well predicted by an RC time constant. The measured capacitances are relatively constant with bias, with small signal resistances reducing as bias increases. The OLEDs with the 30 nm EML have the highest bandwidths as they have the lowest capacitances, and are significantly faster than the devices with a 20 nm EML. Measurements of the 20 nm EML OLEDs on silicon substrates show that their capacitance suggests that due to the low mobility of the materials and hopping nature of the transport and energetic barriers at interfaces, there is a crowding of charge at the Spiro-TTB/α-NPD and BPhen/BAlq interfaces, such that improvement of charge injection at these interfaces and reduction of associated capacitance may improve overall device bandwidth.

6.3 Physical Modelling

The Silvaco simulation introduced in Chapter 4 is extended to produce small signal RC parameters for the OLEDs at different bias points. The simulation applies a DC bias to the OLED, and then performs a sinusoidal steady state analysis by linearisation of Poisson's equation and the carrier continuity equations around the DC operating point, based upon the works of Laux [243]. The output of this is the admittance matrix of the overall device, from which the small signal resistance and capacitance values may be found. This simulation method is directly analogous to the small signal measurements taken by the VNA presented in Chapter 5, and so may be used to analyse the internal workings of the OLED. For computational efficacy, the effect of temperature has not been included.

6.3.1 Simulation Results

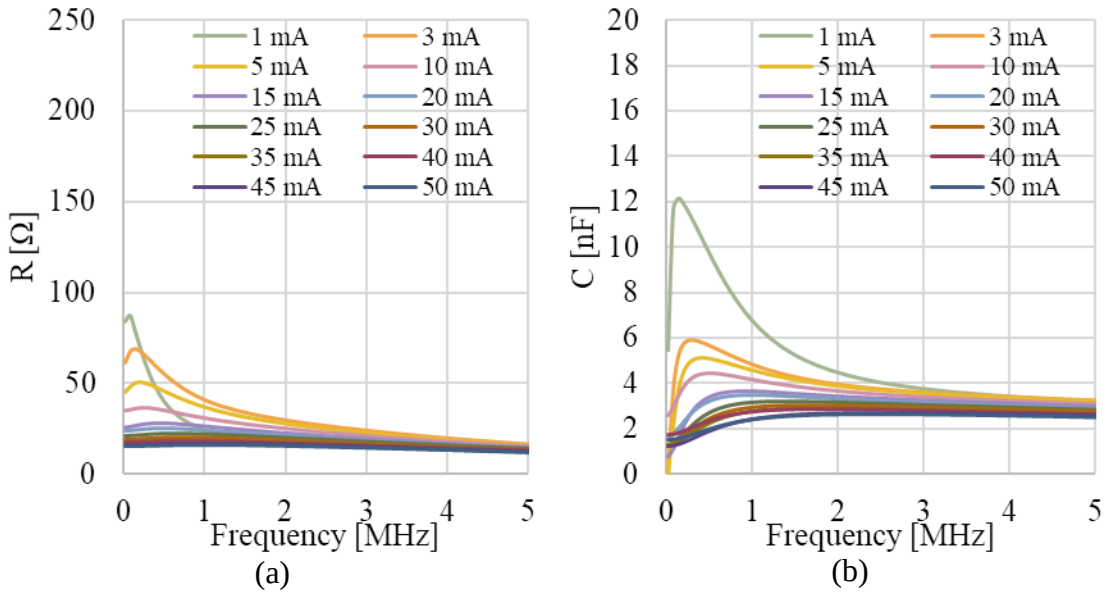

Fig. 6.23: Output (a) resistance and (b) capacitance values against frequency for the simulation of the 9 mm^2 OLEDs with a 20 nm EML.

Fig. 6.23 shows the output resistance and capacitance values for the simulation of a 9 mm^2 OLED with a 20 nm EML. Broadly similar trends to the direct R and C values obtained from the admittance of the S_{11} measurements, are shown, as can be seen from Fig. 6.24 (measurements do not subtract the series resistance R_s parameter for measurement equivalency). The reduction in R with frequency is due to the influence of R_s in both the simulation and the measurements. Of note is that the low frequency small signal resistance is

much higher for the measurements than the simulation. This suggests a higher concentration of trap states in the measured devices than implemented in the simulation.

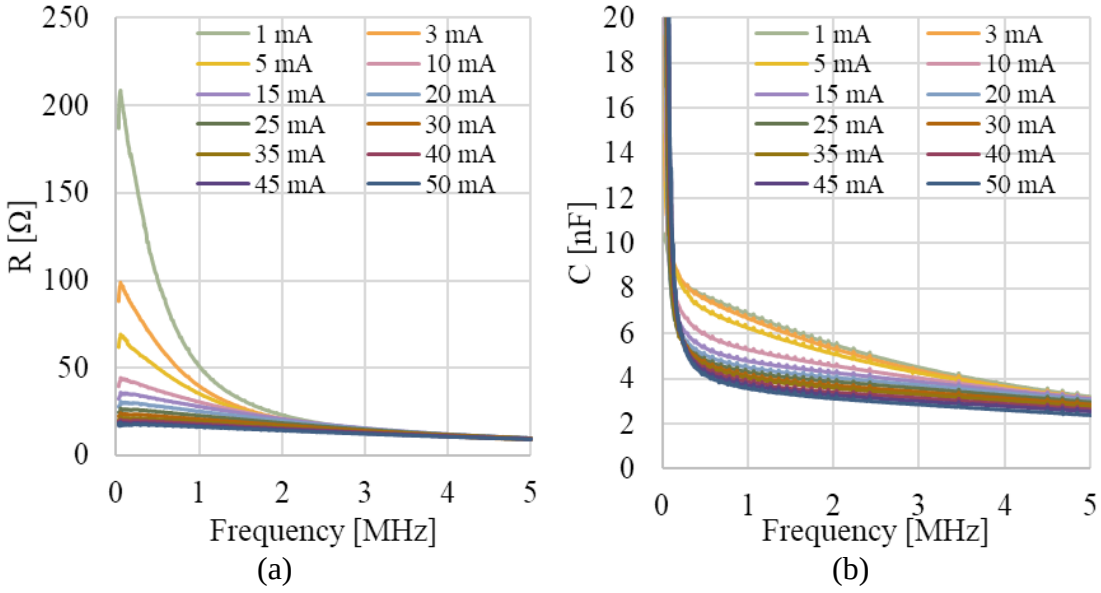

Fig. 6.24: (a) Resistance and (b) capacitance values obtained through measurement of the S_{11} parameters of the 20 nm EML 9 mm^2 OLEDs on silicon.

Similar trends are observed for the 0.12 mm^2, with a reduction in R with frequency due to the effect of the contact resistance R_s. The capacitance simulation does not show the same low-frequency response as measurements, likely due to the influence of the bias-tee (at <100kHz) and due to the frequency response of traps, which is not included in the simulation. The measured reduction in C with frequency is due to the effect of R_s (c.f. R_p, C_p in Fig. 6.15), and has also been observed in the literature [244].

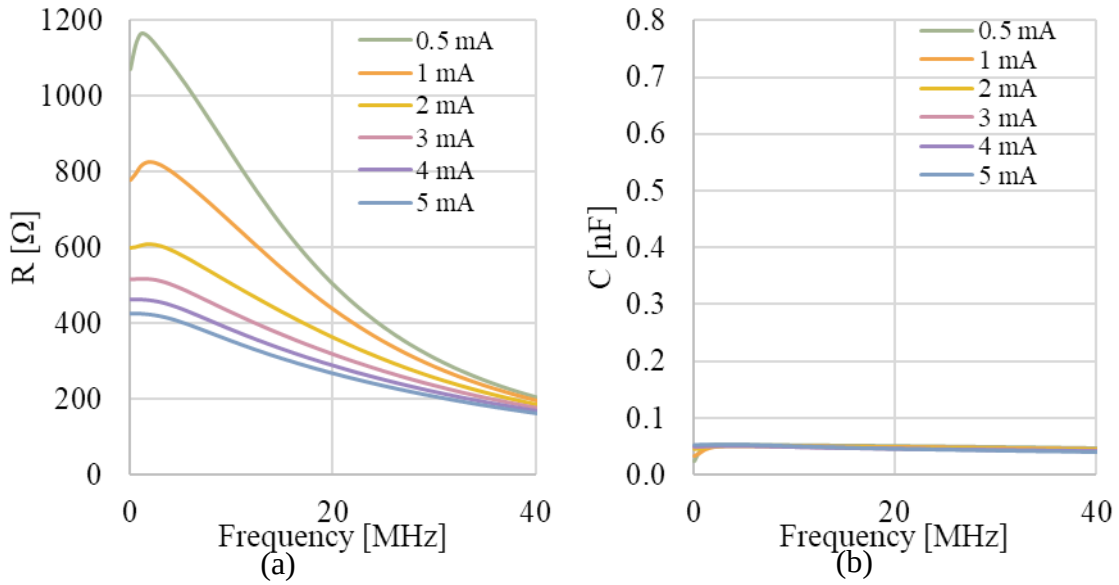

Fig. 6.25: Output (a) resistance and (b) capacitance values against frequency for the simulation of the 0.12 mm^2 OLEDs with a 20 nm EML.

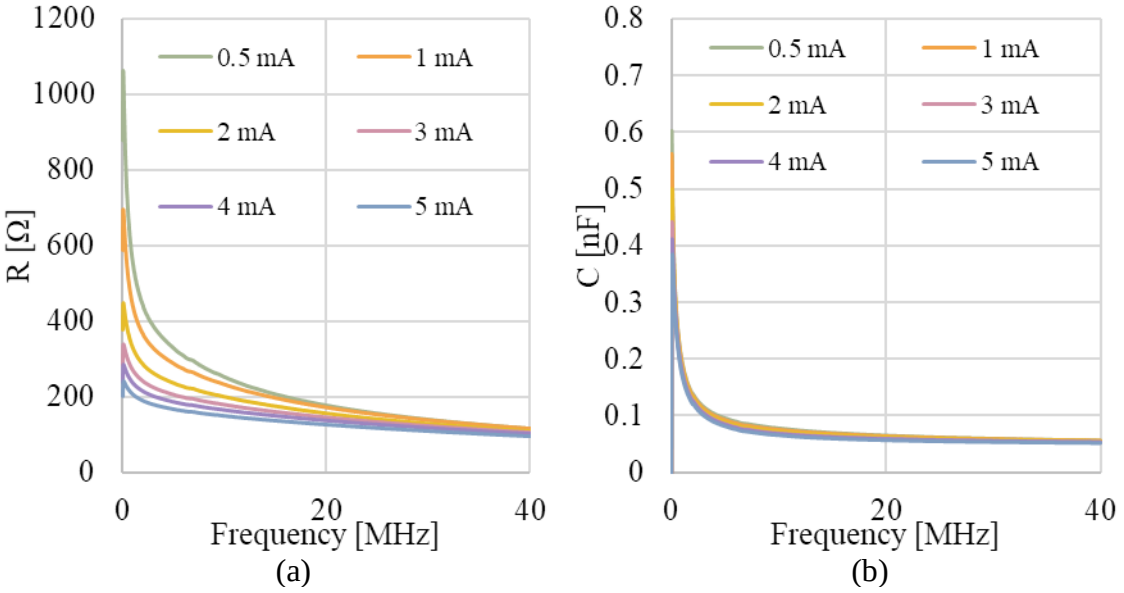

Fig. 6.26: (a) Resistance and (b) capacitance values obtained through measurement of the S_{11} parameters for the 20 nm EML 0.12 mm^2 OLEDs on silicon.

The final capacitance values for the simulation and measurement are in good agreement. In contrast to the 9 mm^2 OLEDs, the measured low-frequency resistance values for the 0.12 mm^2 are lower than the simulated values.

Taking the small signal simulation values for R and C, it is possible to build a fitting model to the S_{21} parameters, in the same fashion as §6.2.1. It is found that taking the constant simulation

high-frequency capacitance (C_∞) and a fixed proportion of the simulation low-frequency resistance ($\alpha R(\omega = 0) \equiv \alpha R_0$) across *all* bias currents for a given device size provides a very good fit to the measured S_{21}. This proportion αR_0 represents a luminescent proportion of the total resistance.

$$H(\omega) \propto \frac{I_1}{I_t} = \frac{1}{1 + j\omega C_\infty \alpha R_0} \tag{6.16}$$

This is in contrast to the $R_o C_1$ fitting in §6.2.1, where R_o is not found to have any constant correlation to low frequency values of R_p or R (the equivalent resistance without the subtraction of R_s). This would suggest that the series resistance R_s, the bias tee and the trap states act to obscure the true value of the resistance values obtained by S_{11} measurements, which can conversely be predicted in simulation.

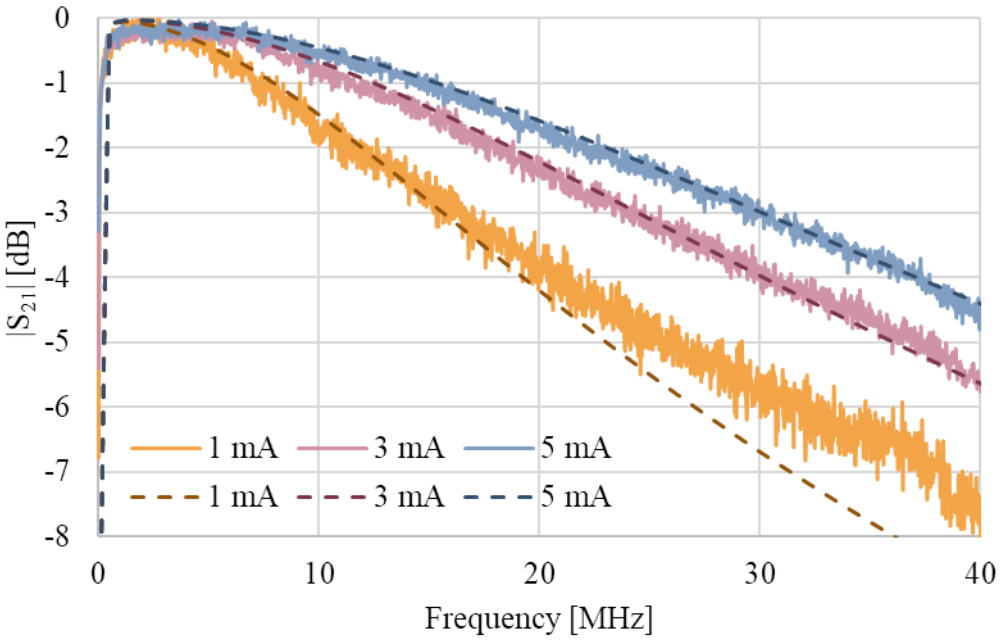

Fig. 6.27: Measurement (solid) and dashed (simulation) $|S_{21}|$ fit for the 0.12 mm^2 OLEDs.

It can be seen that for the low current measurements, the fit shows the same deviation at high frequencies as is seen from the fitting methodology in §6.2.1. By allowing the simulated R_0 to vary with frequency, this low-bias fitting can be improved, as in Fig. 6.28.

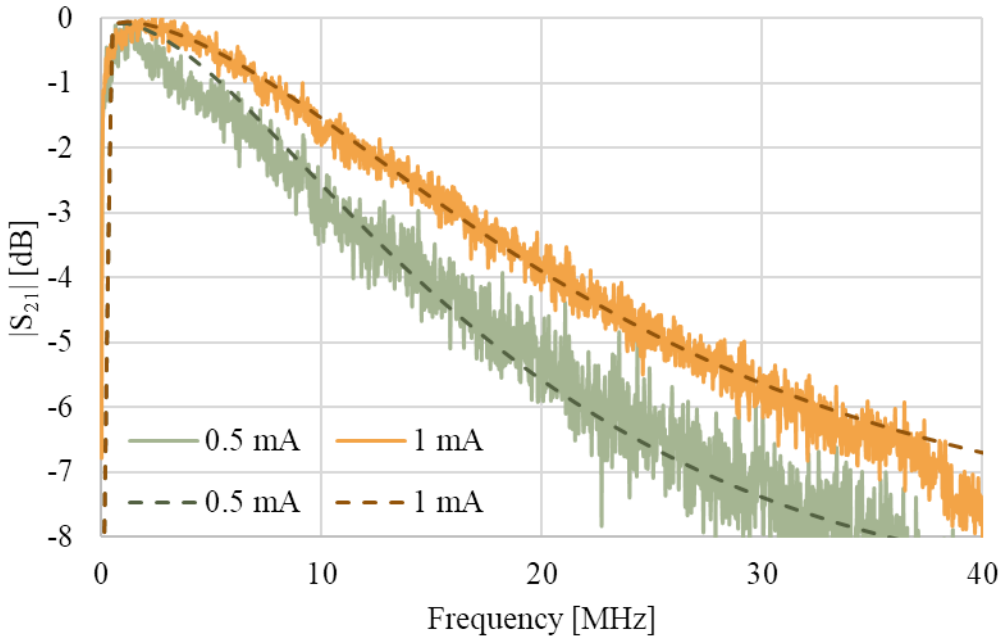

Fig. 6.28: Low bias fitting of the $|S_{21}|$ to 0.12 mm² OLEDs with a 20 nm EML on silicon substrates.

The fit of the 3 dB frequency calculated from the constant α version of the S_{21} against measured 3 dB values may be seen in Fig. 6.29, below. The α used is constant for each bias current but varies between OLED sizes.

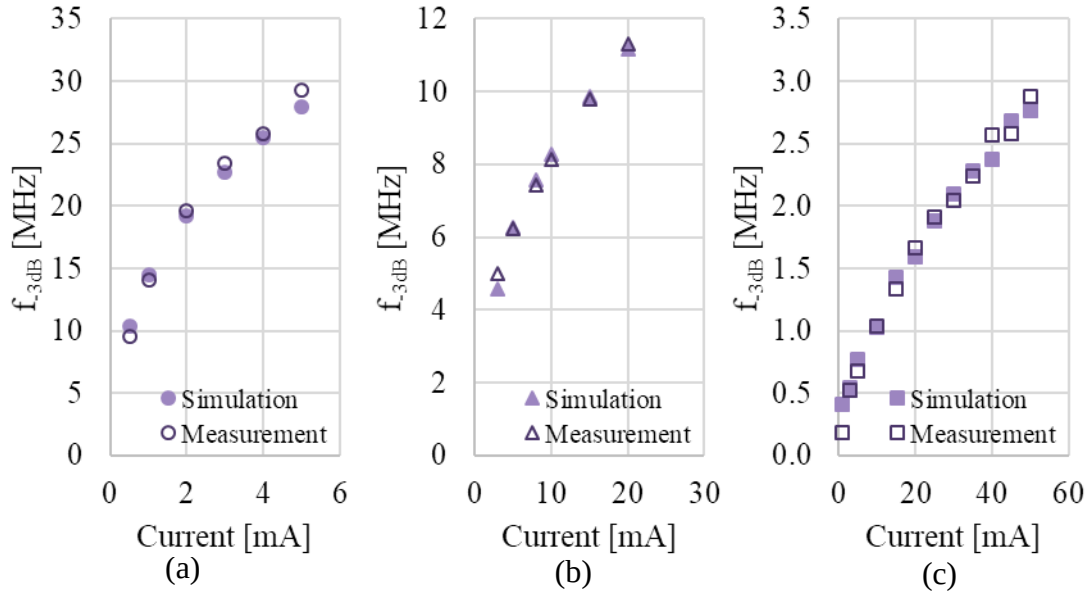

Fig. 6.29: 3 dB bandwidth calculations from simulation and by measurement at different bias currents for the 20 nm EML OLEDs at (a) 0.12 mm², (b) 1.1 mm² and (c) 9 mm² on silicon substrates.

Furthermore, a reasonable fit is found by varying the fitting parameter α for different devices. Fig. 6.30 presents these results for 20 nm EML OLEDs on glass, and Fig. 6.31 presents the same fitting for the simulation run with a 30 nm EML.

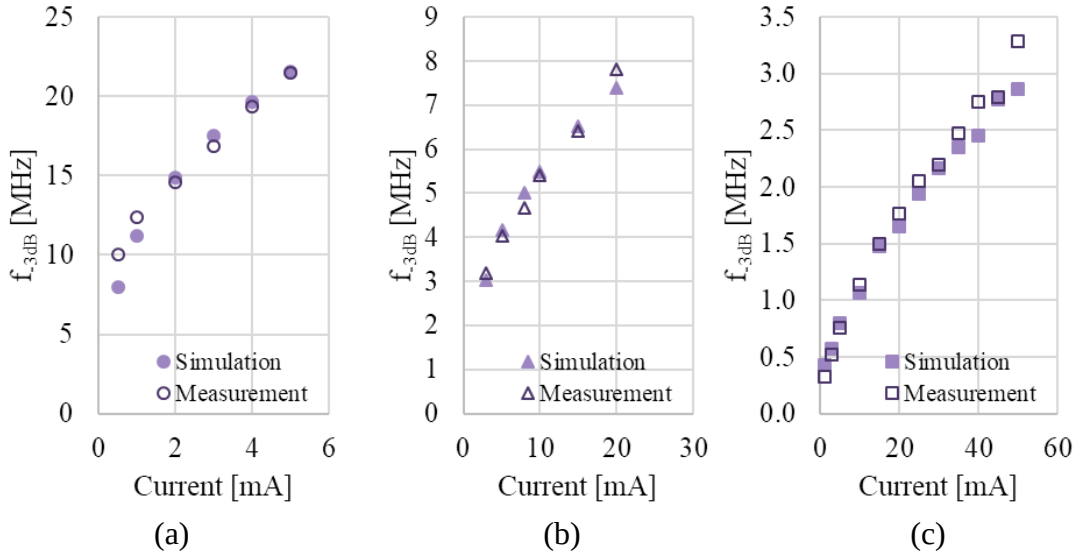

Fig. 6.30: 3 dB bandwidth calculations from simulation and by measurement at different bias currents for the 20 nm EML OLEDs at (a) 0.12 mm^2, (b) 1.1 mm^2 and (c) 9 mm^2 on glass substrates.

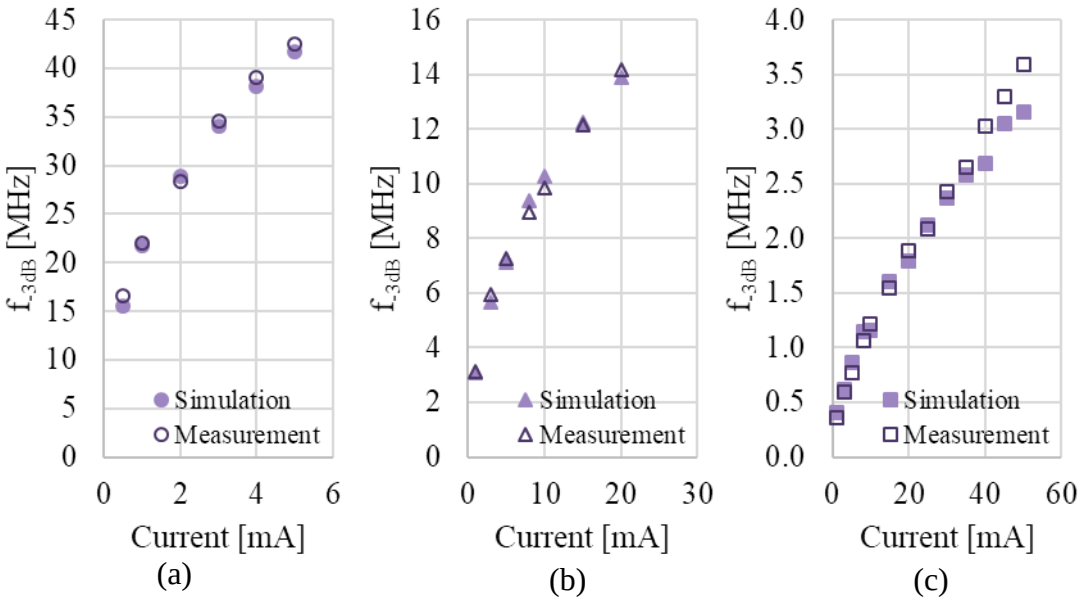

Fig. 6.31: 3 dB bandwidth calculations from simulation and by measurement at different bias currents for the 30 nm EML OLEDs at (a) 0.12 mm^2, (b) 1.1 mm^2 and (c) 9 mm^2 on glass substrates.

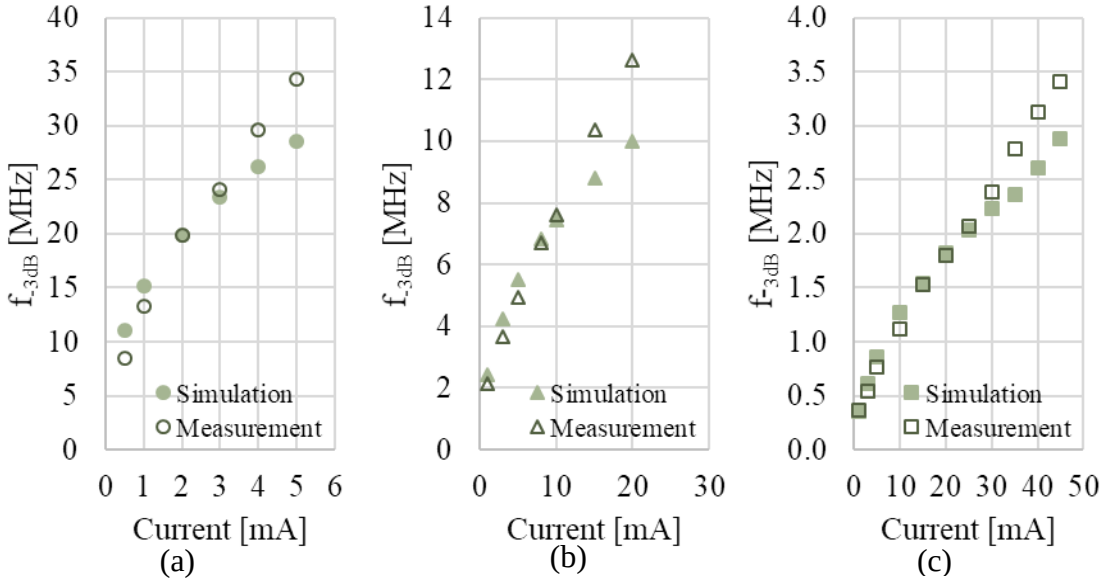

Fig. 6.32: 3 dB bandwidth calculations from simulation and by measurement at different bias currents for the 30 nm EML OLEDs without a BAlq layer at (a) 0.12 mm^2, (b) 1.1 mm^2 and (c) 9 mm^2 on glass substrates.

Fig. 6.32 shows the fit between simulation and measurement for the devices without a BAlq layer. In each device dimension, the simulation underestimates the bandwidth at high bias and overestimates at low-bias. This suggest that one of the layers may have an underestimated field-enhanced mobility factor. With better characterisation of the material mobilities at the thicknesses used in these devices, it may be possible to refine this model.

6.3.2 Trends

An advantage of simulation techniques is that modelling may be used to forecast behaviour and trends. While work remains to consistently characterise a rapidly growing library of organic semiconductor materials, with reasonable understanding of the significant parameters, it is possible to analyse device structure and behaviour in the context of optimisation. By applying the same methodology as detailed in §6.3, it is possible to forecast device performance with variation of parameters. All of the following trends are forecast using a 0.12 mm^2 OLED simulation, and make the assumption that a constant value of α can be used to plot trends. This is a significant assumption, as α correlates the luminescent recombination to the total output resistance and may vary with different device geometries.

Nevertheless, this approximation may be considered valid to calculate rough estimates of bandwidth performance as the device conductance (and therefore resistance) also depends upon

these same parameters of mobility and carrier concentration. Aside from the parameter that is varied, the OLEDs simulated have a structure as introduced in Fig. 4.1, and doping concentrations are maintained.

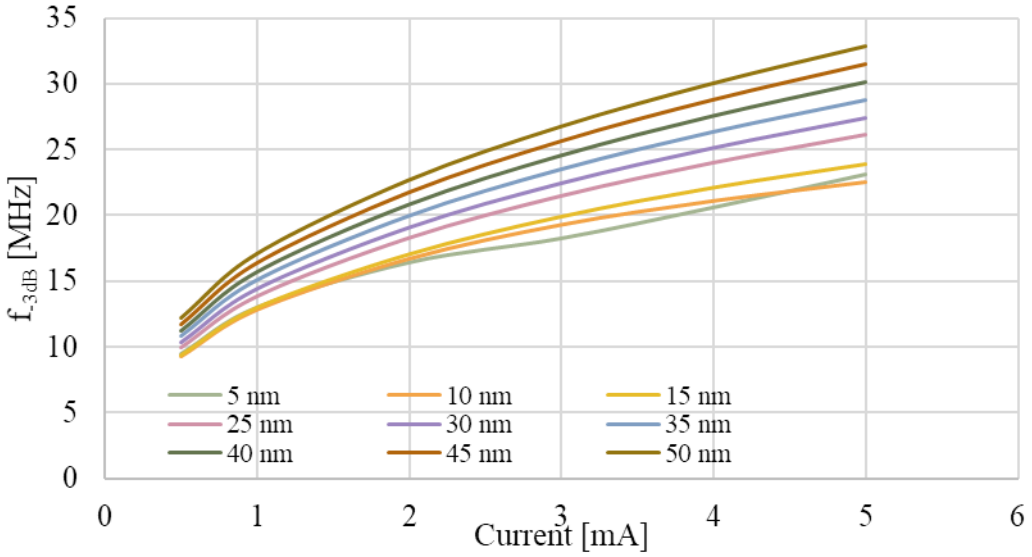

Fig. 6.33: Predicted 3 dB bandwidths for varying thicknesses of Spiro-TTB.

Fig. 6.33 shows the predicted 3 dB bandwidths as the thickness of the doped Spiro-TTB layer is changed. It appears that bandwidth is likely improved with increasing thickness of the Spiro-TTB layer, possibly because both capacitance and mobility improves with layer thickness.

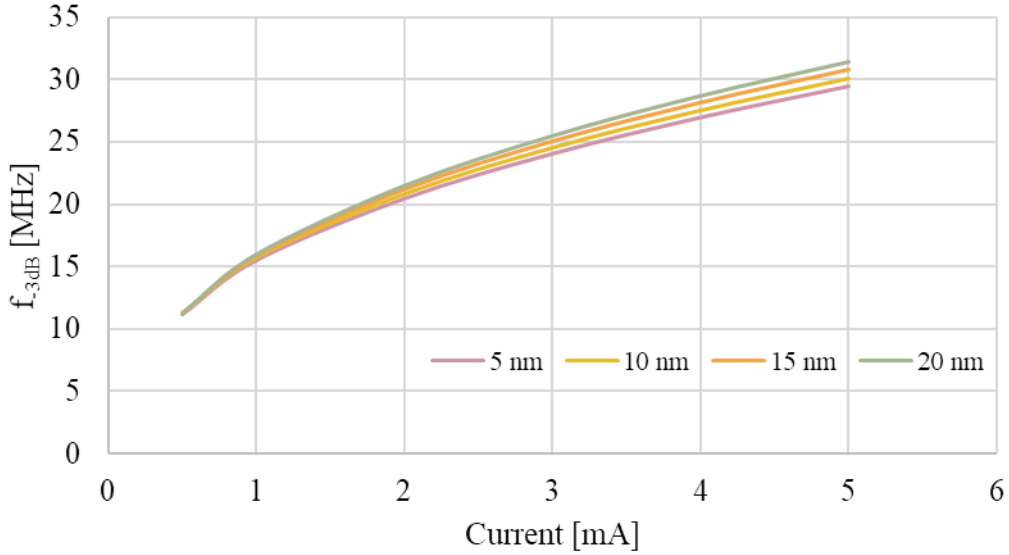

Fig. 6.34: Predicted 3 dB bandwidths for varying thicknesses of α-NPD.

It appears from Fig. 6.34 that electrical bandwidth is only slightly modified by changing the thickness of the α-NPD layer.

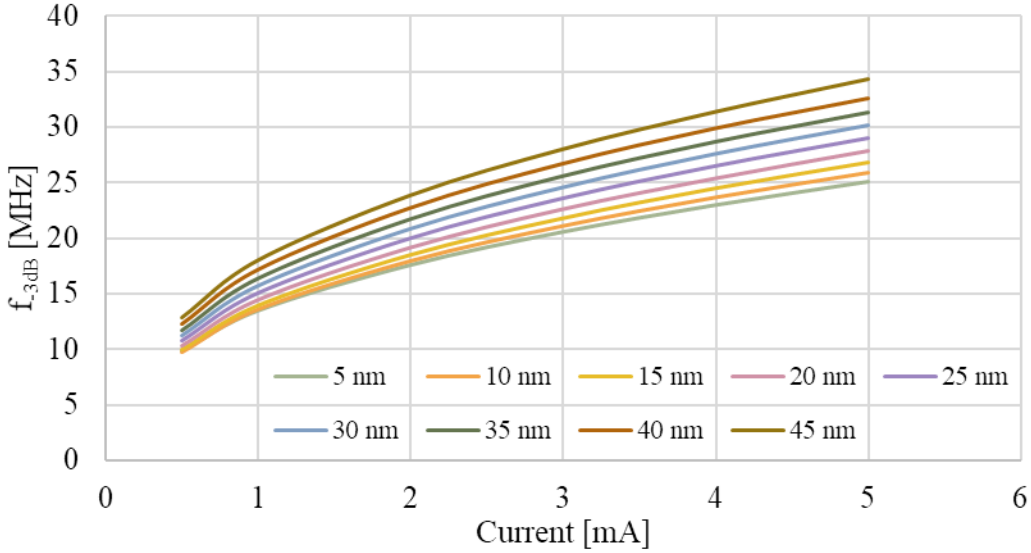

Fig. 6.35: Predicted 3 dB bandwidths for varying thicknesses of the EML.

Simulation predicts that the thickness of the EML can be further increased in order to improve OLED bandwidth (Fig. 6.35); this trend is in agreement with the observed increase in S_{21} bandwidth between the OLEDs with the 20 nm EML and the 30 nm EML. Of course, this is predicated upon a constant value of α, which may not be the case, and further validation is required to confirm the correlation of α to the total resistance. Ideally, this would involve verifying a relationship with the hypothesised Langevin resistance.

$$\alpha R_0 \propto R_{rec} = \frac{E}{AqR_L} \tag{6.17}$$

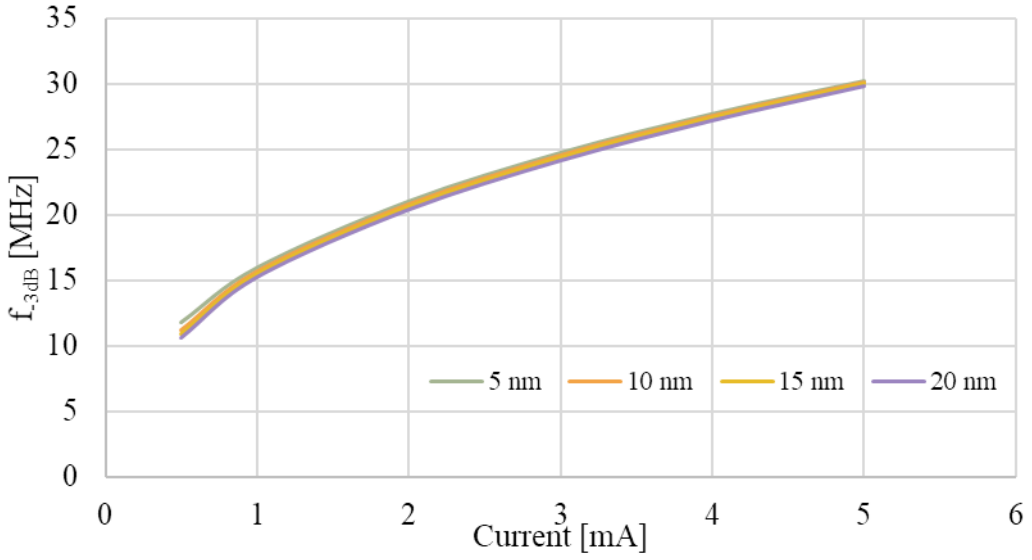

Fig. 6.36: Predicted 3 dB bandwidths for varying thicknesses of BAlq.

In contrast to the hole injecting and transporting layers, the simulation model suggests that increasing the BAlq thickness may in fact very slightly worsen OLED bandwidths (Fig. 6.36), although the overall change is very small. Furthermore, it suggests that OLED bandwidths may be improved by reducing the thickness of the BPhen layer below 15 nm (or increasing it beyond 40 nm), as seen in Fig. 6.37.

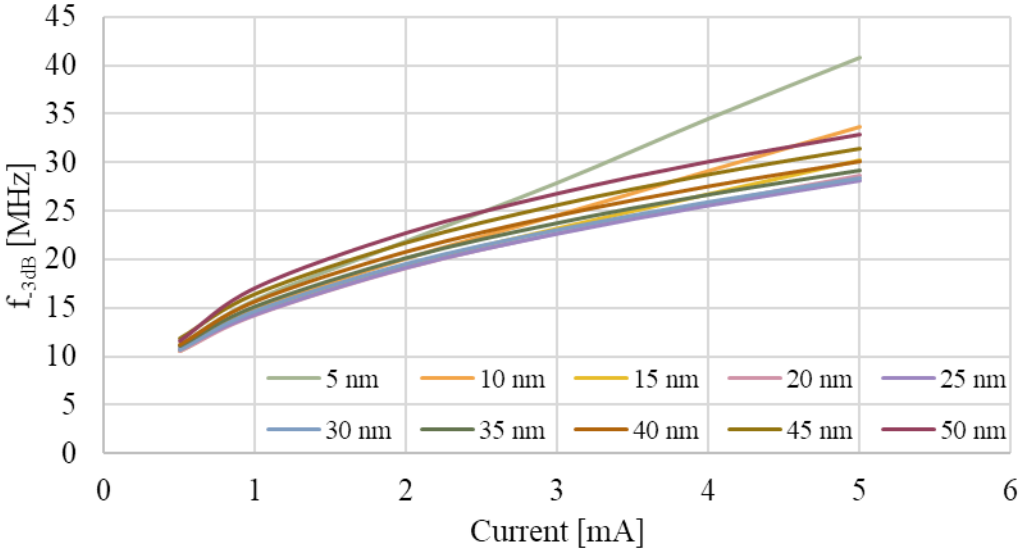

Fig. 6.37: Predicted 3 dB bandwidths for varying thicknesses of BPhen.

Overall, the simulation model suggests that there may be an improvement in bandwidth by reducing the thickness of the BPhen layers and by increasing the thicknesses of the EML, α-NPD and Spiro-TTB layers. This analysis, of course, assumes that α is constant for each of

these devices, that the recombination zone remains within the EML and is not limited by excitonic effects. It is also assumed that any changes in luminescent output power do not limit the overall bandwidth of the optical link and that these devices are manufactured on a thermally conductive substrate such that the devices are more predictable and thermal effects are less significant. However, as measurements in §6.2.1 suggest that capacitance limits the small signal bandwidth of these devices, it is anticipated that these adjustments may improve the capacitance of the OLED and hence improve the bandwidth performance of these devices. It is also expected that with improved knowledge of the device mobilities, HOMO-LUMO levels and analytic determination of α and verification of its proposed relationship between the total device resistance and luminescent resistance that this holistic model can be expanded and improved upon in the future.

6.4 Conclusions

This chapter has introduced a novel method of analysing the small signal modelling of the OLEDs under study. Measurements of the S_{11} parameters have been used to form a small signal equivalent circuit model of the OLED, and have been further used to inform a model that predicts the S_{21} output of the optical link. It is found that this S_{21} response fits an RC response, and that the optical frequency response of the OLEDs may be modelled as RC-limited according to this model. The high-frequency capacitance measured using the S_{11} response is seen to be constant at different bias currents, with the low-frequency response of the OLED attributed to trapping effects. The small signal resistance value for the OLED is found to vary with frequency and with bias, with the high-frequency decay of the resistance attributed to trapping effects. Choosing a portion of the small signal low-frequency resistance in parallel with the capacitance fits the S_{21} response measurements; this fraction may be considered to be analogous to a luminescent portion of the total device resistance. These measurements are taken for a variety of devices in different sizes and configurations. It is believed that this type of analysis is novel to the field of organic LEDs and has not previously been conducted.

It is found that the small signal capacitance and resistance vary with temperature, likely due to the thermally-activated mobility of the carriers. Without this thermal energy, the mobility of the OLEDs is reduced, thereby increasing the small signal resistance. In addition, the capacitance is found to decrease under cooling, likely because there is less accumulation of carriers at interfaces when they do not have the thermal energy to overcome energetic barriers

at the boundaries between layers. It is found that devices on silicon display behaviour that scales well, but the thermal response of the OLEDs means that the behaviour on glass is much more unpredictable. This thermal response also means that the devices on glass exhibit different small signal parameters to the same OLEDs on silicon.

Limitations of the OLED S_{21} model are seen in the devices without an EML. The fit of the response is seen to be poor, as these devices are excitonically limited, and not electrically limited. The S_{11} parameters for these OLEDs are similar to other measured devices, but the S_{21} response is significantly different, and fit of an RC model required non-physical values of resistance much higher than that measured through the S_{11} parametrisation. It is only for the largest 9 mm^2 OLEDs that the small signal model starts to fit the S_{21} response, and this is because at this device area, the RC time constant is of a similar scale to the excitonic charge transfer time limitation.

The physical simulation of the OLEDs introduced in Chapter 4 has also been extended in this chapter to provide equivalent small signal RC parameters. These parameters were used in the same RC-limited S_{21} model as derived from the S_{11} measurements. It was observed in this model that use of a constant proportion α of the low-frequency R parameter demonstrated good fitting to the S_{21} measurements across all bias currents. This is in contrast to the model derived from the S_{11} measurements, where the emissive portion of the resistance, R_o was found to have no constant relation to the R_p parameter. It is hypothesised that this proportionality α relates the Langevin recombination to the OLED small signal resistance and is obscured in measurements due to the bias-tee, the effect of the contact resistance R_s on S_{11} measurements and the carrier trapping effects.

From this, assuming a constant value of α for the 0.12 mm^2 OLEDs, some trends are forecast for device optimisation. It is suggested that thicker Spiro-TTB, α-NPD and EML layers can act to increase the device bandwidth, whereas a thinner BAlq and BPhen layer may act to improve the overall RC-limited bandwidth. As knowledge of organic semiconductor parameters improves with time, this model can then be enhanced in order to better predict and optimise OLED design for communications applications.

7 LINK DEMONSTRATION

This chapter presents the results of transmitting data using both OLEDs on silicon and on glass. It is found that the self-heating of the OLEDs on glass makes it difficult to achieve a stable operating point, and thus limits the bias current. Furthermore, the heating of the devices introduces additional noise, which means that the OLEDs on glass can be biased to a current at which they demonstrate only 11 MHz bandwidth and only achieve reliable error-free data transmission of 30 Mbps using simple on-off keying (OOK), whereas the OLEDs on silicon can be biased to a much higher operating point, and show less noise in the output signal. These OLEDs on silicon with a bandwidth of less than 35 MHz are able to achieve record 130 Mbps unequalised data transmission below the hard decision forward error correction coding limit using simple OOK. However, it is likely that much higher speeds will be achievable through device optimisation and the use of advanced modulation formats and modern equalisation techniques.

7.1 Introduction

Having characterised and modelled the OLEDs in Chapters 4-6, it has been shown that the full-stack OLEDs demonstrate RC-limited emissive bandwidths that depend predominantly upon their electrical characteristics, as well as their substrate performance. It now remains to demonstrate the efficacy of such devices in transmitting data in an optical link.

Current commercially available optical links frequently use externally-coupled inorganic LEDs, lasers and photodiodes, which increases the cost of the overall optical system. However,

organic optical links offer many advantages over their inorganic counterparts; in particular, the low material cost of organic materials, combined with the potential to manufacture integrated organic components directly upon polymer waveguides or polymer optical fibre suggests such components have application in low-cost integrated optical links, such as in cars, optical backplanes in consumer electronics, or systems requiring low-cost electrical isolation. MOST (Media Oriented Systems Transport) is the current optical standard for data transmission within cars, with the current generation (MOST150) operating at 150 Mbps through both electrical and POF links [245]. There is clearly demand for data transmission at the ~Mbps data rate, and the rise of Internet of Things is only set to increase this demand.

Existing end-to-end organic optical links have been demonstrated using POF [84] and polymer waveguides [107], with transmitted data rates of 2.8 Mbps and 5 Mbps respectively. With regards to high-speed OLEDs themselves, the fastest previous published OLED modulation has been at a rate of 100 MHz with an area of only 0.01 mm^2 [107]. This chapter presents the results of using the previously-characterised OLEDs in a POF optical link.

7.2 Experimental Setup

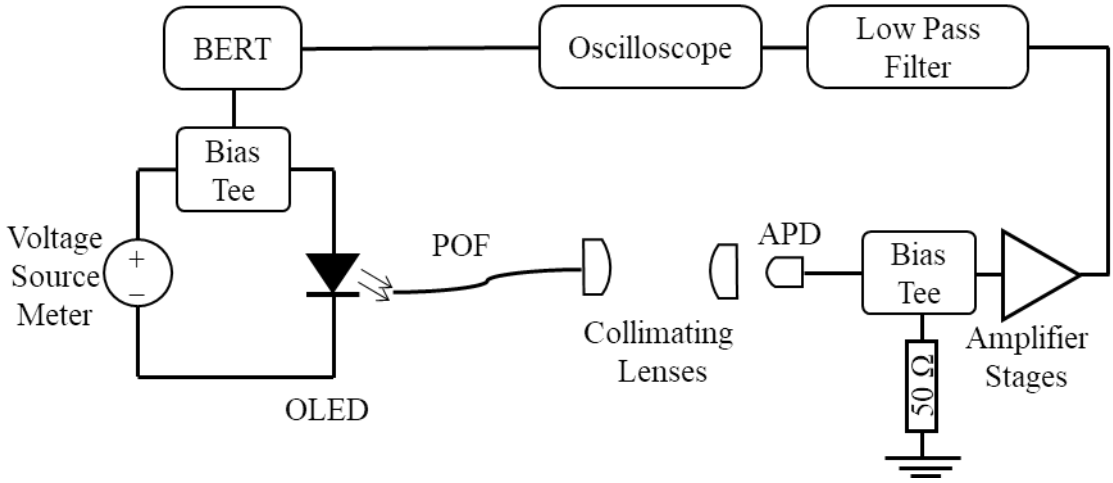

Fig. 7.1: Experimental schematic for the optical link.

The optical link was formed of a 0.12 mm^2 OLEDs on silicon butt-coupled to a 1 mm diameter plastic optical fibre (POF) patch cord which fed the optical signal to an 800 μm diameter avalanche photodiode (APD, First Sensor AD800-11) via a pair of aspheric optical lenses (Thorlabs). The OLED was biased to 6 mA using a Keithley 2400LV source meter and this DC signal was combined with a 0.8 V_{pp} PRBS15 output square pulse signal from an Anritsu

MP2101A BERTWave Bit Error Rate Tester (BERT) using a Mini Circuits 15542 Bias Tee. The output electrical signal from the APD was passed through another Mini Circuits 15542 Bias Tee, amplified by 20 dB by a ZFL-1000LN+ low-noise amplifier, and then again amplified by 25 dB by an SHF B826 broadband amplifier, filtered by an SBLP-300+ 180 MHz low pass filter, and fed into an Agilent Infiniivision DSOX3034T Digital Storage Oscilloscope with a bandwidth of 350 MHz.

Table 7-1: Bandwidth limitations of the equipment

Equipment	Bandwidth
BERT	12.5 Gbps[5]
Bias-Tee	0.1-4200 MHz
POF	200 MHz × 50 m
APD	350 MHz
Amplifier 1	0.1-1000 MHz
Amplifier 2	70 kHz - 25 GHz
Low-Pass Filter	180 MHz
Oscilloscope	350 MHz

As the test equipment has bandwidths much larger than the bandwidths of the OLEDs (by a factor of ~10), it may be assumed that the OLED is the limiting component in this data transmission experiment.

As the BERT is not able to natively generate data rates below 125 Mbps, Matlab was used to generate a PRBS15 signal. This data was then 'stretched' by repeating each symbol a number of times, and uploaded into the BERT as a programmable pattern. By using this 'stretched' pattern and varying the nominal data rate, effective data rates lower than 125 Mbps were achieved. Unfortunately, as the symbols were 'stretched', the BERT was not able to synchronise the data stream to calculate the bit error rate directly, as the slow modulation of the OLED meant that the transition 'sub-symbols' of the overall 'stretched' symbol were detected

[5] As quoted in the specification.

as errors. Therefore, the output data from the BERT and the output optical signal were fed into an oscilloscope for analysis.

The samples obtained by the oscilloscope were fed into Matlab, where all further analysis was undertaken. The data-sequence was split into 2T-spaced eye patterns from which the following measurements were taken.

The Q-factor was calculated according to the following equation [246]:

$$Q = \frac{\mu_1 - \mu_0}{\sigma_1 + \sigma_0} \tag{7.1}$$

Where $\mu_{1,0}$ refers to the mean amplitude of a bit '1' or a bit '0' and $\sigma_{1,0}$ refers to the standard deviation of the distribution of these received '1's and '0's.

The Q-factor was then used to calculate the bit-error rate (BER) according to the following derivation.

$$BER = p(S_1)p(R_0|S_1) + p(S_0)p(R_1|S_0) \tag{7.2}$$

$p(S_{0,1})$ represents the probability that a 0 or a 1 was transmitted, $p(R_0|S_1)$ represents the probability that a 0 was received given that a 1 was transmitted. Assuming a Gaussian distribution for the noise, then $p(R_0|S_1)$ is the probability that the additive Gaussian noise has taken the symbol beyond its threshold. Integrating over the tail-states of the Gaussian:

$$p(R_1|S_0) = \int_{v_{th}}^{\infty} \frac{1}{\sqrt{(2\pi)}\sigma_0} \exp\left(-\frac{1}{2}\left(\frac{r-\mu_0}{\sigma_0}\right)^2\right) dr \tag{7.3}$$

v_{th} is the decision threshold for the symbol, σ_0 is the noise variance and r is the received value (a random variable).

Assuming an equal probability of 1s and 0s, and the same Gaussian white noise this provides the following expression:

$$BER = \frac{1}{2\sqrt{2\pi}} \int_{v_{th}}^{\infty} \exp\left(-\frac{1}{2}\left(\frac{r-\mu_0}{\sigma_0}\right)^2\right) dr + \frac{1}{2\sqrt{2\pi}} \int_{-\infty}^{v_{th}} \exp\left(-\frac{1}{2}\left(\frac{\mu_1 - r}{\sigma_1}\right)^2\right) dr \tag{7.4}$$

Due to the symmetry between the 1s and 0s, this evaluation of BER is equal to the statistical Q-function:

$$Q(x) = \frac{1}{\sqrt{2\pi}} \int_x^{\infty} \exp\left(-\frac{u^2}{2}\right) du = \frac{1}{2} erfc\left(\frac{x}{\sqrt{2}}\right) \tag{7.5}$$

$$erfc(x) = \frac{2}{\sqrt{\pi}} \int_{x}^{\infty} \exp(-t^2)\, dt \tag{7.6}$$

Therefore, the total BER is given by the following equation, where Q is as defined in Eq. (7.1), and not the statistical Q-function.

$$BER = \frac{1}{2} erfc\left(\frac{Q}{\sqrt{2}}\right) \tag{7.7}$$

7.3 Experimental Results

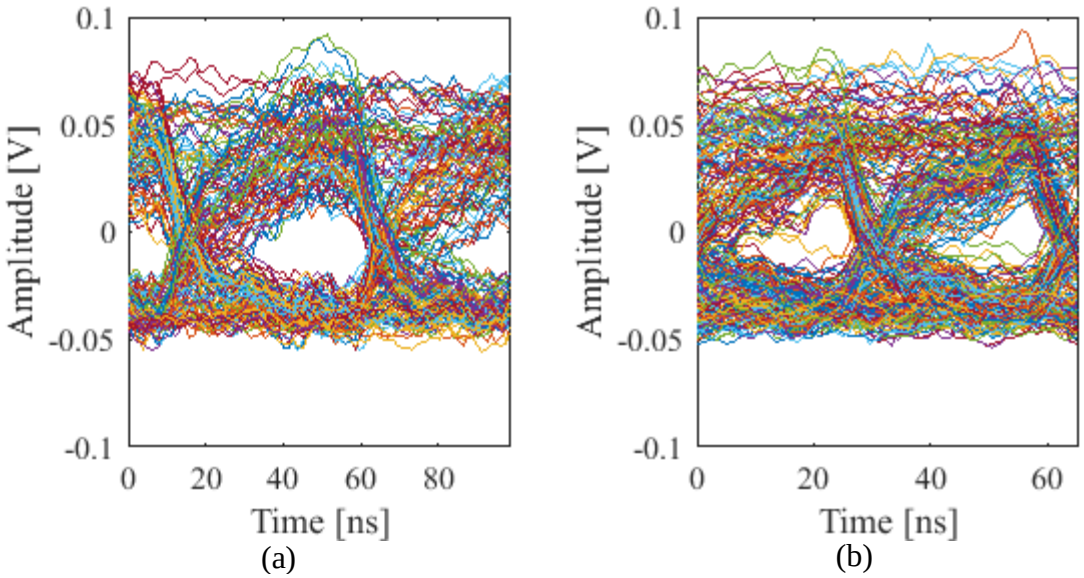

Fig. 7.2: Received eye diagram at (a) 20 Mbps and (b) 30 Mbps for 0.12 mm^2 OLEDs on glass.

Although the OLEDs on glass exhibited higher small signal bandwidths than the equivalent devices on silicon, the thermal effects of the glass meant that once the pulse signal was added to the device, the DC operating point was limited to 0.7 mA (6.0 V), to maintain stability and avoid thermal drift during operation. At this low DC bias, the luminescent power is low and it is not possible to modulate the devices very fast. As a result, the OLEDs experienced significant distortion and noise, further amplified by the APDs and external amplifiers. Fig. 7.2(a) shows the open eye at 20 Mbps, and the effect of the noise can be seen. Even by 30 Mbps (Fig. 7.2(b)) the eye is already starting to close. Unusually, at 20 Mbps, the calculated BER is 4.5×10^{-4}, whereas at 30 Mbps, it is 1.5×10^{-4}. The relative reduction in BER is possibly due to the characteristics of the BERT, as at low-speeds the output voltage magnitude has significant variance which gets better as the data rate increases, as can be seen below in Fig. 7.3.

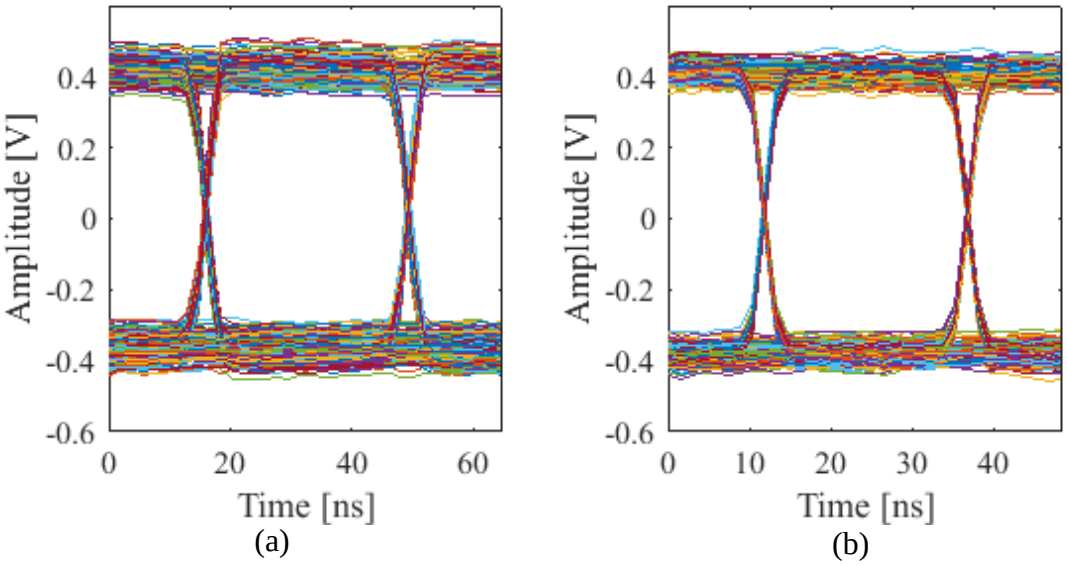

Fig. 7.3: Eye diagram formed from BERT output data stream at (a) 20 Mbps and (b) 30 Mbps.

For the OLEDs on glass, by 40 Mbps (Fig. 7.4(a), below), the eye is closed, and at 80 Mbps (Fig. 7.4(b)) the shape of the eye is almost completely obscured.

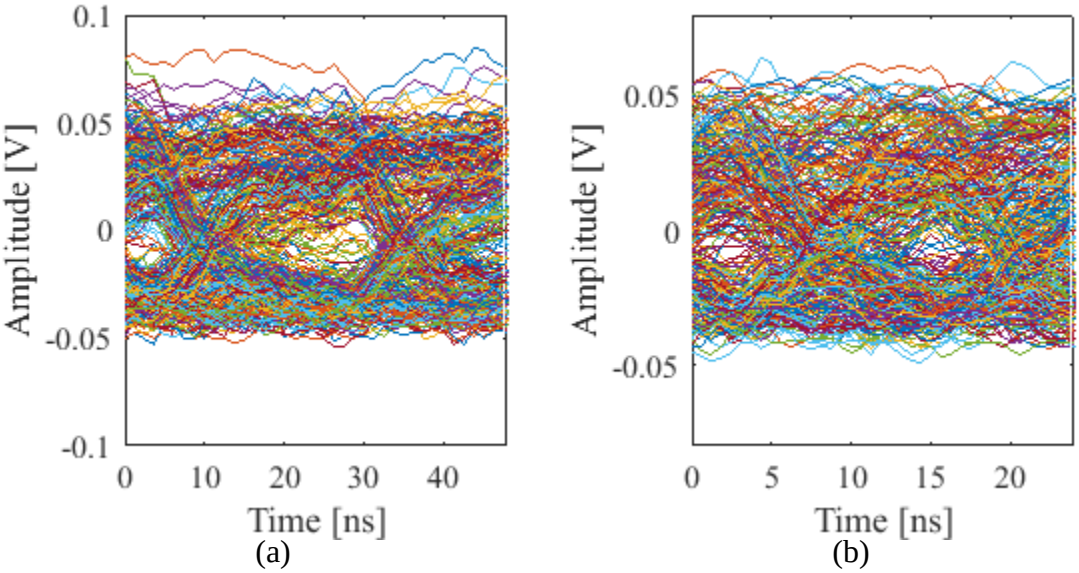

Fig. 7.4: Received eye diagram at (a) 40 Mbps and (b) 80 Mbps for 0.12 mm^2 OLEDs on glass.

Replacing the devices on glass with devices on silicon allows the DC bias of the OLED to be set much higher, and as a result, the eye diagrams of the glass devices (Fig. 7.2 & Fig. 7.4) is significantly improved in the following plots.

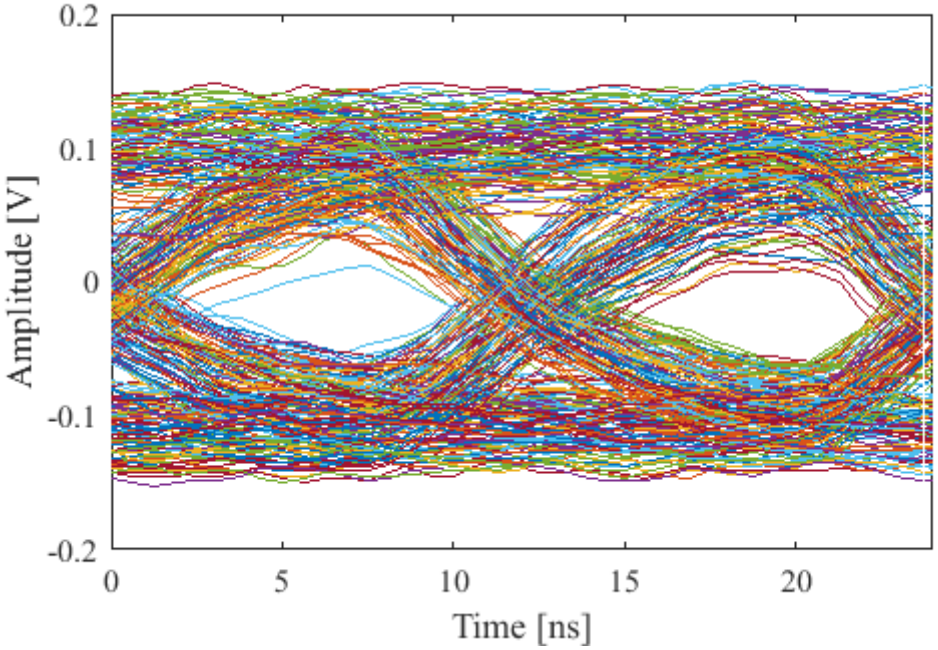

Fig. 7.5: Received eye diagram at 80 Mbps for 0.12 mm^2 OLEDs on silicon.

However, the advantage of devices on silicon is that they are stable under DC operation, and display less noise. The 0.12 mm^2 OLEDs with a 20 nm EML on silicon were able to transmit data with an open eye at up to 120 Mbps at a DC bias current of 6 mA (Fig. 7.5 and Fig. 7.6).

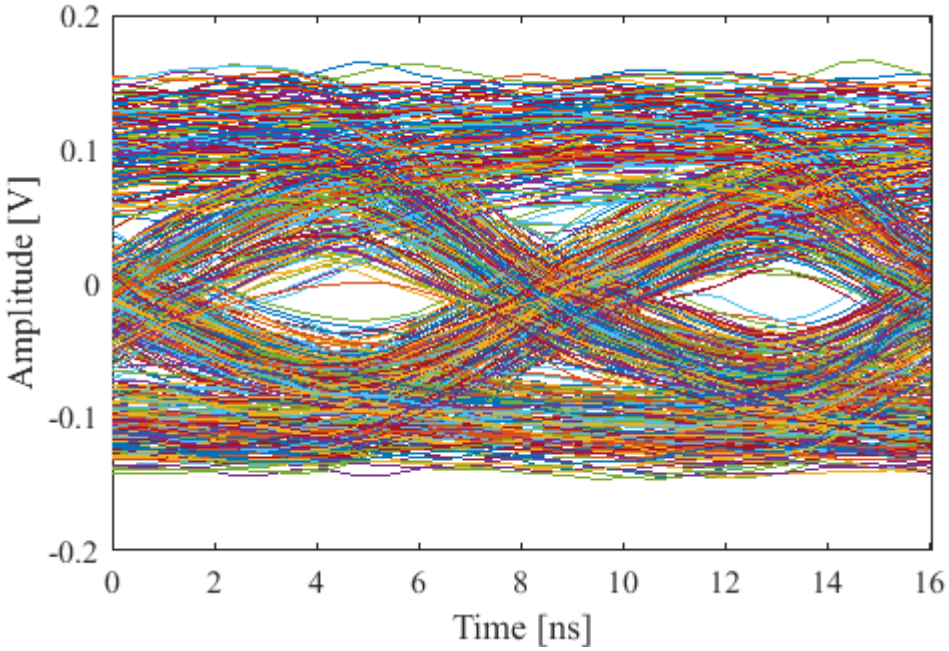

Fig. 7.6: Received eye diagram at 120 Mbps for 0.12 mm^2 OLEDs on silicon.

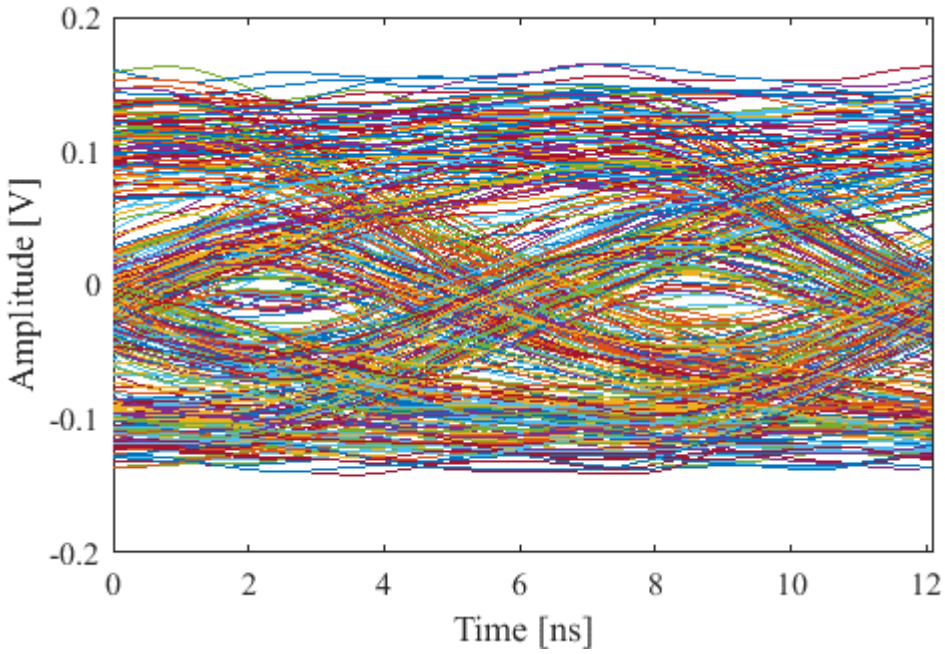

Fig. 7.7: Received eye diagram at 160 Mbps for 0.12 mm^2 OLEDs on silicon.

By 160 Mbps, although the eye is closed at this data rate, this eye can be opened with equalisation indicating that these OLEDs can achieve even higher than 160 Mbps. This is in contrast to the OLEDs on glass substrates, where at 80 Mbps the eye was completely obscured.

The BER of these devices is calculated using the methodology detailed in §7.2, and the results of this are shown below.

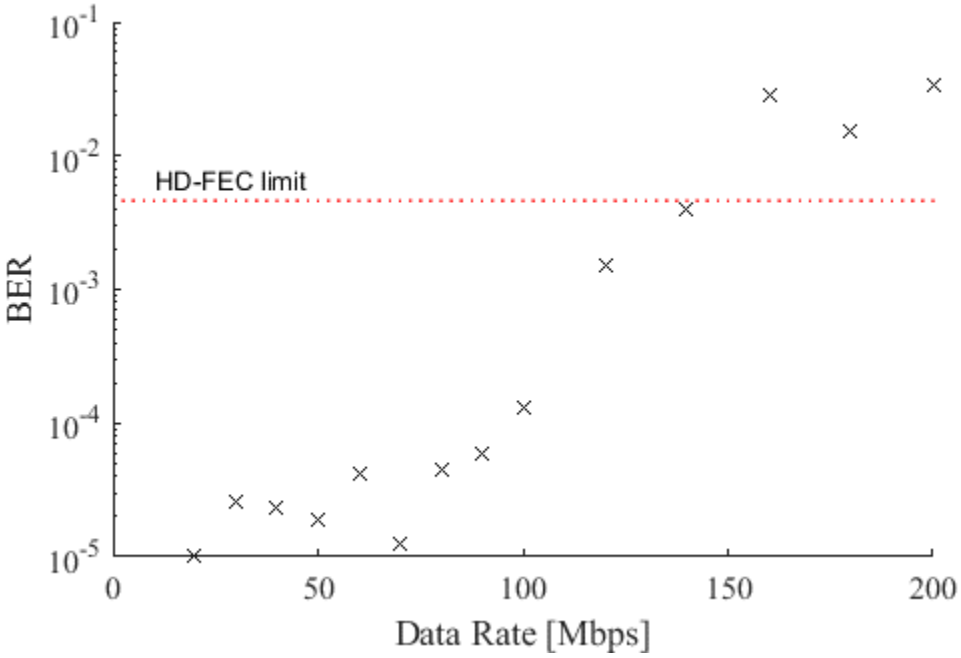

Fig. 7.8: BER against data rate for the 0.12 mm^2 OLEDs on silicon.

It can be seen from Fig. 7.8 that the OLEDs on silicon can achieve 140 Mbps at a bit error rate of less than 4.6×10^{-3}, which corresponds to the hard decision forward error correction limit at a 6.7% overhead [247]. This would mean a record net data rate of 130 Mbps for transmission using OLEDs. Although soft-decision forward error correction could enable even higher data rates, such detection is more complicated to implement and is therefore unlikely to be used in low-cost data links, where simplicity is paramount.

It can be seen in the eye-diagrams that there is significant noise and jitter for all OLEDs, which is clearly limiting the overall data rate. Measurement of the rms jitter (Fig. 7.9) suggests that it is fairly consistent with data rate above around 40 Mbps, which is the point at which the output voltage from the BERT becomes more consistent (Fig. 7.10).

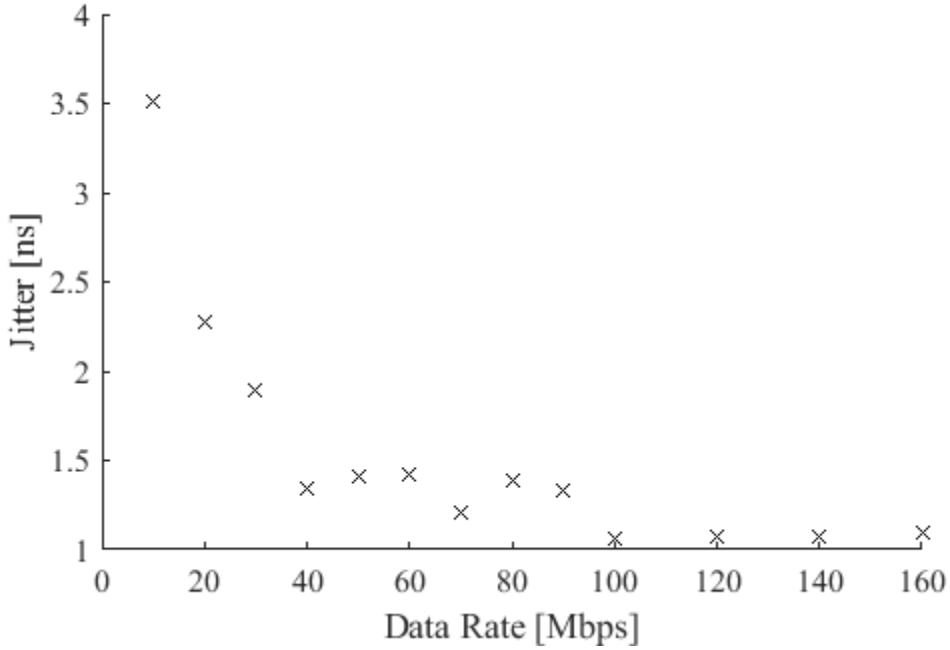

Fig. 7.9: Measurement of the rms jitter with different data rates.

It is suggested that the variance of the output voltage from the BERT may have a significant contribution towards the noisy reduction in the size of the open eye. With an improved input signal quality, it may be possible to get even better data rates.

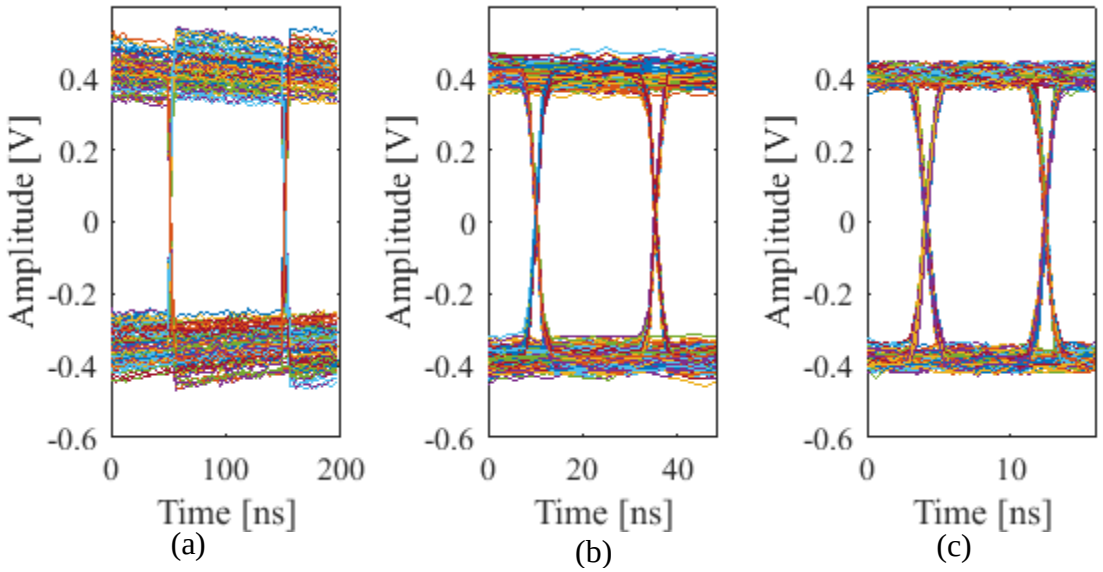

Fig. 7.10: Eye diagram formed from BERT output data stream at (a) 10 Mbps and (b) 40 Mbps and (c) 120 Mbps.

Other methods of potentially increasing the data transmission rate include pulse shaping, use of advanced modulation formats, and equalisation. Use of artificial neural network equalisation techniques have resulted in factors of improvement of over 55 (20 Mbps from an OLED of 350 kHz bandwidth) [87]. However, such advanced equalisation techniques come with power and computational penalty. Simpler and more common types of equalisers are the feed-forward (Fig. 7.11) and decision-feedback (Fig. 7.12) equalisers. As these OLEDs are significantly limited by inter-symbol interference (ISI), such equalisers can help to extract the original signal in systems such as this.

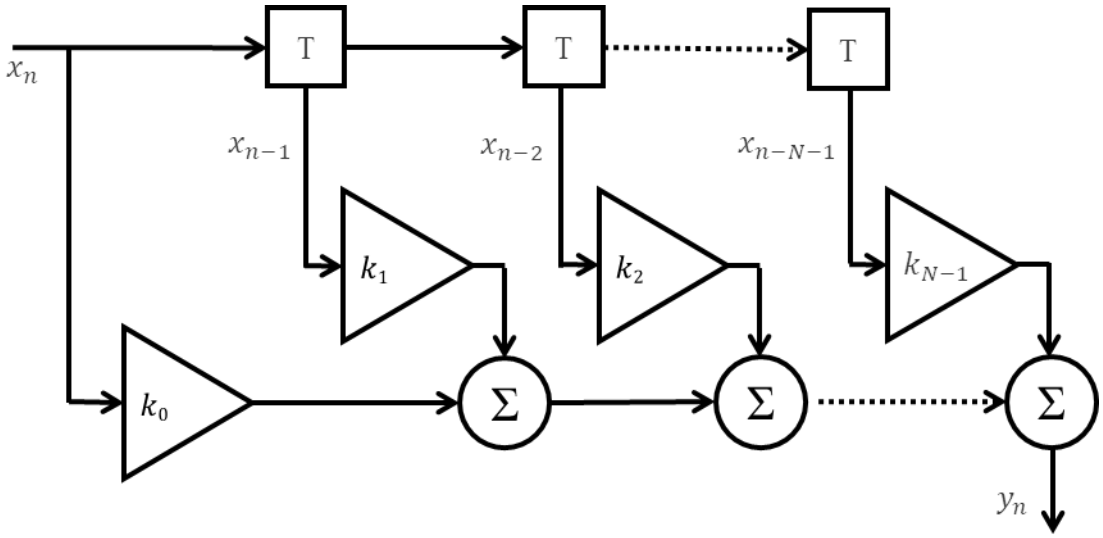

Fig. 7.11: Schematic of a T-spaced N-tap feedforward equaliser.

With feedforward equalisation (FFE), as shown in Fig. 7.11, the output of the equaliser is a weighted sum of previous symbols. Mathematically, this is expressed as:

$$y[n] = \sum_{i=0}^{N-1} k_i x[n-i] \tag{7.8}$$

Unfortunately, the weighted summing means that the FFE acts to enhance noise.

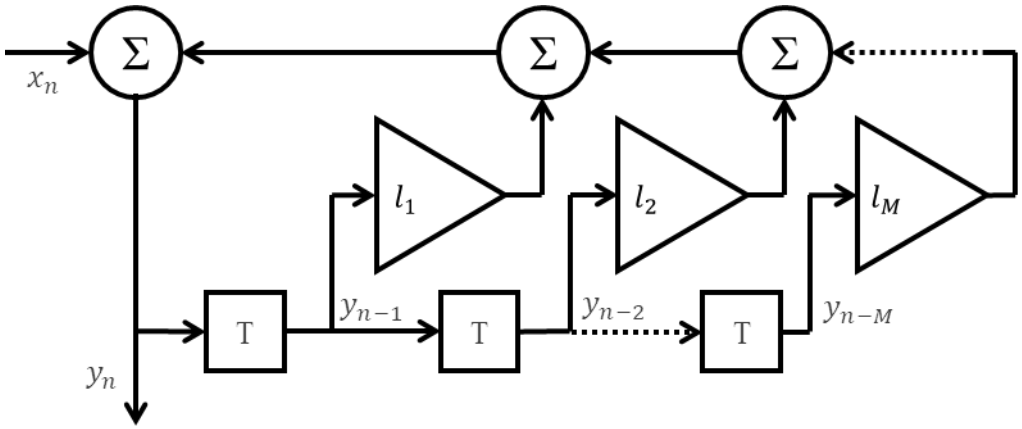

Fig. 7.12: Schematic of a T-spaced M-tap decision feedback equaliser.

However, the decision feedback equaliser (DFE), as shown in Fig. 7.12, does not act to introduce noise. It is based upon a weighted sum of previously-estimated outputs. Mathematically, this is:

$$y[n] = x_n + \sum_{i=1}^{M} l_i y[n-i] \tag{7.9}$$

Indeed, by implementing a very simple 3-tap feedforward equaliser (FFE) using post-processing in Matlab, it has been possible to open the previously-closed eye diagrams, as shown in Fig. 7.13 & Fig. 7.14.

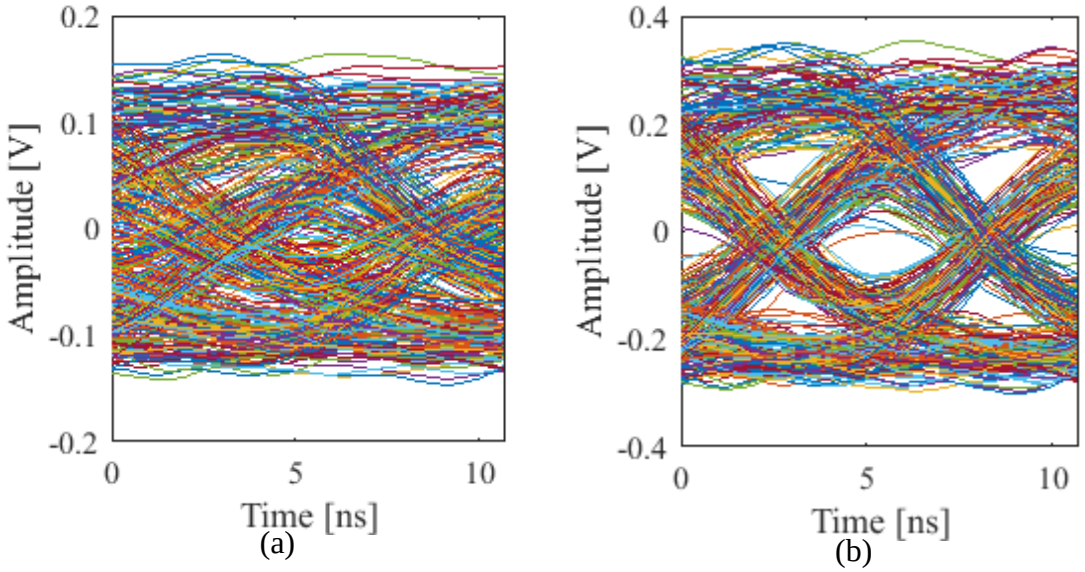

Fig. 7.13: (a) Pre-equalised eye diagram at 180 Mbps, (b) Post-equalisation using an offline 3-tap FFE equaliser.

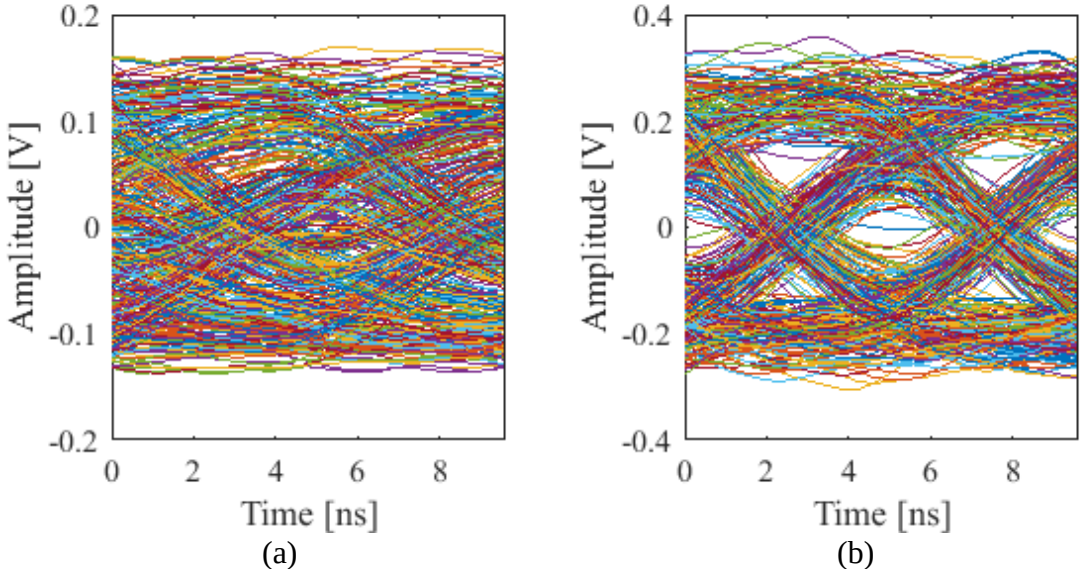

Fig. 7.14: (a) Pre-equalised eye-diagram at 200 Mbps, (b) Post-equalisation using an offline 3-tap FFE equaliser.

The equaliser is an adaptive 3-tap T-spaced FFE implemented using the least-mean-squares algorithm, due to its simplicity and stability over a DFE. As can be seen from Fig. 7.14, the equaliser is able to open the eye at 200 Mbps such that the slicer detects no errors in the transmitted symbols from the 1000 symbols passed through the equaliser. It is likely that with more complex equalisation techniques and algorithms that it will be possible to achieve much higher data rates with OLEDs, at the expense of system and computational complexity (which may not be desirable in a low-cost link). In any case, it is clear that the rate limit of data transmission with these OLEDs has not yet been reached, and many options exist to further optimise the speed of this optical link.

7.4 Conclusions

Although the 0.12 mm^2 OLEDs with a 30 nm EML on glass substrates are measured as having a higher small signal bandwidth than the OLEDs on silicon, it is found that the bias currents required for these high bandwidths do not allow for stable large-signal operation in the presence of self-heating. As a result of the heating and the reduced input signal power, the received signal is very noisy, further reducing the equalisation-free data transmission rate. For application in an integrated low-cost optical link, thermal effects will need to be carefully considered, in particular as any polymer waveguides will likely have poor thermal properties, although this

may be mitigated by appropriate choice of substrates, with the polymer waveguide advantageously providing the necessary encapsulation.

Nevertheless, the work in this chapter has demonstrated record non-equalised net data transmission at a very reasonable 130 Mbps (and equalised transmission at 200 Mbps) by the 0.12 mm^2 OLEDs on silicon along a short 1.5 m POF link. In context, the fastest previous reported OLED has been modulation at a rate of 100 MHz for an OLED with an area more than 10 times smaller at 0.01 mm^2 [107]. This is a promising result, as with further optimisation of the OLED devices, along with implementation of advanced modulation formats and equalisation techniques, it is likely that such OLEDs may in the future be able to achieve quite significant data rates. Reported improvements in the literature have shown an improvement by a factor of over 55 (20 Mbps from an OLED of 350 kHz bandwidth) by using such techniques [87]. Furthermore, integration of these OLEDs for on-board applications would involve much shorter distance transmission, and, in the case of ideal manufacture and encapsulation within a polymer waveguide, would capture more of the luminescent power than externally butt-coupled OLEDs. In any case, it is possible that the response times of an organic photodetector will prove a greater limiting factor than the OLED, and such an integration will prove an interesting challenge.

8 CONCLUSIONS & OUTLOOK

8.1 Conclusions

While OLEDs are a relatively mature technology for use in displays, the consideration of such devices for communications is a more recent development, and as such, there has been little work done in characterising the modulation performance of OLEDs. This thesis presents novel work to address this knowledge gap, and, further, looks at optimising OLEDs for low-cost communications links.

Experimental studies are used to inform a detailed physical simulation-model that reasonably describes the OLED behaviour of this 5-layer OLED stack for the first time. From DC and small-signal measurements, a holistic overview of the device performance and a novel method of evaluating bandwidth performance is reported.

Initial DC measurements of the OLEDs demonstrate strong blue light emission at 495 nm, with turn-on at 2.8 V. Spectral measurements indicate three spectral peaks in the OLED, two of which correspond to the TBPe dopant, and a third longer-wavelength peak that is postulated to arise from an exciplex/charge transfer exciton. In order to better understand the function and behaviour of different layers, partial-stack OLEDs were manufactured, where one layer was missing relative to the complete OLED devices. Exclusion of the α-NPD hole transport layer indicates a higher proportion of this exciplex emission, whereas exclusion of the BAlq hole blocking layer suppresses this exciplex emission. These results suggest that the exciplex is related to electron accumulation in the emissive layer.

Information from these partial-stack OLED measurements and from the literature was used to inform a 5-layer OLED simulation model, which reasonably replicates the measurements obtained. This detailed physical simulation is a drift-diffusion model that solves Poisson's equation, along with the carrier continuity equations. The simulation incorporates the major features of organic materials, such as the Gaussian density of states, Fermi level pinning of doped contact layers, inclusion of excitons in carrier-continuity equations, Langevin recombination and the empirical Poole-Frenkel mobility behaviour, and as such presents the first full-stack OLED model incorporating the materials used in this device.

It is further shown that the current response of the OLED is strongly dependent upon the device substrate. Further investigation indicated that the glass substrates cause significant self-heating, with 9 mm^2 OLEDs on glass substrates measured to have a temperature increase of 18.5°C at 40 mA, whereas the same OLED current density in devices on silicon showed only a 5.6°C increase. This higher operating temperature results in higher mobility and better thermal injection of carriers, resulting in a higher current density for the OLEDs on glass relative to those on silicon. This is further confirmed by measurements of the OLEDs on glass using a heat-sink, where the current-voltage performance is lower relative to the same devices in an uncooled state. This is believed to be due to the thermally-activated hopping mobility exhibited by organic semiconductor materials: put simply, the mobility is reduced as the temperature decreases.

As these OLEDs are designed for use in low-cost communications, evaluation of their small signal response provides an indication of their performance in an optical link. Accordingly, the small signal S_{11} and optical S_{21} response of the OLEDs are taken using a vector network analyser. The S_{21} response allowed the electrical 3 dB bandwidth of the OLEDs to be evaluated, and it was found that the fastest OLEDs were 0.12 mm^2 devices with a 30 nm EML on glass substrates demonstrating a small signal bandwidth of 42 MHz. This is in contrast to 0.12 mm^2 OLEDs with a 20 nm EML on glass substrates exhibiting a 25 MHz bandwidth at the same bias current. Furthermore, upon cooling the OLEDs to 16°C, this bandwidth dropped to just 10 MHz. Interestingly, the OLEDs on silicon exhibit a less noisy and higher-bandwidth S_{21} response than OLEDs on glass for the same bias current.

In order to form a better understanding of the optical performance, an electrical model is fit to the optical performance of the OLEDs. While many OLED studies have used admittance spectroscopy to study the impedance of the OLEDs and thereby deduce an understanding of the

internal electronic properties of the OLED, to the best of my knowledge, this is the first time such a model has been developed in order to understand the small-signal optical frequency response of the OLED. It is found that, although the electrical impedance response is relatively complex, the optical response is well described by a simple RC model. For the first time in organic LEDs, by postulating an emissive resistance existing as a proportion of the total measured small signal resistance (a 'Langevin resistance'), a good fit to the S_{21} optical response was found, thus providing correlation between the measured optical bandwidth of the OLED and the measured impedance. Limitations of this approach were also demonstrated; this model is only valid providing that the exciton lifetime of the OLED is shorter than the electrical response of the OLED. However, this analysis was shown to provide a robust mechanism for estimating the OLED bandwidth across different devices.

Furthermore, corroboration of this approach was found through extension of the DC simulation to small signal analysis. The simulation was shown to provide similar impedance curves to those measured in experiment, providing further validation of both the simulation and the electrical modelling. Extracting RC parameters from this simulation, it was found that once again by using a constant proportion of the simulated total device small signal resistance (the aforementioned 'Langevin resistance'), it is possible to make a good prediction of the OLED optical bandwidth response across different devices at different bias currents. Indeed, it was found for the first time that by using a constant proportion of the simulated resistance, the simulation was able to predict the bandwidth performance at different bias currents.

From this, it is possible to therefore suggested to extend the simulation to device forecasting and optimisation. Based upon the simulated small signal response, suggestions are made as to optimal layer thicknesses in order to improve the device bandwidth. It is believed that this is the first time that this type of experimentally-informed simulation-driven optimisation for bandwidth response has been undertaken for OLED devices. As better parametrisation of OLED materials is undertaken, the ability to optimise device configurations through simulation, rather than through expensive and time-consuming iterative manufacturing, will only become more powerful.

Despite the higher small signal bandwidth measured for the devices on glass substrates, it was found that they cannot be biased at a high operating point and be used for data transmission without thermal instability; therefore, the usable signal power and achievable data rates are much lower than devices on a thermally conductive substrate such as silicon. However, by using

the OLEDs on silicon substrates, a world record 130 Mbps unequalised end-to-end data transmission using these OLEDs was demonstrated using a short 1.5m POF link. With equalisation, transmission at 200 Mbps was achieved using a very simple adaptive 3-tap FFE filter. These results are very promising for the future of low-cost organic optical links.

8.2 Outlook

In the short term, there are further improvements that can be made to the analysis presented in this thesis. With regards to the physical modelling, there are further measurements that would be useful to feed back and further validate the simulation. In the field of inorganic semiconductors, material parameters are relatively well studied and show good replicability. Unfortunately, the reporting of organic semiconductor parameters can vary significantly from group to group, depending upon multiple factors, from the experimental technique used, to the mobility model assumed in the experiment. Even parameters measured in similar manners by different groups, such as HOMO and LUMO levels can show significant variation between reported values. It would be greatly beneficial to the validation of the detailed simulation model presented in this thesis to be able to directly measure such parameters as HOMO-LUMO levels and material mobilities (at a variety of thicknesses). In particular, further measurement of devices fabricated on thermally-conductive substrates would help to remove thermal effects as an experimental variable. Such model validation would significantly improve the reliability of the modelling and technique used here.

Furthermore, experimental validation of the device optimisation presented in Chapter 6 would be very useful; in particular, additional experimentally-validated data points would allow simulation techniques to further grow as a low-cost prototyping methodology. Furthermore, experimental validation of the suggested relationship between emissive resistance and Langevin recombination would help provide further reinforcement of the methodology presented here.

Moreover, the world-record link tests presented in Chapter 7 implemented a very simple intensity-modulated direct detection scheme. However, it would be interesting to investigate more advanced modulation formats in order to improve the overall data rate. Schemes such as quadrature phase-shift keying (QPSK), may offer enhanced bit rate at the expense of bit-error rate. However, since the signal power from small OLEDs is relatively low, the link as it exists

may not be conducive to more complex multi-level schemes than this, as this would worsen the signal to noise ratio and thus the bit-error rate.

Indeed, there is much work still to be done in the field of low-cost organic communications. One of the significant disadvantages of organic semiconductors is their relatively low lifetime and reliability. In this regard, there is still work to be done with regards to evaluating OLED breakdown, and optimisation for stable operation and device lifetime.

In the medium term, the ability to deposit organic semiconductor materials directly onto different substrates means that there are still engineering challenges to overcome in the integration of OLEDs and OPDs in optical links. Further investigation into incorporating such OLEDs directly into waveguides will certainly involve manufacturing challenges. Indeed, inkjet printing of OLEDs is one mechanism that may be further explored for such optical links, as the ability to directly deposit the devices onto substrates at low-temperature is quite advantageous.

Moreover, if similar high-speed study of organic photodiodes is undertaken, with relevant device optimisation, it may be possible to integrate these devices in an all-organic low-cost optical link. The ability to manufacture such devices would facilitate a range of new applications, such as in low-cost sensors, and optical backplanes for moderate-speed electronics. Indeed, future flexible electronics may benefit from using organic optical interconnects, as opposed to electronic wiring. Furthermore, in the absence of high-speed optical sources, the ability to integrate high-speed polymer modulators with polymer waveguides will provide a speed advantage for such applications at relatively low-cost.

In the long-term, the future is bright for low-cost OLED communications links. As a technology still in relative infancy, there is much still to be done to unlock its full potential. With a vast potential library of organic materials yet to be explored and novel organic semiconductor materials continuously being discovered, further developments are undoubtedly in store for the future.

REFERENCES

[1] ‘Ericsson Mobility Report June 2018’, Jun. 2018.

[2] A. Andrae, T. Edler, A. S. G. Andrae, and T. Edler, ‘On Global Electricity Usage of Communication Technology: Trends to 2030’, *Challenges*, vol. 6, no. 1, pp. 117–157, Apr. 2015.

[3] D. A. B. Miller, ‘Device Requirements for Optical Interconnects to Silicon Chips’, *Proc. IEEE*, vol. 97, no. 7, pp. 1166–1185, Jul. 2009.

[4] ‘2018 Solid-State Lighting R&D Opportunities’.

[5] R. H. Partridge, ‘Electroluminescence from polyvinylcarbazole films: 1. Carbazole cations’, *Polymer*, vol. 24, no. 6, pp. 733–738, Jun. 1983.

[6] C. W. Tang and S. A. VanSlyke, ‘Organic electroluminescent diodes’, *Appl. Phys. Lett.*, vol. 51, no. 12, pp. 913–915, Sep. 1987.

[7] M. Pope, H. P. Kallmann, and P. Magnante, ‘Electroluminescence in Organic Crystals’, *J. Chem. Phys.*, vol. 38, no. 8, pp. 2042–2043, Apr. 1963.

[8] W. Helfrich and W. G. Schneider, ‘Recombination Radiation in Anthracene Crystals’, *Phys. Rev. Lett.*, vol. 14, no. 7, pp. 229–231, Feb. 1965.

[9] D. F. Williams and M. Schadt, ‘A simple organic electroluminescent diode’, *Proc. IEEE*, vol. 58, no. 3, pp. 476–476, Mar. 1970.

[10] P. S. Vincett, W. A. Barlow, R. A. Hann, and G. G. Roberts, ‘Electrical conduction and low voltage blue electroluminescence in vacuum-deposited organic films’, *Thin Solid Films*, vol. 94, no. 2, pp. 171–183, Aug. 1982.

[11] J. H. Burroughes *et al.*, ‘Light-emitting diodes based on conjugated polymers’, *Nature*, vol. 347, no. 6293, pp. 539–541, Oct. 1990.

[12] R. Mertens, *The OLED Handbook (2018 Edition)*. 2018.

[13] A. H. Gnauck, R. W. Tkach, A. R. Chraplyvy, and T. Li, ‘High-Capacity Optical Transmission Systems’, *J. Light. Technol.*, vol. 26, no. 9, pp. 1032–1045, May 2008.

[14] M. A. Taubenblatt, ‘Optical Interconnects for High-Performance Computing’, *J. Light. Technol.*, vol. 30, no. 4, pp. 448–457, Feb. 2012.

[15] M. R. Feldman, S. C. Esener, C. C. Guest, and S. H. Lee, ‘Comparison between optical and electrical interconnects based on power and speed considerations’, *Appl. Opt.*, vol. 27, no. 9, pp. 1742–1751, May 1988.

[16] R. T. Chen and C. Choi, *Optical Interconnects*. Morgan & Claypool Publishers, 2007.

[17] M. Lipson, ‘Guiding, modulating, and emitting light on Silicon-challenges and opportunities’, *J. Light. Technol.*, vol. 23, no. 12, pp. 4222–4238, Dec. 2005.

[18] M. Asghari and A. V. Krishnamoorthy, ‘Silicon photonics: Energy-efficient communication’, *Nat. Photonics*, vol. 5, no. 5, pp. 268–270, May 2011.

[19] A. Shacham, K. Bergman, and L. P. Carloni, ‘On the Design of a Photonic Network-on-Chip’, in *First International Symposium on Networks-on-Chip, 2007. NOCS 2007*, 2007, pp. 53–64.

[20] L. Thylen *et al.*, ‘Complementing or replacing silicon and III-Vs: The role of plasmonics and novel materials in future integrated photonics for telecom and interconnects’, in *2011 13th International Conference on Transparent Optical Networks (ICTON)*, 2011, pp. 1–4.

[21] J. A. Dionne, L. A. Sweatlock, M. T. Sheldon, A. P. Alivisatos, and H. A. Atwater, ‘Silicon-Based Plasmonics for On-Chip Photonics’, *IEEE J. Sel. Top. Quantum Electron.*, vol. 16, no. 1, pp. 295–306, Jan. 2010.

[22] K. Vyrsokinos *et al.*, ‘Low energy routing platforms for optical interconnects using active Plasmonics integrated with Silicon Photonics’, in *2012 14th International Conference on Transparent Optical Networks (ICTON)*, 2012, pp. 1–4.

[23] K. Wang, A. Nirmalathas, C. Lim, E. Skafidas, and K. Alameh, ‘High-speed free-space based reconfigurable card-to-card optical interconnects with broadcast capability’, *Opt. Express*, vol. 21, no. 13, p. 15395, Jul. 2013.

[24] A. Walker *et al.*, ‘Design and construction of an optoelectronic crossbar switch containing a terabit per second free-space optical interconnect’, *IEEE J. Sel. Top. Quantum Electron.*, vol. 5, no. 2, pp. 236–249, Mar. 1999.

[25] B. Ciftcioglu *et al.*, ‘A 3-D Integrated Intrachip Free-Space Optical Interconnect for Many-Core Chips’, *IEEE Photonics Technol. Lett.*, vol. 23, no. 3, pp. 164–166, Feb. 2011.

[26] M. C. Larson *et al.*, ‘Multiwavelength VCSEL transmitter for WDM parallel optical fiber interconnects’, in *LEOS ’99. IEEE Lasers and Electro-Optics Society 1999 12th Annual Meeting*, 1999, vol. 2, pp. 764–765 vol.2.

[27] J. Matsui *et al.*, ‘High bandwidth optical interconnection for densely integrated server’, in *Optical Fiber Communication Conference and Exposition and the National Fiber Optic Engineers Conference (OFC/NFOEC), 2013*, 2013, pp. 1–3.

[28] R. Pitwon, A. Worrall, P. Stevens, A. Miller, K. Wang, and K. Schmidtke, ‘Demonstration of fully enabled data center subsystem with embedded optical interconnect’, 2014, p. 899110.

[29] V. Francois and F. Laramee, ‘Multicore Fiber Optimization for Application to Chip-to-Chip Optical Interconnects’, *J. Light. Technol.*, vol. 31, no. 24, pp. 4022–4028, Dec. 2013.

[30] T. Hino *et al.*, ‘A 10 Gbps x 12 channel pluggable optical transceiver for high-speed interconnections’, in *Electronic Components and Technology Conference, 2008. ECTC 2008. 58th*, 2008, pp. 1838–1843.

[31] N. Bamiedakis, A. Hashim, J. Beals, R. V. Penty, and I. White, ‘Low-Cost PCB-Integrated 10-Gb/s Optical Transceiver Built With a Novel Integration Method’, *IEEE Trans. Compon. Packag. Manuf. Technol.*, vol. 3, no. 4, pp. 592–600, Apr. 2013.

[32] X. Wang, W. Jiang, L. Wang, H. Bi, and R. T. Chen, ‘Fully Embedded Board-Level Optical Interconnects From Waveguide Fabrication to Device Integration’, *J. Light. Technol.*, vol. 26, no. 2, pp. 243–250, Jan. 2008.

[33] ‘MOST Cooperation: Introduction’. [Online]. Available: https://www.mostcooperation.com/cooperation/introduction/. [Accessed: 20-Sep-2018].

[34] R. Danilak, ‘Why Energy Is A Big And Rapidly Growing Problem For Data Centers’, *Forbes*. [Online]. Available:

https://www.forbes.com/sites/forbestechcouncil/2017/12/15/why-energy-is-a-big-and-rapidly-growing-problem-for-data-centers/. [Accessed: 25-Sep-2018].

[35] J. Beals *et al.*, 'A terabit capacity passive polymer optical backplane based on a novel meshed waveguide architecture', *Appl. Phys. A*, vol. 95, no. 4, pp. 983–988, Jun. 2009.

[36] D. Thomson *et al.*, 'Roadmap on silicon photonics', *J. Opt.*, vol. 18, no. 7, p. 073003, 2016.

[37] J. Leuthold *et al.*, 'Plasmonic Communications: Light on a Wire', *Opt. Photonics News*, vol. 24, no. 5, pp. 28–35, May 2013.

[38] N. Bamiedakis *et al.*, '40 Gb/s Data Transmission Over a 1-m-Long Multimode Polymer Spiral Waveguide for Board-Level Optical Interconnects', *J. Light. Technol.*, vol. 33, no. 4, pp. 882–888, Feb. 2015.

[39] N. Bamiedakis, A. Hashim, R. V. Penty, and I. H. White, 'A 40 Gb/s Optical Bus for Optical Backplane Interconnections', *J. Light. Technol.*, vol. 32, no. 8, pp. 1526–1537, Apr. 2014.

[40] F. E. Doany *et al.*, '160 Gb/s Bidirectional Polymer-Waveguide Board-Level Optical Interconnects Using CMOS-Based Transceivers', *IEEE Trans. Adv. Packag.*, vol. 32, no. 2, pp. 345–359, May 2009.

[41] R. Dangel *et al.*, 'Development of a low-cost low-loss polymer waveguide technology for parallel optical interconnect applications', in *Biophotonics/Optical Interconnects and VLSI Photonics/WBM Microcavities, 2004 Digest of the LEOS Summer Topical Meetings*, 2004, pp. 2 pp.-.

[42] F. E. Doany *et al.*, 'Terabit/sec-class board-level optical interconnects through polymer waveguides using 24-channel bidirectional transceiver modules', in *Electronic Components and Technology Conference (ECTC), 2011 IEEE 61st*, 2011, pp. 790–797.

[43] K. Schmidtke *et al.*, '960 Gb/s Optical Backplane Ecosystem Using Embedded Polymer Waveguides and Demonstration in a 12G SAS Storage Array', *J. Light. Technol.*, vol. 31, no. 24, pp. 3970–3975, Dec. 2013.

[44] N. Chujo, R. Nomura, T. Yazaki, T. Takai, and N. Matsushima, '7.2-Tb/s compact optical backplane using ribbon fiber sheet and high-density connector', in *2014 IEEE Optical Interconnects Conference*, 2014, pp. 93–94.

[45] R. Dangel *et al.*, ‘Development of Versatile Polymer Waveguide Flex Technology for Use in Optical Interconnects’, *J. Light. Technol.*, vol. 31, no. 24, pp. 3915–3926, Dec. 2013.

[46] K. Yamada *et al.*, ‘High-performance silicon photonics technology for telecommunications applications’, *Sci. Technol. Adv. Mater.*, vol. 15, no. 2, p. 024603, 2014.

[47] P. Dong *et al.*, ‘Low loss shallow-ridge silicon waveguides’, *Opt. Express*, vol. 18, no. 14, pp. 14474–14479, Jul. 2010.

[48] J. Cardenas, C. B. Poitras, J. T. Robinson, K. Preston, L. Chen, and M. Lipson, ‘Low loss etchless silicon photonic waveguides’, *Opt. Express*, vol. 17, no. 6, pp. 4752–4757, Mar. 2009.

[49] G. Li *et al.*, ‘Ring Resonator Modulators in Silicon for Interchip Photonic Links’, *IEEE J. Sel. Top. Quantum Electron.*, vol. 19, no. 6, pp. 95–113, Nov. 2013.

[50] W. Bogaerts *et al.*, ‘Silicon microring resonators’, *Laser Photonics Rev.*, vol. 6, no. 1, pp. 47–73, Jan. 2012.

[51] F. Xia, M. Rooks, L. Sekaric, and Y. Vlasov, ‘Ultra-compact high order ring resonator filters using submicron silicon photonic wires for on-chip optical interconnects’, *Opt. Express*, vol. 15, no. 19, pp. 11934–11941, Sep. 2007.

[52] L.-W. Luo, G. S. Wiederhecker, J. Cardenas, C. Poitras, and M. Lipson, ‘High quality factor etchless silicon photonic ring resonators’, *Opt. Express*, vol. 19, no. 7, pp. 6284–6289, Mar. 2011.

[53] S. Cheung, T. Su, K. Okamoto, and S. J. B. Yoo, ‘Ultra-Compact Silicon Photonic 512 × 512 25 GHz Arrayed Waveguide Grating Router’, *IEEE J. Sel. Top. Quantum Electron.*, vol. 20, no. 4, pp. 310–316, Jul. 2014.

[54] M. Gehl, D. Trotter, A. Starbuck, A. Pomerene, A. L. Lentine, and C. DeRose, ‘Active phase correction of high resolution silicon photonic arrayed waveguide gratings’, *Opt. Express*, vol. 25, no. 6, pp. 6320–6334, Mar. 2017.

[55] T. Fukazawa, F. Ohno, and T. Baba, ‘Very Compact Arrayed-Waveguide-Grating Demultiplexer Using Si Photonic Wire Waveguides’, *Jpn. J. Appl. Phys.*, vol. 43, no. No. 5B, pp. L673–L675, Apr. 2004.

[56] M. Uenuma and T. Motooka, ‘Temperature-independent silicon waveguide optical filter’, *Opt. Lett.*, vol. 34, no. 5, pp. 599–601, Mar. 2009.

[57] B. Guha, A. Gondarenko, and M. Lipson, 'Minimizing temperature sensitivity of silicon Mach-Zehnder interferometers', *Opt. Express*, vol. 18, no. 3, pp. 1879–1887, Feb. 2010.

[58] S. Dwivedi, H. D'heer, and W. Bogaerts, 'A Compact All-Silicon Temperature Insensitive Filter for WDM and Bio-Sensing Applications', *IEEE Photonics Technol. Lett.*, vol. 25, no. 22, pp. 2167–2170, Nov. 2013.

[59] U. Jeong, D. Han, D. H. Lee, K. Lee, J. Kim, and J. H. Park, 'A broadband silicon electro-absorption modulator (EAM) using a Schottky diode', in *Integrated Optics: Devices, Materials, and Technologies XVIII*, 2014, vol. 8988, p. 89881M.

[60] J. Verbist *et al.*, 'Real-time 100 Gb/s NRZ-OOK transmission with a silicon photonics GeSi electro-absorption modulator', in *2017 IEEE Optical Interconnects Conference (OI)*, 2017, pp. 29–30.

[61] P. Verheyen *et al.*, 'Co-integration of Ge detectors and Si modulators in an advanced Si photonics platform', in *Silicon Photonics and Photonic Integrated Circuits III*, 2012, vol. 8431, p. 843114.

[62] Y. Ishikawa, J. Osaka, and K. Wada, 'Germanium photodetectors in silicon photonics', in *2009 IEEE LEOS Annual Meeting Conference Proceedings*, 2009, pp. 367–368.

[63] Z. Wang *et al.*, 'Novel Light Source Integration Approaches for Silicon Photonics', *Laser Photonics Rev.*, vol. 11, no. 4, p. 1700063, Jul. 2017.

[64] A. Moscoso-Mártir *et al.*, 'Hybrid silicon photonics flip-chip laser integration with vertical self-alignment', in *2017 Conference on Lasers and Electro-Optics Pacific Rim (CLEO-PR)*, 2017, pp. 1–4.

[65] T. Shimizu *et al.*, 'Multichannel and high-density hybrid integrated light source with a laser diode array on a silicon optical waveguide platform for interchip optical interconnection', *Photonics Res.*, vol. 2, no. 3, p. A19, Jun. 2014.

[66] B. Song *et al.*, '3D integrated hybrid silicon laser', in *2015 European Conference on Optical Communication (ECOC)*, 2015, pp. 1–3.

[67] M. R. Billah *et al.*, 'Hybrid integration of silicon photonics circuits and InP lasers by photonic wire bonding', *Optica*, vol. 5, no. 7, pp. 876–883, Jul. 2018.

[68] N. Lindenmann *et al.*, 'Photonic wire bonding: a novel concept for chip-scale interconnects', *Opt. Express*, vol. 20, no. 16, pp. 17667–17677, Jul. 2012.

[69] A. W. Fang, E. Lively, Y.-H. Kuo, D. Liang, and J. E. Bowers, 'A distributed feedback silicon evanescent laser', *Opt. Express*, vol. 16, no. 7, pp. 4413–4419, Mar. 2008.

[70] H. Park, A. W. Fang, S. Kodama, and J. E. Bowers, 'Hybrid silicon evanescent laser fabricated with a silicon waveguide and III-V offset quantum wells', *Opt. Express*, vol. 13, no. 23, pp. 9460–9464, Nov. 2005.

[71] S. Keyvaninia *et al.*, 'Heterogeneously integrated III-V/silicon distributed feedback lasers', *Opt. Lett.*, vol. 38, no. 24, pp. 5434–5437, Dec. 2013.

[72] G. Roelkens, D. V. Thourhout, R. Baets, R. Nötzel, and M. Smit, 'Laser emission and photodetection in an InP/InGaAsP layer integrated on and coupled to a Silicon-on-Insulator waveguide circuit', *Opt. Express*, vol. 14, no. 18, pp. 8154–8159, Sep. 2006.

[73] J. Liu, X. Sun, R. Camacho-Aguilera, L. C. Kimerling, and J. Michel, 'Ge-on-Si laser operating at room temperature', *Opt. Lett.*, vol. 35, no. 5, pp. 679–681, Mar. 2010.

[74] S. Chen *et al.*, 'Electrically pumped continuous-wave III–V quantum dot lasers on silicon', *Nat. Photonics*, vol. 10, no. 5, pp. 307–311, May 2016.

[75] J. Wang *et al.*, 'Extremely Low-Threshold Current Density InGaAs/AlGaAs Quantum-Well Lasers on Silicon', *J. Light. Technol.*, vol. 33, no. 15, pp. 3163–3169, Aug. 2015.

[76] S. Wirths *et al.*, 'Lasing in direct-bandgap GeSn alloy grown on Si', *Nat. Photonics*, vol. 9, no. 2, pp. 88–92, Feb. 2015.

[77] A. Y. Liu, R. W. Herrick, O. Ueda, P. M. Petroff, A. C. Gossard, and J. E. Bowers, 'Reliability of InAs/GaAs Quantum Dot Lasers Epitaxially Grown on Silicon', *IEEE J. Sel. Top. Quantum Electron.*, vol. 21, no. 6, pp. 690–697, Nov. 2015.

[78] J. S. Orcutt *et al.*, 'Nanophotonic integration in state-of-the-art CMOS foundries', *Opt. Express*, vol. 19, no. 3, pp. 2335–2346, Jan. 2011.

[79] P. Chaisakul *et al.*, 'Integrated germanium optical interconnects on silicon substrates', *Nat. Photonics*, vol. 8, no. 6, pp. 482–488, Jun. 2014.

[80] Y. Ohmori *et al.*, 'Polymeric optical integrated devices with high-speed operated organic electroluminescent diodes as a light source', in *International Symposium on Optical Science and Technology*, 2002, pp. 106–113.

[81] T. Fukuda, T. Okada, B. Wei, M. Ichikawa, and Y. Taniguchi, 'Influence of carrier-injection efficiency on modulation rate of organic light source', *Opt. Lett.*, vol. 32, no. 13, pp. 1905–1907, Jul. 2007.

[82] T. Fukuda, M. Ohashi, B. Wei, T. Okada, M. Ichikawa, and Y. Taniguchi, 'Transient response of blue organic electroluminescence devices with short fluorescence lifetime of

substituted phenyl/vinyl compound as an emissive layer', *Opt. Lett.*, vol. 32, no. 9, p. 1150, 2007.

[83] Y. Ohmori *et al.*, 'Organic electroluminescent diodes as a light source for polymeric waveguides — toward organic integrated optical devices', *Thin Solid Films*, vol. 393, no. 1–2, pp. 267–272, Aug. 2001.

[84] M. Punke, S. Valouch, S. W. Kettlitz, M. Gerken, and U. Lemmer, 'Optical Data Link Employing Organic Light-Emitting Diodes and Organic Photodiodes as Optoelectronic Components', *J. Light. Technol.*, vol. 26, no. 7, pp. 816–823, Apr. 2008.

[85] I. A. Barlow, T. Kreouzis, and D. G. Lidzey, 'High-speed electroluminescence modulation of a conjugated-polymer light emitting diode', *Appl. Phys. Lett.*, vol. 94, no. 24, p. 243301, Jun. 2009.

[86] Y. Ohmori and H. Kajii, 'Organic Devices for Integrated Photonics', *Proc. IEEE*, vol. 97, no. 9, pp. 1627–1636, Sep. 2009.

[87] P. A. Haigh *et al.*, 'A 20-Mb/s VLC Link With a Polymer LED and a Multilayer Perceptron Equalizer', *IEEE Photonics Technol. Lett.*, vol. 26, no. 19, pp. 1975–1978, Oct. 2014.

[88] H. Mu, I. Reddy, J. Hunt, P. Severs, and S. Patil, 'Fabrication and optical modulation of top-emitting yellow light polymer light-emitting diodes on the FR4 board', *Thin Solid Films*, vol. 519, no. 2, pp. 841–845, Nov. 2010.

[89] Y.-Y. Lin, C. Cheng, H.-H. Liao, S.-F. Horng, H.-F. Meng, and C.-S. Hsu, 'Integration of polymer light-emitting diode and polymer waveguide on Si substrate', *Appl. Phys. Lett.*, vol. 89, no. 6, p. 063501, Aug. 2006.

[90] H. Kajii *et al.*, 'Transient Properties of Organic Electroluminescent Diode Using 8-Hydroxyquinoline Aluminum Doped with Rubrene as an Electro-Optical Conversion Device for Polymeric Integrated Devices', *Jpn. J. Appl. Phys.*, vol. 41, no. 4S, p. 2746, Apr. 2002.

[91] J.-S. Kim, H. Kajii, and Y. Ohmori, 'Characteristics of optical response in red organic light-emitting diodes using two dopant system for application to the optical link devices', *Thin Solid Films*, vol. 499, no. 1–2, pp. 343–348, Mar. 2006.

[92] N. Tessler, G. J. Denton, and R. H. Friend, 'Lasing from conjugated-polymer microcavities', *Nature*, vol. 382, no. 6593, pp. 695–697, Aug. 1996.

[93] I. D. W. Samuel, E. B. Namdas, and G. A. Turnbull, ‘How to recognize lasing’, *Nat. Photonics*, vol. 3, pp. 546–549, Oct. 2009.

[94] I. D. W. Samuel and G. A. Turnbull, ‘Organic Semiconductor Lasers’, *Chem. Rev.*, vol. 107, no. 4, pp. 1272–1295, Apr. 2007.

[95] P. A. Haigh *et al.*, ‘Wavelength-Multiplexed Polymer LEDs: Towards 55 Mb/s Organic Visible Light Communications’, *IEEE J. Sel. Areas Commun.*, vol. 33, no. 9, pp. 1819–1828, Sep. 2015.

[96] P. A. Haigh, Z. Ghassemlooy, and I. Papakonstantinou, ‘1.4-Mb/s White Organic LED Transmission System Using Discrete Multitone Modulation’, *IEEE Photonics Technol. Lett.*, vol. 25, no. 6, pp. 615–618, Mar. 2013.

[97] S. Rajagopal, R. D. Roberts, and S. Lim, ‘IEEE 802.15.7 visible light communication: modulation schemes and dimming support’, *IEEE Commun. Mag.*, vol. 50, no. 3, pp. 72–82, Mar. 2012.

[98] B. Bai, Z. Xu, and Y. Fan, ‘Joint LED dimming and high capacity visible light communication by overlapping PPM’, in *The 19th Annual Wireless and Optical Communications Conference (WOCC 2010)*, 2010, pp. 1–5.

[99] G. Ntogari, T. Kamalakis, J. Walewski, and T. Sphicopoulos, ‘Combining Illumination Dimming Based on Pulse-Width Modulation With Visible-Light Communications Based on Discrete Multitone’, *IEEEOSA J. Opt. Commun. Netw.*, vol. 3, no. 1, pp. 56–65, Jan. 2011.

[100] P. Peumans, V. Bulović, and S. R. Forrest, ‘Efficient, high-bandwidth organic multilayer photodetectors’, *Appl. Phys. Lett.*, vol. 76, no. 26, pp. 3855–3857, Jun. 2000.

[101] T. Morimune, H. Kajii, and Y. Ohmori, ‘Photoresponse Properties of a High-Speed Organic Photodetector Based on Copper-Phthalocyanine Under Red Light Illumination’, *IEEE Photonics Technol. Lett.*, vol. 18, no. 24, pp. 2662–2664, Dec. 2006.

[102] T. Hamasaki *et al.*, ‘Fabrication and characteristics of polyfluorene based organic photodetectors using fullerene derivatives’, *Thin Solid Films*, vol. 518, no. 2, pp. 548–550, Nov. 2009.

[103] J. Mallari *et al.*, ‘100Gbps EO polymer modulator product and its characterization using a real-time digitizer’, in *Optical Fiber Communication (OFC), collocated National Fiber Optic Engineers Conference, 2010 Conference on (OFC/NFOEC)*, 2010, pp. 1–3.

[104] M. Lee *et al.*, 'Broadband Modulation of Light by Using an Electro-Optic Polymer', *Science*, vol. 298, no. 5597, pp. 1401–1403, Nov. 2002.

[105] B. Bortnik *et al.*, 'Electrooptic Polymer Ring Resonator Modulation up to 165 GHz', *IEEE J. Sel. Top. Quantum Electron.*, vol. 13, no. 1, pp. 104–110, Jan. 2007.

[106] P. Groumas *et al.*, 'Tunable 100 Gbaud Transmitter Based on Hybrid Polymer-to-Polymer Integration for Flexible Optical Interconnects', *J. Light. Technol.*, vol. PP, no. 99, pp. 1–1, 2015.

[107] Y. Ohmori *et al.*, 'Realization of polymeric optical integrated devices utilizing organic light-emitting diodes and photodetectors fabricated on a polymeric waveguide', *IEEE J. Sel. Top. Quantum Electron.*, vol. 10, no. 1, pp. 70–78, Jan. 2004.

[108] Y.-Y. Lin, C. Cheng, H.-H. Liao, S.-F. Horng, H.-F. Meng, and C.-S. Hsu, 'Integration of polymer light-emitting diode and polymer waveguide on Si substrate', *Appl. Phys. Lett.*, vol. 89, no. 6, p. 063501, Aug. 2006.

[109] M. Ramuz, L. Bürgi, R. Stanley, and C. Winnewisser, 'Coupling light from an organic light emitting diode (OLED) into a single-mode waveguide: Toward monolithically integrated optical sensors', *J. Appl. Phys.*, vol. 105, no. 8, p. 084508, Apr. 2009.

[110] N. Tessler, Y. Preezant, N. Rappaport, and Y. Roichman, 'Charge Transport in Disordered Organic Materials and Its Relevance to Thin-Film Devices: A Tutorial Review', *Adv. Mater.*, vol. 21, no. 27, pp. 2741–2761, Jul. 2009.

[111] G. Zuo, H. Abdalla, and M. Kemerink, 'Impact of doping on the density of states and the mobility in organic semiconductors', *Phys. Rev. B*, vol. 93, no. 23, p. 235203, Jun. 2016.

[112] B. Maennig, M. Pfeiffer, A. Nollau, X. Zhou, K. Leo, and P. Simon, 'Controlled p-type doping of polycrystalline and amorphous organic layers: Self-consistent description of conductivity and field-effect mobility by a microscopic percolation model', *Phys. Rev. B*, vol. 64, no. 19, p. 195208, Oct. 2001.

[113] V. I. Arkhipov, P. Heremans, E. V. Emelianova, and H. Bässler, 'Effect of doping on the density-of-states distribution and carrier hopping in disordered organic semiconductors', *Phys. Rev. B*, vol. 71, no. 4, p. 045214, Jan. 2005.

[114] Lüssem B., Riede M., and Leo K., 'Doping of organic semiconductors', *Phys. Status Solidi A*, vol. 210, no. 1, pp. 9–43, Dec. 2012.

[115] S. Olthof, W. Tress, R. Meerheim, B. Lüssem, and K. Leo, 'Photoelectron spectroscopy study of systematically varied doping concentrations in an organic semiconductor layer using a molecular p-dopant', *J. Appl. Phys.*, vol. 106, no. 10, p. 103711, Nov. 2009.

[116] M. L. Tietze *et al.*, 'Elementary steps in electrical doping of organic semiconductors', *Nat. Commun.*, vol. 9, no. 1, p. 1182, Mar. 2018.

[117] P. Pahner, 'Charge Carrier Trap Spectroscopy on Organic Hole Transport Materials', p. 239.

[118] I. Salzmann *et al.*, 'Intermolecular Hybridization Governs Molecular Electrical Doping', *Phys. Rev. Lett.*, vol. 108, no. 3, p. 035502, Jan. 2012.

[119] S.-J. Yoo and J.-J. Kim, 'Charge Transport in Electrically Doped Amorphous Organic Semiconductors', *Macromol. Rapid Commun.*, vol. 36, no. 11, pp. 984–1000, Jun. 2015.

[120] M. Kröger, S. Hamwi, J. Meyer, T. Riedl, W. Kowalsky, and A. Kahn, 'P-type doping of organic wide band gap materials by transition metal oxides: A case-study on Molybdenum trioxide', *Org. Electron.*, vol. 10, no. 5, pp. 932–938, Aug. 2009.

[121] M. L. Tietze, L. Burtone, M. Riede, B. Lüssem, and K. Leo, 'Fermi level shift and doping efficiency in p-doped small molecule organic semiconductors: A photoelectron spectroscopy and theoretical study', *Phys. Rev. B*, vol. 86, no. 3, p. 035320, Jul. 2012.

[122] J. Blochwitz *et al.*, 'Interface electronic structure of organic semiconductors with controlled doping levels', *Org. Electron.*, vol. 2, no. 2, pp. 97–104, Sep. 2001.

[123] M. Kühn, E. Mankel, A. Köhn, T. Mayer, and W. Jaegermann, 'Doping mechanism of MoO3 in 4,4′-Bis(N-carbazolyl)-1,1′-biphenyl: A photoelectron spectroscopic study', *Phys. Status Solidi B*, vol. 253, no. 9, pp. 1697–1706, Sep. 2016.

[124] M. Pfeiffer *et al.*, 'Doped organic semiconductors: Physics and application in light emitting diodes', *Org. Electron.*, vol. 4, no. 2, pp. 89–103, Sep. 2003.

[125] I. I. Fishchuk *et al.*, 'Unified description for hopping transport in organic semiconductors including both energetic disorder and polaronic contributions', *Phys. Rev. B*, vol. 88, no. 12, p. 125202, Sep. 2013.

[126] G. Nan, L. Wang, X. Yang, Z. Shuai, and Y. Zhao, 'Charge transfer rates in organic semiconductors beyond first-order perturbation: From weak to strong coupling regimes', *J. Chem. Phys.*, vol. 130, no. 2, p. 024704, Jan. 2009.

[127] C. Groves, 'Simulating charge transport in organic semiconductors and devices: a review', *Rep. Prog. Phys.*, vol. 80, no. 2, p. 026502, 2017.

[128] S. D. Baranovskii, ‘Theoretical description of charge transport in disordered organic semiconductors’, *Phys. Status Solidi B*, vol. 251, no. 3, pp. 487–525, Mar. 2014.

[129] J. O. Oelerich, F. Jansson, A. V. Nenashev, F. Gebhard, and S. D. Baranovskii, ‘Energy position of the transport path in disordered organic semiconductors’, *J. Phys. Condens. Matter*, vol. 26, no. 25, p. 255801, 2014.

[130] G. Paasch, T. Lindner, and S. Scheinert, ‘Variable range hopping as possible origin of a universal relation between conductivity and mobility in disordered organic semiconductors’, *Synth. Met.*, vol. 132, no. 1, pp. 97–104, Dec. 2002.

[131] A. Miller and E. Abrahams, ‘Impurity Conduction at Low Concentrations’, *Phys. Rev.*, vol. 120, no. 3, pp. 745–755, Nov. 1960.

[132] R. A. Marcus and N. Sutin, ‘Electron transfers in chemistry and biology’, *Biochim. Biophys. Acta BBA - Rev. Bioenerg.*, vol. 811, no. 3, pp. 265–322, Aug. 1985.

[133] N. Lu, L. Li, W. Banerjee, P. Sun, N. Gao, and M. Liu, ‘Charge carrier hopping transport based on Marcus theory and variable-range hopping theory in organic semiconductors’, *J. Appl. Phys.*, vol. 118, no. 4, p. 045701, Jul. 2015.

[134] I. I. Fishchuk, V. I. Arkhipov, A. Kadashchuk, P. Heremans, and H. Bässler, ‘Analytic model of hopping mobility at large charge carrier concentrations in disordered organic semiconductors: Polarons versus bare charge carriers’, *Phys. Rev. B*, vol. 76, no. 4, p. 045210, Jul. 2007.

[135] Y. Roichman, Y. Preezant, and N. Tessler, ‘Analysis and modeling of organic devices’, *Phys. Status Solidi A*, vol. 201, no. 6, pp. 1246–1262, May 2004.

[136] J. Cottaar, L. J. A. Koster, R. Coehoorn, and P. A. Bobbert, ‘Scaling Theory for Percolative Charge Transport in Disordered Molecular Semiconductors’, *Phys. Rev. Lett.*, vol. 107, no. 13, p. 136601, Sep. 2011.

[137] B. N. Limketkai, P. Jadhav, and M. A. Baldo, ‘Electric-field-dependent percolation model of charge-carrier mobility in amorphous organic semiconductors’, *Phys. Rev. B*, vol. 75, no. 11, p. 113203, Mar. 2007.

[138] H. Bässler, ‘Charge Transport in Disordered Organic Photoconductors a Monte Carlo Simulation Study’, *Phys. Status Solidi B*, vol. 175, no. 1, pp. 15–56, Jan. 1993.

[139] W. F. Pasveer *et al.*, ‘Unified Description of Charge-Carrier Mobilities in Disordered Semiconducting Polymers’, *Phys. Rev. Lett.*, vol. 94, no. 20, p. 206601, May 2005.

[140] M. Bouhassoune, S. L. M. van Mensfoort, P. A. Bobbert, and R. Coehoorn, 'Carrier-density and field-dependent charge-carrier mobility in organic semiconductors with correlated Gaussian disorder', *Org. Electron.*, vol. 10, no. 3, pp. 437–445, May 2009.

[141] J. Frenkel, 'On Pre-Breakdown Phenomena in Insulators and Electronic Semi-Conductors', *Phys. Rev.*, vol. 54, no. 8, pp. 647–648, Oct. 1938.

[142] W. D. Gill, 'Drift mobilities in amorphous charge-transfer complexes of trinitrofluorenone and poly-n-vinylcarbazole', *J. Appl. Phys.*, vol. 43, no. 12, pp. 5033–5040, Dec. 1972.

[143] J. H. Worne, J. E. Anthony, and D. Natelson, 'Transport in organic semiconductors in large electric fields: From thermal activation to field emission', *Appl. Phys. Lett.*, vol. 96, no. 5, p. 053308, Feb. 2010.

[144] J. Shinar and R. Shinar, 'Organic light-emitting devices (OLEDs) and OLED-based chemical and biological sensors: an overview', *J. Phys. Appl. Phys.*, vol. 41, no. 13, p. 133001, 2008.

[145] J. Frenkel, 'On the Transformation of light into Heat in Solids. I', *Phys. Rev.*, vol. 37, no. 1, pp. 17–44, Jan. 1931.

[146] G. H. Wannier, 'The Structure of Electronic Excitation Levels in Insulating Crystals', *Phys. Rev.*, vol. 52, no. 3, pp. 191–197, Aug. 1937.

[147] T. A. Ford, H. Ohkita, S. Cook, J. R. Durrant, and N. C. Greenham, 'Direct observation of intersystem crossing in charge-pair states in polyfluorene polymer blends', *Chem. Phys. Lett.*, vol. 454, no. 4, pp. 237–241, Mar. 2008.

[148] C.-L. Lee, X. Yang, and N. C. Greenham, 'Determination of the triplet excited-state absorption cross section in a polyfluorene by energy transfer from a phosphorescent metal complex', *Phys. Rev. B*, vol. 76, no. 24, p. 245201, Dec. 2007.

[149] T. Főrster, '10th Spiers Memorial Lecture. Transfer mechanisms of electronic excitation', *Discuss. Faraday Soc.*, vol. 27, no. 0, pp. 7–17, Jan. 1959.

[150] D. L. Dexter, 'A Theory of Sensitized Luminescence in Solids', *J. Chem. Phys.*, vol. 21, no. 5, pp. 836–850, May 1953.

[151] K. F. Chou and A. M. Dennis, 'Förster Resonance Energy Transfer between Quantum Dot Donors and Quantum Dot Acceptors', *Sensors*, vol. 15, no. 6, pp. 13288–13325, Jun. 2015.

[152] P. Langevin, ‘Recombinaison et mobilities des ions dans les gaz’, *Ann. Chim. Phys.*, vol. 28, p. 433, 1903.

[153] C. Deibel, A. Baumann, and V. Dyakonov, ‘Photogeneration and Recombination in Polymer Solar Cells’, in *Physics of Organic Semiconductors*, Wiley-Blackwell, 2013, pp. 575–602.

[154] C. Murawski, ‘Efficiency Roll-Off in Organic Light-Emitting Diodes’, Nov. 2015.

[155] S. M. Han, K. P. Kim, D. C. Choo, T. W. Kim, J. H. Seo, and Y. K. Kim, ‘Equivalent Circuit Models in Organic Light-Emitting Diodes Designed Using a Cole-Cole Plot’, *Mol. Cryst. Liq. Cryst.*, vol. 470, no. 1, pp. 279–287, Aug. 2007.

[156] S. H. Kim, H. Y. Chu, T. Zyung, and Y. S. Yang, ‘Impedance Spectroscopy of π-Conjugated Organic Materials’, *ETRI J.*, vol. 26, no. 2, pp. 156–170, Apr. 2004.

[157] Y. F. Xu *et al.*, ‘Impedance spectroscopy study on transport properties of N,N′-diphenyl-N,N′-bis(1-naphthyl)-1,1′-biphenyl-4,4′-diamine’, *Phys. B Condens. Matter*, vol. 362, no. 1, pp. 35–40, May 2005.

[158] H. M. Kim *et al.*, ‘Admittance Spectroscopic Analysis of Polymer Light Emitting Diodes with the LiF Cathode Buffer Layer’, *Mol. Cryst. Liq. Cryst.*, vol. 459, no. 1, pp. 11/[291]-18/[298], Dec. 2006.

[159] V. S. Reddy, S. Das, S. K. Ray, and A. Dhar, ‘Studies on conduction mechanisms of pentacene based diodes using impedance spectroscopy’, *J. Phys. Appl. Phys.*, vol. 40, no. 24, p. 7687, 2007.

[160] H. Park *et al.*, ‘Admittance spectroscopic analysis of organic light emitting diodes with the CFX plasma treatment on the surface of indium tin oxide anodes’, *Thin Solid Films*, vol. 516, no. 7, pp. 1370–1373, Feb. 2008.

[161] C. K. Suman, J. Yun, S. Kim, S.-D. Lee, and C. Lee, ‘AC impedance spectroscopic studies of transport properties in metal oxide doped α-NPD’, *Curr. Appl. Phys.*, vol. 9, no. 5, pp. 978–984, Sep. 2009.

[162] V. S. Reddy and A. Dhar, ‘Optical and charge carrier transport properties of polymer light emitting diodes based on MEH-PPV’, *Phys. B Condens. Matter*, vol. 405, no. 6, pp. 1596–1602, Mar. 2010.

[163] G. Cummins, I. Underwood, and A. Walton, ‘Electrical characterization and modelling of top-emitting PIN-OLEDs’, *J. Soc. Inf. Disp.*, vol. 19, no. 4, pp. 360–367, Apr. 2011.

[164] W. Brütting, S. Berleb, and A. G. Mückl, ‘Device physics of organic light-emitting diodes based on molecular materials’, *Org. Electron.*, vol. 2, no. 1, pp. 1–36, Mar. 2001.

[165] D. M. Taylor and H. L. Gomes, ‘Electrical characterization of the rectifying contact between aluminium and electrodeposited poly(3-methylthiophene)’, *J. Phys. Appl. Phys.*, vol. 28, no. 12, p. 2554, 1995.

[166] E. Nam *et al.*, ‘Electroluminescence and impedance analyses of organic light emitting diodes using anhydride materials as cathode interfacial layers’, *Thin Solid Films*, vol. 517, no. 14, pp. 4131–4134, May 2009.

[167] L. Zeng *et al.*, ‘Electrical and Optical Impulse Response of High-Speed Micro-OLEDs Under UltraShort Pulse Excitation’, *IEEE Trans. Electron Devices*, vol. 64, no. 7, pp. 2942–2948, Jul. 2017.

[168] H. C. F. Martens, W. F. Pasveer, H. B. Brom, J. N. Huiberts, and P. W. M. Blom, ‘Crossover from space-charge-limited to recombination-limited transport in polymer light-emitting diodes’, *Phys. Rev. B*, vol. 63, no. 12, p. 125328, Mar. 2001.

[169] N. D. Nguyen and M. Schmeits, ‘Numerical simulation of impedance and admittance of OLEDs’, *Phys. Status Solidi A*, vol. 203, no. 8, pp. 1885–1885, Jun. 2006.

[170] P. Kordt *et al.*, ‘Modeling of Organic Light Emitting Diodes: From Molecular to Device Properties’, *Adv. Funct. Mater.*, vol. 25, no. 13, pp. 1955–1971, Apr. 2015.

[171] M. Mesta *et al.*, ‘Molecular-scale simulation of electroluminescence in a multilayer white organic light-emitting diode’, *Nat. Mater.*, vol. 12, no. 7, pp. 652–658, Jul. 2013.

[172] B. Ruhstaller, E. Knapp, B. Perucco, N. Reinke, and D. R. and F. Müller, ‘Advanced Numerical Simulation of Organic Light-emitting Devices’, *Optoelectron. Devices Prop.*, 2011.

[173] S. L. M. van Mensfoort and R. Coehoorn, ‘Effect of Gaussian disorder on the voltage dependence of the current density in sandwich-type devices based on organic semiconductors’, *Phys. Rev. B*, vol. 78, no. 8, p. 085207, Aug. 2008.

[174] S. L. M. van Mensfoort, S. I. E. Vulto, R. A. J. Janssen, and R. Coehoorn, ‘Hole transport in polyfluorene-based sandwich-type devices: Quantitative analysis of the role of energetic disorder’, *Phys. Rev. B*, vol. 78, no. 8, p. 085208, Aug. 2008.

[175] I. Kamohara, M. Townsend, and B. Cottle, ‘Simulation of heterojunction organic thin film devices and exciton diffusion analysis in stacked-hetero device’, *J. Appl. Phys.*, vol. 97, no. 1, p. 014501, Dec. 2004.

[176] D. Gupta and Y. Hong, ‘Understanding the effect of semiconductor thickness on device characteristics in organic thin film transistors by way of two-dimensional simulations’, *Org. Electron.*, vol. 11, no. 1, pp. 127–136, Jan. 2010.

[177] M. Bogdanova *et al.*, ‘Simulation Platform for Multiscale and Multiphysics Modeling of OLEDs’, *Procedia Comput. Sci.*, vol. 29, pp. 740–753, Jan. 2014.

[178] W. Zhou, C. Zimmermann, and C. Jungemann, ‘Numerical Capacitance Analysis of Single-Layer OLEDs Based on the Master Equation’, *IEEE Trans. Electron Devices*, vol. 63, no. 12, pp. 4919–4923, Dec. 2016.

[179] H. Siemund and H. Göbel, ‘Numerical Simulation of Organic Light-Emitting Diodes With Insulating Cathode Buffer Layer’, *IEEE Trans. Electron Devices*, vol. 63, no. 9, pp. 3700–3706, Sep. 2016.

[180] E. Knapp and B. Ruhstaller, ‘Numerical analysis of steady-state and transient charge transport in organic semiconductor devices’, *Opt. Quantum Electron.*, vol. 42, no. 11–13, pp. 667–677, Oct. 2011.

[181] B. Ruhstaller *et al.*, ‘59.1: Invited Paper: Optoelectronic OLED Modeling for Device Optimization and Analysis’, *SID Symp. Dig. Tech. Pap.*, vol. 38, no. 1, pp. 1686–1690, May 2007.

[182] T.-J. Kung *et al.*, ‘Modeling of carrier transport in organic light emitting diode with random dopant effects by two-dimensional simulation’, *Opt. Express*, vol. 25, no. 21, p. 25492, Oct. 2017.

[183] I.-S. Park, S.-R. Park, D.-Y. Shin, J.-S. Oh, W.-J. Song, and J.-H. Yoon, ‘Modeling and simulation of electronic and excitonic emission properties in organic host–guest systems’, *Org. Electron.*, vol. 11, no. 2, pp. 218–226, Feb. 2010.

[184] E. Knapp, R. Häusermann, H. U. Schwarzenbach, and B. Ruhstaller, ‘Numerical simulation of charge transport in disordered organic semiconductor devices’, *J. Appl. Phys.*, vol. 108, no. 5, p. 054504, Sep. 2010.

[185] P. W. M. Blom, M. J. M. de Jong, and M. G. van Munster, ‘Electric-field and temperature dependence of the hole mobility in poly(p-phenylene vinylene)’, *Phys. Rev. B*, vol. 55, no. 2, pp. R656–R659, Jan. 1997.

[186] P. W. M. Blom, M. J. M. de Jong, and S. Breedijk, ‘Temperature dependent electron-hole recombination in polymer light-emitting diodes’, *Appl. Phys. Lett.*, vol. 71, no. 7, pp. 930–932, Aug. 1997.

[187] L. Chunjuan, B. Yajie, Y. Luyue, and W. Yongshun, 'Novel double-doped yellow fluorescent organic light-emitting devices based on MADN', in *2017 IEEE 2nd Information Technology, Networking, Electronic and Automation Control Conference (ITNEC)*, 2017, pp. 1215–1219.

[188] I. H. Lee, W. Song, J. Y. Lee, and S.-H. Hwang, 'High efficiency blue fluorescent organic light-emitting diodes using a conventional blue fluorescent emitter', *J. Mater. Chem. C*, vol. 3, no. 34, pp. 8834–8838, 2015.

[189] T. Schwab, M. Thomschke, S. Hofmann, M. Furno, K. Leo, and B. Lüssem, 'Efficiency enhancement of top-emitting organic light-emitting diodes using conversion dyes', *J. Appl. Phys.*, vol. 110, no. 8, p. 083118, Oct. 2011.

[190] J. KALINOWSKI, 'Excimers and exciplexes in organic electroluminescence', *Mater. Sci.-Pol.*, vol. 27, no. 3, pp. 735–756, 2009.

[191] I. I. Fishchuk *et al.*, 'Temperature dependence of the charge carrier mobility in disordered organic semiconductors at large carrier concentrations', *Phys. Rev. B*, vol. 81, no. 4, p. 045202, Jan. 2010.

[192] H. Bässler and A. Köhler, 'Charge Transport in Organic Semiconductors', in *Unimolecular and Supramolecular Electronics I*, R. M. Metzger, Ed. Springer Berlin Heidelberg, 2011, pp. 1–65.

[193] A. Heck, J. J. Kranz, and M. Elstner, 'Simulation of Temperature-Dependent Charge Transport in Organic Semiconductors with Various Degrees of Disorder', *J. Chem. Theory Comput.*, vol. 12, no. 7, pp. 3087–3096, Jul. 2016.

[194] V. Coropceanu, J. Cornil, D. A. da Silva Filho, Y. Olivier, R. Silbey, and J.-L. Brédas, 'Charge Transport in Organic Semiconductors', *Chem. Rev.*, vol. 107, no. 4, pp. 926–952, Apr. 2007.

[195] G. Nenna *et al.*, 'A Study on Thermal Degradation of Organic LEDs Using IR Imaging', *Macromol. Symp.*, vol. 247, no. 1, pp. 326–332, Feb. 2007.

[196] 'Ultra-Thin Flexible Glass: SCHOTT Advanced Optics | SCHOTT AG'. [Online]. Available: https://www.schott.com/advanced_optics/english/products/wafers-and-thin-glass/glass-wafer-and-substrates/ultra-thin-glass/index.html. [Accessed: 07-Aug-2018].

[197] 'EAGLE XG ® Slim Glass Datasheet'. Corning.

[198] H. Bracht *et al.*, 'Thermal conductivity of isotopically controlled silicon nanostructures', *New J. Phys.*, vol. 16, no. 1, p. 015021, 2014.

[199] A. Delan, M. Rennau, S. E. Schulz, and T. Gessner, 'Thermal conductivity of ultra low-k dielectrics', *Microelectron. Eng.*, vol. 70, no. 2, pp. 280–284, Nov. 2003.

[200] E. W. Lemmon and R. T. Jacobsen, 'Viscosity and Thermal Conductivity Equations for Nitrogen, Oxygen, Argon, and Air', *Int. J. Thermophys.*, vol. 25, no. 1, pp. 21–69, Jan. 2004.

[201] C. Keum *et al.*, 'Improving the thermal stability of OLEDs by doping the electron transport layer with a reactive metal (Conference Presentation)', in *Organic Electronics and Photonics: Fundamentals and Devices*, 2018, vol. 10687, p. 106870R.

[202] T. P. I. Saragi, T. Fuhrmann-Lieker, and J. Salbeck, 'Comparison of Charge-Carrier Transport in Thin Films of Spiro-Linked Compounds and Their Corresponding Parent Compounds', *Adv. Funct. Mater.*, vol. 16, no. 7, pp. 966–974.

[203] S.-W. Wen, M.-T. Lee, and C. H. Chen, 'Recent development of blue fluorescent OLED materials and devices', *J. Disp. Technol.*, vol. 1, no. 1, pp. 90–99, Sep. 2005.

[204] T. Tsuji *et al.*, 'Red-phosphorescent OLEDs employing bis(8-quinolinolato)phenolato-aluminum(III) complexes as emission-layer hosts', *J. Soc. Inf. Disp.*, vol. 13, no. 2, pp. 117–121.

[205] Y. H. Choi, Y. P. Jeon, D. C. Choo, and T. W. Kim, 'Enhancement of out-coupling efficiency due to an organic scattering layer in organic light-emitting devices', *Org. Electron.*, vol. 22, pp. 197–201, Jul. 2015.

[206] N. Bamiedakis, 'Private Communications'.

[207] H. F. Wittmann, J. Grüner, R. H. Friend, G. W. C. Spencer, S. C. Moratti, and A. B. Holmes, 'Microcavity effect in a single-layer polymer light-emitting diode', *Adv. Mater.*, vol. 7, no. 6, pp. 541–544.

[208] M.-H. Ho *et al.*, 'Highly efficient deep blue organic electroluminescent device based on 1-methyl-9,10-di(1-naphthyl)anthracene', *Appl. Phys. Lett.*, vol. 89, no. 25, p. 252903, Dec. 2006.

[209] G. Schwartz, T.-H. Ke, C.-C. Wu, K. Walzer, and K. Leo, 'Balanced ambipolar charge carrier mobility in mixed layers for application in hybrid white organic light-emitting diodes', *Appl. Phys. Lett.*, vol. 93, no. 7, p. 073304, Aug. 2008.

[210] M. Carvelli, A. van Reenen, R. A. J. Janssen, H. P. Loebl, and R. Coehoorn, 'Exciton formation and light emission near the organic–organic interface in small-molecule based double-layer OLEDs', *Org. Electron.*, vol. 13, no. 11, pp. 2605–2614, Nov. 2012.

[211] Silvaco, Inc., ‘ATLAS User’s Manual’. 07-Nov-2014.

[212] J. O. Oelerich, D. Huemmer, and S. D. Baranovskii, ‘How to Find Out the Density of States in Disordered Organic Semiconductors’, *Phys. Rev. Lett.*, vol. 108, no. 22, May 2012.

[213] T. J. Whitcher *et al.*, ‘Investigation into the Gaussian density of states widths of organic semiconductors’, *J. Phys. Appl. Phys.*, vol. 49, no. 32, p. 325106, 2016.

[214] B. Lüssem, C.-M. Keum, D. Kasemann, B. Naab, Z. Bao, and K. Leo, ‘Doped Organic Transistors’, *Chem. Rev.*, vol. 116, no. 22, pp. 13714–13751, Nov. 2016.

[215] H. Ishii *et al.*, ‘Kelvin probe study of band bending at organic semiconductor/metal interfaces: examination of Fermi level alignment’, *Phys. Status Solidi A*, vol. 201, no. 6, pp. 1075–1094, May 2004.

[216] H. Peisert, M. Knupfer, and J. Fink, ‘Energy level alignment at organic/metal interfaces: Dipole and ionization potential’, *Appl. Phys. Lett.*, vol. 81, no. 13, pp. 2400–2402, Sep. 2002.

[217] S. Olthof, ‘Energy level alignment at the interfaces in a multilayer organic light-emitting diode structure’, *Phys. Rev. B*, vol. 79, no. 24, 2009.

[218] B. Jaeckel, J. B. Sambur, and B. A. Parkinson, ‘Ubiquitous Pentacene Monolayer on Metals Deposited onto Pentacene Films’, *Langmuir*, vol. 23, no. 23, pp. 11366–11368, Nov. 2007.

[219] T.-Y. Chu and O.-K. Song, ‘Hole mobility of N,N′-bis(naphthalen-1-yl)-N,N′-bis(phenyl) benzidine investigated by using space-charge-limited currents’, *Appl. Phys. Lett.*, vol. 90, no. 20, p. 203512, May 2007.

[220] H. Xu *et al.*, ‘Thickness Dependence of Carrier Mobility and the Interface Trap Free Energy Investigated by Impedance Spectroscopy in Organic Semiconductors’, *J. Phys. Chem. C*, vol. 120, no. 31, pp. 17184–17189, Aug. 2016.

[221] M. A. Khan *et al.*, ‘Electron mobility of 4,7-diphyenyl-1,10-phenanthroline estimated by using space-charge-limited currents’, *J. Appl. Phys.*, vol. 103, no. 1, p. 014509, Jan. 2008.

[222] J. Staudigel, M. Stößel, F. Steuber, and J. Simmerer, ‘A quantitative numerical model of multilayer vapor-deposited organic light emitting diodes’, *J. Appl. Phys.*, vol. 86, no. 7, pp. 3895–3910, Sep. 1999.

[223] J. Shen and J. Yang, ‘Physical mechanisms in double-carrier trap-charge limited transport processes in organic electroluminescent devices: A numerical study’, *J. Appl. Phys.*, vol. 83, no. 12, pp. 7706–7714, Jun. 1998.

[224] F. Ante *et al.*, ‘Contact Doping and Ultrathin Gate Dielectrics for Nanoscale Organic Thin-Film Transistors’, *Small*, vol. 7, no. 9, pp. 1186–1191, May 2011.

[225] S. Forget *et al.*, ‘Red-emitting fluorescent organic light emitting diodes with low sensitivity to self-quenching’, *J. Appl. Phys.*, vol. 108, no. 6, p. 064509, Sep. 2010.

[226] X. Wang, K. D. Parrish, J. A. Malen, and P. K. L. Chan, ‘Modifying the thermal conductivity of small molecule organic semiconductor thin films with metal nanoparticles’, *Sci. Rep.*, vol. 5, p. 16095, Nov. 2015.

[227] N. Kim, B. Domercq, S. Yoo, A. Christensen, B. Kippelen, and S. Graham, ‘Thermal transport properties of thin films of small molecule organic semiconductors’, *Appl. Phys. Lett.*, vol. 87, no. 24, p. 241908, Dec. 2005.

[228] Q. Wei, C. Uehara, M. Mukaida, K. Kirihara, and T. Ishida, ‘Measurement of in-plane thermal conductivity in polymer films’, *AIP Adv.*, vol. 6, no. 4, p. 045315, Apr. 2016.

[229] J. C. Duda, P. E. Hopkins, Y. Shen, and M. C. Gupta, ‘Thermal transport in organic semiconducting polymers’, *Appl. Phys. Lett.*, vol. 102, no. 25, p. 251912, Jun. 2013.

[230] X. Qi and S. R. Forrest, ‘Thermal analysis of high intensity organic light-emitting diodes based on a transmission matrix approach’, *J. Appl. Phys.*, vol. 110, no. 12, p. 124516, Dec. 2011.

[231] C. Adachi, M. A. Baldo, M. E. Thompson, and S. R. Forrest, ‘Nearly 100% internal phosphorescence efficiency in an organic light-emitting device’, *J. Appl. Phys.*, vol. 90, no. 10, pp. 5048–5051, Oct. 2001.

[232] H. Uoyama, K. Goushi, K. Shizu, H. Nomura, and C. Adachi, ‘Highly efficient organic light-emitting diodes from delayed fluorescence’, *Nature*, vol. 492, no. 7428, pp. 234–238, Dec. 2012.

[233] D. Y. Kondakov, ‘Triplet-triplet annihilation in highly efficient fluorescent organic light-emitting diodes: current state and future outlook’, *Philos. Trans. R. Soc. Math. Phys. Eng. Sci.*, vol. 373, no. 2044, pp. 20140321–20140321, May 2015.

[234] Z. Ghassemlooy *et al.*, ‘Visible light communications: 3.75 Mbits/s data rate with a 160 kHz bandwidth organic photodetector and artificial neural network equalization [Invited]’, *Photonics Res.*, vol. 1, no. 2, pp. 65–68, Aug. 2013.

[235] D. C. O'Brien, L. Zeng, H. Le-Minh, G. Faulkner, J. W. Walewski, and S. Randel, 'Visible light communications: Challenges and possibilities', in *2008 IEEE 19th International Symposium on Personal, Indoor and Mobile Radio Communications*, 2008, pp. 1–5.

[236] H. Chun *et al.*, 'Visible Light Communication Using a Blue GaN LED and Fluorescent Polymer Color Converter', *IEEE Photonics Technol. Lett.*, vol. 26, no. 20, pp. 2035–2038, Oct. 2014.

[237] D. Liu, H. Qin, J. Zhang, and T. Wang, 'Thickness-dependent glass transition temperature and charge mobility in cross-linked polyfluorene thin films', *Phys. Rev. E*, vol. 94, no. 5, p. 052503, Nov. 2016.

[238] V. Shrotriya and Y. Yang, 'Capacitance–voltage characterization of polymer light-emitting diodes', *J. Appl. Phys.*, vol. 97, no. 5, p. 054504, Feb. 2005.

[239] N. D. Barth, V. C. Bender, and T. B. Marchesan, 'An analysis of frequency response on OLED for lighting applications', in *2017 IEEE Industry Applications Society Annual Meeting*, 2017, pp. 1–5.

[240] P. Chulkin, M. Lapkowski, M. R. Bryce, J. Santos, and P. Data, 'Determination of standard redox rate constants of OLED active compounds by electrochemical impedance spectroscopy', *Electrochimica Acta*, vol. 258, pp. 1160–1172, Dec. 2017.

[241] P. Chulkin, O. Vybornyi, M. Lapkowski, P. J. Skabara, and P. Data, 'Impedance spectroscopy of OLEDs as a tool for estimating mobility and the concentration of charge carriers in transport layers', *J. Mater. Chem. C*, vol. 6, no. 5, pp. 1008–1014, 2018.

[242] L. Burtone, D. Ray, K. Leo, and M. Riede, 'Impedance model of trap states for characterization of organic semiconductor devices', *J. Appl. Phys.*, vol. 111, no. 6, p. 064503, Mar. 2012.

[243] S. E. Laux, 'Techniques for Small-Signal Analysis of Semiconductor Devices', *IEEE Trans. Comput.-Aided Des. Integr. Circuits Syst.*, vol. 4, no. 4, pp. 472–481, Oct. 1985.

[244] M. Takata, N. Kouda, S. Ishihara, T. Nagase, T. Kobayashi, and H. Naito, 'Effect of contact resistance on mobility determination by impedance spectroscopy', *Jpn. J. Appl. Phys.*, vol. 53, no. 2S, p. 02BE02, Jan. 2014.

[245] A. Grzemba, Ed., *MOST The Automotive Multimedia Network*. Franzis Verlag GmbH, 2010.

[246] I. Shake, H. Takara, and S. Kawanishi, ‘Simple measurement of eye diagram and BER using high-speed asynchronous sampling’, *J. Light. Technol.*, vol. 22, no. 5, pp. 1296–1302, May 2004.

[247] F. Chang, K. Onohara, and T. Mizuochi, ‘Forward error correction for 100 G transport networks’, *IEEE Commun. Mag.*, vol. 48, no. 3, pp. S48–S55, Mar. 2010.

[248] J.-L. Hou *et al.*, ‘Plasmon-Induced Sub-Bandgap Photodetection with Organic Schottky Diodes’, *Adv. Funct. Mater.*, vol. 26, no. 31, pp. 5741–5747, Aug. 2016.

[249] S. L. M. van Mensfoort, V. Shabro, R. J. de Vries, R. a. J. Janssen, and R. Coehoorn, ‘Hole transport in the organic small molecule material α-NPD: evidence for the presence of correlated disorder’, *J. Appl. Phys.*, vol. 107, no. 11, p. 113710, Jun. 2010.

[250] S. Hofmann, ‘Exciton Dynamics in White Organic Light-Emitting Diodes comprising Triplet Harvesting’, Jul. 2013.

[251] S. L. M. van Mensfoort, R. J. de Vries, V. Shabro, H. P. Loebl, R. A. J. Janssen, and R. Coehoorn, ‘Electron transport in the organic small-molecule material BAlq — the role of correlated disorder and traps’, *Org. Electron.*, vol. 11, no. 8, pp. 1408–1413, Aug. 2010.

[252] C. Fuchs *et al.*, ‘Enhanced light emission from top-emitting organic light-emitting diodes by optimizing surface plasmon polariton losses’, *Phys. Rev. B*, vol. 92, no. 24, Dec. 2015.

[253] T. Matsushima *et al.*, ‘Interfacial charge transfer and charge generation in organic electronic devices’, *Org. Electron.*, vol. 12, no. 3, pp. 520–528, Mar. 2011.

[254] A. Salehi, Y. Chen, X. Fu, C. Peng, and F. So, ‘Manipulating Refractive Index in Organic Light-Emitting Diodes’, *ACS Appl. Mater. Interfaces*, vol. 10, no. 11, pp. 9595–9601, Mar. 2018.

[255] G. Schwartz, ‘Novel Concepts for High-Efficiency White Organic Light-Emitting Diodes’, p. 168.

[256] P. K. Koech *et al.*, ‘Synthesis and Application of 1,3,4,5,7,8-Hexafluorotetracyanonaphthoquinodimethane (F6-TNAP): A Conductivity Dopant for Organic Light-Emitting Devices’, *Chem. Mater.*, vol. 22, no. 13, pp. 3926–3932, Jul. 2010.

[257] H. Nakanotani *et al.*, ‘High-efficiency organic light-emitting diodes with fluorescent emitters’, *Nat. Commun.*, vol. 5, May 2014.

APPENDICES

APPENDIX A – LARGE SIGNAL MEASUREMENTS

Table A - 1: Large signal responses of the 1.1 mm^2 OLEDs to a 0.5 V_{pp} square wave at different DC biases and large signal frequencies

	1 mA	5 mA
100 kHz	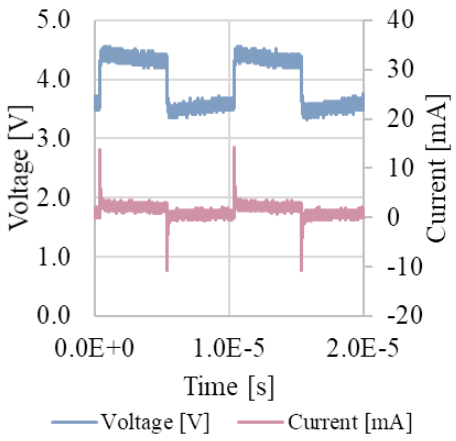	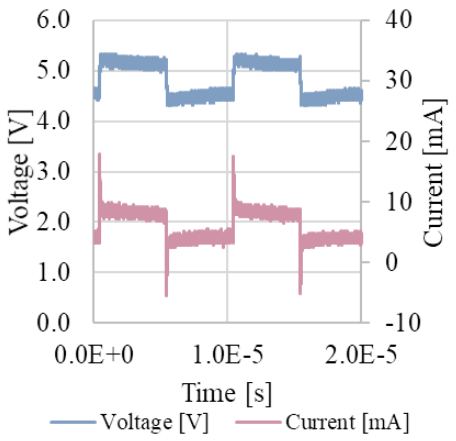
1 MHz	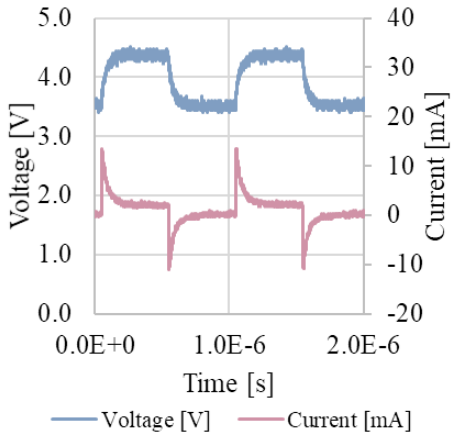	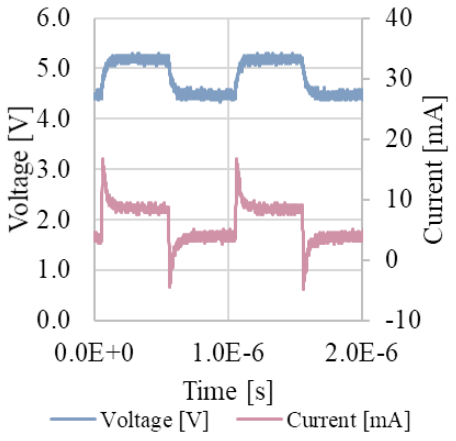
20 MHz	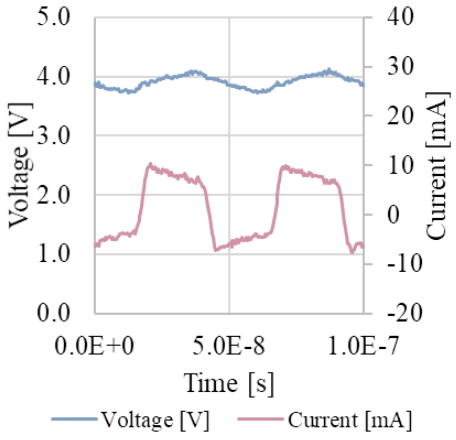	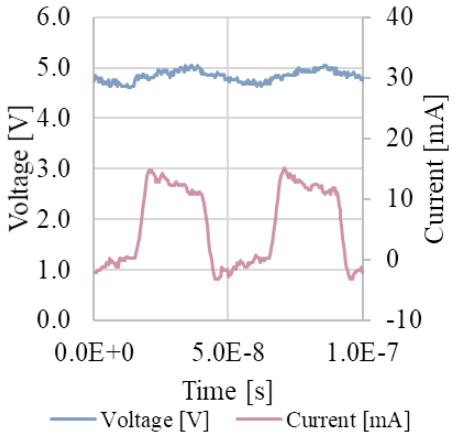

Table A - 2: Large signal responses of the 9 mm^2 OLEDs to a 0.5 V_{pp} square wave at different DC biases and large signal frequencies

	3 mA	20 mA
100 kHz	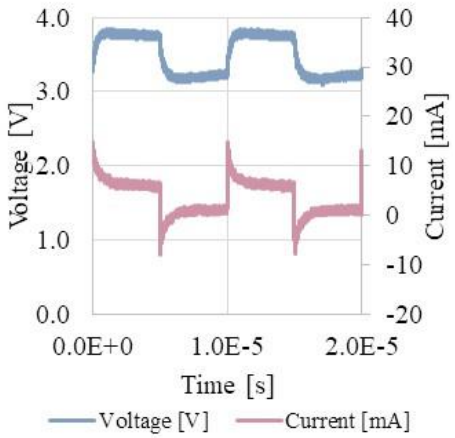	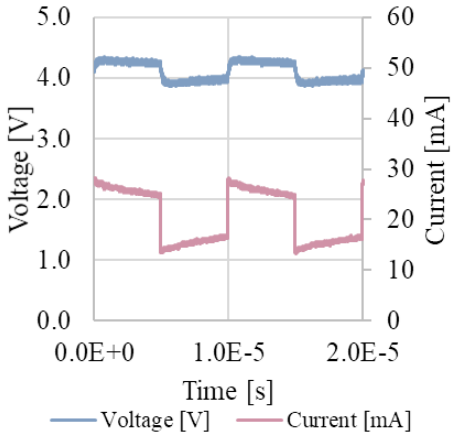
1 MHz	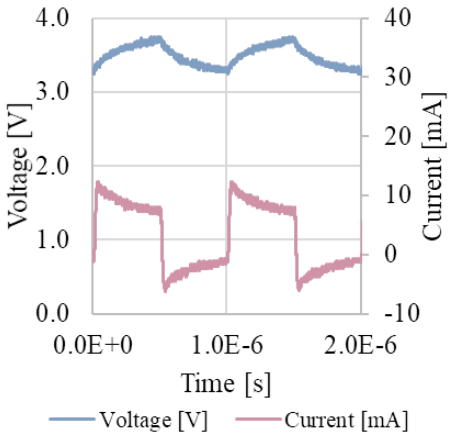	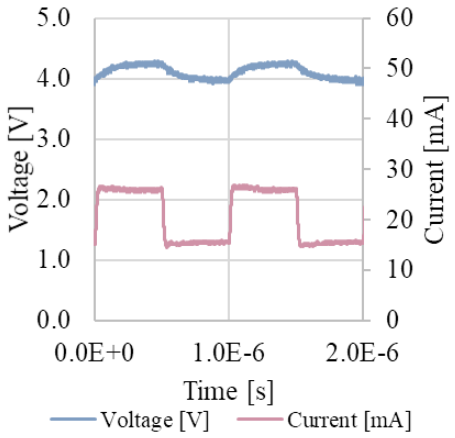
5 MHz	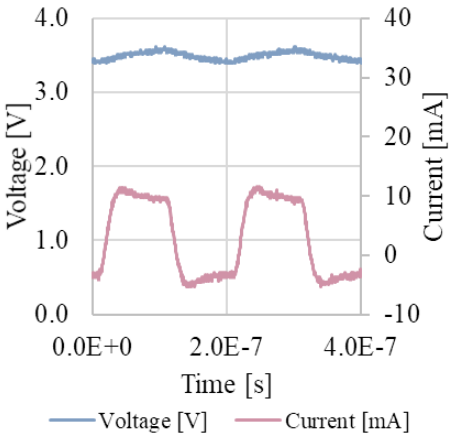	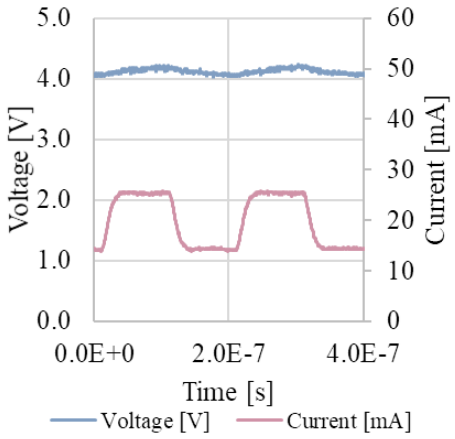

APPENDIX B – SIMULATION PARAMETERS

Table B - 1: Parameters used in Simulation

		Spiro-TTB	α-NPD	MADN	BAlq	BPhen
HOMO [eV]		5.2 [248]	5.4 [249]	5.6 [208]	6.1 [250]	6.4 [217]
LUMO [eV]		1.9 [248]	2.4 [249]	2.6 [208]	2.7 [250]	2.16 [217]
$N_{c,v}$ [cm^{-3}]		6.2×10^{20}	1.24×10^{21}	1.6×10^{21}	3×10^{21} [251]	2.19×10^{21}
$\sigma_{c,v}$ [eV]		0.1	0.11 [249]	0.1	0.09 [251]	0.1
ε_r		3.1 [252]	3.42 [253]	3.1	3.8 [251]	2.92 [254]
μ_{n0}	μ_{t0} [cm^2 V^{-1} s^{-1}]	2×10^{-7}	3×10^{-11}	1×10^{-9} [208]	2.4×10^{-7} [255]	3×10^{-6} [221]
	A [cm^{-1}]	3.0×10^{5}	8.7×10^{5}	4.0×10^{5}[208]	9.0×10^{5} [255]	2.7×10^{5} [221]
μ_{p0}	μ_{t0} [cm^2 V^{-1} s^{-1}]	1.2×10^{-6} [202]	2×10^{-11} [220]	1×10^{-9} [208]	6×10^{-8}	3×10^{-8}
	A [cm^{-1}]	3.0×10^{5}[202]	8.7×10^{5}[220]	4.0×10^{5} [208]	9.0×10^{5}	2.7×10^{5}
γ_n [cm V^{-1}]$^{0.5}$		5×10^{-3}	2×10^{-2}	1.3×10^{-2} [208]	8.6×10^{-3} [255]	1.2×10^{-3}[221]
γ_p [cm V^{-1}]$^{0.5}$		5×10^{-3} [202]	2×10^{-2} [220]	1.3×10^{-2} [208]	8.6×10^{-3}	1.2×10^{-3}
Exciton						
L_{DS} [nm]		10	10	10	10	10
τ_S [ns]		10	3.6	10	10	1.1
L_{DT} [nm]		63.2	63.2	63.2	63.2	63.2
τ_T [µs]		100	100	100	100	100
Doping		p-type		p-type n-type		n-type
Concentration [cm^{-3}]		4×10^{18}		4.26×10^{18}		2×10^{18}
$\Delta E_{gc,v}$ [eV]		-0.27 [256]		0.1, 0.24 [257]		-0.18 [217]
$N_{gc,v}$ [cm^{-3}]		7.83×10^{19}		4.26×10^{19}		1.14×10^{20}
$\sigma_{gc,v}$ [eV]		0.05		0.05		0.05

APPENDIX C – SIMULATION INPUT FILE

```
#Building a multi-layered device
#Al (80)/4 wt%-F6-TCNNQ:Spiro-TTB(40)/NPB(10)/2.76wt%-TBPe-
MADN(30)(Blue) OR Ir(MDQ)2NPB (20)(Red)/BAlq2(10)/2wt%-
Cs:BPhen(40)- blue OR (60) - red/Ag(30)

set BATCH = Device24

set Shape_Factor = 9

set Al_thick = 0.08
set TTB_thick = 0.04
set NPB_thick = 0.01
set MADN_thick = 0.03
set BAlq2_thick = 0.01
set BPhen_thick=0.04
set Ag_thick = 0.03

set vf = 6.0
set vs = 2.8
set size = L
set temp = 300

assign name=logfile
c.value=${BATCH}_${size}_${TTB_thick}_${NPB_thick}_${MADN_thic
k}_${BAlq2_thick}_${BPhen_thick}_${temp}K

set Al_y = $Al_thick
set TTB_y = $Al_y + $TTB_thick
set NPB_y = $TTB_y + $NPB_thick
set MADN_y = $NPB_y + $MADN_thick
set BAlq2_y = $MADN_y + $BAlq2_thick
set BPhen_y = $BAlq2_y + $BPhen_thick
set Ag_y = $BPhen_y + $Ag_thick

set Al_workf = 4.3

set O_RSTEXCITON = 0.25
set O_LDSEXCITON = 0.01
set O_TAUSEXCITON = 10e-9

#TTB Parameters

set TTB_HOMO = 5.2
set TTB_LUMO = 1.9
set TTB_affinity = $TTB_LUMO
set TTB_eg300 = $TTB_HOMO - $TTB_LUMO

#NPB Parameters
```

```
set NPB_HOMO = 5.4
set NPB_LUMO = 2.4
set NPB_affinity = $NPB_LUMO
set NPB_eg300 = $NPB_HOMO - $NPB_LUMO

#MADN Parameters
set MADN_HOMO = 5.6
set MADN_LUMO = 2.6
set MADN_affinity = $MADN_LUMO
set MADN_eg300 = $MADN_HOMO - $MADN_LUMO

set TBPe_HOMO = 5.36
set TBPe_LUMO = 2.7
set TBPe_affinity = $TBPe_LUMO
set TBPe_eg300 = $TBPe_HOMO - $TBPe_LUMO
set TBPe_ED = $MADN_LUMO - $TBPe_LUMO
set TBPe_EA = $MADN_HOMO - $TBPe_HOMO

#BAlq2 Parameters

set BAlq2_HOMO = 6.1
set BAlq2_LUMO = 2.7
set BAlq2_affinity = $BAlq2_LUMO
set BAlq2_eg300 = $BAlq2_HOMO - $BAlq2_LUMO


#BPhen Parameters

set BPhen_HOMO = 6.4
set BPhen_LUMO = 2.16
set BPhen_affinity = $BPhen_LUMO
set BPhen_eg300 = $BPhen_HOMO - $BPhen_LUMO


set Ag_workf = 3.3

go atlas simflags="-P 10"

mesh smooth = 1 space.mult = 1.0 width=1e6*$Shape_Factor

x.mesh l = -0.5     spacing = 0.25
x.mesh l = 0.5      spacing = 0.25

y.mesh l = 0.0                      spacing = 0.01
y.mesh l = $Al_y                 spacing = 0.0001
y.mesh l = $Al_y + 0.5*$TTB_thick  spacing = 0.001
y.mesh l = $TTB_y                spacing = 0.0001
y.mesh l = $TTB_y + 0.5*$NPB_thick spacing = 0.001
y.mesh l = $NPB_y                spacing = 0.0001
y.mesh l = $NPB_y + 0.5*$MADN_thick     spacing = 0.001
y.mesh l = $MADN_y               spacing = 0.0001
y.mesh l = $BAlq2_y              spacing = 0.0001
```

```
y.mesh l = $BAlq2_y + 0.5*$BPhen_thick  spacing = 0.001
y.mesh l = $BPhen_y           spacing = 0.0001
y.mesh l = $Ag_y              spacing = 0.01

region  number = 1  name = TTB user.material = TTB     y.min =
$Al_y y.max = $TTB_y
region  number = 2  name = NPD user.material = NPA
      y.min = $TTB_yy.max = $NPB_y
region  number = 3  name = MADN user.material = MADN   y.min =
$NPB_y    y.max = $MADN_y
region  number = 4  name = BAlq2 user.material = BAlq2 y.min =
$MADN_y   y.max = $BAlq2_y
region  number = 5  name = BPhen user.material = BPhen y.min =
$BAlq2_y  y.max = $BPhen_y

elec num = 1 name = anode material = Aluminum y.min = 0.0
y.max = $Al_y
elec num = 2 name = cathode material = Silver y.min = $BPhen_y
y.max = $Ag_y

interface s.m y.min = $Al_y-0.001 y.max = $Al_y+0.001
interface s.s thermionic y.min = $TTB_y-0.001 y.max =
$TTB_y+0.001
interface s.s thermionic y.min = $NPB_y-0.001 y.max =
$NPB_y+0.001
interface s.s thermionic y.min = $MADN_y-0.001 y.max =
$MADN_y+0.001
interface s.s thermionic y.min = $BAlq2_y-0.001 y.max =
$BAlq2_y+0.001
interface s.m y.min = $BPhen_y-0.001 y.max = $BPhen_y+0.001

doping uniform region = 1 conc = 4e18 p.type
doping uniform region=3 conc=4.26e18 p.type
doping uniform region=3 conc=4.26e18 n.type
doping uniform region = 5 conc = 2e18 n.type

material region=1 user.default=organic
user.group=semiconductor eg300=$TTB_eg300 permittivity=3.1
affinity=$TTB_affinity ntc.gauss=6.2e20 sigc.gauss=0.1
ntv.gauss=6.2e20 sigv.gauss=0.1 GNTV.GAUSS=7.83e19
GSIGV.GAUSS=0.05 GDEV.GAUSS=-0.27 lds.exciton=$O_LDSEXCITON
taus.exciton=$O_TAUSEXCITON rst.exciton=$O_RSTEXCITON
material region=2 user.default=organic
user.group=semiconductor eg300=$NPB_eg300 permittivity=3.42
affinity=$NPB_affinity ntc.gauss=1.24e21 sigc.gauss=0.11
ntv.gauss=1.24e21 sigv.gauss=0.11 rst.exciton=$O_RSTEXCITON
lds.exciton=$O_LDSEXCITON taus.exciton=3.6e-9
material region=3 user.default=organic
user.group=semiconductor eg300=$MADN_eg300
affinity=$MADN_affinity permittivity=3.1 ntv.gauss = 1.6e21
ntc.gauss=1.6e21 sigv.gauss=0.1 sigc.gauss=0.1
GNTV.GAUSS=4.26e19 GSIGV.GAUSS=0.05 GDEV.GAUSS=$TBPe_EA
```

```
GNTC.GAUSS=4.26e19 GSIGC.GAUSS=0.05 GDEC.GAUSS = $TBPe_ED
rst.exciton=$O_RSTEXCITON lds.exciton=$O_LDSEXCITON
taus.exciton=$O_TAUSEXCITON
material region=4 user.default=organic
user.group=semiconductor eg300=$BAlq2_eg300 permittivity=3.8
affinity=$BAlq2_affinity ntv.gauss=3e21
ntc.gauss=3e21 sigv.gauss=0.09  sigc.gauss=0.09
rst.exciton=$O_RSTEXCITON lds.exciton=$O_LDSEXCITON
taus.exciton=$O_TAUSEXCITON
material region=5 user.default=organic
user.group=semiconductor eg300=$BPhen_eg300 permittivity=2.92
affinity=$BPhen_affinity ntv.gauss=2.19e21 ntc.gauss=2.19e21
sigv.gauss=0.1  sigc.gauss=0.1
GNTC.GAUSS=1.14e20 GSIGC.GAUSS=0.05 GDEC.GAUSS =-0.18
rst.exciton=$O_RSTEXCITON lds.exciton=$O_LDSEXCITON
taus.exciton=1.1e-9

models pfmob langevin  excitons  print  temperature = $temp

mobility region = 1 mun0=2e-7*exp(30*$TTB_thick) mup0=1.2e-
6*exp(30*$TTB_thick) gammap.pfmob =-5e-3 gamman.pfmob =-5e-3
TON.PFMOB=540 TOP.PFMOB=540 e0n.pfmob=2e7 e0p.pfmob=2e7
mobility region = 2 mun0=3e-11*exp(87.1*$NPB_thick) mup0=2e-
11*exp(87.1*$NPB_thick) gammap.pfmob=-2e-2 gamman.pfmob=-2e-2
TON.PFMOB=540 TOP.PFMOB=540 e0n.pfmob=2e7 e0p.pfmob=2e7
mobility region = 3 mun0=1e-9*exp(40*$MADN_thick) mup0=1e-
9*exp(40*$MADN_thick) gammap.pfmob=-1.3e-2 gamman.pfmob=-1.3e-
2 TON.PFMOB=540 TOP.PFMOB=540 e0n.pfmob=2e7 e0p.pfmob=2e7
mobility region = 4  mun0=2.4e-7*exp(90*$BAlq2_thick) mup0=6e-
8*exp(90*$BAlq2_thick) gamman.pfmob=-8.6e-3 gammap.pfmob=-
8.6e-3 TON.PFMOB=540 TOP.PFMOB=540 e0n.pfmob=2e7 e0p.pfmob=2e7
mobility region = 5 mun0=3e-6*exp(26.9*$BPhen_thick) mup0=3e-
8*exp(26.9*$BPhen_thick) gamman.pfmob=-1.2e-3 gammap.pfmob=-
1.2e-3 TON.PFMOB=540 TOP.PFMOB=540 e0n.pfmob=2e7 e0p.pfmob=2e7

odefects region = 1 cont ha=1e18 hd=1e18 tca=1200 tcd=1200
numa=30 numd=30
odefects region = 2 cont ha=1e18 hd=1e18 tca=1200 tcd=1200
numa=30 numd=30
odefects region = 3 cont ha=1e18 hd=1e18 tca=1200 tcd=1200
numa=30 numd=30
odefects region = 4 cont ha=1e18 hd=1e18 tca=1200 tcd=1200
numa=30 numd=30
odefects region = 5 cont ha=1e18 hd=1e18 tca=1200 tcd=1200
numa=30 numd=30


ointdefect s.s cont y.min = $TTB_y-0.001 y.max = $TTB_y+0.001
numa=24 numd=24 ha=1.4e10 hd=1.4e10 tca=5500 \
tcd=5500 sigae=1e-16 sigah=1e-14 sigde=1e-14 sigdh=1e-16
ointdefect s.s cont y.min = $NPB_y-0.001 y.max = $NPB_y+0.001
numa=24 numd=24 ha=1.4e10 hd=1.4e10 tca=5500 \
```

```
tcd=5500 sigae=1e-16 sigah=1e-14 sigde=1e-14 sigdh=1e-16
ointdefect s.s cont y.min = $MADN_y-0.001 y.max =
$MADN_y+0.001 numa=24 numd=24 ha=1.4e10 hd=1.4e10 tca=5500 \
tcd=5500 sigae=1e-16 sigah=1e-14 sigde=1e-14 sigdh=1e-16
ointdefect s.s cont y.min = $BAlq2_y-0.001 y.max =
$BAlq2_y+0.001 numa=24 numd=24 ha=1.4e10 hd=1.4e10 tca=5500 \
tcd=5500 sigae=1e-16 sigah=1e-14 sigde=1e-14 sigdh=1e-16

contact name = anode resistance = 2.5*$Shape_Factor*1e6
contact name = cathode resistance = 2.5*$Shape_Factor*1e6

method newton itlimit = 50 autonr

output u.langevin u.radiative e.field j.total con.band
val.band band.param charge e.mobility h.mobility gaussian.band
e.velocity h.velocity

save outfile = $"logfile"_structure.str

solve init
solve vanode=0
solve vanode=0.00125
solve vanode=0.0025
solve vanode=0.005
solve vanode=0.01

log outfile=LIV_$"logfile".log
save outfile = $"logfile"_0.01V.str

set v1 = 0.01
set v2 = 0.5
set nstep = 20

set s1 = exp(log($v2/$v1)/$nstep)
solve vstep = $s1 vmult vfinal=$v2 name = anode qscv
l.wave=0.495

set v3=1.0
set s2 = exp(log($v3/$v2)/$nstep)
solve vstep = $s2 vmult vfinal=$v3 name = anode  qscv
l.wave=0.495

set v4 = 2.0
set s3 = exp(log($v4/$v3)/$nstep)
solve vstep = $s3 vmult vfinal=$v4 name = anode  l.wave=0.495

set nstep = 25
set v5=4.0
set s4 = exp(log($v5/$v4)/$nstep)
solve vstep = $s4 vmult vfinal=$v5 name = anode qscv
l.wave=0.495 outfile=4V_DC.sta MASTER ONEFILEONLY
```

```
set nstep=30
set v7 = 6.0
set s6 = $s4
solve vstep = $s6 vmult vfinal=$v7 name = anode l.wave=0.495
outfile=6V_DC.sta qscv MASTER ONEFILEONLY

set nstep=30
set v7b = $vf
set s6b = exp(log($v7b/$v7)/$nstep)
solve vstep = $s6b vmult vfinal=$v7b name = anode l.wave=0.495
qscv

set nstep = 50
set v8 = $vf
set s7 = exp(log($v8/$v7)/$nstep)
save outfile=$"logfile"_$"vf"V.str

LOAD INFILE = 6V_DC.sta

log outfile = LIV3_$"logfile".log

extract init inf="LIV_$"logfile".log"

set fs = 6e6
set fstart = 30e3
set nfs = 100

if cond = ($size = "L")
      loop steps = 13
      stmt l1 = 1:1
      assign name = i1 n.value = (1, 3, 5, 8, 10, 15, 20, 25,
30, 35, 40, 45, 50)
      extract name="v$l1" x.val from curve(v."anode",
1e3*i."anode") where y.val = $i1
      solve vanode = $v$"l1" name = anode AC freq = $fstart
fstep=(($fs-$fstart)/$nfs) nfsteps = $nfs l.wave=0.495
      l.end
if.end

quit
```